Micro-fabricated Diffractive Optics for Quantum Sensors and Atomic Clocks

James P. McGilligan

Abstract

This thesis describes the design, construction and experimental realisation of a cold-atom, atomic clock. Diffractive optics are used to address the size constraints of the typical laser cooling apparatus to facilitate a portable device. The design and measurement of a wide range of grating parameters, including period, duty cycle, etch depth, and coating are characterised for optimum performance in a cold-atom system.

The grating magneto-optical trap (GMOT) demonstrates an atom number and temperature competitive with state-of-the-art experiments, while greatly simplifying the optical footprint. The compact nature of the GMOT facilitates proof-of-principle quantum sensing for future miniaturised atomic devices and instruments. These initial measurements include in situ magnetometry from compensating effects of homogeneous and inhomogeneous magnetic fields. Coherent population trapping was studied on the D_1 line of rubidium to realise a high contrast superposition state for clock measurements. These initial clock measurements lead to the development of a microwave regime atomic clock, based on a Raman-Ramsey interrogation of the clock states. The theory and construction of this clock are discussed, with an outlook to the development and demonstration of a second generation experiment.
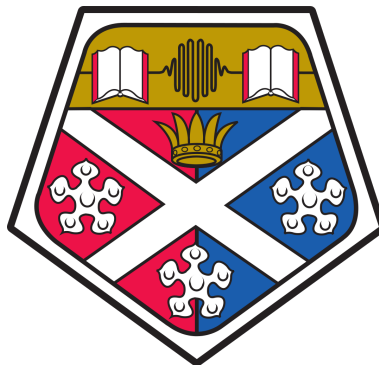
Supervisors: Dr. Aidan S. Arnold,
Prof. Erling Riis,
Dr. Paul F. Griffin.

Examiners: Prof. William D. Phillips,
Prof. Andrew Daley.

Micro-fabricated Diffractive Optics for Quantum Sensors and Atomic Clocks

James P. McGilligan

A thesis submitted in partial fulfilment
of the requirements for the degree of
Doctor of Philosophy

Department of Physics
University of Strathclyde

August 16, 2017

Contents

Declaration

I confirm that no part of the material offered has previously been submitted by myself for a degree in this or any other University. Where material has been generated through joint work, the work of others has been indicated.

James P. McGilligan
Glasgow, August 16, 2017

Acknowledgements

Now, following the completion of my thesis I have the opportunity to look back and thank all the people who have helped me reach this stage.

Paraphrasing Isaac Newton, I believe that one can only see so far when standing on the shoulders of giants. The first giants, to whom I owe a huge debt of gratitude to, are my supervisors, Aidan, Erling and Griff. During my PhD I have learned invaluable skills and knowledge passed down from these three, such that any achievements from my current and future career in physics are owed to them. They have always been a source of knowledge and motivation, where I have never found their doors to be shut or their positivity to be hindered. More than teaching physics, they have created a friendly and exciting work environment, that I have had the pleasure of being part of during the past four years of my studies. Cheers guys!

As well as my supervisors, the EQOP team at Strathclyde is composed of numerous other academics, engineers and PhD students, all of whom I am grateful for their contribution to making my PhD years such an enjoyable experience, especially those who have had to endured sharing a lab or office with me through that time. Thanks to all those from the team who filled the four years in EQOP with football games, camping trips, paintball tournaments and occasionally physics.

I have been lucky enough to not only have my parents and brothers support, but to be born into a large family, full of amazing people who have always encouraged me from an early age to push for whatever I wanted in life. These people have drove me and made me who I am today, with my achievements being heavily owed to them.

The largest and earliest giant in my life, who has encouraged me from day one, is my mum. Mum, you have supported me my whole life, always believing in me and making sacrifices to help me and give me the best possible chance at life. I owe you not only for my academic achievements, but for any and all happy events in the life that you made for me. I could not have asked for a more amazing role model and mum, thank you.

Christina, firstly I owe you for putting up with me during stressful times of my studies, that on its own is a hard job. You have been an amazing pillar of strength and kindness, carrying me at times to where I am today. I am indebted to you for your patience, support and love throughout the years, always lifting my head in hard times and being a source of motivation. I know no matter what I do next, I will have your support as we tackle our next adventures together.

For your time, companionship and love,
this thesis is dedicated to Bobby McGilligan.

Chapter 1

Introduction

1.1 Early measurements of time

Precision measurement has become an integral part of our everyday lives. From setting an alarm, driving to work, connecting to the internet, or cooking our dinner, the importance of metrological measurements in our daily routine is not immediately obvious but remains vital, none arguably more so than the measurement of time. Increased timing capabilities have shaped the technological evolution of ancient civilisations; over the past century we have gained an order of magnitude, on average, on timing precision every decade [1]. This work should be clearly seen as going hand-in-hand with the concurrent technological developments in science and communications.

Throughout history, clocks have appeared in many shapes and sizes, all building upon the same simple concept of an oscillator and a counter. The oscillator is the component of the clock with a periodic behaviour, producing a consistent frequency. The counter is simply the component that records this period to indicate the passage of time.

The understanding of clock fundamentals can be dated back to early man's

| Celestial | Sundial | Pendulum | Quartz | Atomic |
| 5000 BCE | 3500 BCE | 1656 | 1920 | 1948 |
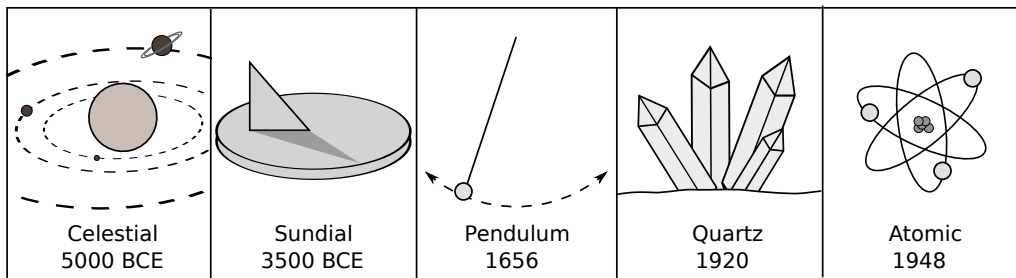
Figure 1.1: Graphical representation of the five key clock advancements through history

inquisitiveness at the period of celestial bodies. These celestial oscillations would have very low frequencies, making it easy for early man to count the oscillations. The ancient Sumerians of Tigris-Euphrates, in today's Iraq, used the position of the sun and moon as early as 5,000 BC to break the year into 12 months of 30 days [2]. This accuracy of time would have greatly benefited early man by providing foresight of the seasons, allowing provisions to be made for crop harvest and could be associated with animal migration to prepare for seasonal hunts.

The next notable advancement of the clock was not until 3,500 BC, when the Egyptians developed the sundial [3]. The sundial would map the position of the sun in the sky, relative to north or south, through the angle of the shadow it casts on a stationary object. The Egyptians learned that they could then use this shadow to estimate the length of a day and their position in the cycle of that day. The drawback of the sundial was that it only worked during the day. This was a problem for time keeping at night, which was required by religious leaders who needed time information for nightly prayer. It was because of this that the Egyptians developed the water tower clock [3, 4]. This was typically a tower that, once filled with water, was designed to take one hour to empty. A simple structure like this presented the Egyptians with a timing accuracy on the order of one hour.

The mechanical era of the clock began in the 16th century with the realisation of the pendulum. Galileo was the first to note the relation between the period of a pendulum relative to the length of the oscillator. The pendulum clock was pioneered in 1656 by C. Huygens, who created the escapement, a device aimed at maintaining the motion of a swinging pendulum for long time periods. The pendulum could then swing with a stable period that was read out by mechanical gears, controlling the motion of the clock arms [5]. The work produced by Huygens paved the way for the development of John Harrison's marine chronometer and a viable solution to the longitude problem. The ability to define a timing accuracy to one second on a portable clock revolutionised navigation, with sailors now capable of using time to determine their longitude through comparison of their local time with that at their origin point [6].

The early work on the pendulum was further improved in the 1920s by a railroad engineer by the name of W. H. Shortt. Shortt devised the idea of using two pendula, one of which was used in a low pressure environment and infrequently perturbed only to maintain the accuracy of the other 'slave' pendulum [5]. The key technological outcome here was not necessarily the improved timing accuracy, but rather the idea of a 'master' clock using an electrical signal to synchronise an array of 'slave' clocks. This led to a common time through networks of clocks controlled by a single master time keeper, ultimately providing stability and increased precision to transportation services and railway networks.

Around the same time J. W. Horton and W. A. Marrison from Bell Laboratories developed the first quartz crystal oscillator clock. This clock was based on the piezo-electric effect, where the application of an AC voltage would induce elastic vibrations across the quartz crystal that could be implemented as an electronic oscillator. Alternatively, if an oscillation or strain

is applied, the quartz will produce an oscillating voltage that can be stabilised with electronic feedback. An electronic counter was implemented to assess the oscillation period, as a time standard. The measured timing error from the initial quartz studies provided a drift of 0.1 milliseconds a day [5]. Frequency standardisation to this level played a pivotal role in the technological capabilities of computers and digital control systems throughout the 20$^{\text{th}}$ century.

The quest for more accurate time was motivated by the timing requirement in applications such as precision measurements, laboratory calibration, navigation, and frequency standardisation in modern technology. This push led to the currently most accurate method for measuring the passage of time: the atomic clock.

1.2   Realisation of an atomic clock

The basis of the atomic clock is to read out an atomic resonance as the clock oscillator. The motivation to use atoms as an oscillator is that, unlike oscillators of the past, atoms will not wear out and, assuming the atom is unperturbed by external fields, will continuously produce the same oscillation frequency for a given transition.

Accuracy

In 1913 Bohr introduced the hydrogen model, based around the idea that atomic energy levels have distinct values. These energy levels, separated in energy by $E = hf$, where h is Plancks constant and f a frequency, could be accessed and probed via absorption and emission processes to produce electromagnetic energy at the frequency, f [7]. The accuracy of the atomic clock is derived from measuring the atomic frequency when the internal atomic
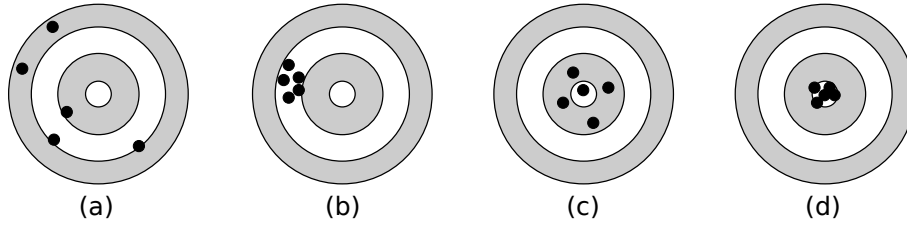
Figure 1.2: Target-board representation of four precision vs. accuracy scenarios. (a): Not accurate or precise. (b): Precise but not accurate. (c): Accurate but not precise. (d): Accurate and precise.

states are free from external perturbation. The ultimate achievable accuracy for an atomic clock will depend on the clock transition's sensitivity to perturbations and shifts, such as magnetic and optical shifts, which are discussed later. However, an accurate clock does not imply a precise clock, see the illustration of the difference in Fig. 1.2.

Precision

The precision or stability of the clock represents the reproducibility of a frequency measurement over a given time period. This is typically defined by the Allan variance of the clock. This technique, discussed in detail later in Sect [12.5], is the *IEEE Board of Frequency and Time's* selected statical analysis method for the performance of an oscillator with a specific number of oscillators, N, over an integration period, τ [4, 8, 9]. The stability for an atomic clock utilising a Ramsey-spectroscopy based experiment, discussed later in Sect. [12], is ultimately limited by the quantum-projection-noise-limit,

$$\sigma_y(\tau) = \frac{1}{Q}\sqrt{\frac{T_c}{\tau}}\frac{1}{\sqrt{N}}, \tag{1.1}$$

where T_c is the cycle time for each measurement, and Q is the quality factor defined as

$$Q = \frac{f_o}{\Delta f_a}, \tag{1.2}$$

where f_o is the resonance frequency and Δf_a is the width of the resonance frequency distribution. Thus one can summarise that it would be preferable to have a large f_o and small Δf_a.

Timeline

Lord Kelvin is thought to have been the first to suggest using atoms as clock oscillators, as early as 1879 [5]. However, the first atomic clock based on firm principles was not proposed until 1939 by I. Rabi, following his publishing of 'The Molecular Beam Resonance Method for Measuring Nuclear Magnetic Moments' [10]. Rabi concluded that one could use the magnetic resonance in an atomic beam as a spectroscopic technique for an atomic clock, with his spectroscopic methods earning him the Nobel prize in 1944. His proposed atomic clock was based upon caesium atoms as the atomic oscillator, however the first working atomic oscillator was instead based on a quartz crystal oscillator stabilised by a resonance transition in ammonia molecules, capable of a relative timing stability at 2×10^{-8}. This was created by H. Lyons at the United States National Bureau of Standards, NBS, and was used as a frequency standard from its first operation in 1948 [5]. The evolution of the atomic clock from Lyons first demonstration is illustrated in Figure 1.3 where the relative uncertainty is plotted against the year the clock was demonstrated.

Around the same time that Lyons demonstrated the ammonia frequency standard, Norman Ramsey published a critical improvement to Rabi's clock technique, known as the separated oscillatory field method, or to everyone else as the Ramsey method [11]. In Rabi's method, the atomic resonance was measured with a single, long resonance region, leading to Doppler shifts and power broadening among other uncertainties. Ramsey overcame this by using two short microwave pulses sequentially, narrowing the measured reso-
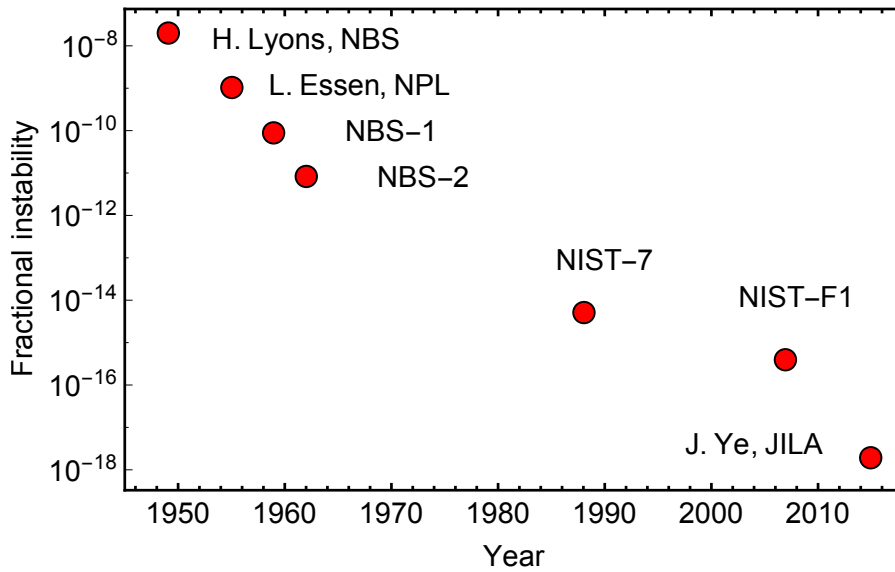
Figure 1.3: Timeline of the fractional instability of atomic clocks over the years

nance by orders of magnitude [12]. This technique involved the imparting of phase information into an atomic state, which is allowed to precess freely for a given time, T, then probed with a second pulse to map the phase information back into population. This measurement technique resulted in a frequency linewidth inversely proportional to the phase evolution time, $\Delta f_a = 1/(2T)$, discussed in more detail in Sect. [12.1].

Shortly after Ramsey published this technique, the Lyons team at NBS and a team lead by L. Essen at the United Kingdom's National Physical Laboratory, NPL, demonstrated the first caesium atomic clock resonances in 1952 and 1955 respectively. This worked by measuring the ground-state hyperfine splitting in a thermal caesium beam, demonstrating a clock with an accuracy exceeding that of a quartz clock for the first time with an uncertainty of 1×10^{-9}. The advanced measurement capabilities were recognised in 1967 with the redefinition of the second to 9,192,631,770 periods of the hyperfine splitting in the ground state of a caesium 133 atom [5, 13]. The Lyons experiment became the national time standard and was named NBS-1.

Between then and 1988, NBS/NIST improved the apparatus through optical state selection, increased vacuum capabilities and other techniques until demonstration of NIST-7, which could provide accuracy of 1 nanosecond per day. This was the most accurate time standard until the introduction of the atomic fountain, initially demonstrated in 1989 by S. Chu at Stanford [14]. This experimental technique used a cold atomic sample, launched into a ballistic path, with the resulting long interrogation times providing narrow linewidths. Furthermore, the low velocity spread in cold atoms further reduced frequency shifts, hindering the performance of thermal atom clocks at the time. The atomic fountain clocks that were later developed, soon superseded the caesium beam clock as a national time keeper, with teams in NPL, NIST and SYRTE each developing fountains capable of integrating down to a fractional instability of 10^{-15} [15].

Since these clocks probe the microwave transitions of caesium, further precision is to be gained by implementing a larger Q factor; made possible by increasing the transition frequency into the optical domain [16]. The potential of optical frequency standards was vastly improved in 2005 when H. Katori *et al.* published 'An optical lattice clock' [17] and revolutionised the attainable stability of neutral atom clocks by initially taking advantage of the optical transitions available in laser cooled Yb and Sr, whilst using the 'magic wavelength' properties of an optical lattice to free the atoms from trapping perturbations [17–19].

Simultaneous to the neutral atom clock advancements, the measurement accuracy of the ion atom clock was catching up. Since the electrostatic trapping of ionised atoms was demonstrated by H. Dehmelt and W. Paul in the 1950's, there had been a large research propagation towards the realisation of ion clocks [1]. Following the realisation of cold ion trapping, with single ion trap

lifetimes vastly exceeding their neutral atom counterparts, continuous operation microwave clocks were demonstrated in 1980, realising a frequency stability of 3.6×10^{-11} [20]. The achievable precision of ion clocks was vastly improved by the probing and addressing of optical states made available in species such as Al^+, Hg^+ and Yb^+ [21–23].

A notable contribution to the readout and feedback of optical transitions was with the realisation of the optical frequency comb, used to down convert optical frequencies to electronic counters in the microwave range [24, 25]. The optically addressable transitions available in neutral and ionised atoms have since produced clocks capable of producing a timing precision to the 10^{-18} level [18, 26–29]. Measurements at this level permit testing fundamental physics, such as general relativity and variations in the fine structure constant [26, 30].

1.3 Realisation of a compact neutral atom clock

Precise frequency metrology has played a critical role in the development of modern technological capabilities such as telecommunication, global navigation satellite systems (GNSS), manufacturing and cyber security. More importantly, precision metrology is a scientific driver to understand the subtle discrepancies occurring between experiment and theoretical predictions for fundamental physics. With the current clocks used in satellites and industrial systems becoming aged, the UK is actively pursuing new modalities to enable future innovation.

With global cyber security predicted to be worth £164 billion by 2021 and GNSS currently driving a £21 billion industry [31], a large emphasis has been

placed on international institutions to target this market with miniature atomic clocks. Currently, like many precision metrological devices, GNSS systems require an atomic clock reference to provide the accuracy that is often sought after for navigation, geological studies, civil engineering and time stamping. To tackle this problem effectively, these institutions must understand the necessity for future devices to meet the size, weight and power consumption required to have the greatest technological impact.

The most notable advancement in this field to-date, was the development of the Chip-Scale-Atomic-Clock, CSAC in the team of J. Kitching and L. Hollberg at NIST [32]. Kitching and Hollberg realised a micro-fabricated clock package containing all optics, photo-detectors, vapour cell and vertical-cavity surface-emitting laser, VCSEL. Frequency modulation of the VCSEL provided the microwave sideband used to complete the three-level atomic structure sought after for coherent population trapping, CPT, in a Cs vapour. CPT, discussed in detailed in Sect. [2.4], was used to generate a narrow frequency reference via dark state pumping in a Λ configuration of the internal atomic levels. The micro-scale vapour cell was constructed using microelectromechanical systems, MEMS, techniques and anodic bonding [32], containing Cs and a buffer gas mixture to minimise decoherence effects from atom-wall collisions [33]. The CSAC was later commercially replicated by Microsemi (Symmetricom) into a <17 cm^3 package, requiring <120 mW of power with an Allan variance at 1 hour of $\sigma_y(\tau) = 5 \times 10^{-12}$ [34].

In the past decade a number of teams have also demonstrated compact atomic clocks, covering a variety of oscillators, achievable scalability and short term performance, as given in Table 1.1. Recent developments from NIST have focussed on the long-term stability of compact clocks by moving to Raman-Ramsey interrogation of cold atoms, with recent results demonstrating measurements at 10^{-13} in a litre-scale package. The increased scale

Table 1.1: Miniature atomic clock teams

Team	Oscillator	Scale (W m^3)	σ_τ@100s	Citation
McGilligan (Strathclyde)	Cold ^{87}Rb		1×10^{-11}	This thesis
Kitching (NIST)	Cold ^{87}Rb		1.8×10^{-12}	[35, 36]
Muclock (Muquans)	Cold ^{87}Rb	50	2×10^{-14}	[37]
CSAC (Microsemi)	^{87}Rb vapour	2×10^{-6}	3×10^{-11}	[32, 34]
Boudot (FEMTO-ST)	Cs vapour		2.3×10^{-13}	[38]
de Clercq (LNE-SYRTE)	Cs vapour		3×10^{-13}	[39]

of the cold atom clock is due to the scalability of vacuum requirements as well as the optical area required for laser cooling.

Alternatively, the teams at SYRTE and FEMTO-ST use existing, well established vapour cell technology and buffer gas mixtures to achieve highly precise frequency standards [38–41]. To maintain coherence within the atomic vapour long enough to make useful clock measurements, typically requires the presence of a buffer gas mixture or specially coated cell windows. However, the introduction of buffer gasses leads to temperature dependent pressure shifts, which require stabilisation and active monitoring. A further limitation to the achievable accuracy in vapour cells arises due to cell coatings, such as paraffin, degrading over time. The degradation of cell coatings results in a time dependent increase to the number of decoherence events caused by atom-wall collisions.

During my PhD, I focussed my efforts onto the development of a compact atomic clock that exceeds the stability of small-scale predecessors by using cold atoms. The implementation of cold atoms gains orders of magnitude in accuracy due to avoiding the perturbations required for the interrogation of their thermal counterparts. With this in mind, I used the knowledge of grating magneto-optical traps, developed at Strathclyde [42], to realise a scalable compact cold-atom source that I could use as a micro-fabricated platform for

precision measurements.

1.4   Thesis layout

This document is divided into four sections, leading to the development of the compact, cold-atom clock. Part 1 explores the atomic theory required in understanding the physics of an atomic clock. Part 2 focuses on the design and characterisation of the diffractive optics as the basis of a compact apparatus. Part 3 discusses the construction of a cold-atom platform using the diffractive optics, characterising the performance achievable in such a system, as well as proof of principle experiments made possible on such a platform. Finally, part 4 consolidates the previous work into the demonstration of a functioning clock based on a simple Raman-Ramsey sequence.

Part I: Theory

- Chapter 2 develops the foundations for a theoretical understanding of the atomic interactions that induce optical and magnetic shifts, as well as the preparation of superposition states via coherent population trapping.

- Chapter 3 provides a comprehensive study of laser cooling and trapping techniques required for cold atom generation.

Part II: Compact optics

- Chapter 4 introduces the routes that have been taken, leading to the design of micro-fabricated diffractive optics, that are optimised for generating balanced radiation pressure.

- Chapter 5 characterises the grating diffraction efficiency and critical parameters for optimising the next generation of diffractive optics.

Part III: Cold atoms

- Chapter 6 discusses the construction of the laser cooling apparatus, spectroscopic techniques and vacuum preparation.

- Chapter 7 looks at implementing the gratings into a laser cooling set-up, and defining the critical parameters of atom number and temperature

- Chapter 8 focusses on the maximum achievable atom number from studying the phase space of our system.

- Chapter 9 implements the grating MOT as a compact platform for quantum sensing. This study includes using Larmor precessions to null static and gradient fields for a low temperature molasses. Finally, a neutral atom array is generated from a single incident laser coupled to a grating with patterned magnetic coils.

Part IV: An atomic clock

- Chapter 10 begins our study of coherent population trapping in a thermal system, leading to the construction of the clock apparatus

- Chapter 11 develops a further understanding of the theory and experimental realisation of high contrast coherent population trapping in the grating magneto-optical trap.

- Chapter 12 introduces the Raman-Ramsey technique as a method for generating narrow fringes in the frequency domain, whose stability is determined using an Allan variance of the measured frequency to verify the performance of our compact, cold-atom clock.

Part V: Conclusions

- Chapter 11 consolidates the work discussed throughout this thesis with an outlook to future miniaturisation.

1.5 Publications arising from this work

- J. P. Cotter, J. P. McGilligan, P. F. Griffin, I. M. Rabey, K. Docherty, E. Riis, A. S. Arnold and E. A. Hinds, *Design and fabrication of diffractive atom chips for laser cooling and trapping,* Applied Phys. B. **122**, 1-6 (2016).

- J. P. McGilligan, P. F. Griffin, E. Riis and A. S. Arnold, *Diffraction grating characterisation for cold atom experiments*, J. Opt. Soc. Am.. **33**, 1271-1277 (2016).

- J. P. McGilligan, P. F. Griffin, E. Riis and A. S. Arnold, *Phase-space properties of magneto-optical traps utilising micro-fabricated gratings* , Opt. Exp. **23**, 8948-8959 (2015).

- J. P. McGilligan, P. F. Griffin, R. Elvin, S. J. Ingleby, E. Riis and A. S. Arnold, *Grating chips for quantum technologies* ,Scientific Reports. **7**, 384 (2017).

- J. P. McGilligan, R. Elvin, P. F. Griffin, E. Riis and A. S. Arnold, *Utilising diffractive optics towards a compact cold atom clock*, IEEE Explore 2016 European Frequency and Time Forum (EFTF), 1-2 (2016).

- J. P. McGilligan, P. F. Griffin, E. Riis and A. S. Arnold, *A compact cold-atom clock based on Lin⊥Lin Raman-Ramsey method*, in preparation (2017).

1.6 Conferences

- European Group on Atomic Systems 2014, Lille, France. Grating chips for quantum technologies. **(Poster Presentation)**

- Division of Atomic, Molecular and Optical Physics 2015, Columbus, Ohio, USA. Grating chips for quantum technologies. **(Oral Presentation)**

- NIST/JILA 2015, Boulder, Colorado, USA. **(Invited Speaker)**

- European Frequency and Time Forum 2016, York, UK. Utilising diffractive optics towards a compact cold atom clock. **(Oral Presentation)**

- CNES Workshop on Miniature Atomic Clocks, 2016, Paris, France. **(Invited Speaker)**

1.7 Outreach and public engagement

- International year of light ceremony. Royal Society of Edinburgh. Portable magneto-optical trap live demonstration (2015)

- Pint of Science. **Invited speaker** on atomic clocks (2016)

- Quantum Technology Showcase, London. Grating microwave atomic clock live demonstration (2016)

Part I

Theory

Chapter 2

Atomic interaction with electromagnetic fields

Knowledge of the atomic state population and energy level shifts are required to thoroughly understand the mechanisms involved in developing a cold-atom clock. This chapter introduces a theoretical analysis of atomic interactions with optical and DC magnetic fields through the Schrödinger picture of a simple two-level atom. This leads to the optical Bloch equations, used to derive the populations, coherences and energy level shifts occurring for the two-level atom under external perturbation. Finally, the optical Bloch equations are extended to the three-level atom and the phenomenon of coherent population trapping.

2.1 The Schrödinger picture for a two-level atom

In this section we look at a simple two-level atom interacting with an electric field, coupling a ground state $|g\rangle$ to the excited energy level $|e\rangle$ separated in energy $\hbar\omega_{eg}$, as depicted in Fig. 2.1. The evolution of this two-level system

17
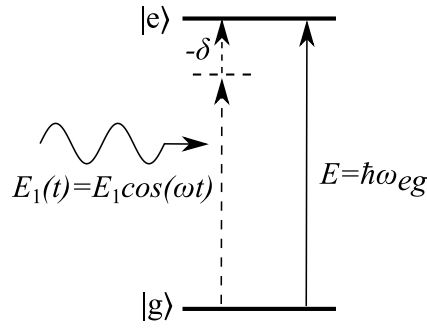
Figure 2.1: Energy levels of a two-level atom linked by one laser field, with angular frequency ω and detuning from resonance δ.

is governed by the time-dependent Schrödinger equation,

$$i\hbar \frac{d}{dt}|\Psi\rangle = \mathcal{H}|\Psi\rangle, \tag{2.1}$$

where we can describe the wavefunction at any time t in Dirac notation,

$$|\Psi(r,t)\rangle = \sum_n c_n(t)|n\rangle e^{-i\omega_n t} = c_e(t)e^{-i\omega_e t}|e\rangle + c_g(t)e^{-i\omega_g t}|g\rangle, \tag{2.2}$$

where c_e and c_g are the atomic excited and ground states amplitudes respectively, and $|n\rangle$ is the energy level with internal energy, $E_n = \hbar\omega_n$.

Combining Eqns. (2.2) and (2.1) provides a simple interpretation of the time-dependent state amplitudes such that,

$$i\hbar \dot{c}_k(t) = \sum_n c_n(t)e^{-i\omega_{nk} t}\langle k|\mathcal{H}|n\rangle. \tag{2.3}$$

Under the dipole assumption, we assume that the wavelength of the incident electric field is much larger than the size of the atom, such that the incident electric field can be regarded as a plane wave, $\vec{E}_1(t) = \vec{E}_1 \cos(\omega t)$, where one can describe the interaction with the atomic electric dipole, $\vec{d}$, through the interaction Hamiltonian,

$$H_i = -\vec{d} \cdot \vec{E}_1(t) = -\vec{d} \cdot \vec{E}_1 \cos(\omega t). \tag{2.4}$$

Substituting Eqn. (2.4) into Eqn. (2.3) results in the rate equations:

$$i\dot{c}_g(t) = \Omega e^{-i\omega_{eg}t}\cos(\omega t)c_e(t) = \frac{\Omega}{2}\big(e^{i(\omega_{eg}-\omega)t} + e^{-i(\omega_{eg}+\omega)t}\big)c_e(t), \qquad (2.5)$$

$$i\dot{c}_e(t) = \Omega e^{i\omega_{eg}t}\cos(\omega t)c_g(t) = \frac{\Omega}{2}\big(e^{i(\omega_{eg}+\omega)t} + e^{-i(\omega_{eg}-\omega)t}\big)c_g(t), \qquad (2.6)$$

where $\Omega = -\vec{E}_1\frac{\langle e|\vec{d}|g\rangle}{\hbar}$ is the Rabi frequency, ω_{eg} is the resonance frequency, and $e^{i\omega t}/e^{-i\omega t}$ represent the emission/absorption of a photon for that state respectively.

At this point, the rotating wave approximation, RWA, is applied to eliminate fast oscillation terms that do not contribute to the dynamics of the system on the time scales of concern in the experiments reported here [7]. The remaining frequency components can be simplified further by defining $\delta = \omega - \omega_{eg}$,

$$i\dot{c}_g(t) = c_e(t)\frac{\Omega}{2}e^{i\delta t}, \qquad (2.7)$$

$$i\dot{c}_e(t) = c_g(t)\frac{\Omega}{2}e^{-i\delta t}. \qquad (2.8)$$

Furthermore, if we introduce a new set of variables with time dependencies,

$$\tilde{c}_g(t) = c_g(t)e^{-i\frac{\delta t}{2}}, \qquad (2.9)$$

$$\tilde{c}_e(t) = c_e(t)e^{i\frac{\delta t}{2}}, \qquad (2.10)$$

then differentiating Eqns. (2.9)-(2.10) w.r.t time, reintroduces a time dependence such that [43],

$$i\dot{\tilde{c}}_g(t) = i\dot{c}_g(t)e^{-i\delta t/2} + \frac{\delta}{2}c_g(t)e^{-i\delta t/2}, \qquad (2.11)$$

$$i\dot{\tilde{c}}_e(t) = i\dot{c}_e(t)e^{i\delta t/2} - \frac{\delta}{2}c_e(t)e^{-i\delta t/2}. \qquad (2.12)$$

Combining Eqns. (2.7)-(2.12) yields a matrix description of the two-level atomic interaction as,

$$i\hbar \frac{d}{dt} \begin{pmatrix} \tilde{c}_g(t) \\ \tilde{c}_e(t) \end{pmatrix} = \frac{\hbar}{2} \begin{pmatrix} \delta & \Omega \\ \Omega & -\delta \end{pmatrix} \begin{pmatrix} \tilde{c}_g(t) \\ \tilde{c}_e(t) \end{pmatrix}. \tag{2.13}$$

2.2 Optical Bloch equations

Up until this point, we have described this system in the Schrödinger picture. However, as we move away from reversible processes to include dissipation, such as spontaneous emission, then the same system must be treated using the density matrix formalism.

To include the effect of spontaneous emission, the atom is considered to be coupled to a reservoir that permits the emission of a photon, and decay from excitation. The coupling of such as system is described by the Lindblad superoperator $\mathcal{L}(\rho)$ [44],

$$\mathcal{L}(\rho) = -\frac{1}{2}(\sigma^+\sigma^-\rho + \rho\sigma^+\sigma^-) + \sum \sigma^-\rho\sigma^+ \tag{2.14}$$

where $\sigma^- = \sqrt{\Gamma}|g\rangle\langle e|$ and its adjoint operator $\sigma^+ = \sqrt{\Gamma}|e\rangle\langle g|$, and ρ is the density matrix given as [45],

$$\rho = \begin{pmatrix} \rho_{ee} & \rho_{eg} \\ \rho_{ge} & \rho_{gg} \end{pmatrix} \tag{2.15}$$

where the diagonal elements represent the atomic state populations, and the off-diagonal elements are the atomic state coherences. This Lindblad form is required to preserve ρ as a density matrix, such that $\text{Tr}(\rho)=1$.

We begin by including the Lindblad formalism with the general form of the master equation, known as the Liouville equation, which is the density oper-

ator equivalent of the Schrödinger equation [46], given by,

$$\dot{\rho} = -\frac{i}{\hbar}[\mathcal{H}, \rho] - \mathcal{L}(\rho), \tag{2.16}$$

where the two-level Lindblad operator defined as:

$$\mathcal{L}(\rho) = \Gamma \begin{pmatrix} \rho_{ee} & -\rho_{ge}/2 \\ -\rho_{eg}/2 & -\rho_{ee} \end{pmatrix}. \tag{2.17}$$

With this master equation, one can derive the populations and coherences of a two-level system described in Eqn. (2.13), where ρ_{ee} is the excited state population, with the off-diagonal elements of the matrix ρ_{ge} and ρ_{eg} representing the states coherences, such that:

$$\frac{d}{dt} \begin{pmatrix} \rho_{ee} & \rho_{eg} \\ \rho_{ge} & \rho_{gg} \end{pmatrix} =$$

$$\frac{-i}{2} \left(\begin{pmatrix} \delta & \Omega \\ \Omega & -\delta \end{pmatrix} \begin{pmatrix} \rho_{ee} & \rho_{eg} \\ \rho_{ge} & \rho_{gg} \end{pmatrix} - \begin{pmatrix} \rho_{ee} & \rho_{eg} \\ \rho_{ge} & \rho_{gg} \end{pmatrix} \begin{pmatrix} \delta & \Omega \\ \Omega & -\delta \end{pmatrix} \right)$$

$$- \Gamma \begin{pmatrix} \rho_{ee} & -\rho_{ge}/2 \\ -\rho_{eg}/2 & -\rho_{ee} \end{pmatrix}. \tag{2.18}$$

Expanding Eqn. (2.18) produces the optical Bloch equations for a two-level atom [47],

$$\dot{\rho}_{ee} = \frac{i\Omega}{2}(\tilde{\rho}_{eg} - \tilde{\rho}_{ge}) - \Gamma \rho_{ee}, \tag{2.19}$$

$$\dot{\rho}_{gg} = \frac{i\Omega}{2}(\tilde{\rho}_{ge} - \tilde{\rho}_{eg}) + \Gamma \rho_{ee}, \tag{2.20}$$

$$\dot{\tilde{\rho}}_{eg} = -\dot{\tilde{\rho}}_{ge} = \frac{i\Omega}{2}(\rho_{ee} - \rho_{gg}) + i\delta\tilde{\rho}_{eg} - \frac{\Gamma}{2}\tilde{\rho}_{eg}. \tag{2.21}$$
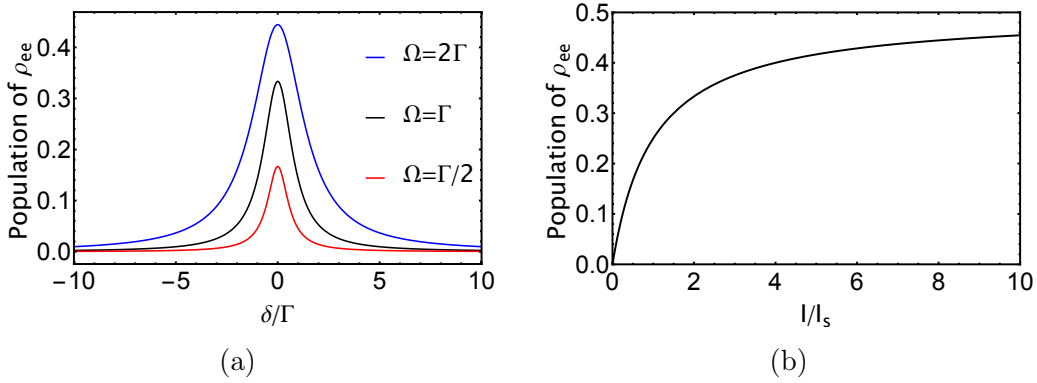
Figure 2.2: a):The excited state population of a two level atom with spontaneous emission for $\Omega = 2\Gamma, \Gamma$ and $\Gamma/2$ when $\delta/\Gamma = 1$. b):The excited state population as a function of the on resonance saturation parameter when $\delta = 0$.

Steady state

When the systems dynamics have damped out we reach the steady state, expressed analytically by setting the time derivative to zero such that $\dot{\rho} = 0$, and noting that $\rho_{ee} + \rho_{gg} = 1$ [48].

$$\rho_{ee} = \frac{1}{2} \frac{\Omega^2/2}{\delta^2 + (\Gamma/2)^2 + \Omega^2/2}, \tag{2.22}$$

$$\tilde{\rho}_{ge} = \frac{\Omega}{2} \Big(\frac{\delta}{\Omega^2/2 + (\Gamma/2)^2 + \delta^2} - \frac{i(\Gamma/2)}{\Omega^2/2 + (\Gamma/2)^2 + \delta^2} \Big). \tag{2.23}$$

The steady state allows us to look at an atom driven by a laser field with spontaneous emission. From Eqn. (2.22) we can plot the excited state population as a function of the detuning, δ, for a range of Rabi frequencies. Fig. 2.2 (a) illustrates a power broadening associated with the increased Rabi frequency, Ω, leading to a population saturation at $\rho_{ee} = \rho_{gg} = 0.5$.

Saturation parameter

Following Ref. [7], the saturation parameter, S, defines the population saturation of a chosen transition as a function of a incident field Rabi frequency,

Ω, such that,

$$S = \frac{\Omega^2/2}{\delta^2 + \Gamma^2/4} = \frac{s_0}{1 + (2\delta/\Gamma)^2}, \tag{2.24}$$

where s_0 is the on resonance saturation parameter, defined as:

$$s_0 = \frac{2\Omega^2}{\Gamma^2} = \frac{I}{I_s}, \tag{2.25}$$

where I is the laser intensity and I_s is the saturation intensity.

Substituting Eqn. (2.25) into Eqn. (2.22) describes the intensity required to saturate the excited state using,

$$\rho_{ee} = \frac{1}{2} \frac{I/I_s}{1 + I/I_s + (\frac{2\delta}{\Gamma})^2}. \tag{2.26}$$

The steady state saturation of ρ_{ee} is depicted in Fig. 2.2 (b), where the population of the excited state is depicted as a function of the on resonance saturation parameter. The excited state population reaches an asymptotic limit for larger I/I_s and is half of the maximum value at $I = I_s$.

2.2.1   Electric susceptibility

Derivation of the density matrix formalism can also be used to determine the absorption and dispersion coefficients of the atomic medium through the linear susceptibility, χ. The susceptibility of the medium is related to the polarisation, P, through [45]:

$$P = \epsilon_0 \chi \vec{E}(t) = \frac{\epsilon_0 \vec{E}}{2} (\chi \, e^{-i\omega t} + \chi^* e^{i\omega t}), \tag{2.27}$$

where ϵ_0 is the permittivity of free space, and $\vec{E}(t)$ is the incident electric field. The polarisation, described as the dipole moment per unit volume, is

represented by:

$$P = N \operatorname{Tr}(\rho\, d) = N\, d_{eg}(\tilde{\rho}_{eg} e^{-i\omega t} + \tilde{\rho}_{ge} e^{i\omega t}), \tag{2.28}$$

where N is the atomic number density, and d is the dipole operator.

Incorporating these equations permits calculation of the susceptibility as [45],

$$\chi = \frac{2Nd_{eg}^2}{\hbar\Omega\epsilon_0}\tilde{\rho}_{eg}. \tag{2.29}$$

Adding the result of $\tilde{\rho}_{eg}$ from the density matrix, Eqn. (2.23), allows the susceptibility to be broken down into the real and imaginary parts, $\chi = \chi_R + i\chi_I$,

$$\chi_R = \frac{Nd_{eg}^2}{\epsilon_0\hbar} \frac{\delta}{\Omega^2/2 + (\Gamma/2)^2 + \delta^2}, \tag{2.30}$$

$$\chi_I = \frac{-Nd_{eg}^2}{\epsilon_0\hbar} \frac{(\Gamma/2)}{\Omega^2/2 + (\Gamma/2)^2 + \delta^2}, \tag{2.31}$$

where χ_R and χ_I are the real and imaginary components of the susceptibility respectively.

The real and imaginary susceptibilities can be directly related to the refractive index of the medium, $n = \sqrt{1+\chi} \approx 1 + \chi/2 = n_R + n_I$. This relation is then used to determine the relative real and imaginary parts of the refractive index to the susceptibility:

$$n_R = 1 + \frac{\chi_R}{2}, \tag{2.32}$$

$$n_I = \frac{\chi_I}{2}. \tag{2.33}$$

These results are analogous to the familiar Kramers-Kronig relations, which show how the real and imaginary parts of the atomic mediums refractive

index, relating to the absorption and dispersion respectively, are directly proportional to the electric susceptibility [49].

2.3 Atomic shifts induced with optical fields

So far we have discussed light interaction with an atomic medium in the context of optical pumping and susceptibility. However, the light field interaction also imparts an atomic dipole moment, shifting the potential energy, which is known as the AC-Stark shift. To understand how light-atom interactions occur in the situation of an optical potential, we must first consider a two-level atom with a ground state $|g\rangle$ and excited state $|e\rangle$ separated in energy by $E = \hbar\omega_{eg}$, where ω_{eg} is the resonance frequency.

Such a system has been derived within the Schrödinger picture in Sect. [2.1], with the matrix form written as,

$$i\hbar\frac{d}{dt}\begin{pmatrix} \tilde{c}_g(t) \\ \tilde{c}_e(t) \end{pmatrix} = \frac{\hbar}{2}\begin{pmatrix} \delta & \Omega \\ \Omega & -\delta \end{pmatrix}\begin{pmatrix} \tilde{c}_g(t) \\ \tilde{c}_e(t) \end{pmatrix}, \tag{2.34}$$

with eigenenergies given by,

$$E = \pm\frac{\hbar}{2}\sqrt{\delta^2 + \Omega^2}. \tag{2.35}$$

If the Rabi frequency is small in comparison to the detuning, $\Omega \ll \delta$, then the effect of interactions on the ground and excited states must be determined with second order perturbation theory [46]. The energy shift experienced by the state is given as,

$$\Delta E = \pm\frac{\hbar\Omega^2}{4\delta}, \tag{2.36}$$

where plus and minus are designated to the ground and excited state of Fig. 2.3 respectively.
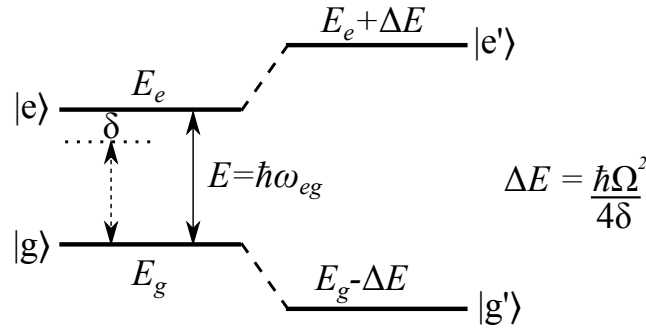
Figure 2.3: Energy levels of a two-level atom before and after perturbation from an external light field, detuned δ from resonance. Both states are shifted ΔE by the AC-Stark shift.

2.4 Coherent Population Trapping

The phenomena of coherent population trapping, CPT, was first observed by Alzetta *et al.* in 1976 [50] when they detected a drop in fluorescence when optically pumping sodium in a three-level Λ configuration. This was explained around the same time by the two separate theoretical groups of Arimondo and Orriols [51] and Whitley and Stroud [52]. Both groups noticed the creation of a non-absorbing state, that could be optimally populated when the relative detuning between the probing fields is equal to the ground state splitting.

2.4.1 Λ Configuration

The criteria for three-level CPT requires two optical fields to couple three electronic states, as in the Λ configuration illustrated in Fig. 2.4, which is the only configuration addressed in this thesis. This configuration is composed of two ground-states, $|b\rangle$ and $|c\rangle$, coupled to an excited state, $|a\rangle$, with an energy separation $E_{an} = \hbar\omega_{an}$ for $n = b, c$ to the ground states. The ground state coupling is induced by two electric fields, $\vec{E}_1(t) = \vec{E}_1 \cos(\omega_1 t)$ and $\vec{E}_2(t) = \vec{E}_2 \cos(\omega_2 t)$, each with a respective detuning from resonance, $\delta_1 = \omega_{ab} - \omega_1$ and $\delta_2 = \omega_{ac} - \omega_2$. The frequency difference between the
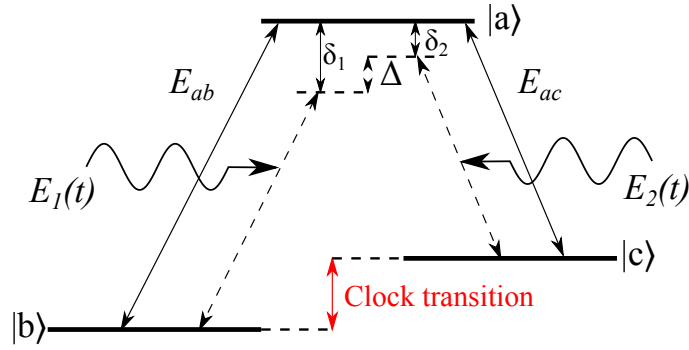
Figure 2.4: Three-level atom in the Λ configuration with two incident light field which separately drive the $|b\rangle \to |a\rangle$ and $|c\rangle \to |a\rangle$ transition, with respective detuning's of δ_1 and δ_2 from resonance. The frequency difference between each δ is the Raman detuning, Δ. Solid lines indicate the resonance transition.

relative detuning's, $\Delta = \delta_1 - \delta_2$, is referred to as the Raman detuning.

Dipole transitions between $|b\rangle \longleftrightarrow |c\rangle$ are not allowed due to the parity of the ground states, thus the interaction between the atoms and light is based on the atomic state evolution in $|b\rangle \longleftrightarrow |a\rangle$ and $|c\rangle \longleftrightarrow |a\rangle$, creating a coherence between the two ground states. When the separation between the two laser frequencies becomes comparable to the ground-state splitting, i.e. $\Delta = 0$, a coherent superposition of the ground states decouples from the electric field. This superposition does not interact with the electric field, hence it has been known as a *'dark state'* [53]. Once an atom is then excited to state $|a\rangle$ it can either of the decay to the *'dark state'* or *'bright state'*. Once in the dark state the atom is no longer interacting with the optical fields. If instead, the atom decays to a bright state, then it will continue to absorb photons and transit back to $|a\rangle$ where it can again fall into the dark state. Atoms will continue to be optically pumped into this superposition until the steady state is achieved.

The relative phase of the superposition will determine the creation of a dark or bright state, where the imprinted superposition phase is a summation of

both electric field phases. If the electric fields maintain a constant phase during the optical pumping time, the atoms will achieve a dark state. However, if the electric fields phases change during optical pumping, then atoms will instead be pumped to a bright state. A thorough discussion and derivation of the dark state criteria is provided in Sect. [11].

At this point, since the atoms no longer interact with the optical fields, the vapour becomes transparent to $\vec{E}_1(t)$ and $\vec{E}_2(t)$. This phenomena decouples the excited state, such that the atomic population exists in a superposition of $|b\rangle$ and $|c\rangle$. The ground-state splitting can be precisely determined when maximum transmission is achieved due to the transparency of the decoupled state. This transparency is referred to as electromagnetically induced transparency, EIT [45].

2.4.2 Optical Bloch Equations

The evolution of the three-level Λ configuration is governed by the Hamiltonian, $\mathcal{H} = H_0 + H_i$. The internal energy of this system is described as $H_0 = \sum_n E_n |n\rangle\langle n|$, while the interaction Hamiltonian, H_i, is expanded to its three-level equivalent:

$$H_i = -\vec{d} \cdot \vec{E}(t) = -\vec{d} \cdot \vec{E}_1 \cos(\omega_1 t) - \vec{d} \cdot \vec{E}_2 \cos(\omega_2 t). \qquad (2.37)$$

The interaction Hamiltonian, H_i, has been simplified by removing the terms that represent the absorption of a photon whilst dropping the atom from $|a\rangle$ to a lower state, or emitting a photon and raising the atom to the excited state. This logical simplification is accounted for by the RWA and greatly simplifies the calculation with little expense to the reliability of the final result [47, 54], such that the simplified interaction can be described as,

$$H_i = \frac{\hbar\Omega_1}{2}(|a\rangle\langle b|e^{i\omega_1 t} + |b\rangle\langle a|e^{-i\omega_1 t}) + \frac{\hbar\Omega_2}{2}(|a\rangle\langle c|e^{i\omega_2 t} + |c\rangle\langle a|e^{-i\omega_2 t}), \quad (2.38)$$

such that the resulting Hamiltonian can be rewritten as,

$$\mathcal{H} = \begin{pmatrix} \hbar\omega_a & (\hbar\Omega_1/2)e^{-i\omega_1 t} & (\hbar\Omega_2/2)e^{-i\omega_2 t} \\ (\hbar\Omega_1/2)e^{i\omega_1 t} & \hbar\omega_b & 0 \\ (\hbar\Omega_2/2)e^{i\omega_2 t} & 0 & \hbar\omega_c \end{pmatrix}, \tag{2.39}$$

where Ω_1 and Ω_2 are the Rabi frequencies that represents the coupling of the laser to the atomic dipole of states $|a\rangle \to |b\rangle$, and $|a\rangle \to |c\rangle$ respectively.

The diagonal terms of the matrix are solely the energies of the three atomic states in question, while the off-diagonal terms depict the possible dipole transitions made available by the laser interaction. However, this description remains incomplete as it lacks the relaxation terms produced by spontaneous emission, collisions and other damping mechanisms [51]. These terms can be derived from the Lindblad form of the optical Bloch evolution equation:

$$\dot{\rho} = -\frac{i}{\hbar}[\mathcal{H}, \rho] - \mathcal{L}(\rho), \tag{2.40}$$

where m represents the available decay modes from channels $|i\rangle \to |j\rangle$ due to emission of a photon, $\mathcal{L}(\rho)$ is the three-level Lindblad operator in the form of Eqn. (2.14), and ρ is the three-level density matrix,

$$\begin{pmatrix} \rho_{aa} & \rho_{ab} & \rho_{ac} \\ \rho_{ba} & \rho_{bb} & \rho_{bc} \\ \rho_{ca} & \rho_{cb} & \rho_{cc} \end{pmatrix}. \tag{2.41}$$

Solving the Lindblad form provides the density matrix for the full optical

Bloch equations of the Λ configuration [54]:

$$\dot{\rho}_{aa} = \frac{i\Omega_2}{2}(\rho_{ac}e^{i\omega_2 t} - \rho_{ca}e^{-i\omega_2 t}) + \frac{i\Omega_1}{2}(\rho_{ab}e^{i\omega_1 t} - \rho_{ba}e^{-i\omega_1 t}) - \Gamma_a\rho_{aa}, \quad (2.42)$$

$$\dot{\rho}_{bb} = \frac{i\Omega_1}{2}(\rho_{ba}e^{i\omega_1 t} - \rho_{ab}e^{-i\omega_1 t}) - \Gamma_b\rho_{bb} + \frac{\Gamma_a}{2}\rho_{aa}, \quad (2.43)$$

$$\dot{\rho}_{cc} = \frac{i\Omega_2}{2}(\rho_{ca}e^{i\omega_2 t} - \rho_{ac}e^{-i\omega_2 t}) - \Gamma_c\rho_{cc} + \frac{\Gamma_a}{2}\rho_{aa}. \quad (2.44)$$

The derived results can be simplified further by transforming into a rotating frame to eliminate the time-dependence of the density matrix such that,

$$\rho_{ij} = \tilde{\rho}_{ij}, \quad (2.45)$$

$$\rho_{ab} = \tilde{\rho}_{ab}e^{-i\omega_1 t}, \quad (2.46)$$

$$\rho_{ac} = \tilde{\rho}_{ac}e^{-i\omega_2 t}, \quad (2.47)$$

$$\rho_{bc} = \tilde{\rho}_{bc}e^{-i(\omega_2 - \omega_1)t}. \quad (2.48)$$

Substituting Eqns. (2.45)-(2.48) into Eqn. (2.42)-(2.44) produces the three-level optical Bloch equations:

$$\dot{\rho}_{aa} = \frac{i\Omega_2}{2}(\tilde{\rho}_{ac} - \tilde{\rho}_{ca}) + \frac{i\Omega_1}{2}(\tilde{\rho}_{ab} - \tilde{\rho}_{ba}) - \Gamma_a\rho_{aa}, \quad (2.49)$$

$$\dot{\rho}_{bb} = \frac{i\Omega_1}{2}(\tilde{\rho}_{ba} - \tilde{\rho}_{ab}) - \Gamma_b\rho_{bb} + \frac{\Gamma_a}{2}\rho_{aa}, \quad (2.50)$$

$$\dot{\rho}_{cc} = \frac{i\Omega_2}{2}(\tilde{\rho}_{ca} - \tilde{\rho}_{ac}) - \Gamma_c\rho_{cc} + \frac{\Gamma_a}{2}\rho_{aa}, \quad (2.51)$$

$$\dot{\tilde{\rho}}_{ab} = -(\gamma_{ab} - i\delta_1)\tilde{\rho}_{ab} + \frac{i\Omega_1}{2}(\rho_{aa} - \rho_{bb}) - \frac{i\Omega_2}{2}\tilde{\rho}_{cb}, \quad (2.52)$$

$$\dot{\tilde{\rho}}_{ac} = -(\gamma_{ac} - i\delta_2)\tilde{\rho}_{ac} + \frac{i\Omega_2}{2}(\rho_{aa} - \rho_{cc}) - \frac{i\Omega_1}{2}\tilde{\rho}_{bc}, \quad (2.53)$$

$$\dot{\tilde{\rho}}_{cb} = -(\gamma_{cb} - i(\delta_1 - \delta_2))\tilde{\rho}_{cb} + \frac{i\Omega_1}{2}\tilde{\rho}_{ca} - \frac{i\Omega_2}{2}\tilde{\rho}_{ab}, \quad (2.54)$$

where $\rho_{aa} + \rho_{bb} + \rho_{cc} = 1$.

The behaviour of the system can be understood by looking at the steady state, $\dot{\tilde{\rho}} = 0$, when setting $\delta_2 = 0$ and using the simplified two-photon detun-
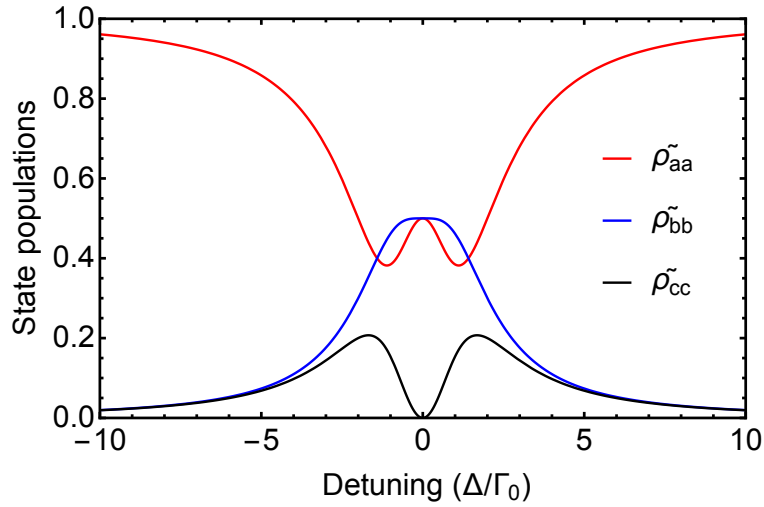
Figure 2.5: Theoretical steady-state populations of the three levels of the Λ configuration. For simplicity the Rabi frequencies $\Omega_1/\Omega_2 = 1$.

ing, $\Delta \equiv \delta_1$, to determine the atomic state populations as a function of Δ. In Fig. 2.5, the populations of the diagonal terms of the density matrix are plotted, setting $\Omega_1 = \Omega_2$ for simplicity. The excited state population of $|a\rangle$ goes to zero at $\Delta = 0$, when E_1 becomes resonant for transitions between $|b\rangle \longleftrightarrow |a\rangle$. The results show that for large detuning, the atomic population begins in $|a\rangle$. However, as the detuning reaches 0 the populations are evenly split between $|b\rangle$ and $|c\rangle$, whilst $|a\rangle$ becomes unpopulated. Since no atoms are being excited to $|a\rangle$, then they are decoupled from the light field in a dark state.

2.4.3 Electromagnetically Induced Transparency

With respect to the refractive index, the most important term of the density matrix is the solution of the off-diagonal $\tilde{\rho}_{ab}$, as this allows determination of the absorption and dispersion coefficients through the linear susceptibility, χ, as discussed in Sec. [2.2.1],

$$\chi = \frac{2Nd_{ab}^2}{\hbar\Omega_1\epsilon_0}\tilde{\rho}_{ab}. \tag{2.55}$$
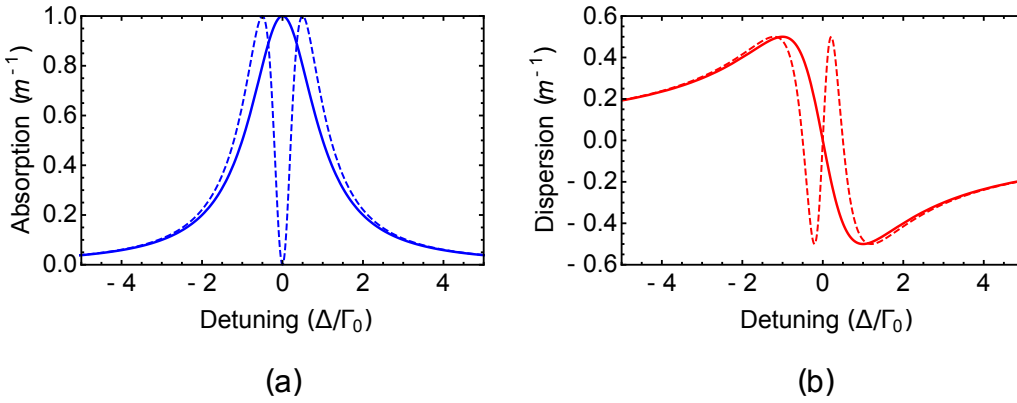
Figure 2.6: Theoretical absorption, (a), and dispersion, (b), demonstrating EIT. For the Figure $\Delta = \delta_1$ is varied whilst $\delta_2 = 0$. $\Omega_2 = \Omega_1$ while $\gamma_{ab}/\gamma_{ac} = 1$ and $\gamma_{bc} = 0$. The solid lines are the peaks seen from two-level theory. Dashed lines depict three-level EIT.

Adding the result of $\tilde{\rho}_{ab}$ from the density matrix results in the susceptibility, which can be separated down into imaginary and real components, the absorption and dispersion respectively [55], as has been discussed in Eqns. (2.30) and (2.31).

The results of the absorption and dispersion were used to generate Fig. 2.6, which demonstrates that at $\Delta = 0$ the absorption of laser light vanishes. The decoupling from the incident optical fields makes the atomic vapour appear transparent; hence, this phenomena is known as Electromagnetic Induced Transparency, EIT.

2.5 Magnetic Trapping

The idea that the presence of a magnetic field could be used to specify the quantisation axis of an atom was first realised in the famous experiment by Otto Stern and Walter Gerlach [56], who observed a splitting of atomic spin states in the presence of a perturbing magnetic field. The basis behind the magnetic trapping of neutral atoms is the force induced upon the atomic magnetic dipole by a perturbing magnetic field. In the case of an atom with

magnetic moment, $\vec{\mu}$, in the presence of a magnetic field, $\mathbf{B}$, the potential experienced by the atom is,

$$U(r) = \vec{\mu} \cdot \mathbf{B}. \tag{2.56}$$

If $\mathbf{B}$ is non-uniform then the atom will experience a force:

$$F = -\vec{\mu} \cdot \nabla \mathbf{B}. \tag{2.57}$$

Since the magnetic moment, $\vec{\mu}$, is anti-parallel to the total angular momentum of the atom, $\mathbf{F}$, the atom is attracted to the field minimum for $\mathbf{F}$ parallel to $\mathbf{B}$ or a field maximum for $\mathbf{F}$ anti-parallel to $\mathbf{B}$ [57]. In a local magnetic field, only atoms in m_F states whose potential energy increases with $\mathbf{B}$ can be trapped, by creating a field minimum in the non-uniform magnetic field [58].

2.5.1 Atomic interaction with a static magnetic field

Fine structure

The atomic fine structure arises due to a coupling between the orbital angular momentum, $\mathbf{L}$, of the outer electron and its spin angular momentum, $\mathbf{S}$, through [59],

$$\mathbf{J} = \mathbf{L} + \mathbf{S}. \tag{2.58}$$

where $\mathbf{J}$ is the total angular momentum within the range $|L-S| \leq J \leq L+S$. For the alkali earth metals the angular momentum configuration is determined by the single outer valence electron. Since the ground state S shell has $L = 0$ and a single electron spin $S = 1/2$, the total angular momentum of the ground state is $J = 1/2$. This information is provided in the notation

of the electronic configuration,

$$n^{2S+1}L_J \tag{2.59}$$

where n is the principle quantum number, and $L = 0, 1, 2...$ denoted by the letters $L =$S, P, D... for the available orbitals.

This fine structure gives rise to the excited state of the P shell possessing two total angular momentum states, $P_{1/2}$ and $P_{3/2}$. Transitions to these states from the $S_{1/2}$ ground-state are referred to as the D_1 and D_2 transitions respectively. The energy difference between these fine structure spectral lines is determined from the scalar product of $\mathbf{L} \cdot \mathbf{S}$ such that their relative energy shift, E_{fs}, is given as [7],

$$E_{fs} = A_{fs}(\mathbf{L} \cdot \mathbf{S}) = \frac{A_{fs}}{2}(J(J+1) - L(L+1) - S(S+1)), \tag{2.60}$$

where A_{fs} is the spin-orbit constant.

Hyperfine structure

The hyperfine structure of the alkali atoms arises due to the interaction of the magnetic flux density of the electron, $\mathbf{B}_e$, with the magnetic momentum associated with the nucleus, μ_I, to form the Hamiltonian

$$H_{\mathrm{hfs}} = -\mu_I \cdot \mathbf{B}_e, \tag{2.61}$$

where the nuclear magnetic moment is related to the nuclear spin, $\mathbf{I}$, through

$$\mu_I = g_I \mu_N \mathbf{I}, \tag{2.62}$$

where μ_N is the nuclear magnetic dipole.

This hyperfine interaction can also be expressed in terms of coupling the electronic angular momentum, **J**, to the total nuclear angular momentum, **I**, by,

$$\mathbf{F}=\mathbf{J}+\mathbf{I}, \tag{2.63}$$

where **F** is the total atomic angular momentum within the range $|J - I| \leq F \leq J + I$.

Similarly to Eqn. (2.60), the scalar product of **J** and **I** are solved to describe the hyperfine splitting energy,

$$E_{hfs} = A_{fs}(\mathbf{J} \cdot \mathbf{I}) = \frac{A_{fs}}{2}(F(F + 1) - L(L + 1) - S(S + 1)). \tag{2.64}$$

The degeneracy of the hyperfine states is broken into $2|F|+1$ degenerate sublevels when the atom is in the presence of an external magnetic field. If the applied magnetic field is small in comparison to the hyperfine splitting between the atomic ground states, then the interaction Hamiltonian is written as,

$$H_B = \frac{\mu_B}{\hbar}(g_J J_z + g_I I_z)\mathbf{B}_z, \tag{2.65}$$

where g_I is the nuclear g-factor, which is $g_I = 1.353$ for ^{85}Rb and $g_I = \frac{\mu_N}{\mu_B}2.751$ for ^{87}Rb. g_J is the Landé factor [59], given by,

$$g_J = g_L \frac{J(J + 1) - S(S + 1) + L(L + 1)}{2J(J + 1)} + g_S \frac{J(J + 1) + S(S + 1) - L(L + 1)}{2J(J + 1)}, \tag{2.66}$$

where g_S is the electron spin g-factor and $g_L = \frac{1}{1+m_e/m_n}$ accounts for the ratio of electronic and nuclear mass.

For the case of the 5^2S$_{1/2}$ ground-state of ^{87}Rb, $J = 1/2$, $L = 0$, and $S = \pm 1/2$. If the splitting is described in terms of **F** being a good quantum number, then the projection of the atomic magnetic moment onto the field

vector is given as,

$$\Delta E_{Fm_F} = -g_F \mu_B m_F \mathbf{B}, \tag{2.67}$$

where μ_B is the Bohr magneton and g_F is the Landé g-factor's projection on $\mathbf{F}$, represented as

$$g_F = g_J \frac{F(F+1) - I(I+1) + J(J+1)}{2F(F+1)} + g_I \frac{\mu_N}{\mu_B} \frac{F(F+1) + I(I+1) - J(J+1)}{2F(F+1)}. \tag{2.68}$$

Eqn. (2.67) demonstrates that the perturbing magnetic fields induce shifts of the atomic magnetic sub-levels, as illustrated in Fig. 2.7. This magnetic shift is referred to as the Zeeman effect. For larger fields the energy shifts of the ground-state manifolds can be calculated easily by using the Breit-Rabi equation [59]:

$$E_{|F,m_F\rangle} = -\frac{\Delta E_{hfs}}{2(2I+1)} + g_I \mu_B m_F \mathbf{B} \pm \frac{\Delta E_{hfs}}{2} \left(1 + \frac{4m_F}{2I+1} x + x^2\right)^{1/2}, \tag{2.69}$$
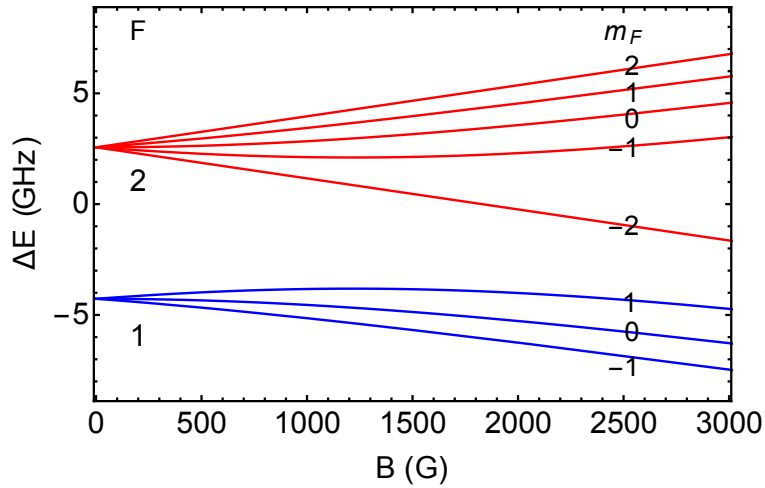
Figure 2.7: Theoretical depiction of the Zeeman effect leading to the splitting of the m_F sub-levels of the ^{87}Rb ground state as a function of the experienced magnetic field.

where the $\pm$ corresponds to the magnitude of the m_F state, $\Delta E_{hfs} = A_{hfs}(I + 1/2)$, A_{hfs} is the magnetic dipole constant, and x is given by:

$$x = \frac{(g_J \mu_B - g_I \mu_N)\mathbf{B}}{\Delta E_{hfs}}. \qquad (2.70)$$

Chapter 3

Laser cooling and trapping

The proposal of the laser by Schawlow and Townes in 1957 [60] and realisation by Maiman in 1960 [61] revolutionised physics, pioneering new fields of study and establishing contemporary experimental capabilities. The name 'laser' originated from the acronym 'light amplification by stimulated emission of radiation'. The emission comes by means of a pumped gain medium, which can be amplified by selective feedback mechanisms. The advantage provided by the laser over the standard lamp light source is the temporal and spatial coherence of the output emission, allowing collimation and tightly focusing beams, which led to the realisation of lithographical processes and ablation capabilities. However, the greatest advancement provided by the laser, in the context of this thesis, is the establishment of laser cooling.

When referring to laser cooling, the description of temperature arises from the Maxwell-Boltzmann distribution of an atomic ensemble's speed:

$$f(v) = 4\pi v^2 \sqrt{\left(\frac{m}{2\pi k_B T}\right)^3} e^{-\frac{mv^2}{2k_B T}}, \tag{3.1}$$

where v is the speed, m the mass, k_B the Boltzmann constant and T the temperature.
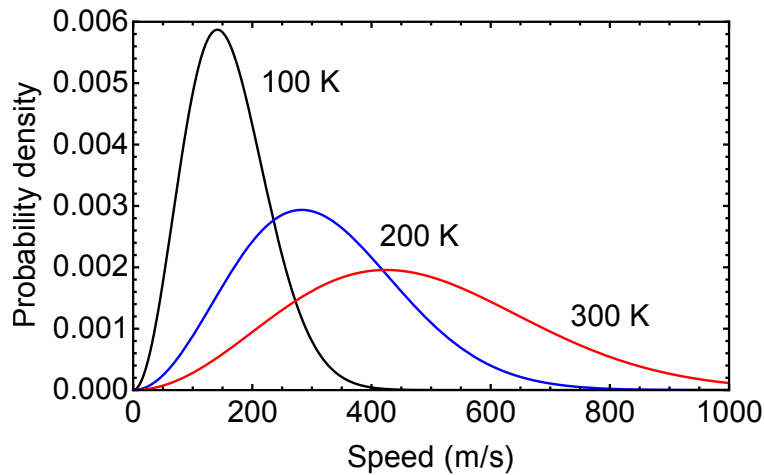
Figure 3.1: Maxwell Boltzmann distribution illustrates the speed spread of an atomic distribution as a function of temperature.

Using Eqn. (3.1), the average one dimensional speed of the atomic system can be related to the temperature. Three velocity distributions are plotted as a function of their probability density with a note of the associated system temperature in Fig. 3.1. This figure depicts the relationship between temperature and the spread of the atomic speed, such that a lower temperature depicts a narrower speed distribution and larger probability density. This temperature description facilitates the need for colder atomic temperatures to achieve the lower speed distributions sought after for long interrogation times in precision measurements.

The historical timeline of laser cooling dates back as far as the 17th century, when Keppler first theorised the possibility of radiation pressure. His idea was adopted from the assumption that comet tails where due to a repulsive light pressure from the sun. His idea was later found to not be the only mechanism involved, however, the concept of radiation pressure from light was correct. It was not until 1873 when Maxwell's theory of light [62] demonstrated that light does exert a small pressure equal to its energy over volume. The first laboratory demonstrations of this pressure were realised

by Lebedev, and Nichols and Hull in 1901 for the exertion of radiation pressure on macroscopic objects [63]. In 1933, the force exerted by light was demonstrated by O. Frisch, when a beam of sodium atoms were deflected when illuminated by a discharge lamp [63]. It was not until 1970, following the invention of the laser, that the concept of radiation pressure was later validated in a paper published by A. Ashkin entitled 'Acceleration and trapping of particles by radiation pressure' [64]. In this paper Ashkin noted the acceleration of freely suspended particles by the effects of radiation pressure from a continuous laser source. The author observed trapping of particles when in the presence of counter-propagating beams and acceleration of particles when in the presence of one.

The idea of radiation pressure was adapted for Doppler cooling simultaneously by Hansch and Schawlow [65] for neutral atoms and by Wineland and Dehmelt for trapped ions [66]. The Doppler cooling proposals stated that by creating a laser beam detuned below resonance, then due to the Doppler effect shifting the perceived laser frequency as a function of atomic velocity, one could slow the motion of an atom propagating towards the laser. This cooling technique was experimentally demonstrated by Wineland *et al.* in 1978 for a cloud of Mg ions held in a penning trap [67, 68], soon followed by W. D. Phillips and H. Metcalf in 1982 with the deceleration of an atomic beam by means of a counter-propagating laser [69]. It was not until 1985, when a paper published with the title 'Three-Dimensional Viscous Confinement and Cooling of Atoms by Resonance Radiation Pressure' employed the Doppler cooling technique in three dimensions [70]. It was here that S. Chu *et al.* noted the observation of what they referred to as an 'optical molasses'.

3.1   One-dimensional molasses

The mechanisms of laser cooling can be derived from the momentum transferred during the absorption/emission process. When an atom absorbs a photon it is excited into a state of higher energy, but also recoils with a momentum,

$$p = mv = \hbar k, \tag{3.2}$$

where m is the atomic mass, $k = \frac{2\pi}{\lambda}\vec{k}$, where $\vec{k}$ is the direction of propagation and $\lambda = c/\nu$.

This momentum may be passed on through stimulated emission of a photon, such that there is no net momentum change. If the emission is spontaneous, i.e. can radiate with spatial symmetry from the atom, then it does not contribute to the net momentum change. Over many cycles of this process, the atom travelling towards the light has a momentum push in the direction of the laser's propagation, slowing the atom down, and eventually changing its trajectory. If we assume that the two-level atom is in steady state, such that the rate of decay $\Gamma\rho_{ee}$ is balanced with the absorption rate, then the force experienced by the atom can be described by,

$$F = \frac{dp}{dt} = \Gamma\rho_{ee}\hbar k = R(I, \Delta)\hbar k. \tag{3.3}$$

This force gives way to a time-averaged acceleration of

$$a = \frac{\hbar k R(I, \Delta)}{m}, \tag{3.4}$$

where $R(I, \Delta)$ is the rate a two-level atom absorbs photons from the laser light, determined from the steady state decay such that

$$R(I, \Delta) = \Gamma\rho_{ee} = \frac{\Gamma}{2}\frac{I/I_s}{(1 + I/I_s + (\frac{2\Delta}{\Gamma})^2)}, \tag{3.5}$$

(a)

(b)
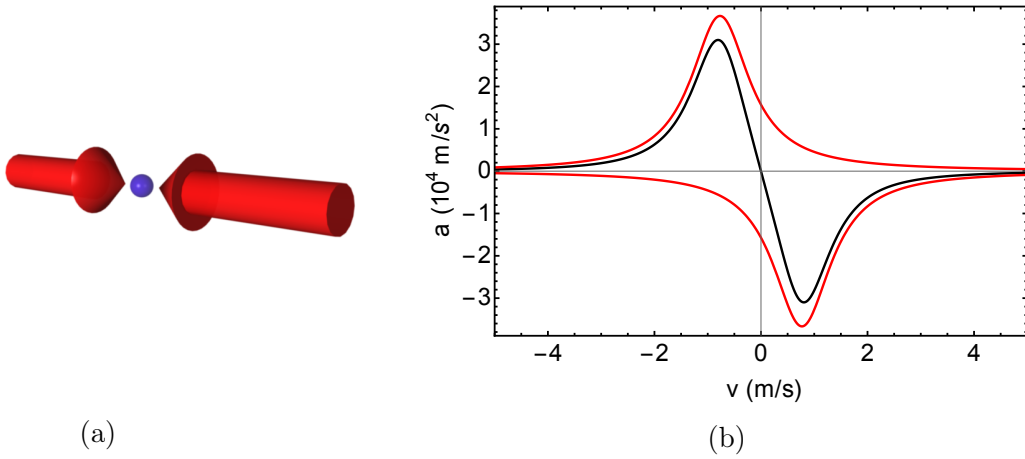
Figure 3.2: a):Two counter-propagating laser beams. b):The velocity dependent acceleration experienced by atoms in optical molasses. The red lines represent the acceleration caused by each individual laser, propagating against one another. The black line represents the sum of contributions from both lasers. For this figure $I = I_s$, $I_{tot} = 2I_s$ and $\Delta = -\Gamma/2$.

where $\Gamma = 2\pi\Gamma_\nu = 2\pi\times6.07$ MHz is the natural line-width of the excited state for ^{87}Rb, Δ is the detuning of the laser with respect to the atomic resonance ω_0, I is the intensity, and $I_s = \frac{I\Gamma^2}{2\Omega^2}$ is the saturation intensity, where Ω is the Rabi frequency.

If the two-level atom were to be positioned between two counter-propagating lasers, with the same frequency and intensity, as illustrated in Fig. 3.2 (a), then the combined force is given as,

$$F = \frac{\hbar k\Gamma}{2}\left(\frac{I/I_s}{1 + I_T/I_s + (\frac{2\Delta-2kv}{\Gamma})^2} - \frac{I/I_s}{1 + I_T/I_s + (\frac{2\Delta+2kv}{\Gamma})^2}\right), \qquad (3.6)$$

where I_T is the total intensity as a result of cross saturation [71].

The force derived in Eqn. (3.6) leads to a velocity dependent acceleration, seen in Fig. 3.2 (b). In the 1-dimensional scenario, it could be easily misunderstood that the atoms would see no effect from the two lasers since they propagate in opposite directions and impart an equal force. However, the Doppler effect leads to a symmetry break in the force seen by a moving

atom, shifting the absorbed photon frequency by

$$\omega' = \omega \left(1 + \frac{v}{c}\right),$$ (3.7)

where ω' is the observed frequency for an atom moving towards a photon, ω is the light frequency, v is the atomic velocity, and c is the speed of light.

Fig. 3.2 (b) shows that once the atom is slowed to zero velocity, it will experience equal forces from each laser. In order for this effect to lead to cooling, the laser frequency must be red-detuned toward resonance with the beam propagating opposite its velocity.

Applying this technique in three-dimensions is referred to as optical molasses, OM, due to the atoms slow viscous movement, like thick molasses treacle. The temperature of such a system is measured by turning off the laser beams, and allowing the atoms to ballistically expand. The rate of expansion is a critical indication of the average atomic velocity, which allows the average ensemble temperature to be determined.

The Doppler limit

The Doppler limit is the theoretical temperature that was assumed to be the coldest achievable temperature from laser cooling. To calculate the Doppler limit we continue working in the one-dimensional cooling scheme, where the force experienced on an atom between two counter-propagating lasers has been derived in Eqn. (3.6). In the approximation that $|kv| \ll \Gamma$ and $|kv| \ll \Delta$ Eqn. (3.6) is simplified to [72]

$$F = 4\hbar k \frac{I}{I_s} \frac{kv(2\Delta/\Gamma)}{[1 + (2\Delta/\Gamma)^2]^2}.$$ (3.8)

This simplified description demonstrates a damping force for all velocities when the incident laser is red-detuned, $\Delta < 0$ and an acceleration for $\Delta > 0$. This damping force can be related to the loss rate of kinetic energy with $(dE/dt)_{\text{cooling}} = Fv$. The damping rate reduces the average velocity of the atoms to zero, whilst at the same time heating is induced by the random direction of the absorption/emission process. In the regime of low intensity ($I/I_s \ll 1$), the momentum built up during these random walk cycles has been shown to lead to a heating rate [72],

$$(dE/dt)_{\text{heating}} = \hbar^2 k^2 R(I, \Delta)/m = \frac{\hbar^2 k^2 \Gamma}{m} \frac{I/I_s}{1 + (2\Delta/\Gamma)^2}, \qquad (3.9)$$

where $R(I, \Delta)$ is the magnitude of the scattering rates from both beams.

The system's steady state will be realised when the cooling and heating rates are at equilibrium, $(dE/dt)_{\text{cooling}} + (dE/dt)_{\text{heating}} = 0$, such that the mean square velocity can be written as

$$v^2 = \frac{\hbar\Gamma}{4m} \frac{1 + (2\Delta/\Gamma)^2}{2|\Delta|/\Gamma}. \qquad (3.10)$$

The thermal energy of a one-dimensional cooling scheme can be described by $k_B T/2 = mv^2/2$, which when substituted into Eqn. (3.10), results in the Doppler cooling limit of

$$k_B T = \frac{\hbar\Gamma}{4} \frac{1 + (2\Delta/\Gamma)^2}{2|\Delta|/\Gamma}. \qquad (3.11)$$

When $\Delta = -\Gamma/2$ the low intensity minimum is realised as [72–74]

$$T_D = \hbar\Gamma/2k_B. \qquad (3.12)$$

In the case of rubidium, where $\Gamma = 2\pi \times 6.07$ MHz, a Doppler temperature of 145 μK is predicted. Although this technique realises a cold atomic sample,

optical molasses is not an atomic trap due to the fact that atoms are free to diffuse and over time their Brownian motion will lead them towards the boundary of the lasers excitation region and lead to atomic losses.

3.2   Magneto-optical trap

The purpose of the magneto-optical trap, MOT, is to introduce a position dependent scattering force by combining the optical force with the Zeeman effect, which was discussed in Sect. [2.5.1]. The earlier discussion illustrated the degenerate splitting of **F** levels into $2\,|\mathrm{F}|+1$ sub-levels when in the presence of an applied magnetic field, with the distance between the Zeeman sub-levels increasing as a function of magnetic field. The nature of a gradient magnetic field is thus capable of shifting the magnetically sensitive sub-levels as a function of position, such that a laser detuned below resonance will have an increased probability of absorption events in larger magnetic fields.

To fully understand this mechanism, I refer to the atomic configuration depicted in Fig. 3.3. In this scenario we look at one ground state, $|F = 0,\, m_F = 0\rangle$, and three manifolds of the non-degenerate excited state, $|F = 1, m_F = -1, 0, 1\rangle$, when in the presence of a magnetic field. As the atom travels into a position of higher magnetic field, the shift of the excited energy levels increases, changing the resonance frequency with position.

If we employ a one-dimensional cooling scheme, then the description is simplified to two counter-propagating lasers, denoted by $\mathrm{L_1}$ and $\mathrm{L_2}$. Both laser fields posses the same circular polarisation and are red-detuned from resonance, represented by the solid grey line. In the one-dimensional scheme, $\mathrm{L_1}$ would drive σ^- transitions when anti-parallel with **B** and σ^+ when parallel with **B**. The frequency difference between the laser detuning and atomic resonance with $|F = 1, m_F = -1\rangle$ decreases with position. Thus, probability
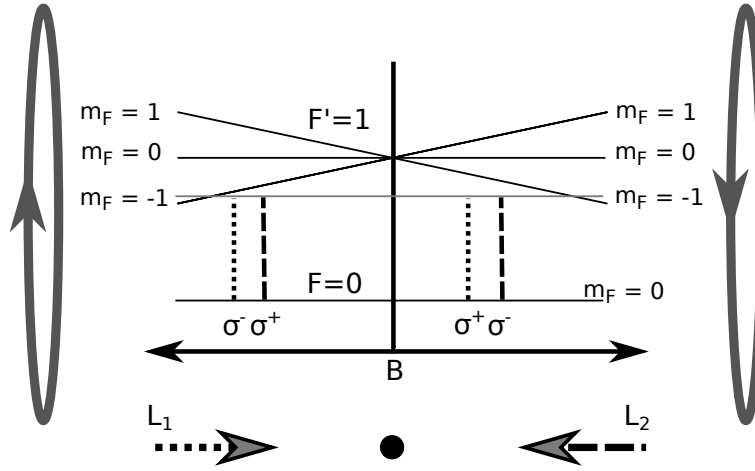
Figure 3.3: Schematic of transitions in a one-dimensional magneto-optical trap. Solid black lines denote non-degenerate energy levels, whilst the solid grey line depicts the laser red-detuning from the degenerate resonance frequency. Dotted/dashed lines correspond to the polarisation and detuning of laser L_1/L_2 respectively. Grey loops represent the anti-Helmholtz configuration discussed in Sect. [3.2.1].

of the atom absorbing from L_1 increases as the atom travels towards this laser, producing a position dependent scattering force and accelerating the atom along the direction of laser propagation. If the atom were to surpass the zero field region and continue towards L_2, an equal and opposite force would be experienced, as now the atom is more likely to absorb a photon from L_2 than L_1. The position dependent scattering force brings the atom back to zero magnetic field until an equilibrium is reached at the centre of the field.

The first experimental demonstrations of a MOT were carried out by Rabb *et al.* in 1987 [75] and has since become the workhorse for the field of cold atomic physics. This demonstration was carried out in three dimensions with three pairs of counter-propagating beams in a low pressure vapour cell.

MOT atom number and density

In the case of the vapour cell MOT, the trap will be able to capture atoms that are travelling with a velocity lower than the trap's capture velocity, v_c,

typically on the order of 10 m/s [76]. The number of atoms in the lower tail of the Boltzmann distribution that are loaded into the trap is described by

$$N(t) = N_0(1 - e^{-t/\tau}),$$ (3.13)

where τ is the time constant for the trap to reach its steady state, N_0 [76, 77]. The trapped atoms will also have collisions with the background atoms, leading to a collisional loss, expressed as

$$\frac{1}{\tau} = n_{\mathrm{Rb}}\sigma_{\mathrm{Rb}}v_{\mathrm{Rb}} + n_{\mathrm{b}}\sigma_{\mathrm{b}}v_{\mathrm{b}},$$ (3.14)

where subscript Rb and b correspond to parameters of rubidium and the background gases, n is the density, v the velocities and σ is the collisional cross sections, which for rubidium is $\sigma = 2 \times 10^{-17}\,\mathrm{m}^2$ [77–79].

The steady state atom number, N, is predicted by using the standard method of Ref. [79]: treat the MOT as a spherical target region with radius r and cross-section $4\pi r^2$, then find the flux of atoms incident on the target, with speeds less than the capture velocity v_c of the MOT slowing region. This method excluded the loss rate from cold atom collisions within the trap as this only becomes significant in the regime of high density traps. Using this method to determine the steady state MOT number yields,

$$N = \frac{4\pi r^2}{8\sigma}\left(\frac{v_c}{v_T}\right)^4,$$ (3.15)

where $v_T = \sqrt{2k_BT/m}$ is a thermal velocity in the (hot) background vapour, m is the atomic mass and r is the radius of the trap surface area formed by the laser light [77].

The capture velocity discussed increases for a large overlap volume, by reason of the longer interaction time within the cooling region compared to a smaller

trap. As a result of this, the trapped atom number scales as a function of the overlap volume due to the larger slice of the Boltzmann distribution that the light can cool. Once the atom number is known, the density can be determined from,

$$n_0 = \frac{N}{(2\pi)^{3/2}\sigma_x\sigma_y\sigma_z},$$ (3.16)

where $\sigma_{x,y,z}$ denotes the MOT cloud Gaussian widths in x, y and z respectively, arising from the Maxwell-Boltzmann distribution of atoms in the MOT. [71].

3.2.1 Magnetic fields from coils

The discussion of the MOT so far has described the necessity for a magnetic gradient field to produce a position dependent scattering force. For a full understanding of the field geometry created from coil geometries requires numerical solutions to Biot-Savart law,

$$d\mathbf{B} = \frac{\mu_0 I}{4\pi} \frac{d\mathbf{l} \times (\mathbf{r} - \mathbf{r'})}{|\mathbf{r} - \mathbf{r'}|^3},$$ (3.17)

where $\mu_0 = 4\pi \times 10^{-7}$ H/m is the permeability of free space, $\mathbf{B}(r)$ is the magnetic field at point $\mathbf{r}$ from a wire element with current I and length $d\mathbf{l}$, centred at position $\mathbf{r'}$.

For experimental convenience we wind circular coils, which we shall model here, without loss of generality. It has been shown [80], that when solved in a cylindrical polar co-ordinate basis, the magnetic field from a circular coil, $\mathbf{B}(r, z)$, can be determined for any position (r, z) from the relation of elliptic
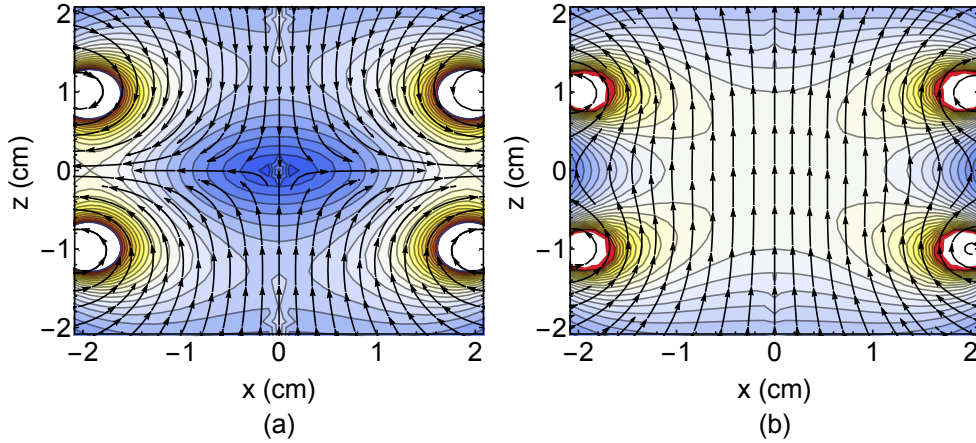
Figure 3.4: Magnetic field generated for circular coil configurations. Colour scale depicts the magnetic field strength, and lines indicate the magnetic field vector orientation. (a): Anti-Helmholtz coil pair in the vertical axis uses opposing current flow to produce a magnetic minima at their centre. (b): Helmholtz coils with symmetric current flow produces an almost homogenous static magnetic field at the centre.

integrals,

$$\mathbf{B}_r(r,z) = \frac{\mu_0 I z}{2\pi r}\sqrt{\frac{m}{4\alpha r}}\left[\frac{2-m}{2-2m}E - K\right], \qquad (3.18)$$

$$\mathbf{B}_z(r,z) = \frac{\mu_0 I}{2\pi r}\sqrt{\frac{m}{4\alpha r}}\left[rK + \frac{\alpha m - r(2-m)}{2-2m}E\right], \qquad (3.19)$$

where r and z are the radial and axial co-ordinates, α is the coil radius, $m = \frac{4\alpha r}{z^2 + (\alpha + r)^2}$ and the functions E and K refer to the corresponding elliptic integrals $E(m) = \int_0^{\pi/2}(1 - m\sin^2\theta)^{1/2}d\theta$ and $K(m) = \int_0^{\pi/2}\frac{d\theta}{(1-m\sin^2\theta)^{1/2}}$.

These equations were used to simulate a pair of coils with diameter, d, and separation, $s = d/2$, differing in current flow orientations. Fig. 3.4 (a) illustrates the case of two coils with opposite current flow magnitude, such that a quadrupole magnetic field is generated, with a magnetic minima at the centre as is required in the MOT. The magnetic minimum arises from Maxwell's equation $\vec{\nabla}\cdot\vec{B} = 0$, implying

$$\frac{dB_x}{dx} = \frac{dB_y}{dy} = -\frac{1}{2}\frac{dB_z}{dz}, \qquad (3.20)$$

such that the gradient in x and y is half that in the z. The case of parallel current flow, known as the Helmholtz configuration and shown in Fig. 3.4 (b), produces a static magnetic field that is approximately homogenous in the central region.

3.3   Sub-Doppler cooling

Early experimental achievements of laser cooling yielded data with a striking disagreement of temperature between experiment and theory. Temperature calculations in the initial experimental molasses curiously offered temperatures of 43 ± 20 μK for sodium, almost six times smaller than the predicted limit [73, 81]. The understanding and experimental demonstration of the concepts at work led to Steven Chu, Claude Cohen-Tannoudji and William D. Phillips being awarded the Physics Nobel Prize in 1997 for their respective contributions [72, 81, 82]. The flaw in the Doppler consideration was understood to be the theoretical assumption of a two-level atom, whereas experimentally only 'real' atoms are used. A further flaw in the Doppler theory assumes that the light field polarisation contribution in molasses and MOT can be treated independently from counter-propagating beams, as if there was no standing wave. In reality this is not a valid assumption, as the counter-propagating beams create a polarisation-dependent standing wave.

The additional cooling mechanisms that arise from the standing wave contribution are commonly known as polarisation gradient or sub-Doppler cooling. The realisation of these cooling techniques redefined the temperature limits to standard laser cooling. This cooling occurs due to a combination of optical pumping and the corresponding position-dependent transition rates between electronic states. The one-dimensional illustration of standing waves created from different polarisation combinations is visualised in Fig. 3.5.
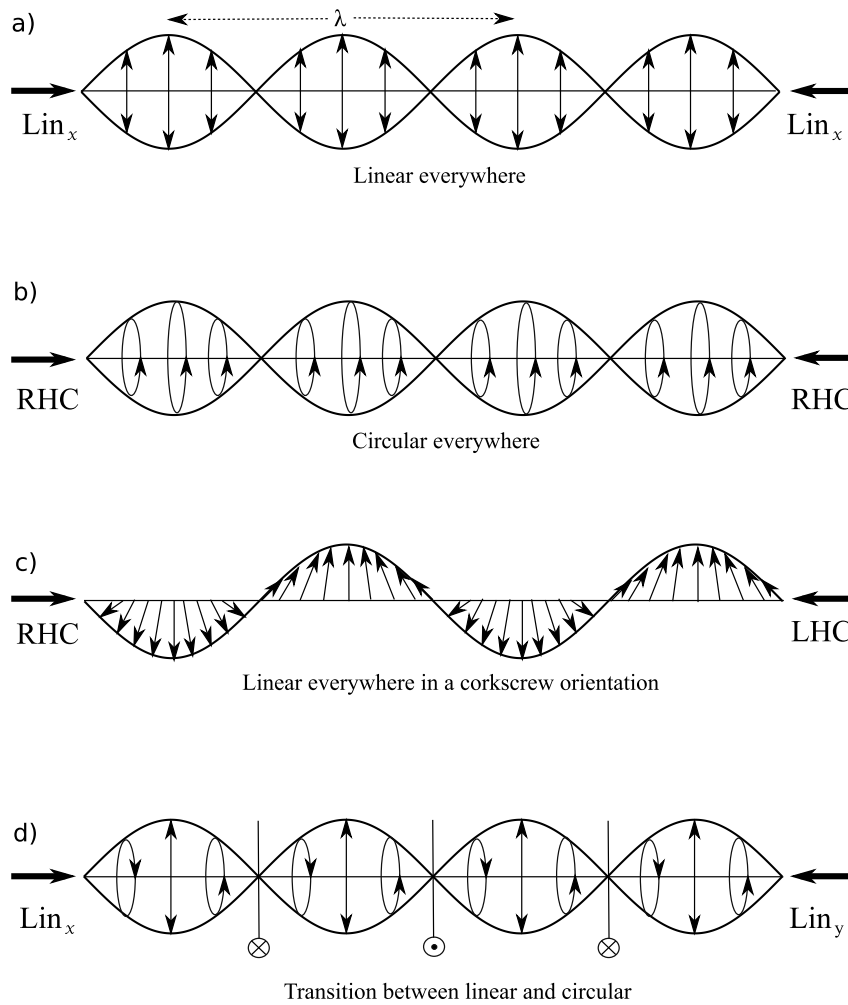
Figure 3.5: The one-Dimensional polarisation gradients produced from standing waves of varying light combinations. The RHC/LHC here correspond to the circular polarisation being right/left hand circular respectively. Similarly, $Lin_{x/y}$ correspond to horizontal/vertical linear polarisation.

Fig. 3.5 is composed of the interference created in the standing wave from a combination of linear horizontal, Lin_x, linear vertical, Lin_x, and right/left-hand circularly polarised light, RHC/LHC. Each one-dimensional standing wave is composed from two Lin_x Lin_x, RHC-RHC, RHC-LHC and Lin_x Lin_y polarised counter-propagating light waves, which can be seen with their respective electric field components [83]. Note that this notation is to highlight the rotation of polarisation of one beam, with respect to the polarisation of the counter-propagating beam, such that the notation of Fig. 3.5 (c) could

be written as RHC-LHC or LHC-RHC.

Sisyphus effect

According to Greek legend, Sisyphus was the king of Ephyra, who was punished by the great God Zeus for his deceitfulness. His punishment was to endure the rolling of a boulder up a mountain side, only for it to roll back to the bottom again. The Sisyphus cooling technique gained its namesake from this punishment due to motion of the atom in its standing wave configuration.

The Sisyphus cooling mechanism is created when two linearly polarised beams with axis of polarisation perpendicular to each other generate a standing wave as depicted in Fig. 3.5 (d). This standing wave interference differs between having σ^+, π and σ^- as the dominant transitions over a period of $\lambda/2$, due to the polarisation changing with position along z.

The simplest analysis of this standing wave is for the case of an electronic configuration composed of a $F = 1/2$ ground state coupled to a $F' = 3/2$ excited state, as illustrated in Fig. 3.6 (a) and (b) for the transitional strengths and standing wave orientation respectively. Early studies found that varying shifts come from the varying polarisations, and can be calculated with help of the Clebsch-Gordan coefficients [46]. The shifts are easily mapped out in the case of an atom in the $m_F = -1/2$ state (dashed line), spatially located at a $\lambda/8$ period in the standing wave, where the initial zero position was chosen for equal shifts on the ground states. The position of $\lambda/8$ in the standing wave polarisation is orientated as σ^-, whose Clebsch-Gordan coefficients are $\sqrt{3}$ times as strong for driving transitions from the $m_F = -1/2$ ground state than from the $m_F = +1/2$.

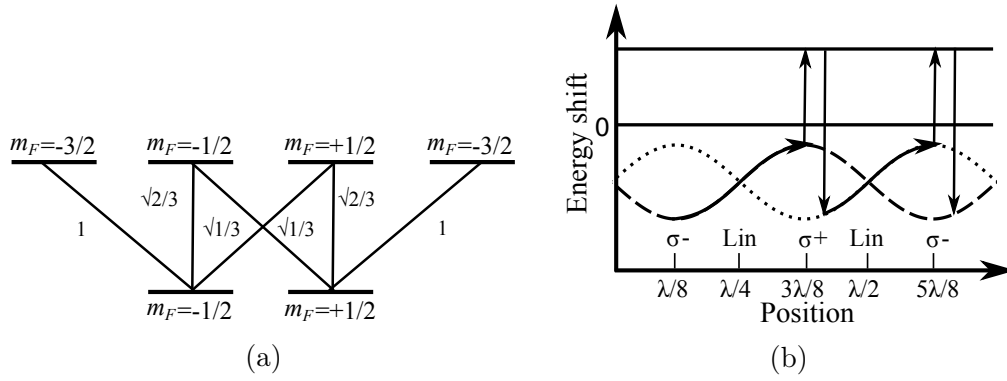If the atom moves into a region of space where the standing wave polari-

Figure 3.6: a): Energy levels of the assumed $F = 1/2$ to $F = 3/2$ transition. Bold lines represent energy levels, with narrow lines illustrating allowed transitions and respective Clebsch-Gordan coefficients. b): Graphical representation of an atom moving through the Sisyphus standing wave with varying polarisations, periodically Stark shifting the ground state with respect to the solid zero perturbation state.

sation is σ^+ orientated, such as $3\lambda/8$, then the atom has moved from a place where the $m_F = -1/2$ state is the lowest energy state, to it being the highest energy state. This increase in the internal energy decreases the kinetic energy of the atom. This process is only made irreversible by the introduction of optical pumping. When the atom is at the top of the potential the σ^+ polarisation optically pumps the atom to the excited state. Once in the excited state, spontaneous emission will allow the atom to drop to the lowest energy ground state, the $m_F = 1/2$ level (dotted line) for this position. The emission process changes the atomic state such that the potential energy gained from climbing is lost without increasing the kinetic energy. Following the atom's trajectory through the standing wave demonstrates the time spent climbing the light potentials gradient, resulting in a net damping force. This additional damping coefficient has been shown to lead to [57, 72, 82],

$$k_B T \approx \frac{\hbar \Gamma^2}{4|\Delta|} \frac{I}{I_s} \propto \frac{I}{|\Delta|}. \tag{3.21}$$

The Sisyphus temperature description simplifies the full experimental scenario for achieving sub-Doppler temperatures to a linear relationship of in-

tensity and detuning. Although this approximation was made for the simplified $F = 1/2$ to $F = 3/2$ state [82] it has been demonstrated for a $F = 2$ to $F' = 3$ in sodium [63].

Induced orientation effect

A more commonly used experimental cooling configuration is the three-dimensional $\sigma^+ \sigma^-$ standing wave, however, here we focus on the one-dimensional analysis seen in Fig. 3.5 (c). The corkscrew standing wave created is linearly polarised everywhere, with the axis of polarisation completing a full rotation every wavelength [72]. During this rotation, the shifts on the ground sub-levels remain constant such that Sisyphus cooling will not occur.

In the simplified assumption of a $J = 1$ to $J = 2$ transition, a stationary atom between two counter-propagating lasers will equally populate the ground sub-levels. However, in the situation of an atom moving on the axis of propagation, an asymmetry in the ground states leads to to more absorption from the counter-propagating laser [72]. This asymmetric absorption produces a previously unaccounted for damping force for this cooling mechanism. The theoretical model put together by Dalibard and Cohen-Tannoudji studies this damping coefficient [72, 82] and gives the resolution of the temperature:

$$k_B T = \frac{\hbar \Gamma^2}{2|\Delta|} \frac{I}{I_s} \left[\frac{29}{300} + \frac{254}{75} \frac{1}{1 + (2\Delta/\Gamma)^2} \right] \tag{3.22}$$

3.3.1 Further cooling

In the general case of sub-Doppler cooling mechanisms, the atomic temperature is limited by the kinetic energy given to an atom at rest during the absorption of a single photon. This energy provides the momentum required

for a photon recoil, with corresponding temperature [57]:

$$k_B T_{recoil} = \frac{\hbar^2 k^2}{m} = \frac{h^2}{m\lambda^2} \tag{3.23}$$

For sodium this equation realises a new ideal temperature limit of 2.4 μK, compared to the Doppler limit 240 μK. Much like the previous limits applied to laser cooling, the recoil limit did not remain for long due to methods such as velocity-selective coherent population trapping, Raman cooling and evaporative cooling [84–86].

Part II

Compact optics

Chapter 4

Publication: Design and fabrication of diffractive atom chips for laser cooling and trapping

J. P. Cotter, J. P. McGilligan, P. F. Griffin, I. M. Rabey, K. Docherty, E. Riis, A. S. Arnold and E. A. Hinds.[1]

It has recently been shown that optical reflection gratings fabricated directly into an atom chip provide a simple and effective way to trap and cool substantial clouds of atoms. In this chapter we describe how the gratings are designed and micro-fabricated and we characterise their optical properties, which determine their effectiveness as a cold-atom source. We use simple ray optics to understand how the morphology of the gratings determines the power in the diffracted beams.

---

[1]The work presented in this chapter is extracted from and expands upon the published results. The published version is provided in Appendix C

4.1   Path to a micro-fabricated MOT

Cold-atom technologies have dominated precision measurements in recent years [87–89]. The preference for cold atoms partly arises from the increased interrogation time that is provided in an isolated environment, allowing higher precision to be taken from a measurement [90]. Although many metrological experiments benefit from cold-atom measurements [91], the standard apparatus required is typically too large for portable devices. Despite the fact that current miniaturised metrological devices have proven highly successful [92], their precision is limited by their use of thermal atoms.

The most common cold-atom source is the standard magneto-optical trap (MOT) [70, 76] which typically utilises 6 independent beams, each with its own alignment and polarisation optics. However, the minimum number of beams required for cooling is $N + 1$, where N is the number of dimensions the cooling is in. Thus for 3-dimensional cooling, one would only need the 4 electric fields orientated to fulfil the balanced molasses condition,

$$\sum_{i=1}^{N} I_i \vec{k_i} = 0, \tag{4.1}$$

Where I is the laser intensity and $\vec{k}$ is the wave-vector.

One trap that takes advantage of Eqn. (4.1) for a simplified cooling scheme is the pyramid MOT [93]. The pyramid MOT utilises a single incident laser beam onto a highly reflective coating covered pyramid in the orientation of Fig. 4.1. The incident beam area is aligned to strike each of the four pyramid walls, to produce reflected orders where the $\vec{k}$ sum to zero to satisfy the molasses condition with five electric fields.

A crucial draw back to the pyramid set-up is the formation of the overlap
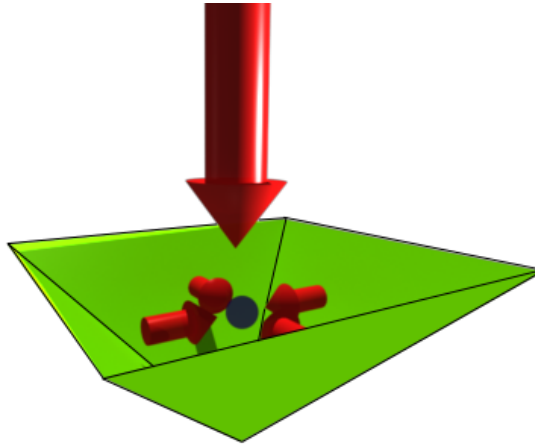
Figure 4.1: Composition of the pyramid MOT with one incident beam and four reflected orders.

volume within the pyramidal structure, such that poor optical access contributes to an experimental difficulty in measurement and characterisation. Additionally, complications in the micro-fabrication of the pyramid design limit the reproducibility and feasibility of it being deployed for mass production. These issues were overcome by the introduction of the simplified tetrahedral mirror MOT, seen in Fig. 4.2 (a).

The simple construction of the mirror MOT is composed of three dielectric mirrors placed on an precision tetrahedral mount to reflect the incident beam for a balanced radiation force [94]. The MOT formation point in this set-up is above the mirrors' highest point, facilitating an increased optical access from the pyramid MOT. The total area can be reduced further by following in the steps of Fresnel and replacing the mirrors with the planar surface of a diffraction grating. The first grating MOT, seen in Fig. 4.2 (b), now uses the diffracted orders of the three linear gratings to simplify and reduce the scale of the apparatus [95].

The micro-fabrication of such diffractive optics has led to a mass producible, robust, compact cold-atom platform. A long exposure image of the final

(a)

(b)

(c)
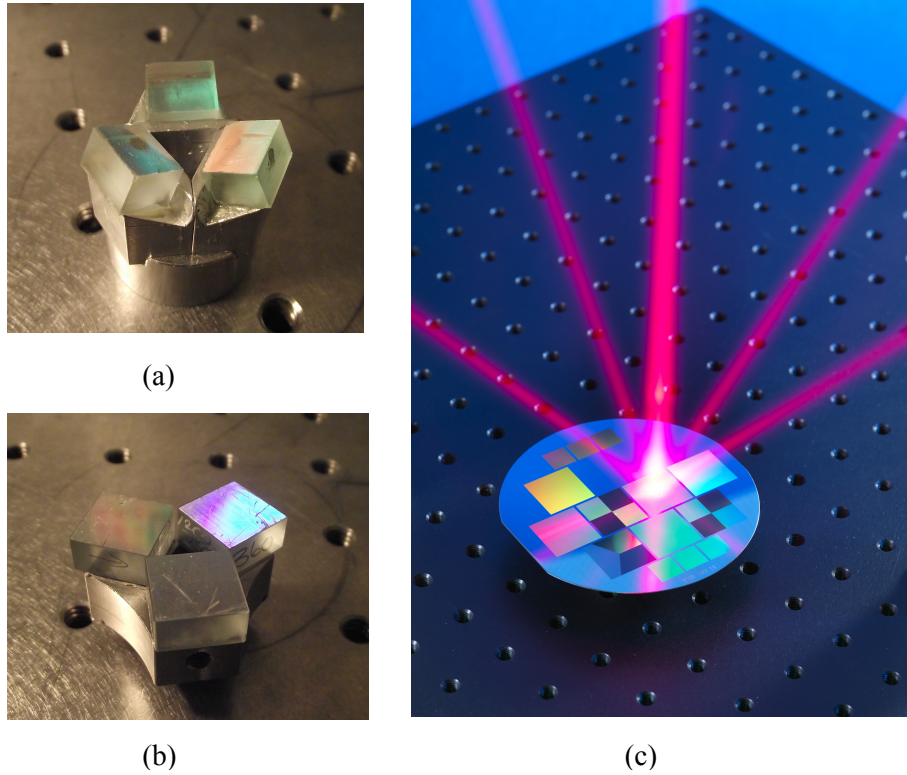
Figure 4.2: a) Mirror MOT set-up uses one incident beam onto three angled mirrors. b) Three mounted gratings to diffract light in the same pattern as the pyramid scheme. c) Long exposure image of laser incident upon an etched wafer in the pattern of chip C. Copyright of NPL.

e-beam lithography etched wafer can be seen in Fig. 4.2 (c) before it was cleaved to individual grating chips. Once cleaved, the 2×2 cm grating chips are aligned with a single, circularly polarised, incident beam to produce a region of balanced radiation force. The optical set-up discussed is depicted in Fig. 4.3, for the two geometries realised within this thesis.

Fig. 4.3 (a) illustrates the triangular (TRI) geometry, with three one-dimensional grating chips rotated around the grating centre by $2\pi/3$. Each linear grating diffracts two first diffracted orders, $n_x = \pm 1$, at an angle, θ, with only the positive order from each grating contributing to the optical cooling volume. Fig. 4.3 (b) depicts the checkerboard/circle geometry, utilising a single two-dimensional grating chip, patterned with either squares or the circles, as seen inset for a period, d. This geometry produces four
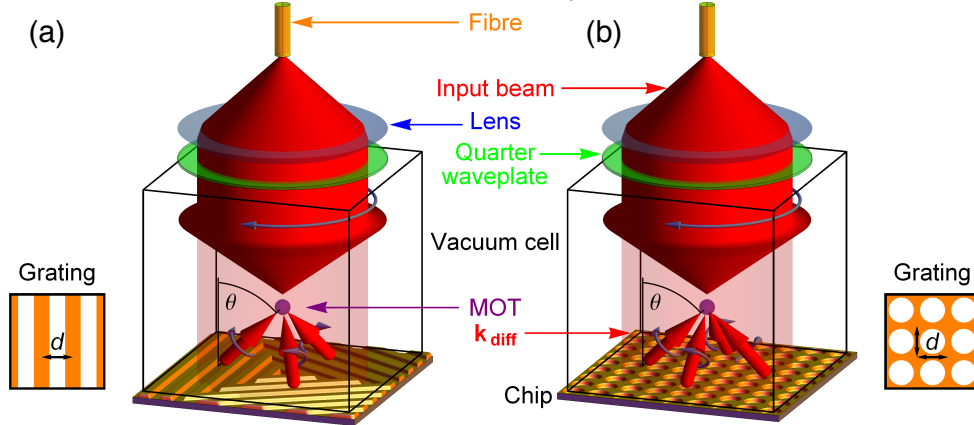
Figure 4.3: Micro-fabricated grating magneto-optical trap, coupled to a single incident optical fibre (orange), with the output collimated by and circularly polarised by a combination of lens (blue) and quarter wave-plate (green) respectively. The grating chip is placed beneath the vacuum cell to generate a balanced radiation force between the incident and diffracted light (small red arrows). (a): Triangular (TRI) grating chip geometry with three linear one-dimensional gratings producing three diffracted orders used for cooling. (b): Checkerboard/circle grating chip geometry with a single two-dimensional array with a period d.

first diffracted orders, $n_x = \pm1, n_y = \pm1$, each contributing to the cooling volume. In either graphical representation the grating is placed beneath the vacuum system to demonstrate the ease of switching between geometries experimentally without the need to brake vacuum.

4.2 Diffraction theory

Previous efforts made towards producing a reliable theory of diffraction require a typically complex calculation [96, 97]. However, here we look to introduce a simplified diffraction theory for determination of the first and zeroth order diffraction efficiencies.

The diffraction grating is composed of a combination of reflecting elements arranged in a periodic array, separated by a distance comparable to the wave-

length of study, as seen in Fig 4.4. The reflective elements peaks and troughs are etched into the substrate to produce a grating that is directly analogous to transmissive slits [98].

When studying a diffraction grating of period d with incident light of wavelength λ at an angle α to the grating normal, then a diffracted order will be produced at angle θ determined by the grating equation, $m\lambda = d(\sin\alpha + \sin\theta)$, where m is an integer representing the diffracted order concerned. For incident light perfectly perpendicular to the grating ($\alpha = 0$), the grating equation simplifies to the Bragg condition,

$$m\lambda = d\sin\theta, \tag{4.2}$$

where θ is now the angle of diffraction.

Fig. 4.4 shows how the total electric field can be represented as the sum of diffracted orders from the trough and peak of the grating, which are weighted by their relative sizes pd and $(1-p)d$, respectively and phase shifted by the path difference between $AB = d/2\sin\theta$ $(= m\lambda/2$ from Eq. 4.2) and $CDE = h(1 + \cos\theta)$, i.e.:

$$E_{\text{tot}} \propto p + (1 - p)\,\exp\left[i\pi(m - 2h(1 + \cos\theta)/\lambda)\right], \tag{4.3}$$
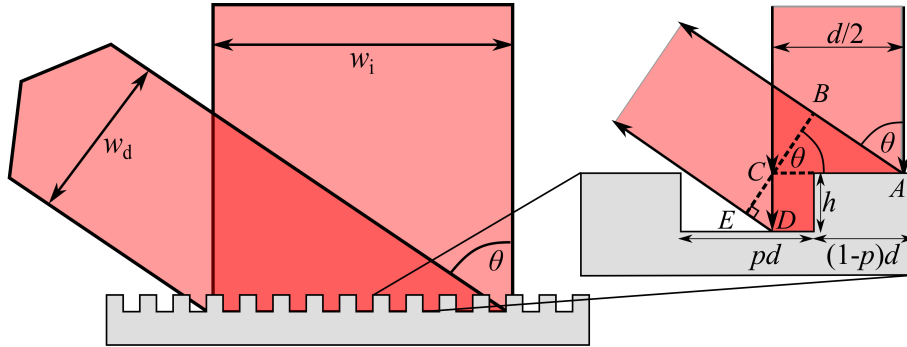
Figure 4.4: Surface of a binary diffraction grating of etch depth h, diffraction angle θ, period d and duty cycle p and (1-p) for trough and peak respectively.

where h is the etch depth, and λ the wavelength of incident light. This gives a simple "phasor" model of the diffraction efficiency.

Since it is desirable to have maximum diffraction efficiency into the first order, we therefore want to minimise the light going into the zeroth order. For this to occur we would expect that an etch depth of $\lambda/4$ on a double pass would produce a $\lambda/2$ destructive interference of the zeroth order. Fig. 4.5 shows the total electric field for $m{=}0$ and $+1$ as a function of the normalised etch depth, h/λ, and the duty cycle, p. From this plot, we see that a minimum in the zeroth order and maximum in the first order is centred around an etch depth of $\lambda/4$ and 50:50 duty cycle.

Using this electric field, in the case of 50/50 duty cycle, $p = 1 - p = 0.5$, and a 1D grating then the intensity efficiency, η_1, in the first diffracted orders can be calculated via

$$\eta_1 = R\frac{|1 + \exp\left[i\pi(1 - 2h(1 + \cos\theta)/\lambda)\right]|^2}{8}, \tag{4.4}$$

where R is the reflectivity of the coating metal used, and the equation is valid for the symmetric diffraction orders $m = \pm 1$.

Eqn. (4.4) now provides a simple relation between the intensity of the light diffracted in the first order relative to the angle of diffraction. A simple model could thus assume that, for perfect diffraction and no second order, the zeroth order can be described by,

$$\eta_0 = R(1 - 2\eta_1), \tag{4.5}$$
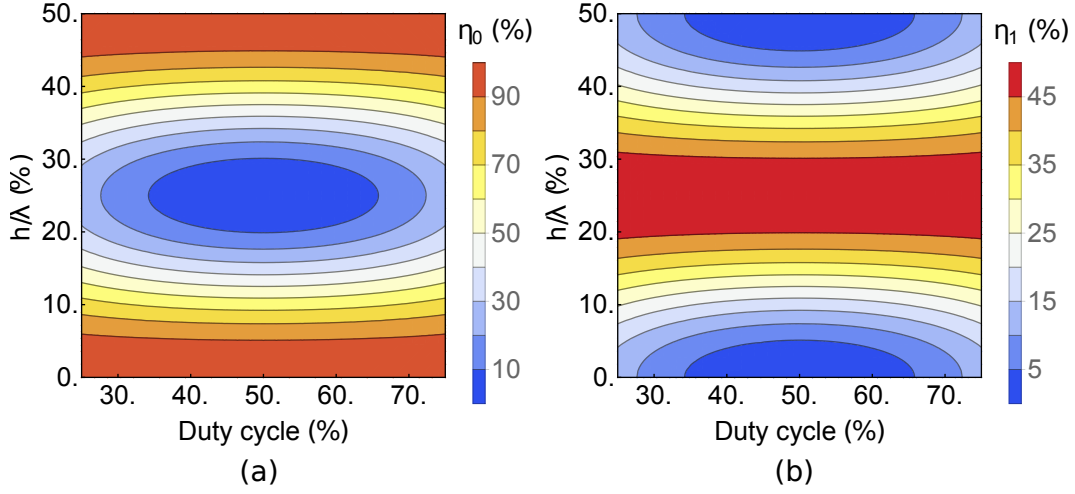
Figure 4.5: Power present for individual diffracted orders, normalised with the incident light and plotted as a function of the duty cycle, p, and normalised etch depth, h/λ, where we assume $R = 100\ \%$. a): The case of m=0. b): The case of m=+1.

If the etch depth, h, is designed such that $h = \lambda_B/4$, where λ_B is the design wavelength and $\cos\theta \approx 1$, then Eqn. (4.4) simplifies further to,

$$\eta_1 = R\frac{\left(1 + \exp(i\frac{\pi\lambda_B}{\lambda})\right)^2}{8}. \tag{4.6}$$

Note that to apply first order diffraction efficiencies, η_1, to two-dimensional (2D) gratings, we simply multiply by $1/2$, to account for twice as many diffracted beams.

To determine how these diffracted efficiencies relate to creating a balanced radiation pressure we must account for the vertical intensity balance between the incident, I_i, and all diffracted orders, I_d, described as $\frac{I_d}{I_i} = \eta_1\frac{w_i}{w_d} = \frac{\eta_1}{\cos\theta}$, where w_i (Fig. 4.4) is the incident beam waist and w_d is the diffracted beam waist. The radial balance is not considered as this is automatic if the beam centre is positioned on the grating centre, such that the identical diffracted orders contribute equally. The net intensity on the grating $I_i(1-\eta_0)$ is ideally

balanced with the component of the diffracted intensity which is anti-parallel with the incident light, i.e. $NI_{\mathrm{d}}\cos\theta$ where N accounts for the number of diffracted first orders, which simplifies to $NI_{\mathrm{i}}\eta_1$. Thus, the balance between incident and diffracted light, perpendicular to the grating and taking the zeroth order into account, is described mathematically through the dimensionless quantity,

$$\eta_{\mathrm{B}} = N\eta_1/(1-\eta_0), \tag{4.7}$$

where η_{B} is the net intensity balance, which is ideally one.

4.3 Fabrication techniques

The theoretical analysis, discussed in the previous section, revealed a variety of grating parameters that could provide a balanced radiation pressure to facilitate laser cooling. The first generation of grating chips designed from this theory varied in geometry, periodicity and fabrication method. Fig. 4.6 provides scanning electron microscope, SEM, images of the first four gratings to present a scale and optical geometry.

Chip A consists of three 8 mm linear gratings etched into a 32 mm silicon wafer using photolithography. This micro-fabrication technique uses intense light to transfer a reticle onto the surface of the chosen substrate, in our case a silicon wafer. Chemical treatment, such as a wet/dry etch, can then be used to engrave the pattern into the surface of the substrate [42].

The etching process begins by developing a reticle onto chromium-coated quartz with an electron beam. The silicon wafer, coated with photo-resist, is exposed to 365 nm light through the reticle. After the resist has developed, the exposed silicon is removed by means of reactive-ion etching using an inductively coupled $\mathrm{SF}_6/\mathrm{C}_4\mathrm{F}_8$ plasma. The grating is then cleaned of any
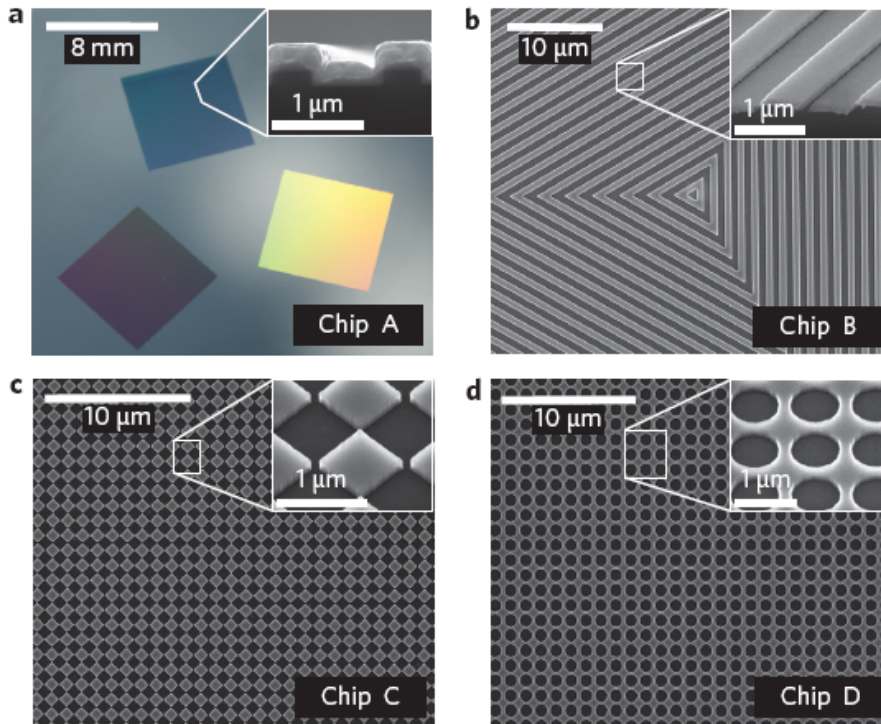
Figure 4.6: a: Chip A consists of three linear 8 mm × 8 mm gratings of pitch d=1,200 nm. b: Chip B is again a linear grating, following the pattern of Chip A to the intersection in the centre. This covers an area of 20 mm × 20 mm and has a pitch of d=1.400 nm. c: Chip C is an array of squares filling an area of 2 cm × 2 cm, with a pitch of d=1,080 nm. d: Chip D is the same as C but with circles rather than squares. The inset images are taken via a scanning electron microscope (SEM), and show the cleaved cross-section through the coated grating. The apparent distortion of the inset images of chip C and D is due to imaging at an angle.

organic compounds by use of a piranha solution. As is illustrated in Fig. 4.6 (a) inset, this etching method can produce highly isotropic etch depths with a few nm accuracy, emphasised by the optical study discussed in Sect. [4.4]. Finally, the grating is sputter coated with a 5 nm layer of chromium to act as an adhesion layer between the substrate and sputter-coated top layer, typically 100 nm of aluminium.

Chips, B, C and D were fabricated using electron beam lithography as opposed to photolithography. This fabrication technique uses a focused beam of electrons that are exposed to a photoresist layer onto a substrate [99]. The

electron beam changes the solubility of the photoresist, permitting chemical etching to remove unwanted regions, leaving behind the desired pattern [100, 101]. In our case, after application of the photoresist and electron beam surface patterning, the cleaning method is the same as for the photolithographically etched grating. Chip B uses linear gratings in the same shape as chip A, but extends the 8 mm × 8 mm gratings until the three gratings meet, increasing the grating surface area to 20 mm × 20 mm. Chips C and D were also created by the same methods as B, however, these are two dimensional gratings, i.e. for an incident beam the grating will produce four first order diffracted beams, rotated around the grating plane by $\pi/2$ relative to the last. Chips, B, C, and D were manufactured by Kelvin Nanotechnology.

4.4 First-generation optical characterisation

Following the fabrication process, the diffraction efficiency was measured to determine the gratings optical properties and verify the fabrication characteristics. This study looked at the diffraction efficiency, polarisation purity and grating period compared to the theoretical expectations and scanning electron microscope measurements made prior to optical tests, seen in Fig. 4.7 (a) and (b).

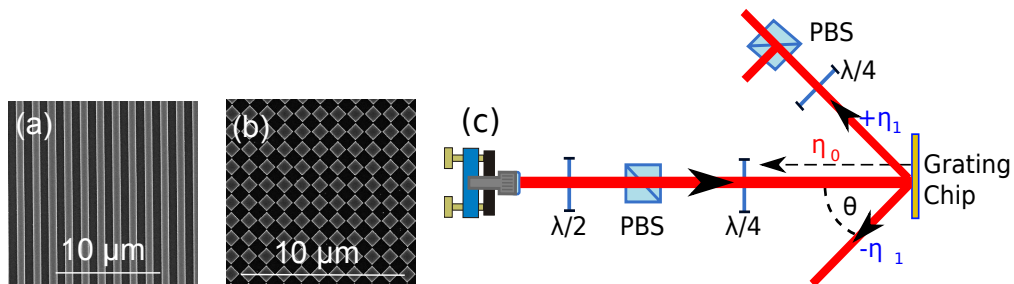Figure 4.7: (a) (b): Scanning electron microscope images of 1D and 2D gratings respectively. (c): Set-up used for grating efficiency and polarisation purity analysis. Abbreviations are $\lambda/2$ and $\lambda/4$ for the half and quarter wave-plates respectively, PBS for polarising beam splitter, η_i represents the relative power in the ith order of diffraction and θ is the angle of diffraction.

Firstly, Eqn. (4.4) was used to calculate the theoretical diffraction efficiency of the first and zeroth orders for the intended grating period following the micro-fabrication process. Table 4.1 provides the theoretical diffraction efficiencies for grating chips A, B, C and D, as a comparison for the experimentally measured results. The theoretical calculation included an 18 % loss to the total diffraction efficiency that is discussed later in Sect. [5.2].

The optical measurements employed circularly polarised light at 780 nm, illustrated in Fig 4.7 (c), to replicate MOT conditions. The light propagated approximately 1 m along the optics bench before being retro-reflected from a flat area of the chip to ensure a perpendicular incident beam. Retro-reflection through the PBS was used for critical alignment of the incident $\lambda/4$ wave-plate, to ensure a good circular handedness. The grating chip was mounted on a three axes translation stage, with a power meter used to measure the first diffracted orders efficiency, η_1, at an angle θ, whilst being able to measure the zeroth order and its polarisation after rejection from the PBS.

The reflectivity of each chip was tested first by measuring the power in the reflected light from a flat, un-etched area. This provided R=82.2 % for chip A and R=97.2 % for the chip B. The optical parameters measured during characterisation are provided in Table 4.2, which include the diffracted order powers normalised against the incident beam, periodicity, d, inferred from

Table 4.1: 1st Generation Grating Chips Theory

Grating	$\eta_{\pm1}$ (%)	η_0 (%)	d (nm)
A	37.6	2.9	1200
B	38.3	1.3	1400
C	18.9	2.3	1080
D	18.9	2.3	1080

Table 4.2: 1st Generation Grating Chips Experiment

Grating	$\eta_{\pm 1}$ (%)	η_0 (%)	d (nm)	σ (%)
A	34.5 ± 3.5	12.1 ± 1.1	1185 ± 3	92.2 ± 5.3
B	38.1 ± 0.1	0.5 ± 0.1	1479 ± 5	98.2 ± 0.8
C	20.0 ± 0.3	2.0 ± 0.3	1057 ± 1	98.0 ± 0.4
D	20.1 ± 0.2	3.2 ± 0.1	1053 ± 1	98.4 ± 0.3

the measured angle using the Bragg condition, and the polarisation purity of the diffracted light, σ. Chip A was seen to produce 34.5 ± 3.5 % in the first diffracted order, compared to the 39.1 % prediction from Eqn. (4.4) when inserting the measured grating dimensions and reflectivity. Of this 34.5 ± 3.5 %, only 92.2 ± 5.3 % polarisation purity was measured. The measured power in the zeroth order was found to have a significantly larger 12.1 ± 1 %, compared to the predicted 2.8 %. This variation between experiment and theory is due predominantly to variations in the periodicity across the three individual grating sections of this chip, measuring a $d=1185\pm3$ nm compared to the expected $d = 1200$ nm.

Conducting the same experiment on the three sections of chip B produced theoretical and experimental values of $\eta_{\pm 1}=$(38.3 %, 38.1$\pm$0.1 %) and $\eta_0=$(1.3 %, 0.5$\pm$0.1 %) respectively. As well as the diffraction efficiency matching the theoretical prediction, the polarisation purity in this order was measured at 98.2 ± 0.8 %. Chips C and D revealed a comparable overlap between theory and experiment, where C demonstrated $\eta_{\pm 1}=$(18.9 %, 20.0$\pm$0.3 %) and $\eta_0=$(2.3 %, 2.0$\pm$0.3 %), and $\eta_{\pm 1}=$(18.9 %, 20.1$\pm$0.2 %) and $\eta_0=$(2.3 %, 3.2$\pm$0.1 %) for D. Following this study, we concluded that the variation in polarisation in chip A, as well as error associated with $\eta_{\pm 1}$ compared to chip B, were significantly compromised for gratings fabricated with photolithography instead of e-beam lithography.

Chapter 5

Publication: Diffraction-grating characterisation for cold-atom experiments

J. P. McGilligan, P. F. Griffin, E. Riis, and A. S. Arnold.[1]

We have studied the optical properties of gratings micro-fabricated into semi-conductor wafers, which can be used for simplifying cold-atom experiments. The study entailed characterisation of diffraction efficiency as a function of grating coating, periodicity, duty cycle and geometry over a number of gratings. The critical parameters of experimental use, such as diffraction angle and wavelength, are also discussed, with an outlook to achieving optimal ultra-cold experimental conditions.

---

[1]The work presented in this chapter is extracted from and expands upon the published results. The published version is provided in Appendix D

5.1 Second-generation optical characterisation

To produce the ideal grating, a thorough investigation of the fabrication parameters affect on the diffraction efficiency would be required. This study was aimed towards an understanding of how metal coatings, periodicity, duty cycles and geometry affect the diffraction efficiency, a crucial parameter for generating a balanced radiation pressure. To determine the optimum settings for future diffraction gratings, we commissioned the construction of over one hundred 2 mm× 2 mm gratings, produced with a variety of periodicities, duty cycles, geometrical layouts, coating metals, and coating thicknesses. In order to measure the properties of the large quantity of diffraction gratings, we constructed a dedicated testing station, as seen in Fig. 4.7, using an incident-collimated, circularly polarised beam of known wavelength and power.

Once the grating was mounted in the set-up, the zeroth order was carefully aligned to ensure the incident light was perpendicular to the grating. The inherent need for this alignment will be discussed later. The position of the diffracted order was noted, and θ measured. This allowed the periodicity to be inferred through the Bragg condition, Eqn. (4.2). The diffracted order is measured for diffracted power, then passes through a $\lambda/4$ plate and polarising beam splitter, PBS, to measure any degradation of polarisation that may have occurred during diffraction. The typical results of this investigation can be seen in Figs. 5.1 and 5.2, with their larger associated dataset presented in Figs. 5.3, 5.4, 5.5 and Figs. 5.6 for the diffraction efficiencies and polarisation purity respectively.

Fig. 5.1 depicts how the relative diffracted powers and beam intensity balance varies with diffraction angle, θ for 1D and 2D gratings. The circles and squares represent gratings with spatial dimension etched:unetched duty
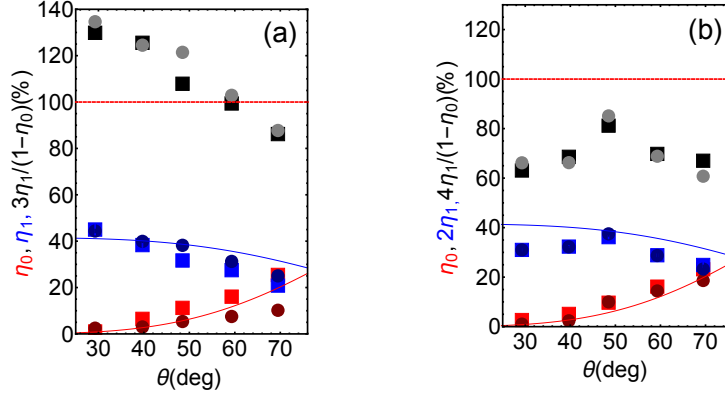
Figure 5.1: η_B vs. θ. (a): 1D gratings with 80 nm Au coating. (b): 2D gratings with 80 nm Au coating. Blue and red represent the 1st and 0th diffracted orders respectively, with black illustrating the radiation balance, and duty cycles of 60% and 50% represented for all data sets by circles and squares respectively.

cycles over one grating period of 40%:60% and 50%:50% respectively. Both data sets provided have a coating of 80 nm Au; however, further investigation was carried out into thicker coatings of Au as well as Al, with both 1D and 2D geometries. The results provided in Fig. 5.1 are typical of all data sets recorded. Associated Figs. 5.3, 5.4 provide detailed diffraction efficiency and polarisation purity information, respectively for 1D and 2D gratings with two different thicknesses of gold and aluminium coatings. Moreover, Fig. 5.5 shows that, for the 1D gratings, gold with a thin 20 nm alumina coating has similar reflectivity to plain gold. The purpose of the alumina coating was to introduce a layer between the Au surface of the grating and the Rb metal vapour inside the vacuum system, which corrodes the Au.

The first point of interest in Fig. 5.1 is the decrease of the 1st diffracted order relative to diffraction angle. As the first order decreases, the light in the zeroth order increases at the same rate, maintaining a close to constant total power. This decay appears weaker in the gratings with 40%:60% duty cycle, making this the preferable choice to 50%:50% duty cycle. Analysis of the larger data sets suggests that a thicker coating material causes no no-
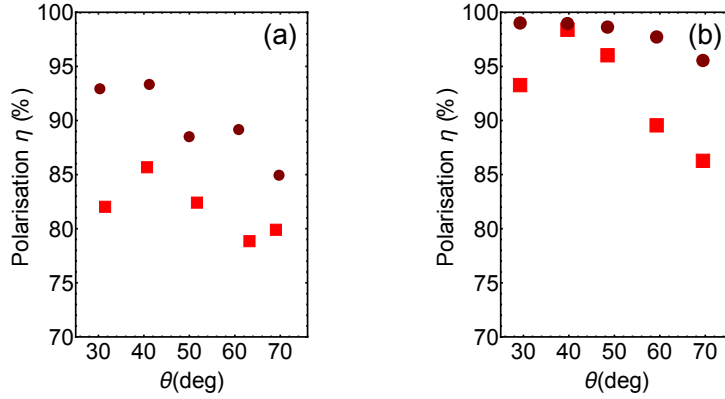
Figure 5.2: Diffraction angle vs. polarisation purity. (a): 1D gratings with 80 nm Au and Alumina layer. (b): 1D gratings with 80 nm Au, with duty cycles of 60% and 50% (circles and squares).

table change in the 1D or 2D gratings. A gold coating produces a stronger diffracted order than that of the aluminium of similar coating depth due to the higher reflectivity of gold. The results from all data sets suggest the duty cycle that are 60%:40% duty cycle produces a lower zeroth order for large θ, whilst maintaining a comparable first order diffraction efficiency. The reasoning for the lower zeroth order is not completely understood, but may be related to the effective duty cycle aiding the coating of the wafer [102].
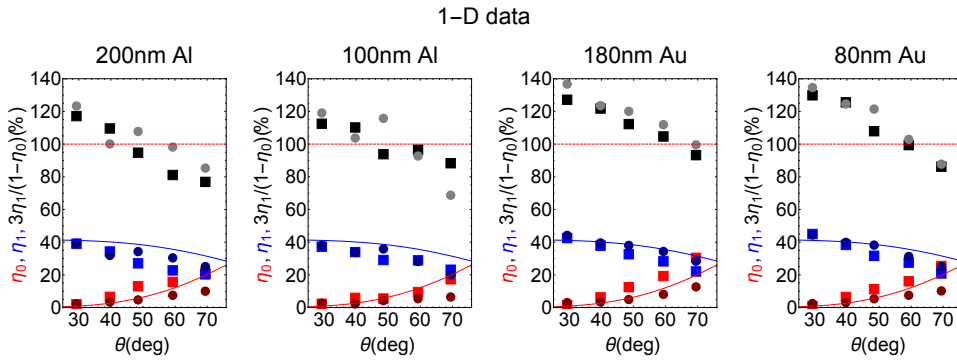
Figure 5.3: Diffracted orders for 1D gratings as a function of θ. The squares and circles represent gratings with 50% and 60% duty cycle respectively. Red: Zeroth order. Blue: First order. Black: Intensity balance

Figure 5.4: Diffracted orders for 2D gratings with discrete periodicities. The squares and circles represent gratings with 50% and 60% duty cycle respectively. Red: Zeroth order. Blue: First order. Black: Intensity balance
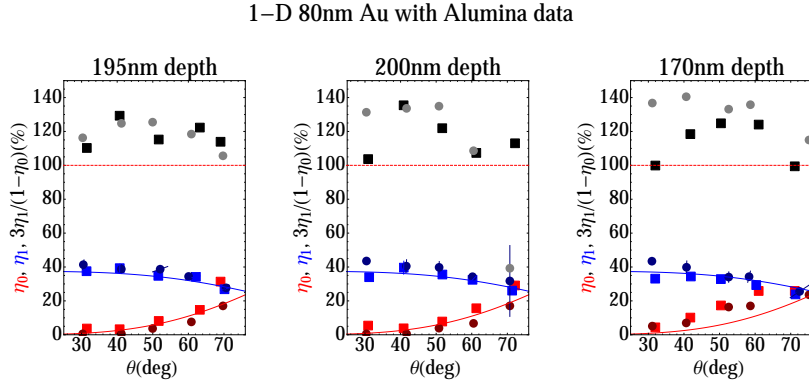
Figure 5.5: Diffracted orders for 1D gratings as a function of θ. The squares and circles represent gratings with 50% and 60% duty cycle respectively. Red: Zeroth order. Blue: First order. Black: Intensity balance

Fig. 5.1 also illustrates the balance of light force from Eqn. (4.7) for the intended experimental geometry as a function of diffraction angle. The dashed line at 100% represents axial balance between the incident downward beam and diffracted upward orders. This balancing force is notably higher in the 1D gratings compared to the 2D gratings, as the 1D gratings only diffract into 2 beams rather than 4. However, with appropriate neutral density filtering of the incident beam, the beam imbalance can be corrected to produce well balanced radiation forces [103] required for laser cooling [70, 82]. Using a 4 beam configuration with a linear grating provides close to ideal balance
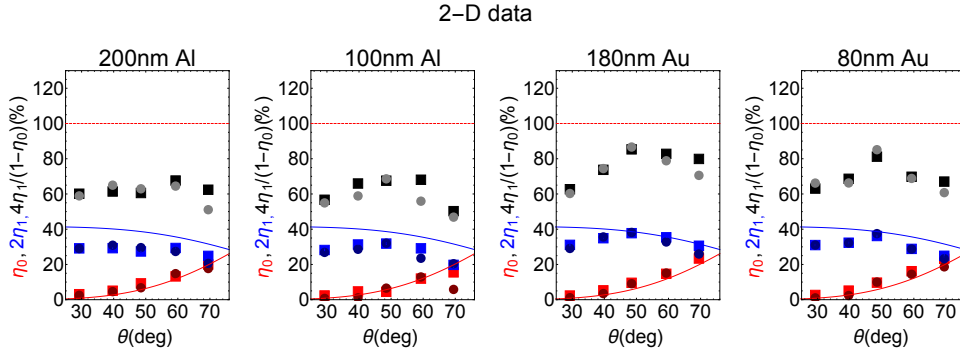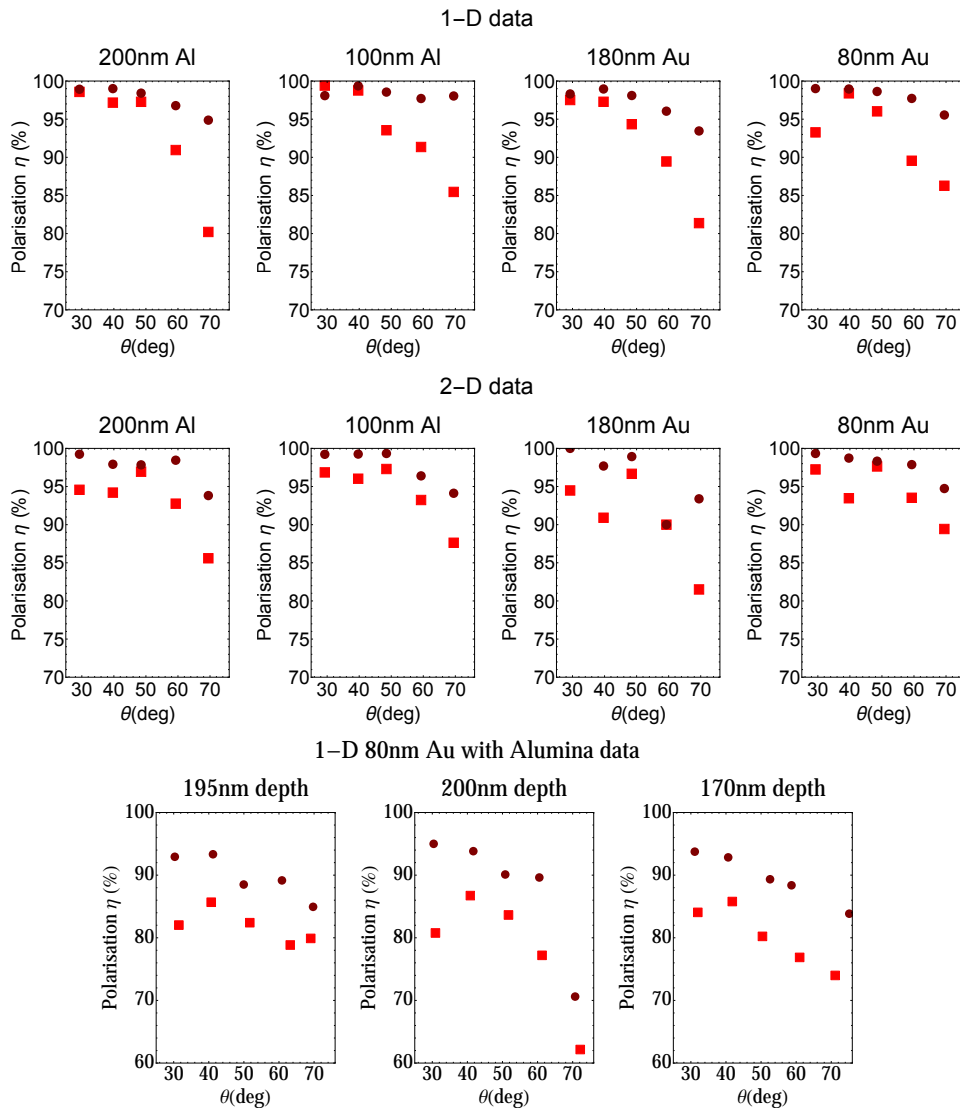
Figure 5.6: Diffracted orders for 1D and 2D gratings with discrete periodicities. The light and dark colours represent gratings with 50% and 60% duty cycle respectively. Red: Zeroth order. Blue: First order. Black: Zeroth plus 2 x first order.

already without need for further adaptations to the apparatus. Testing was also carried out on Au coated gratings with a top layer of alumina. Although there was no difference in diffraction efficiency between the gratings with and without the alumina, for unknown reasons the additional layer was observed to degrade the polarisation purity of the diffracted order, Fig. 5.2.

The polarisation purity, η, refers to the ratio of correctly handed circular

light (for MOT operation) to total light after the polarisation analyser PBS in the first diffracted order. When measured against periodicity, this was typically above 95% for a 60%:40% duty cycle (circles). The lower duty cycle of 50%:50% (squares) consistently produced a weaker purity, which was noted to worsen in the case of an alumina coating. This side effect of using alumina coating could be mildly detrimental to experiments requiring in-vacuo gratings as the trapping force is proportional to $2\eta - 1$ [95]. An interesting point to note is that a circular polarisation purity of 90 % can be achieved with an elliptically polarised beam with an intensity ratio of 4:1 in the two perpendicular polarisation components, as discussed in Ref. [95].

5.2   Lost light

As has been made evident from the study of diffraction efficiency, the total diffracted power remains lower than the incident power by approximately $\approx$18 %. The theoretical reasoning for this can be conceived as the shadowing of the beam occurring against trough walls could produce diffraction losses in due to absorption [102] . Here, we discuss an experimental measurements of the losses. An initial investigation into the lost light was carried out through the study of periodic etching errors diffracting light into unintentional locations [104]. This was carried out by taking long exposure images around a 90° plane of diffraction and normalising the range of exposure time to determine the relative power in the minuscule peaks found.

To experimentally examine this, a beam collimated with a $1/e^2$ diameter of 1.3 mm was incident upon the grating. The first diffracted order was blocked with a small circular card to prohibit the main diffracted order from saturating a beam profiler. The measurement data was composed of 38 images taken through a 90° radius of 28.5 cm in the plane of diffraction using the set-up described in Fig. 4.7, with the exposure times ranged between 300 ms and
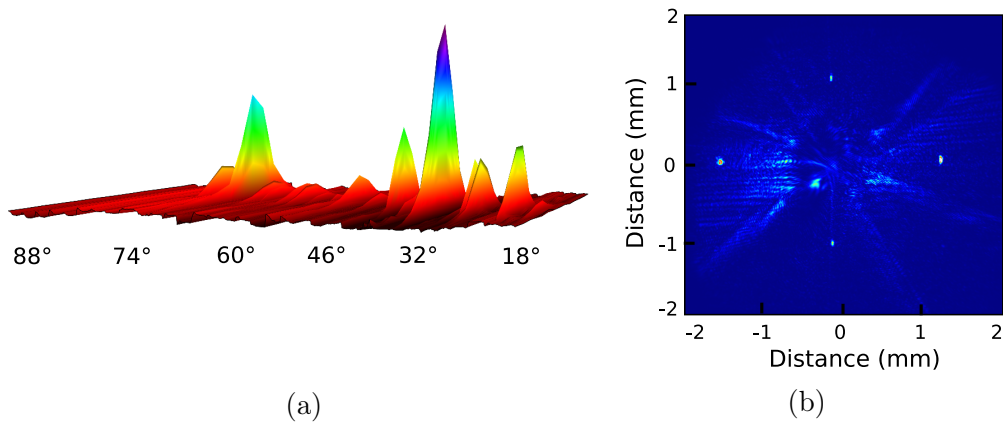
Figure 5.7: (a):Beam profile taken at a fixed height through a rotational axis of a linear grating. The contour map illustrates the power detected from the scatter as a function of detection angle. The largest feature is the first diffracted order, which is divided by 10^2 for comparison. (b): Long exposure image taken in vicinity of the first diffracted order with this strong order blocked with a card, revealing 'islands' of light above and below the central order.

100 μs. The resulting images were converted into a 3 dimensional contour plot, seen in Fig. 5.7 (a), where the largest peak is the first diffraction order, which has been reduced by a factor of 100 to avoid under-emphasising the lower levels detected. Light being scattered into the other regions detected is likely caused by imperfections to the grating period during the etching process.

With the largest region of scatter being within a few degrees of the main diffracted order, a long exposure image was taken of this region with the first order blocked by card. This method allows detection of small light levels on either side of the blocked central beam, as verified in Fig. 5.7 (b). This image reveals small islands of equal separation distance to the central diffracted beam, on the horizontal and vertical axis. This is most likely diffraction occurring due to the periodicity of the micro-fabrication process, where small sections are etched at a time, leaving a weak stitching period on top of the grating period. Integration of the collected light reveals that $\approx 1\%$ of the incident light was lost due to micro-fabrications limitations.

5.2.1 Absorption detection

A further investigation into the whereabouts of unaccounted light was carried out through a studying the absorption profile of a grating chip. For this, a small thermistor was attached in such a way that it was well insulated to the back of a 4 mm × 4 mm Au coated diffraction grating with thermal paste. The grating was mounted inside a insulted box to reduce thermal fluctuations from the environment. The incident laser power was set at 318 mW whilst recording the temperature variations, resulting in Fig. 5.8.

A 1.5 kΩ resistor was attached to the back of the grating with thermal paste, isolated from directly contacting the grating, to apply known amounts of power into the grating to determine the absorption rate. This heating rate could then be matched to that of the laser heating as a voltage calibration to convert to power. The best fitting calibration data from the Ohmic heating was taken at a voltage of 7.70 V, which corresponds to 39.5 mW. Two further data runs were taken at laser powers of 205.4 mW and 130.6 mW with their calibrations voltages being 6.33 V and 5.12 V, corresponding to 26.7 mW and 17.5 mW respectively. This gives an average absorption ratio of 12.9±0.5 %.
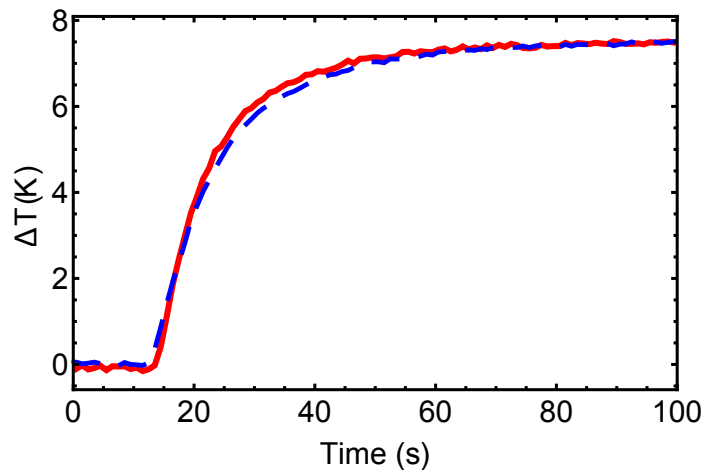
Figure 5.8: Temperature change of 1-D Au coated grating heated with 318 mW of laser light (red) and calibrated with an Ohmic heating of 39.5 mW (dashed blue).

In order to account for thermal gradients in the area of the grating, the measurement procedure was also carried out for a plane Au coated wafer. Since plain Au has a known 3 % absorption at 780 nm [105] we could use any measured reflectivity deviations from theory to account for thermal gradients, that could be used to normalise the absorption results. Including this correction factor of the Au reflectivity results in 12±2 % of the incident light being absorbed by the diffraction grating for a range of powers.

5.3   Grating critical parameters

When implementing the diffraction grating into an experimental set-up, it is mounted perpendicular to the incident beam, however, the cruciality of the angle of the incident light was unknown. We investigated the sensitivity of this using the same set-up as in Fig. 4.7 (c), with variable tilt applied to the grating mount. Whilst in this configuration, a known amount of light was incident upon the grating, held at a variable tilt angle whilst the diffracted orders where measured. This procedure was carried out for both 1-D and 2-D gratings, the results of which are seen in Fig. 5.9 (a) - (b).

The blue and red data sets represent the opposite first diffracted orders, with black representing the zeroth, with best fitting lines and parabola applied. Fig. 5.9 (a)- (b) demonstrates that a small deviation from 90° will symmetrically imbalance the first diffracted orders, and increase the unwanted zeroth order. This asymmetry vs angle is markedly more for 2-D gratings (b) in comparison to 1-D gratings (a).

It would also be of importance to know how the diffraction gratings' diffracted efficiency varies with the wavelength of incident light, as a wide bandwidth of wavelengths could unlock other alkaline earth metals as possible species to
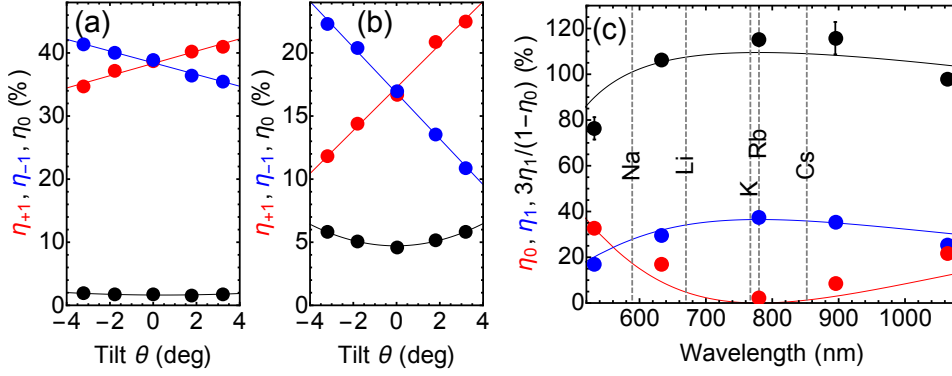
Figure 5.9: Left: The power in the relative diffracted orders vs. the grating angle tilt, with simple linear/parabolic fits for (a): Al 1-D grating, d=1478 nm. (b): Au 2-D grating, d=1056 nm. Right: (c): The wavelength of incident light upon the same grating as in (a) is varied and the powers of the first and zeroth diffracted orders are recorded and fit against theory of Equ. (4.6). Black data points represent the intensity balance from Equ. (4.7). The same set-up as in Fig. 4.7 was used with the exception of a Fresnel rhomb aligned to act as a $\lambda/4$ wave-plate due to its achromatic retardance.

be used in the grating MOT configuration. Additionally, knowing the diffraction efficiency dependence upon λ would also provide understanding of etch depth through Eqn. (4.4), where $h = \lambda/4$. For this investigation the same set-up was used as in Fig. 4.7, with five different lasers, covering a range of wavelengths seen in Fig. 5.9 (c). The red and blue data points depict the measurements of first and zeroth diffracted orders, with the fits derived from Equ. (4.6). The black data points again depict the intensity balance from Equ. (4.7). As is illustrated, the grating would deliver reasonably balanced cooling within ± 200 nm of the design wavelength of 780 nm and would be useful for cooling a variety of alkali metals.

Part III

Cold atoms

Chapter 6

Experiment: Laser spectroscopy and vacuum systems

The foundations of a cold-atom experiment are focussed around the lasers, electronics and vacuum system. This chapter discusses the construction of the external cavity diode laser, ECDL, and laser locking apparatus. Furthermore, the preparation and baking of the vacuum system is discussed for a compact apparatus.

6.1   Rubidium

Rubidium, Rb, was first discovered by Bunsen and Kirchof in 1861, choosing the name from the Latin for "deepest red", representing the colouring of the metal [93]. The alkali-metal appears in group 1 of the periodic table, occurring naturally in two isotopes, ^{85}Rb and ^{87}Rb, with an abundance ratio of approximately 3:1 respectively. Rubidium has recently been a preferred alkali atom for cold-atom experiments, being the first element to be condensed to a Bose-Einstein condensate by Carl Wieman and Eric Cornell in 1995 [106], earning them the physics Nobel prize along with Wolfgang Ketterle for the same achievement with sodium [107].
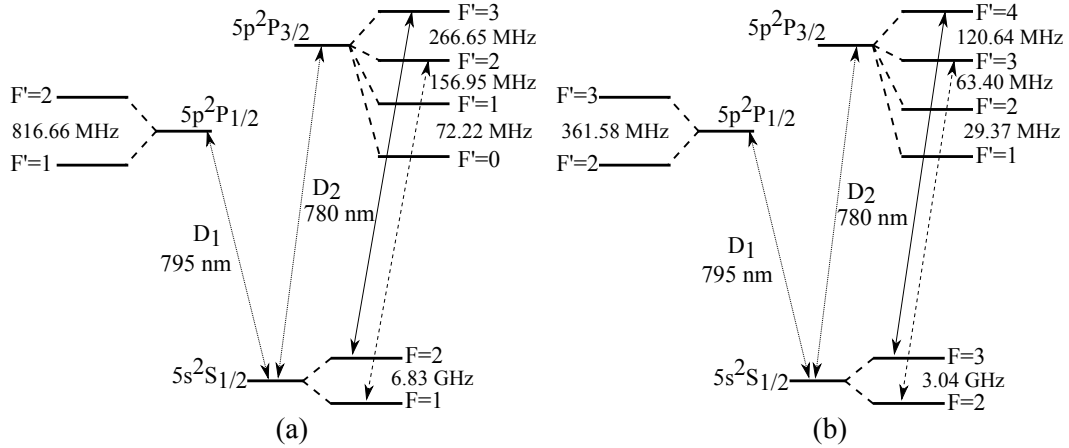
Figure 6.1: Electronic configuration in Rb. Solid blue and red lines indicate the cooling and re-pump transitions respectively. Solid and dashed lines depict the cooling and re-pump transitions respectively. Dotted lines denote the D_1 and D_2 manifolds. a): ^{87}Rb atomic structure. b): ^{85}Rb atomic structure

The ground state of Rb is $5^2S_{1/2}$. This is provided from the total angular momentum, $\mathbf{J}$, obtained by coupling the orbital angular momentum, $\mathbf{L}$, of the outer electron to the spin angular momentum, $\mathbf{S}$, through $\mathbf{J} = \mathbf{L} + \mathbf{S}$ [59]. In the case of Rb, the inner four electron shells are filled, such that the single outer $n = 5$ valence electron determines the angular momentum configuration. Since the ground state S shell has $L = 0$ and $S = 1/2$, the total angular momentum is $J = 1/2$.

The hyperfine structure of the alkali atoms arises from the total atomic angular momentum, $\mathbf{F}$, whose coupling of $\mathbf{J}$ to the total nuclear angular momentum $\mathbf{I}$, is described as $\mathbf{F}=\mathbf{J}+\mathbf{I}$. The ^{87}Rb and ^{85}Rb isotopes have total nuclear angular momenta of $I = 3/2, 5/2$ respectively, producing two $\mathbf{F}$ ground state manifolds of $F = 1, 2$ for ^{87}Rb and $F = 2, 3$ for ^{85}Rb, as illustrated in Fig. 6.1 (a) and (b) respectively. The hyperfine splitting frequency between these ground states occurs at 6.83468261090429(9) GHz and 3.0357324390(60) GHz [59].

The dipole transitions between electronic states are governed by the conservation of angular momentum, such that selection rules apply. As is shown in Ref. [108], the selection rules realise the requirement of $\Delta L = \pm 1$ for the electric dipole, with the magnetic levels limited to $\Delta m = 0, \pm 1$ for $\pi, \sigma^{\pm}$ polarised light. Laser cooling of Rb uses the transition the D_2 $5s^2S_{1/2} \rightarrow 5p^2P_{3/2}$, with a natural linewidth of $\Gamma = 2\pi \times 6.07$ MHz, requiring a laser linewidth $\Gamma_L < \Gamma$ to effectively laser cool with a small detuning from resonance. In the case of ^{87}Rb the cooling transitions is driven from the $F = 2$ manifold of the ground state, to the excited $F' = 3$. However, due to resonant scattering on the $F = 2 \rightarrow F' = 3$ transition, atoms are leaked into the $F = 2$. From this state, the atomic population will eventually fall into the $F = 1$ ground state, where the atoms will no longer be interacting with the cooling light. To counter this, typically a re-pumping beam is applied to drive the $F = 1$ to $F' = 2$ excited state, optically pumping the atoms back into a cyclic transition of cooling.

6.2 External cavity diode laser

The cooling transition for ^{87}Rb at 780 nm is readily available in laser diodes due to mass production for driving compact disc players and subsequently with higher powers in laser printers. Because of this, laser diodes at 780 nm can be purchased cheaply, with many typically capable of producing above 100 mW of output emission. As well as the output power demonstrating a high sensitivity to current and temperature fluctuations, the standard laser diode has a typical linewidth of around 100 MHz, above that required for laser cooling of atomic rubidium. This broadened linewidth depends on a combination of laser gain, cavity losses and experimental noise, with the limiting linewidth described by the Schawlow-Townes limit [109]. This can be physically interpreted as a spectral broadening introduced by spontaneous emission into the laser mode, which introduces phase noise in the out-coupled

electric field. A simple solution to reduce the linewidth is to increase the cavity length of the laser. Extending the cavity length both reduces the number of spontaneously emitted photons into the laser mode, but also increases the total number of photons in the cavity [110]. This is provided by the external cavity diode laser, ECDL, which for a cavity length $L=1$ cm has been shown to generate a linewidth as low as 300 kHz without any sophisticated locking electronics [111, 112].

The ECDL extends the typical diode cavity by collimating the diode output onto a frequency dependent reflector, such as a blazed diffraction grating, as seen in Fig. 6.2. In our case, a commercial ThorLabs 1800 grooves/mm grating was aligned to reflect first order diffracted light into the diode can, providing feedback and hence lowering the zeroth order output power threshold. The grating is mounted in the Littrow configuration [111], on an adjustable baseplate, which facilitates fine tuning of the wavelength and free spectral range. This baseplate is attached to a piezo-electric actuator, enabling the laser frequency to be controlled by an externally applied voltage. At this stage, the standard Strathclyde ECDL design has been implemented across all our laser cooling experiments [85, 91, 113, 114], using a schematic design similar to that proposed by Scholten *et al* and Arnold *et al* [111, 115]. Our design introduces a mirror and two pivot points to decouple alignment of the horizontal and vertical axes.

The laser frequency is strongly affected by temperature fluctuations, which cause changes in the cavity length and thus must be stabilised in order to maintain reasonable frequency stability. For this, a Peltier cooler was mounted to the housing of the ECDL, with a 10 kΩ thermistor inserted into the ECDL body for active feedback. The Peltier was controlled by a commercial FTP-4000 temperature controlling unit and set to maintain 19°C. The ECDL current was supplied to the diode using a low noise ThorLabs
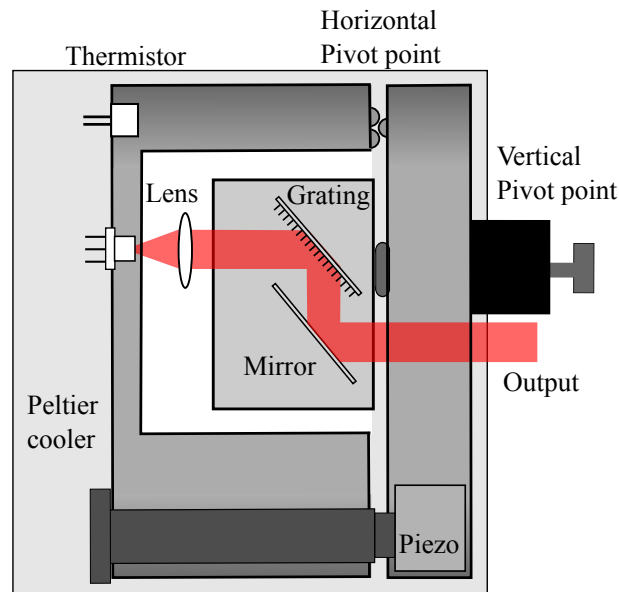
Figure 6.2: Composition of the Strathclyde external cavity diode laser.

LD1255R current driver. The variable resistor configuration of the LD1255R permits fine tuning of the diode current and thus the output frequency.

6.3 Saturated absorption spectroscopy

Spectroscopic techniques have been used for decades to quantify the emission lines of atomic media [116]. This proves useful for the resolution of the hyperfine atomic structure as a frequency reference for laser locking and stability. One such spectroscopic method is saturated absorption spectroscopy, SAS. This method is among the most commonly employed vapour cell spectroscopic techniques due to its relative ease and capability to observe the Doppler-free saturated absorption spectra for alkali atoms [117]. Although named saturation spectroscopy, the dominant mechanism of this technique is hyperfine pumping.

Due to the atoms possessing a random velocity, $\vec{v}$, their Doppler shifted frequency from resonance, ω, is written as $\omega_D = \omega + \vec{k} \cdot \vec{v}$. If now the pump/probe

is red-detuned, then atoms propagating towards the pump will absorb only pump light, whilst atoms propagating away from the pump will absorb only probe. This effect arises since both beams have the same frequency but different $\vec{k}$ such that,

$$\vec{k}_{\text{pump}} \cdot \vec{v} = -\vec{k}_{\text{probe}} \cdot \vec{v}. \tag{6.1}$$

Because of this shift, the two light fields interact with different atomic velocity groups. In this scenario, the pump beam will induce the atoms to undergo the transition to the excited state. If the laser is optically pumping the $F = 2 \rightarrow F' = 1$ transition, then the atom can decay to the $F = 1$ ground state where it is no longer interacting with the laser. If instead, the atom decays to $F = 2$ then it will be reintroduced to optical pumping. Over a few cycles the laser optically pumps the population from the $F = 2$ to the $F = 1$ ground state. Since the frequency of the pump/probe is detuned from resonance, the probe interacts with atoms in a different velocity group, which undergo the same process at this relative frequency.

If however, the atoms have zero velocity along the beam, then the frequencies of both beams will meet that of the resonance frequency, $\omega_D = \omega$, then both beams address the same atoms. In this scenario, the population of atoms in $F = 2$ is depleted by the pump, such that less atoms undergo transitions from the probe light. This leads to an increased transmission of probe light through the atomic vapour.

The hyperfine pumping mechanism begins to fail on cyclic transitions between ground and excited states due to the poor atomic depletion of the addressed state. To counter the poor optical pumping, if we employ an incident intensity of $I \geq I_s$, the optical pumping rate will saturate the transition. Saturation of a transition refers to an approximately equal atomic population in the ground and excited states. It is due to this process that the probe
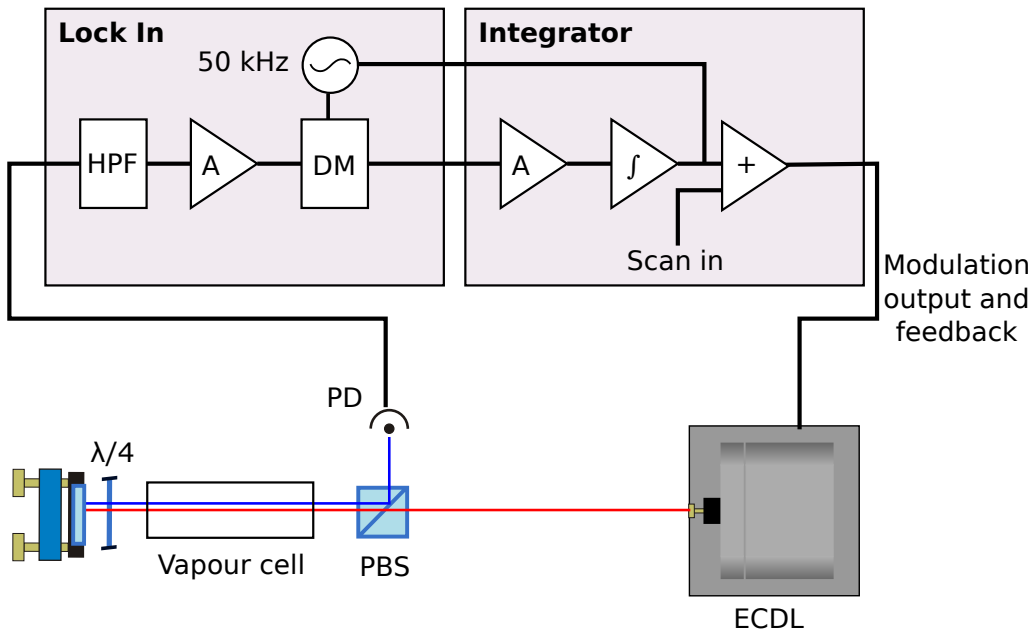
Figure 6.3: Servo locking loop for the saturated absorption spectrometer. HPF: High pass filter, DM: Demodulator, A: Amplifier, +: Adder amplifier, $\int$: Integrator.

beam becomes free from absorption and the hyperfine structure can be resolved in cyclic transitions.

The absorption signal from the probe beam is focussed onto a photodiode, as demonstrated in Figs. 6.4, 6.5 for the trapping and re-pumping transitions of ^{87}Rb and ^{85}Rb respectively.

The absorption spectra depicted contain features relating to direct ground to excited state transitions, as well as cross-over features occurring when ω_D is half-way between two excited state transitions. In the case of ^{87}Rb, illustrated in Fig. 6.4, the cross-overs occur at $\left(\frac{\omega_1+\omega_2}{2}\right), \left(\frac{\omega_1+\omega_3}{2}\right), \left(\frac{\omega_2+\omega_3}{2}\right)$. The cross-over absorption arises when the laser frequency has an equal separation between two excited transitions, atoms with a non-zero velocity permit absorption from the pump and probe simultaneously to both excited states. This typically relates to the cross-over spectra attaining an increased amplitude compared to the direct transitions.

Figure 6.4: Saturated absorption spectroscopy raw and error signals (top and bottom) for the cooling and re-pumper (left and right) transitions of ^{87}Rb.

Such spectroscopy, used in conjunction with the large free spectral range of the ECDL, gives rise to multiple absorption spectra. However, these absorption peaks do not provide a suitable zero-crossing for frequency feedback and laser locking. To counter this, the absorption is converted to a suitable error signal with zero crossings by differentiation of the modulated signal. The error signals are generated when applying a dither frequency to the current and or piezo, resulting in the absorption features with zero crossings seen in Figs 6.4 and 6.5 (c) and (d) for the trapping and re-pumping transitions.

The integrator can then be used to provide feedback in an electronic servo loop to maintain the laser frequency at the zero crossing. The locking circuit used for the D$_2$ apparatus is adapted from the PhD thesis of Aidan Arnold [71]. The laser can be locked to the zeros of the error signal, where the feedback has a linear response about zero. The stability provided by locking to the derivative has been seen to stay locked for days before jumping to a
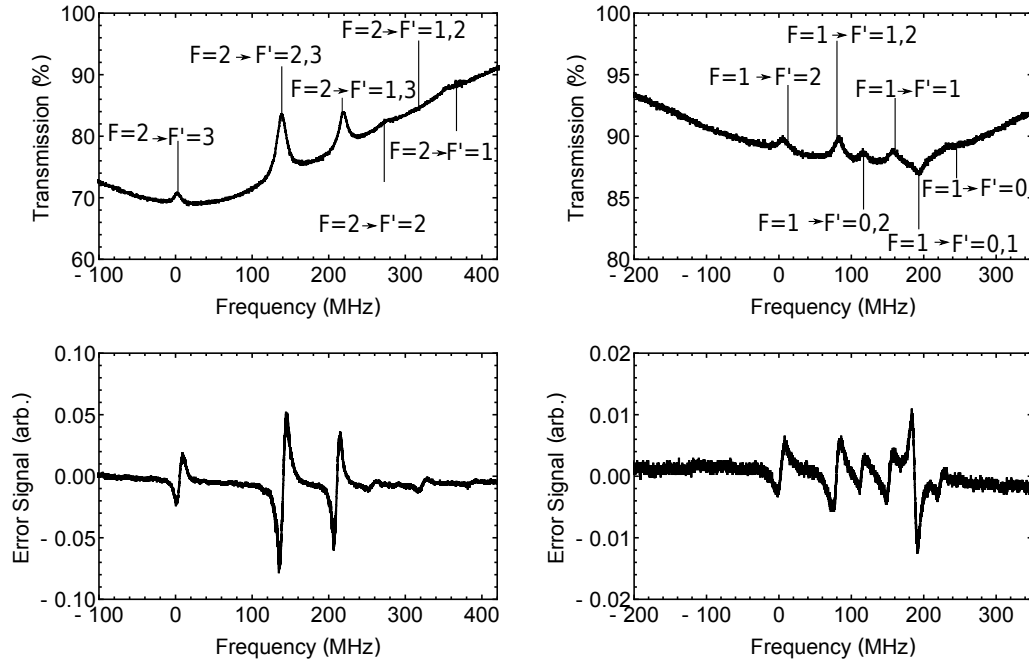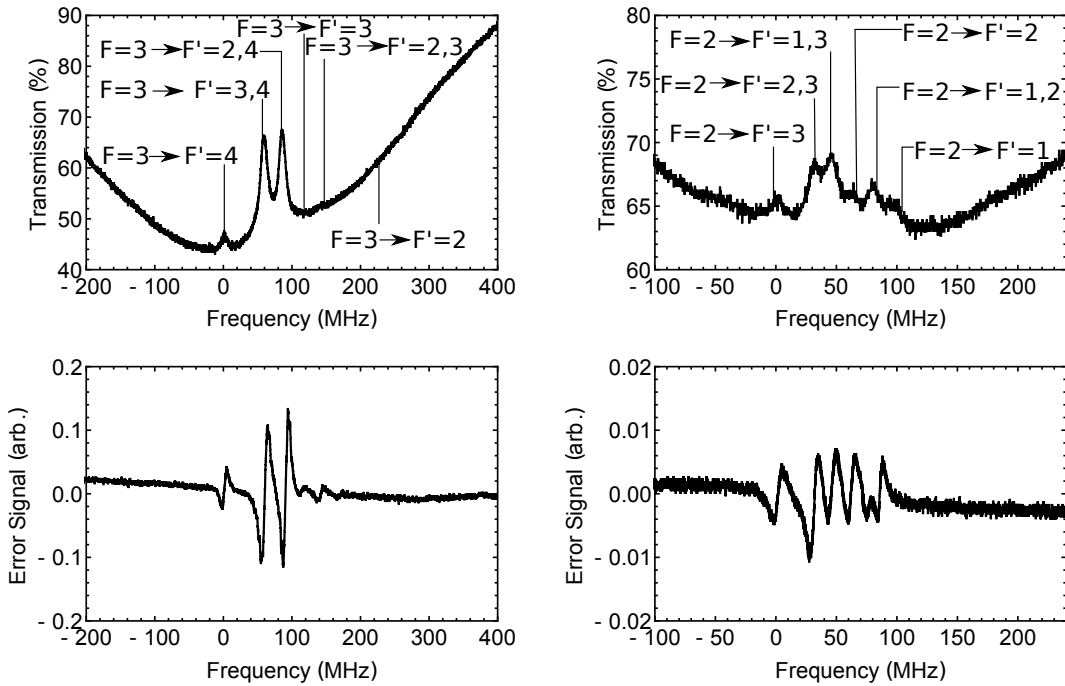
Figure 6.5: Saturated absorption spectroscopy raw and error signals (top and bottom) for the cooling and re-pumper (left and right) transitions of ^{85}Rb.

different transitional frequency.

Piezo modulation

Modulation is the process of varying the properties of a carrier wave with the additional information in a modulation wave. To generate the error signals in Figs 6.4 and 6.5 the frequency of the laser is deliberately modulated with the piezo. The error signal amplitude is linearly proportional to the modulation depth, such that we found a good operational modulation depth of <1 MHz at 50 kHz modulation frequency.

Zeeman modulation

The piezo modulation discussed has an inherent flaw of modulating the laser frequency output, which propagates through the experiment. In some instances this is not suitable and a modulation free output from the laser is
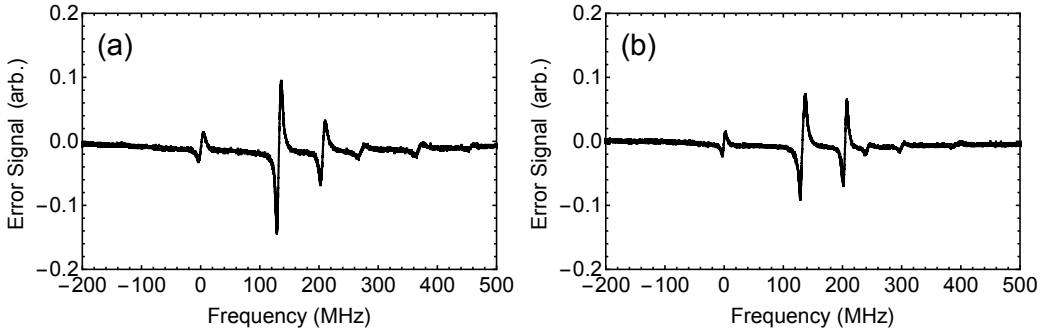
Figure 6.6: Comparison of Sat-Spec using Zeeman or current modulation. Left: Zeeman modulated error signal of trapping laser. Right: Current modulated error signal of trapping laser.

required instead. One technique employed is modulation of the magnetic field about the spectroscopic cell by modifying the current through a solenoid. The solenoid then modulates the atomic resonances, using the Zeeman effect, at the modulation frequency. This modulation technique ensures that only the light interacting with the atoms in the SAS vapour will see the modulation.

Our Zeeman solenoid was constructed from copper wire formed around the vapour cell, where the magnetic field strength is directly related to current passing through the wire by

$$B = \mu_o n I, \tag{6.2}$$

where n is the number of turns per unit length, I is the current and μ_0 is the magnetic permeability of the vacuum, $4\pi \times 10^{-7} \mathrm{Hm}^{-1}$.

Using the solenoid we apply an oscillating axial field with a peak of approximately 1 G, which produces a frequency shift of 1 MHz at the atoms. A signal generator, Agilent 33210A, was used to produce the field, which was optimised empirically to a frequency of 60 kHz, illustrated in Fig. 6.6.

6.3.1 Beat measurements

To ensure that the laser linewidth taken from the Zeeman method was still suitable for the experiments, the beat-note of the the two lasers used in our cooling experiments was taken. Beat measurements were taken for two current-modulation-locked lasers and for a current-modulation-locked laser against a Zeeman-modulation-lock.

The beat-note between the lasers is obtained by coupling equal intensities of both laser beams into the one optical fibre, optimised for maximum output into an amplifying photodiode, the signal of which can be observed on a spectral analyser to generate measurements, an example of which is shown in Fig. 6.7. The central frequency, seen in each set of beat-notes, of 203 MHz is due to the 78 MHz separation of the locks, plus a 125 MHz AOM used in the beam path of the trap laser. Fig. 6.7 reveals a total linewidth of both current-modulated lasers as 0.9 MHz. A best fitting Lorentzian and Gaussian are plotted on top of the experimental data in red and blue respectively, with the results indicating a Lorenztian fit best. Assuming that both beams have equal Lorentzian profile linewidths, then the total measured linewidth is the sum of both individuals, resulting in an individual laser linewidth of 450 kHz. The linewidth of the Zeeman-lock is then determined by beating it with one of the current-modulation-locked lasers, in the same manner. From Fig 6.7 the resulting beat note can be seen to have a slightly larger linewidth of 1.3 MHz, implying that the Zeeman-lock laser has a linewidth of 850 kHz. For the experiments reported here, this is a negligible difference with the Zeeman modulation being a viable replacement to current and piezo modulation, generating equal sized derivative signals whilst keeping a <1 MHz linewidth for locking onto the Rb D_2 line.
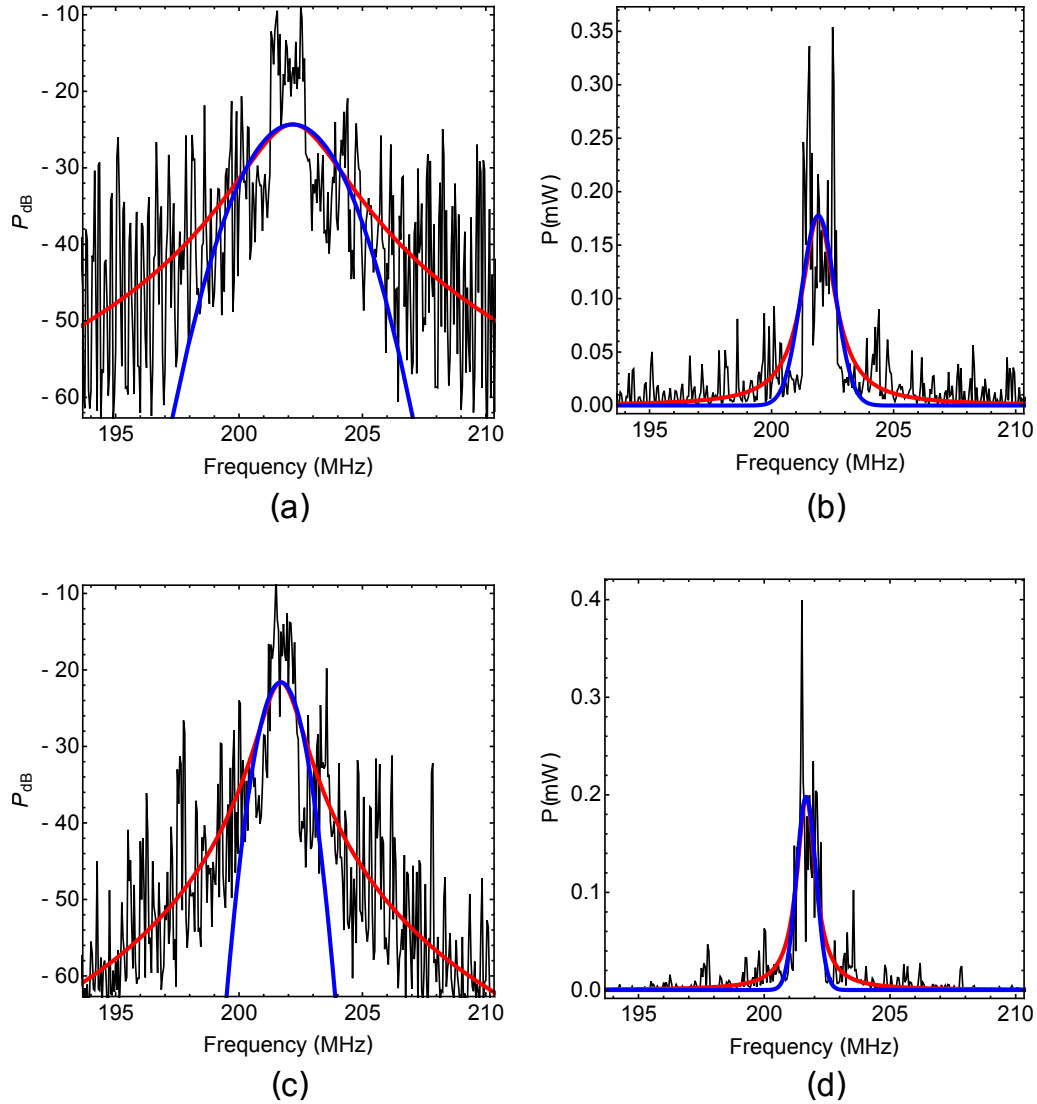
Figure 6.7: Beatnotes of trap and re-pump laser at equal intensity using different modulation methods with Lorentzian fits, red, and Guassian fits, blue. (a) (b): Zeeman modulation of the re-pump and current modulation of the trap, power represented in dB and mW scale respectively. (c) (d): Current modulation only, power represented in dB and mW scale respectively.

6.4 Vacuum system

For efficient laser cooling, the atoms must be free from thermal collisions that increase the average energy of the ensemble, as discussed in the description of the MOT lifetime, Eqn. (3.14). To reduce such collisions, the Rb is dispensed into an ultra-high vacuum, UHV, chamber with a pressure on the order

of 10^{-9} mbar. The key steps taken prior to construction to achieve such pressures in a hand-built vacuum system can be summarised as:

- Cleaning the components

- Building and baking

- Helium leak-check

- Degassing the dispensers

- Initialising the ion-pump

- Closing-off the pumping system and temperature drop-down

The process of cleaning the vacuum components is critical to avoid contamination of the chamber during construction. All components that were going to be used were therefore submerged in ethanol and bathed in an ultra-sonic bath overnight. The clean parts were then rinsed in methanol and soaked in distilled water, before finally being stored in aluminium foil until required for construction.

Building and baking

During the progression of this thesis, two vacuum chambers were built and baked, with the outlook towards a more compact system. The initial system was composed of a Varian Starcell 20 L/s ion pump with a Midivac controller, connected to the chamber body with the dispensing getters and two vacuum glass cells for large optical access to the diffractive optics. After assembly of the vacuum, a turbo pump, backed by a mechanical rotary pump, is introduced to evacuate the unwanted compounds. The connection point for this pump is constructed with an all-metal closing valve, to shut off the effects of the pump once the desired pressures are achieved. All connections are sealed using Conflat (TM) knife-edges and annealed copper gaskets.
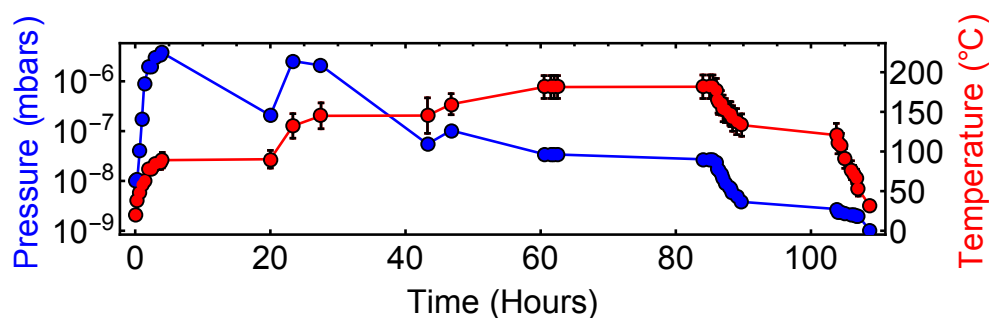
Figure 6.8: Pressure and temperature vs. time during the baking procedure. Data points are connected by solid lines to allow ease of following the rise and fall.

Before continuing, a residual gas analyser, RGA, was used to monitor the compounds present inside the chamber whilst connected to the turbo pump. Whilst monitoring the RGA, helium was sprayed around the joints and critical sections of the chamber for the purpose of detecting any poor connections that allow helium permeation into the system, which would show up as a helium spike on the RGA in real time.

The vacuum system's pressure was initially brought down overnight with the turbo pump before the baking process began. The baking procedure is mapped out in Fig. 6.8. The chamber was first wrapped in heater tape, covered in clean aluminium foil to homogeneously spread the heat across the surface of the vacuum system. Whilst still connected to the turbo pump, the temperature of the system was slowly increased to dispense any unwanted materials in the chamber down into the pump. This initially caused a spike in the pressure measured at the pump. Over the course of two days, this temperature is brought up to 200 °C and held there for a further two days. During this time, the dispensing getters were degassed into the pump at 3 A for a day, after which the ion pump was turned on. The valve was then closed, and temperature slowly brought back down, dropping the pressure down to a final value of 10^{-9} mbar. The pressure is limited by the background gasses
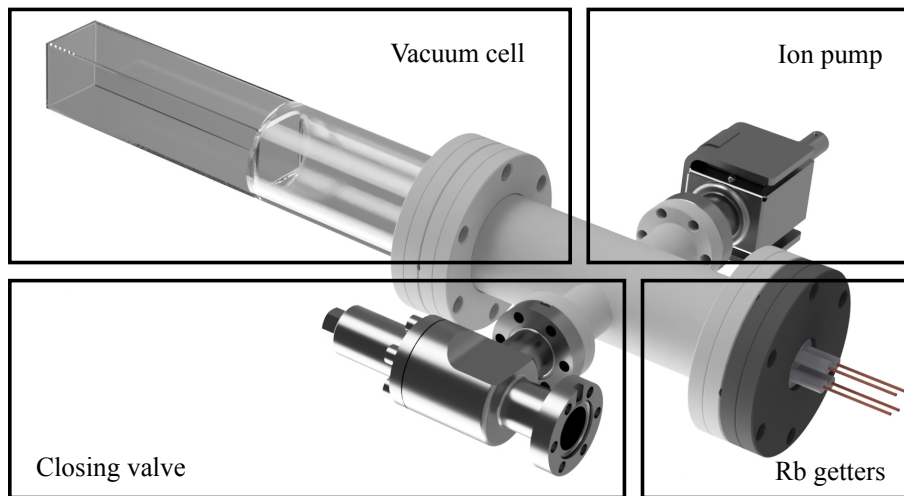
Figure 6.9: Illustration of compact vacuum system, with the key components highlighted.

in this single chamber set-up.

The same baking procedure was applied to the second system; composed of a MDC Vacuums 4-way cross (CF 40), connected to a flange with two dispensing SAES getters, a Gamma Vacuums 3S-DI ion pump and a Precision Glassblowing anti-reflection-coated cell, as illustrated in Fig. 6.9. This system was used for the majority of the experimental discussions of this thesis due to the reduction in stray magnetic fields and reduced scale.

Ion-pump gradient fields

Through the duration of my studies, it was noted that the original vacuum system was limiting the experimental capabilities due to the magnetic gradients produced from the 40 L/s ion-pump. The extent of the variations of magnetic fields is mapped out in Fig. 6.10 (a) for the older system. This figure was compiled from the total magnetic field readings taken with a commercial Stefan-Mayer flux gate at numerous points around the vacuum system. In this map, the atomic sample would be located at (0.2 m, 0.2 m), represented with a black rectangle.
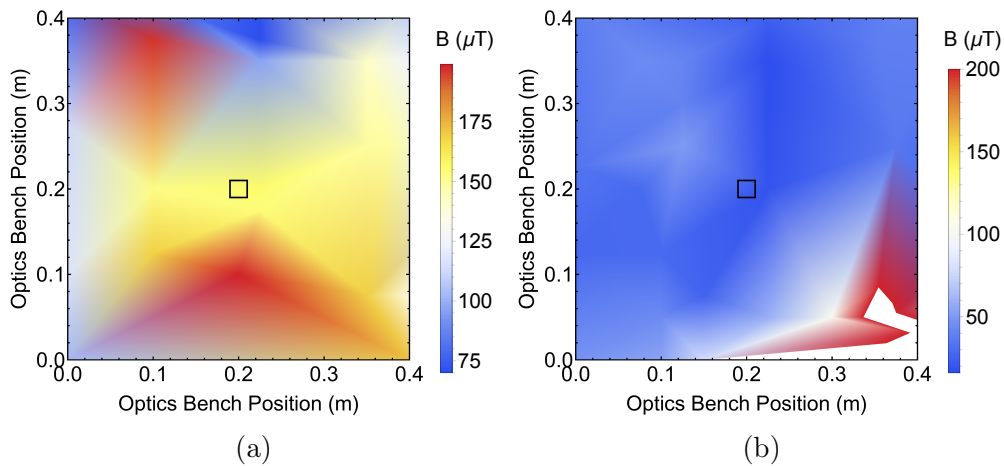
Figure 6.10: Magnetic field environment mapped out by fluxgate, where the atomic sample would be located at (0.2 m, 0.2 m), represented with a black rectangle. (a): Magnetic field in vicinity of first vacuum system with 20 L/s ion pump. (b): Magnetic field in the vicinity of second vacuum system with 2 L/s ion pump.

Although the MOT phase uses trapping coils with a magnetic gradient much larger than the environment, the achievement of sub-Doppler temperatures in optical molasses will be hindered, as is tested in Sect. 9.1. To avoid gradients limiting the future experiments cooling capabilities, the smaller system already discussed uses a much smaller ion pump, 2L/s, which additionally has some Mu-metal shielding. Not only was the second systems volume reduced, but the gradient mapping of Fig. 6.10 (b) reveals a greatly reduced magnetic environment in the region of the Rb vapour. The saturated region on this plot was from the new ion pump being located at a lower height than the previous system, such that the region directly around this was saturated with the magnetic field, however this did not propagate to the region of interest.

Chapter 7

Experiment: Grating chips as a source of cold atoms

7.1 Optical set-up and experimental controls

The essential criteria of a MOT are multiple, polarised, laser beams constraining an atom in three dimensions, with the region aligned with a magnetic minimum. To meet the laser requirements, the optical set up in Fig. 7.1 was constructed. The simple layout illustrated consists of trap and re-pump lasers with orthogonal polarisations, such that they could be combined on a PBS and fibre coupled to the grating chip. However, as time advanced the setup was developed further to meet the experimental needs. For the typical ^{87}Rb MOT, the trap was locked to the $F = 2 \rightarrow F' = 2, 3$ crossover by means of saturated absorption spectroscopy. Two Linos 30 dB optical isolators were placed afterwards to reduce any reflections or emission feeding back into the ECDL to generate interfering etalon effects [118]. The trapping beam was fibre coupled into a ThorLabs TPA780P20 tapered amplifier, capable of producing an output up to 2 W, described further in Sec. 7.1.1.
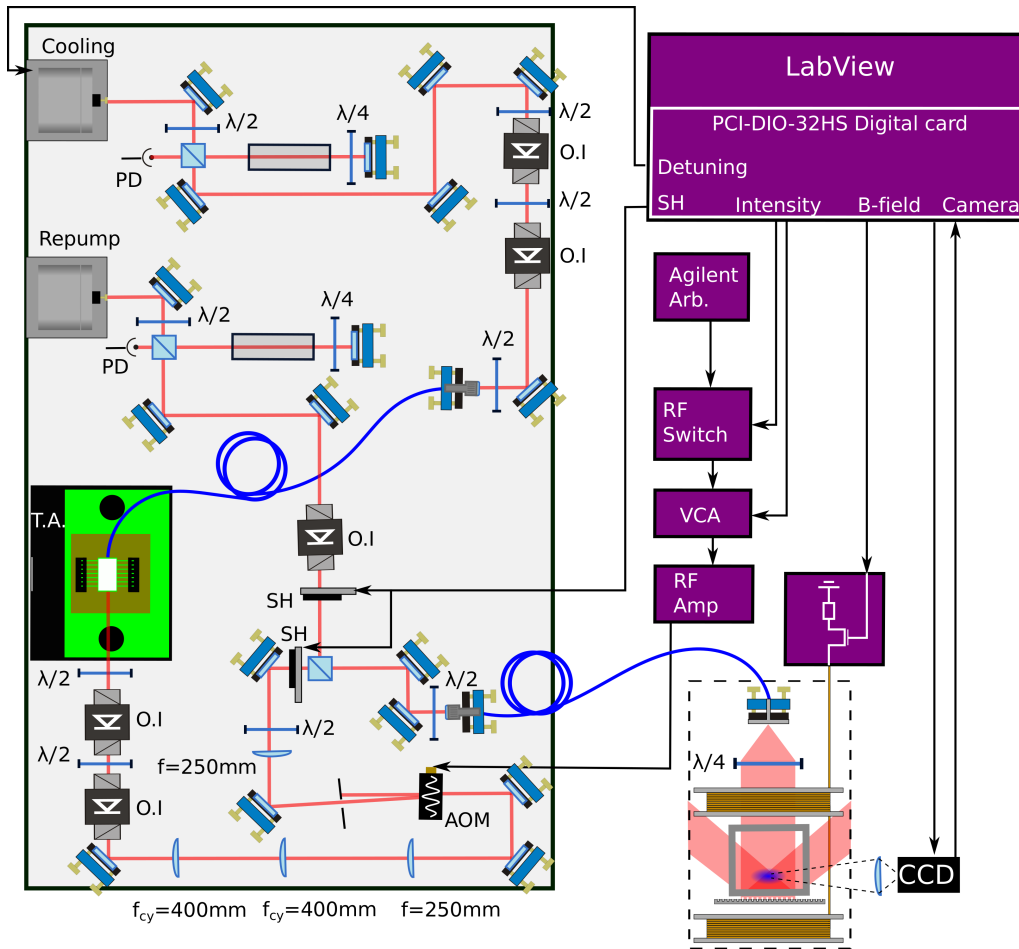
Figure 7.1: Cooling optics bench layout as well as the schematic of the digital control. PD: Photo-diode. AOM: Acousto-optic modulator. SH: Shutter. T.A.: Tapered amplifier. O.I: Optical isolator. f_{cy}: Cylindrical lens

The output beam astigmatism is corrected with two cylindrical lenses, discussed in Sect. [7.1.1]. Once corrected, the amplifier output was focussed through an Isle-Optic (LM130) acousto-optic modulator, AOM, via 250 mm focal lenses. In our case, the experimental controls were all digitally sourced from a LabVIEW-run National Instruments digital card (PCI-DIO-32HS), the output of which was split into an array of 0-5 V digital channels. An arbitrary function generator (Agilent) was used to drive the AOM, with the power controlled by an RF-switch (Minicircuits ZASWA-2-50DR+), and voltage-controlled attenuator (Minicircuits ZAD-1-1+), before being amplified with an AA Opto-Electronic (AMP.A-B-34-20.425) amplifier to provide the AOM

with 35 dBm of RF power at the frequency required.

The re-pump ECDL is locked directly to the $F = 1 \rightarrow F' = 2$ transition by saturated absorption spectroscopy. Due to the relatively small percentage of re-pump required for laser cooling, and typical output power of > 40 mW, no optical amplification was required. A Linos optical isolator was also used for the re-pump to avoid back reflections from optical elements and the fibre.

Homebuilt mechanical shutters were implemented for both cooling and re-pump independently, with shutting times on the scale of 0.5 ms. This was found to be critical to reduce light leakage from the AOM when creating the superposition states discussed later. Both beams were then combined on a PBS with orthogonal polarisations, and coupled into a polarisation maintaining fibre (Thorlabs P3-630PM-FC). The MOT coils were designed such that 4 A will produce a gradient field of 15 G/cm for trapping. These are controlled by a homebuilt MOSFET circuit to produce a range of DC current values.

7.1.1 Tapered amplifier

The optical set-up was built around the implementation of a Thorlabs TPA780P20 butterfly packaged, tapered amplifier. This was mounted into the Thorlabs LDC2500B current and temperature controller, providing computer control of the current supply between 0 and 2.5 A, whilst maintaining the butterfly package at room temperature via a heat-sink and assisting fan. When coupled with an input seed of 20 mW, the TA could produce an output power up to $\simeq 2$ W.

As has been observed with other tapered amplifiers, the output beam is astigmatic and dominated by spontaneous emission at low current [119].
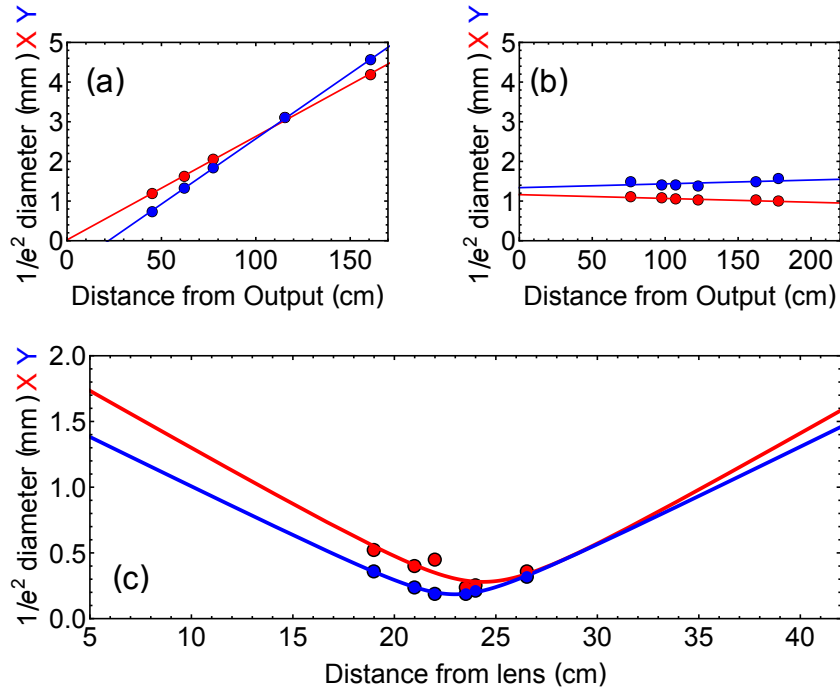
Figure 7.2: Beam waist measurements along the propagation of the tapered-amplifier output. (a): Before any corrections a strong astigmatism dominates the expansion profile. (b): After collimation with cylindrical lenses. (c): The focii along both axis were observed to overlap sufficiently after astigmatic corrections.

Spontaneous emission was also observed exiting the input fibre, hence the need for 60 dB isolation between the trap laser and the TA. A further 60 dB of optical isolation was added after the TA.

The astigmatic output beam was profiled over 2 m of propagation to map the expansion of the orthogonal components of the beam waist, as seen in Fig. 7.2 (a). This propagation was corrected with the implementation of cylindrical lenses, to address each axis individually. The positions and focal lengths of these cylindrical lenses were determined from Gaussian optics and placed as seen in Fig. 7.1, producing the expansion depicted in Fig. 7.2 (b). To test if the beam was sufficiently collimated, the focus of both axes from a spherical lens, with f=25 cm, was profiled to ensure both axes converge at the same point, as illustrated in Fig. 7.2 (c). The solid lines indicate the best fitting

beam waist calculations from Gaussian beam optics, $w^2(x) = w_0^2(1 + (\frac{\lambda x}{\pi w_0^2})^2)$, where w_0 is the initial beam waist and λ is the wavelength. This is a good indication that the beam was well collimated before focussing, enabling up to 70 % fibre coupling efficiency.

7.1.2 Imaging

Two CCD JAI-M50 cameras were used in the experiment; one for fluorescence imaging and the other for real-time monitoring of the MOT. Both cameras were mounted horizontally on the optical table to ensure a good optical access to the atomic sample. The real-time camera was connected to a monitor, while the main experimental camera was set in interlaced mode and externally triggered to allow for acquisition of timed data. The exposure time could be varied between 0.1 ms - 17 ms, although a timing of 1 ms was typically used.

To measure the number of atoms in the grating magneto-optical trap, GMOT, we employ the method of fluorescence imaging, to capture the scattered photons from the sample when applying a resonant light field for a short period of time, < 1 ms. A fraction of the fluorescence produced is within the solid angle of the magnification lens, which focuses the scattered light onto the CCD camera. We make the reasonable assumption that the MOT scatters equal amounts of light in all directions, discussed further in Sect. [8.2], such that the number of photons measured in the solid angle can be directly related back to the total fluorescence. Knowledge of the camera properties, such as pixel size (6 μm $\times$12 μm) and magnification (M=0.80), allow the cloud image to be related to the actual sample size.

For most experimental circumstances, the atomic distribution measured will

fit a Gaussian distribution:

$$n(x, y, z) = n_0 \exp\left(-\frac{x^2}{2\sigma_x^2} - \frac{y^2}{2\sigma_y^2} - \frac{z^2}{2\sigma_z^2}\right), \tag{7.1}$$

where $\sigma_{x,y,z}$ are the cloud widths in (x, y, z) respectively and

$$n_0 = \frac{N}{(2\pi)^{3/2}\sigma_x\sigma_y\sigma_z}. \tag{7.2}$$

For calculation of the atom number from the collected light we must consider the scattering rate per atom, $R(I, \Delta)$, and multiply by the relative solid angle of the collecting lens Ω_d, and the energy per photon hc/λ such that the MOT atom number is [71],

$$N = \frac{4\pi}{\Omega_d}\frac{2\lambda}{hc\Gamma}\frac{1}{R(I, \Delta)}\frac{I}{\eta} \tag{7.3}$$

where I is the current measured by the detector, and η is the detection efficiency of the system.

7.2 Grating magneto-optical trap

The light from the optics bench was fibered over to the vacuum system and mounted for vertical alignment onto the horizontally mounted grating, as depicted in Fig. 4.3. The output light is freely expanding until reaching a $1/e^2$ beam diameter of 2 cm where it is collimated and circularly polarised. The grating chip is mounted beneath the vacuum system, close to the glass surface to ensure as much of the overlap volume is within the chamber as possible. The crucial steps taken for aligning the grating are listed as:

- Retro-reflection of the incident beam to guarantee the grating is perpendicular with respect to incident light

- Ensure the incident light is aligned very well to the chip centre for the linear gratings
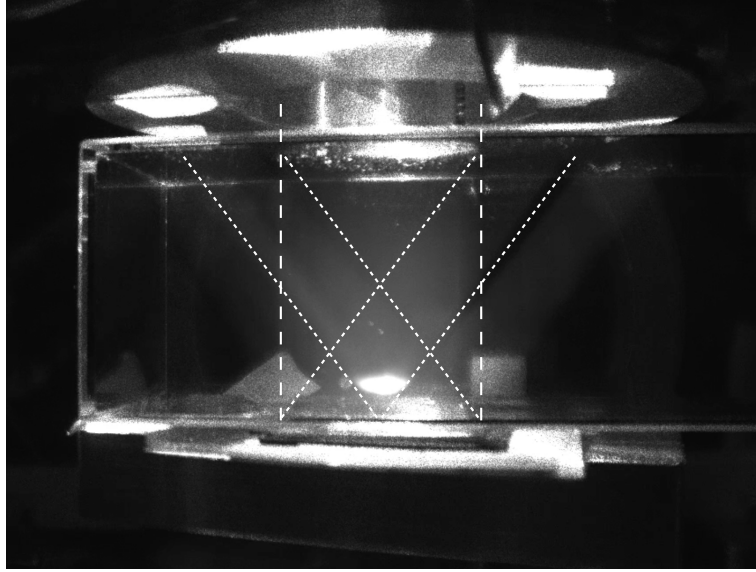
Figure 7.3: Photograph of the grating MOT from a Tri one-dimensional grating chip. The dashed lines indicate the incident and diffracted beams from a 1180 nm period grating placed outside of vacuum system.

- The quadrupole minimum should be positioned within the grating overlap volume

The retro-reflection was carried out by using a small bare, un-etched section of the chip, which could act as a reflector. By using an aperture to minimise the incident beam waist, the retro-reflected beam could be aligned to better than mrad precision. Typically, the second requirement, alignment with the centre of the grating, would also be met with a smaller beam if using a one-dimensional Tri-grating geometry, such that all diffracted orders are only visible when aligned to the grating centre point. Ensuring the quadrupole magnetic minimum is within the beam overlap volume with careful alignment of the coil position, and has the correct handedness with respect to the incident polarisation, satisfies the final criterion for laser cooling.

The initial atom number measurements examined the response due to the power in the incident beam. During these measurements the re-pump was locked to resonance and the trap detuned $\approx \Gamma$ with a 15 G/cm quadrupole
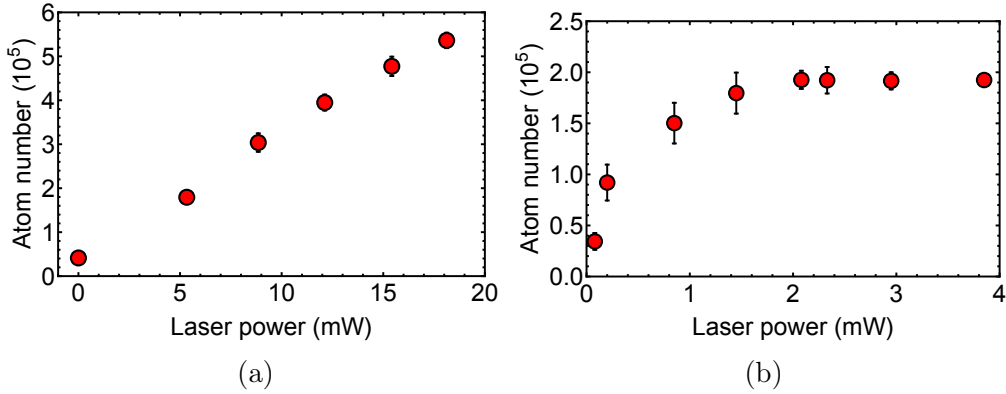
Figure 7.4: The captured atom number as a function of the incident laser power. (a): Atom number as a function of the trap laser power for a re-pump power of 3 mW. (b): Atom number as a function of the re-pump power for a trap power of $\approx$7 mW.

field parallel with the incident light. The results of this initial study are seen in Fig. 7.4 (a) and (b) for the trap and re-pump respectively.

Fig. 7.4 (a) demonstrates that for low powers, the atom number has a linear response to trapping power. As expected, this is not the case for the re-pumping light, due to needing relatively few scattering events to return from the dark $F = 1$ state to the cooling cycle. The initial atom number measurements were used to optimise and characterise the grating MOT set-up and experimental components, as is discussed throughout this thesis.

7.3 Atom number in small grating magneto-optical traps

The compact nature of the grating magneto-optical trap is an ideal platform for future miniature atomic metrological devices. The performance of these instruments, such as atomic clocks and gravimeters, is limited by a $\sqrt{N}$ dependence in the Allan variance and quantum projection noise [120, 121]. Due to this limitation, the atom number achievable in the GMOT for smaller

beam diameters becomes crucial for future implementation in compact devices.

The standard MOT is typically composed of three sets of retro-reflected beams, of which the overlap volume determines the number of atoms that can be cooled within this region. The atom number, N, scaling with the beam diameter, d, has been shown in Ref. [122] as,

$$N = \frac{4\pi r^2}{8\sigma} \left(\frac{v_c}{v_T}\right)^4 \tag{7.4}$$

where σ is the collisional cross section, v_c is the capture velocity, v_T is the velocity of the thermal background, and $r = d/2$ is the radius of the overlap volume.

The capture velocity is defined as the maximum velocity an atom can posses and still have its velocity brought to zero after travelling through a cooling overlap volume of diameter, d. With the surface area of the overlap volume scaling as d^2, the authors noted the six-beam atom number scaling of $d^{3.6}$ for d larger than 2.3 mm, compared to a d^6 scale for smaller MOTs. A similar study was carried out in Ref. [123] on a micro-fabricated pyramid MOT where the critical d occurs at a larger 6 mm.

To determine the optimum atom number achievable in small beam experiments with the GMOT, the incident beam diameter was varied whilst the atom number was measured via fluorescence imaging. For these measurements a one-dimensional grating of period 1189 nm (discussed in Ref. [124]) was implemented. An aperture was used in the incident beam to adjust the incident beam diameter, with the diameter of the aperture measured with digital callipers. Unlike similar literature, for each beam size the optimum atom number was found by adjustments to the coil trap zero position, the
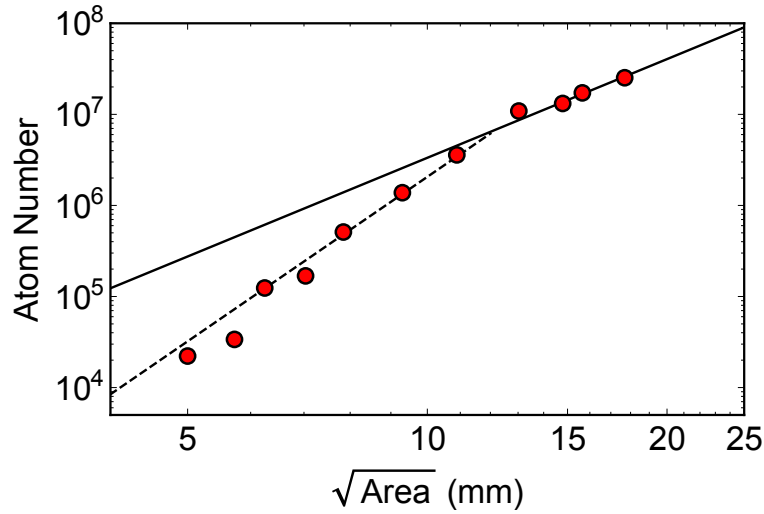
Figure 7.5: Atom number in the GMOT as a function of beam diameter. Dashed/solid black lines indicates the $d^6/d^{3.6}$ scaling respectively.

cooling intensity and the detuning frequency to find the best achievable atom number for a given capture volume. The atom numbers measured experimentally are plotted in Fig. 7.5, where the dashed and solid black lines indicates the d^6 and $d^{3.6}$ scaling respectively.

This initial study reveals a critical diameter of $d \approx 11$ mm, as opposed to the $d \approx 3$ mm measured for the six-beam MOT and $d \approx 6$ mm in the pyramid MOT. A d^6 gradient extending to 11 mm indicates an decreased cooling capability for small beam measurements in the GMOT, compared to the standard six-beam MOT, suggesting a lower capture velocity in the Tri overlap volume, compared to a similar beam size with a six-beam apparatus. This initial investigation could be extended to other periodicities for 1-D and 2-D grating chips to find the optimum performance in small beam set-ups. Additionally, an investigation of the optimal profile of the incident beam, e.g. Gaussian or top-hat, would be of clear interest.

7.4 Atom number dependence on polarisation

The study of the impact of polarisation purity on the confinement of atoms in the grating MOT increases in complexity from the standard six-beam MOT due to the diffracted beams making an angle, θ, with the magnetic field axis that breaks the symmetry of the system. The consideration of the diffracted beams with propagation vectors $\vec{k}_j$ must account for the angular deviation between the electric field polarisation vector, $\vec{\epsilon}$, and the confining B field, such that $\cos\theta = \frac{\vec{k}_j \cdot \vec{B}}{|\vec{k}_j| \cdot |\vec{B}|}$. Previous work derived in Refs. [94, 114] expands upon Eqn. 3.6 to show that the force of an individual laser upon an atom can be expressed as

$$\vec{F}_j \approx \hbar \vec{k}_j \frac{\Gamma}{2} \frac{I_j}{I_{sat}} \left(K + C(\vec{k}_j \vec{v} - \mu_F |\vec{B}| s \cos\theta) \right), \tag{7.5}$$

where $\vec{k}_j$ is the respective propagation vector, s is the polarisation handedness (-1,1), $K = (1 + \frac{\sum_j I_j}{I_{sat}} + 4\frac{\Delta^2}{\Gamma^2})^{-1}$ and $C = \frac{8\Delta K^2}{\Gamma^2}$.

In the case of the 6-beam MOT, the cooling beams are aligned along the key axes of the gradient field, where $|\vec{k}_j \cdot \vec{B}| = 1$ such that trapping is optimised for purely circularly polarised light. However, if we implement this with the 1-D grating discussed in Ref. [124], the diffracted orders now make an angle with respect to the gradient magnetic field axes, corrupting the polarisation purity. In this scenario, Eqn. 7.5 can be applied with the relevant vectors of the grating chips incident electric field, $\vec{k}_1 = \vec{k}(0, 1, 0)$, and diffracted orders, $\vec{k}_{d=1,2,3} = \vec{k}(\cos(d\frac{2\pi}{3})\sin\theta, \sin(d\frac{2\pi}{3})\sin\theta, \cos\theta)$.

The polarisation contribution from the tetrahedral configuration led to the full force calculation provided in Ref. [114], where the author realised that the poor quantisation of the diffracted polarisation leads to a critical π contribution of the trapping force. To experimentally probe the trapping force
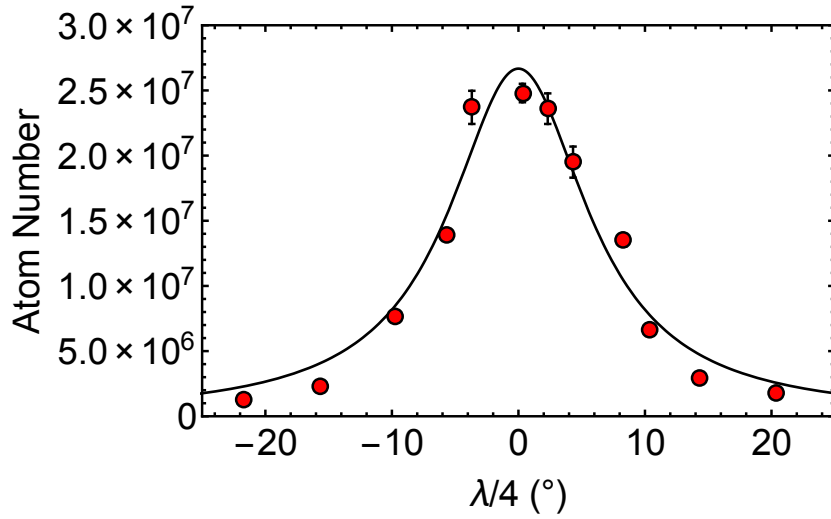
Figure 7.6: Atom number in the GMOT as a function of rotation in the circular polarisation. Solid black line illustrates the best fitting Lorentzian.

dependence on the incident polarisation, the atom number was measured for rotations of the quarter wave-plate. Since all cooling light is derived from a single beam, the rotation of the input wave-plate degrades all electric field polarisations. The measured sensitivity to polarisation, seen in Fig. 7.6, reflects a full-width-half-maximum, FWHM, trap range of $\pm 10°$ from a Lorentzian fit, depicted with a solid black line. Unlike the standard 6-beam MOT, where the polarisation of a single trapping beam can be disregarded and the trap maintains confinement, the GMOT demonstrates a narrow range of incident circular polarisations to achieve effecting trapping. Similarly to the 6-beam MOT, the atom number is maximised for a purely circular incident polarisation.

7.5   Temperature

The selected temperature measurement procedure used time-of-flight, TOF, measurements to track the clouds ballistic expansion whilst isolated from external perturbations. TOF measurements were first systematically investigated by Lett *et al.* [72], where atom number was measured with a probe

as a function of time to determine the average expansion rate of the cloud. Similarly, images can be taken with fluorescence imaging at different drop times to determine the width of the cloud, where the width evolution follows the Stefan-Boltzmann distribution:

$$\sigma_i^2(t) = \sigma_{i0}^2 + \frac{k_B T_i}{m} t^2, \tag{7.6}$$

where σ_i is the width of the cloud for a given drop time, t, σ_{io} is the initial cloud width before releasing for expansion, k_B is the Boltzmann constant, T_i the temperature and m the atomic mass.

This method is applied to experimental data by plotting the square of the cloud width against the square of the drop time. The resulting line follows the distribution in Eqn. (7.6), where the slope of the line is $k_B T/m$ and σ_{io} denotes the intercept of the y axis.

The final 'temperature' in a given direction is given by the balance between the heating and the velocity damping constant γ. In our system the effective temperature parallel to and perpendicular to the grating are therefore

(a)   (b)
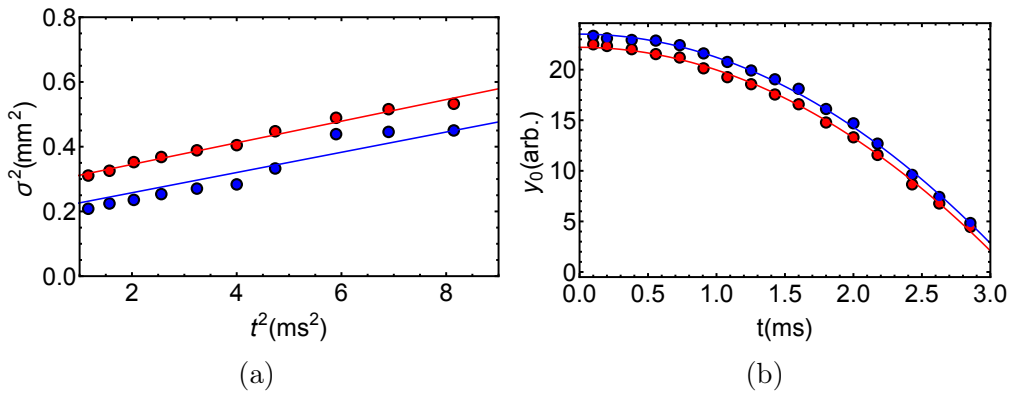
Figure 7.7: Time of flight fits in the MOT for the y, red, and x, blue, axes distributions. The fits for each axis are unconstrained and independent from each other. a) The expansion of the cloud width squared, σ^2, against the time squared, t^2. b) The y_0 position of the cloud as it drops during time of flight allows calculation of the camera magnification.

not expected to be the same. However, this is typically only prominent for lower temperature measurements. The linear fits reveal a MOT temperature of $T_{(r,z)} = (349 \pm 8, 327 \pm 15)$ μK. The motion of the centre of mass in the y axis is tracked in Fig. 7.7 (b), using independent one-dimensional fits to find the centre of mass of the cloud, depicting the expected projectile motion $s = ut + \frac{1}{2}at^2$. In the case of the MOT, the initial velocity $u = 0$ and $a = g = 9.8$ m/s, such that the camera magnification can be determined from $s = \frac{1}{2}Mgt^2$ to be M=0.8.

7.5.1 Optical Molasses

Molasses is experimentally realised simply by reducing the trap intensity whilst increasing the red-detuning, as $T \propto I/\Delta$ [which was shown in Eqn. (3.21)]. To increase the detuning of the light field in real time, a DC voltage between 0-5 V is sent to the laser locking electronic circuits. This voltage overrides the locking mechanism, to unlock the laser and introduce a voltage jump on the spectroscopy signal, pulling the output frequency detuning. To calibrate this voltage step to a known frequency, the MOT atom number was measured for a varied step voltage, with an outlook to map-
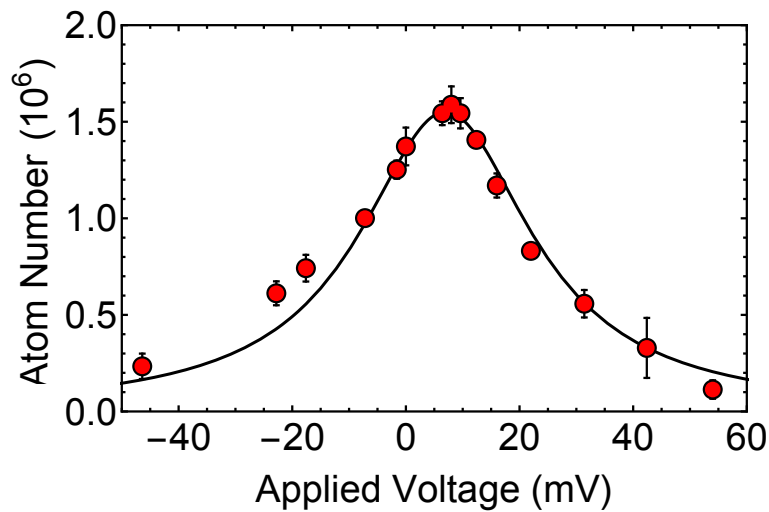
Figure 7.8: Calibration of the detuning from mV to MHz for a known initial detuning. Black line is the best fitting Lorentzian.

ping a distinct AOM detuning. The data from this calibration is provided in Fig. 7.8 with the data points in red and a best fitting Lorentzian in black. This data provided a calibrated link between the frequency of the laser and the applied voltage jump.

Initially, to reach optical molasses the atoms were loaded in the MOT phase for 2 seconds. The molasses phase of the experiment was composed of a two-stage detuning. During stage one, the molasses frequency was jumped to a detuning of $\Delta = 30$ MHz and held constant for for 6 ms. The second stage of molasses varied the frequency detuning, with the results depicted in Fig. 7.9. The results of Fig. 7.9 (a) illustrate the second stage detuning when the frequency was held constant at 60 MHz for a time between 1 and 6 ms. A clear correlation arises for lower temperatures at longer molasses durations before a plateaux is reached. For (b) the second stage detuning was held for 5 ms with a detuning of between 30 and 70 MHz. As expected from the relation in Eqn. (3.21), the final atomic temperature is inversely proportional to the magnitude of the detuning, δ, with the best performance
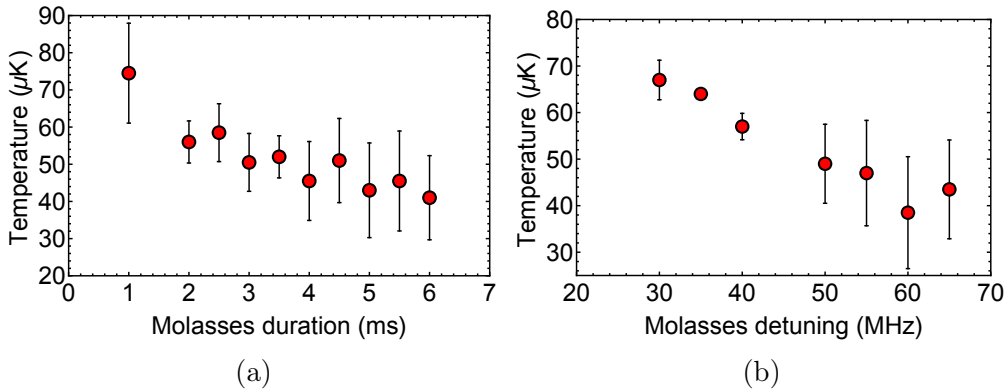
Figure 7.9: Variance of average molasses temperature as a function of critical parameters. Both data sets were taken following a first stage molasses cooling for 3 ms at $\Delta = 30$ MHz. (a) Average temperature measured for a variable second stage molasses time at $\Delta = 60$ MHz. (b): Average temperature measured as a function of the second phase molasses detuning, applied for 5 ms. Error bars were calculated from the deviation of axial and radial temperatures.

reached at approx 60 MHz. These initial experiments resulted in the average ensemble temperature of $\approx 30\mu\mathrm{K}$.

Chapter 8

Publication: Phase-space properties of magneto-optical traps utilising micro-fabricated gratings

J. P. McGilligan, P. F. Griffin, E. Riis, and A. S. Arnold.[1]

We have used diffraction gratings to simplify the fabrication, and dramatically increase the atomic collection efficiency, of magneto-optical traps using micro-fabricated optics. The atom number enhancement was mainly due to the increased beam capture volume, afforded by the large area ($4\,\text{cm}^2$) shallow etch ($\sim 200\,\text{nm}$) binary grating chips.

Here we provide a detailed theoretical and experimental investigation of the on-chip magneto-optical trap temperature and density in four different chip

---

[1]The work presented in this chapter is extracted from and expands upon the published results. The published version is provided in Appendix E

geometries using ^{87}Rb, whilst studying effects due to MOT radiation pressure imbalance. With optimal initial MOTs on two of the chips we obtain both large atom number (2×10^7) *and* sub-Doppler temperatures $(50\,\mu\text{K})$ after optical molasses.

8.1 Introduction

We have recently highlighted the benefits of using surface-patterned chips to make MOTs with relatively large numbers of ultracold atoms [42], compared to prior micro-fabricated magneto-optical traps (MOTs) [93, 123]. The design requires only the alignment of a single input laser beam, and extends our previous work on tetrahedral mirror [94] and grating [95] geometries, which are four-beam [125] equivalents of pyramidal MOTs [126].

Here we study the atom-number characteristics of four different chip systems, and more complete details of different fabrication methods for the chips are discussed by Cotter *et al.* [102]. One chip style comprises three one-dimensional gratings arranged in a pattern with 3-fold rotational symmetry (we used chips with periods of $d = 1470\,\text{nm}$ and $d = 1200\,\text{nm}$), in the Tri geometry. The other chip style is a two-dimensional grating generated with circular regions centred in square unit cells of side length $d = 1080\,\text{nm}$, in the checkerboard/circle geometry. Both geometries and optical set-up are illustrated in Fig. refmicrogmot. Hereafter the chips will be referred to as TRI$_{15}$, TRI$_{12}$ and CIR. Although we have used chips TRI$_{15}$ and CIR previously (chips B and C in Nshii *et al.* [42]), purely for number characterisation, here we present density and temperature data for these chips. Moreover, we also investigate MOTs with improved capture efficiency for the 1D structure (i.e. the new chip TRI$_{12}$) and improved radiation balance for the 2D structure (chip CIR$_{\text{ND}}$: identical to CIR but with an input beam intensity spatially sculpted with a neutral density filter).

8.2 Doppler temperature in the grating magneto-optical trap

Whilst sub-Doppler cold atom temperatures can be reached in optical molasses [73, 82, 127], the conditions for atom collection in a MOT are in stark contrast to those required to reach the lowest temperatures: a MOT needs high beam intensities relative to the saturation intensity ($I \gg I_S$), detuning of a few natural line-widths $\Delta \approx -2\Gamma$ and a magnetic gradient $\approx 10\,\mathrm{G/cm}$ for a typical alkali metal vapour cell MOT with $25\,\mathrm{mm}$ beam diameter. For this reason the considerably simpler Doppler theory is a good description for our MOT temperature. The standard 3D Doppler result for a sample of atoms uniformly and isotropically illuminated in three dimensions by light of total intensity I_T, with corresponding saturation parameter $\beta_T = I_T/I_S$, and detuning Δ [128] is:

$$T_U = T_D \frac{1 + \beta_T + 4\Delta^2/\Gamma^2}{-4\Delta/\Gamma}, \qquad (8.1)$$

as derived in Sect. [8.2], where $T_D = \frac{\hbar\Gamma}{2k_B}$.

In our ^{87}Rb experiment we cool using the rubidium D_2 transition which has a natural line-width $\Gamma = 2\pi \times 6.07$ MHz. The standard Doppler temperature minimum in the limit of low intensity and detuning $\Delta = -\Gamma/2$ is T_D, i.e. 146 μK for rubidium, with the more general lowest temperature $T_D\sqrt{1 + \beta_T}$ minimised at a detuning $\Delta = -\sqrt{1 + \beta_T}\,\Gamma/2$. Throughout this paper, for consistency, we use the saturation intensity averaged over all polarisations and magnetic sub-levels $I_S = 3.57$ mW/cm^2. However, we note that using the stretched state saturation intensity $I_S = 1.67$ mW/cm^2 for the theoretical temperature of Eq. (8.1) leads to much better agreement with our experimentally measured temperatures (Sec. 8.5).

For our gratings if the incident beam has a spatially uniform intensity I_0 and wavevector $\mathbf{k}_0 = k\{0, 0, -1\}$, for balanced optical pressure from N diffracted orders each should ideally carry an intensity of $I_i = I_0/(N \cos \alpha)$ with $i \in \{1, ..., N\}$. The wavevectors of the diffracted beams are $\mathbf{k}_i = k\{\sin \alpha \sin \frac{2\pi i}{N}, \sin \alpha \cos \frac{2\pi i}{N}, \cos \alpha\}$, where α is the angle the diffracted orders make to the grating normal $\{0, 0, 1\}$ ($\alpha = 2\theta$, Ref. [94, 95]). The total intensity is therefore $I_T = \sum_{i=0}^{N} I_i = (1 + \sec \alpha) I_0$, with each beam of intensity I_i contributing a relative intensity-dependent heating proportional to its intensity along the beam direction due to absorption, and an equal associated heating rate due to spontaneous emission. The heating from spontaneous emission is assumed for simplicity to be isotropic, with the heating rate for light with a wavevector $\mathbf{k}_i = \{k_{i_x}, k_{i_y}, k_{i_z}\}$ proportional to $\hbar^2 R_i k^2 \{\frac{1}{3}, \frac{1}{3}, \frac{1}{3}\}$ in the x, y and z dimensions, for a scattering rate

$$R_i(\mathbf{v}) = \frac{\Gamma}{2} \frac{I_i/I_S}{1 + \beta_T + 4(\Delta - \mathbf{k}_i \cdot \mathbf{v})^2/\Gamma^2}, \text{ with } R_i(\mathbf{0}) = \frac{I_i}{I_S} R = \beta_i R. \quad (8.2)$$

Assuming circularly-dipolar (as opposed to isotropic) spontaneous emission from a circularly polarised atom adds complexity and does not significantly alter the predicted temperatures. The heating due to absorption is apportioned $\hbar^2 R_i \{k_{i_x}{}^2, k_{i_y}{}^2, k_{i_z}{}^2\}$ in the three spatial dimensions. The total heating rate near zero velocity in each dimension is thus:

$$\mathbf{D} = \sum_{i=0}^{N} \hbar^2 \beta_i R \left\{ k_{i_x}{}^2 + \frac{k^2}{3}, k_{i_y}{}^2 + \frac{k^2}{3}, k_{i_z}{}^2 + \frac{k^2}{3} \right\} \quad (8.3)$$

which simplifies to

$$\mathbf{D} = \hbar^2 k^2 \frac{I_0}{6 I_S} R \left(\{2, 2, 8\} + \sec \alpha \left\{ 3 \sin^2 \alpha + 2, 3 \sin^2 \alpha + 2, 6 \cos^2 \alpha + 2 \right\} \right) \quad (8.4)$$

In balanced laser cooling the relative damping constants can be determined by the Taylor expansion of the total force equation $\mathbf{F} = \sum_{i=0}^{N} \hbar \mathbf{k}_i R_i(\mathbf{v})$ about

$\mathbf{v} = \mathbf{0}$. The damping constants in the xy directions ($\gamma_\parallel$ parallel to the grating) and z direction ($\gamma_\perp$ perpendicular to the grating) are thus given by [94]:

$$
\begin{aligned}
\mathbf{F}(\mathbf{v}) &\approx -\gamma \cdot \mathbf{v} = -\{\gamma_\parallel v_x, \gamma_\parallel v_y, \gamma_\perp v_z\} \\
\{\gamma_\parallel, \gamma_\perp\} &= \gamma_6 \left\{ \frac{\sin\alpha\tan\alpha}{4}, \frac{1+\cos\alpha}{2} \right\}, \quad \text{where } \gamma_6 = \frac{-16\hbar I_0 k^2 R\Delta}{I_S \Gamma^2 (1 + \beta_T + \frac{4\Delta^2}{\Gamma^2})}
\end{aligned} \tag{8.5}
$$

is the damping force in a standard 6-beam MOT. The temperature in each dimension can then be determined as proportional to the ratio of the diffusion $\mathbf{D}$ (Eq. (8.4)) to the damping γ (Eq. (8.5)):

$$
\{T_\parallel, T_\perp\} = \frac{T_U}{6} \left\{ 3 + \csc^2(\alpha/2), 3 + \sec\alpha \right\}, \tag{8.6}
$$

which reduces to the standard isotropic temperature T_U when $\alpha = \arccos(1/3)$. Note this temperature only depends on the grating diffraction angle and not on the number of diffracted orders N.

The temperatures obtained experimentally (Sec. 8.5) do not reflect the theoretical temperature disparity in the directions parallel and perpendicular to the grating. The model above only includes forces due to absorption of light *directly* from the laser beams, however for MOTs with larger atom number and light scattering rate (like in our experiment), there will be a significant contribution to the forces in the MOT due to the $1/r^2$ repulsion from closely packed atoms with inter-particle spacing r due to absorption of spontaneously emitted light from neighbouring atoms [129–131]. These forces effectively mix the energies across dimensions, creating a more uniform temperature distribution. The theoretical temperature we use in both dimensions is therefore $T = \frac{2}{3}T_\parallel + \frac{1}{3}T_\perp$, which agrees surprisingly well with experimental values given the simplicity of the model.

For completeness and to determine theoretical MOT density, one can also

derive the spring constant κ of the trap, expanding the total force $\mathbf{F}$, but this time relative to position. The α dependencies of the damping constants are $\{\kappa_\parallel, \kappa_\perp\} \propto \{\frac{1}{4} \sin\alpha \tan\alpha, 1 - \cos\alpha\}$, the same as derived by Vangeleyn *et al.* in [94]. The damping therefore reduces to an isotropic $\frac{2}{3}$ $\left(\frac{1}{3}\right)$ of the standard 6-beam MOT radial (axial) κ values, if the GMOT has $\alpha = \arccos(1/3)$ and laser beams of the same intensity as the standard MOT. Under these conditions the GMOT should be spatially isotropic – it will have equal rms cloud radii as a standard MOT in both directions parallel to the grating, but twice the standard MOT extent in the direction perpendicular to the grating. An important caution against using this Doppler spring constant to determine density, however, is that the experimental spring constant of a trap is notoriously difficult to determine, and the reradiative forces [129–131] discussed in the previous paragraph make simple models of the effective spring constant considerably more difficult.

8.3 Theory: Doppler atom number

In order to predict the number of atoms in the MOT, we use the standard method of Lindquist *et al.* [79]: treat the MOT as a spherical target region with radius r and cross-section $4\pi r^2$, then find the flux of atoms incident on the target, with speeds less than the capture velocity v_c of the MOT slowing region. In the ideal case of a rubidium-dominated vapour both loading and loss mechanisms are proportional to atomic density, which is therefore irrelevant for calculating atom number. It is necessary to know the collisional cross section of cold atoms as seen by hot atoms, which for rubidium is $\sigma = 2 \times 10^{-17}\,\mathrm{m}^2$ [78] (similar to caesium [79]). We make the assumption of a 1D optical molasses from two counter-propagating laser beams. The total

acceleration is modified by a pre-factor η to allow for geometric effects:

$$a = v\frac{dv}{dx} = \eta\frac{hk\Gamma I}{2mI_S}\left(\frac{1}{1 + \frac{I_T}{I_S} + 4\frac{(\Delta - kv)^2}{\Gamma^2}} - \frac{1}{1 + \frac{I_T}{I_S} + 4\frac{(\Delta + kv)^2}{\Gamma^2}}\right). \quad (8.7)$$

By rearranging one arrives at an equation of the form $f(v)dv = Bdx$, where $f(v)$ is a quartic polynomial in v and B is a constant. This equation can then be integrated to analytically determine $x(v)$. The integration constant is chosen such that $x(0) = 0$. Setting $x(v_c) = 2r$ (atoms are stopped over a distance of twice the MOT radius) and subsequently inverting gives v_c, the capture velocity. The total steady-state number of atoms in the MOT is then [79]:

$$N = \frac{4\pi r^2}{8\sigma}\left(\frac{v_c}{v_T}\right)^4, \quad (8.8)$$

where $v_T = \sqrt{2k_B T/m}$ is a thermal velocity in the (hot) background vapour.

We note that the saturation intensity features in the theoretical temperature and both theoretical and experimental atom number through the capture velocity, and we therefore consistently use the saturation intensity averaged over all polarisations and magnetic sub-levels $I_S = 3.57\,\text{mW/cm}^2$, which is valid for small detunings [71, 132]. There are, however, arguments for using a value closer to the stretched state saturation intensity $I_S = 1.67\,\text{mW/cm}^2$ [133]. We used this value in our previous work on atom number [42] as a precaution to prevent over-counting the atom number, although for high levels of saturation the effect of changing I_S on experimental atom number is negligible.

8.4   Experimental control

Until this point in the thesis, the MOT detuning has been manually controlled with an RF supply. However, for larger data sets with the detuning

as a variable, an automated computer control is favourable. In the case of characterising detuning range of the MOT, an offset was introduced to the electronic servo controlling the frequency lock point, similar to the discussion in Sect. 7.5.1. To generate a variable lock point, the non-inverting amplifier of the integrator circuit introduced in Ref. [71], was converted to an adder. The additional voltage applied through the adder will produce a controllable output to the integrator circuit, which will in turn send an offset to the zero-cross-over of the error signal. This variable voltage controlled lock point can be applied to the linear region of the error signal generated in saturated absorption spectroscopy for a tuneable frequency.

A voltage calibration to frequency was achieved by determining the voltages required to reach the upper and lower peaks of the error signal with a known frequency deviation between the available transitions. This technique provided a lockable frequency range of 14 MHz. The trap light frequency, determined by the AOM, was set at 124.12 MHz, with 7 MHz range of control on either side of the frequency. For a fully automated experimental control of the frequency, a TTi TG5011 arbitrary function generator, run by LabView, was used to send voltage controls to the adder circuit for lock point control. For a quick response of the intensity, a voltage controlled attenuator, VCA, (mini circuits ZAS-3+) was used to run the power input to the AOM. The VCA has a non-linear output, therefore the input voltage must be carefully calibrated if a linear output of the intensity is sought after.

The implementation of the VCA meant that a cold atomic sample could be loaded, held and dropped under ballistic expansion in order to determine a number and temperature for a given detuning and intensity. This intensity control is only possible on the trapping light as the re-pump follows an individual path where combination with the trap light occurs after the AOM.

8.5 Phase-space characterisation

The experimental conditions were very similar to those detailed in the Methods section of Nshii *et al.* [42]. One major difference is that we now have analogue as opposed to binary intensity control, using an acousto-optic modulator (AOM) after our tapered amplifier prior to fiber-coupling. After the MOT reached steady-state atom number, the atoms were ballistically released for 0, 1.5 or 2 ms, and Gaussian fits were used to extrapolate cloud rms radii and thereby MOT temperatures. To build up statistics each drop time was iterated five times. For intensities above and below $10 \, \text{mW/cm}^2$ the fluorescent imaging exposure times were $430 \, \mu\text{s}$ and $150 \, \mu\text{s}$, respectively.

Figures 8.1 (Chips TRI_{15} and TRI_{12}) and 8.2 (Chips CIR and CIR_{ND}) illustrate the intensity- and detuning-dependence of a variety of MOT parameters: theoretical atom number (a), experimental MOT atom number (b) and spatial density (c) as well as the theoretical Doppler temperature (d) with the temperatures experimentally measured in the directions both parallel (e) and perpendicular (f) to the grating. Note that the theoretical atom number saturates at about three times lower intensity than that observed experimentally – we seem to need three times more laser power experimentally than we would theoretically expect. This discrepancy may be considered relatively minor given the very simple nature of the theoretical model, however we believe further investigation, and full comparison to a standard 6-beam MOT may still be warranted.

In prior measurements of $T_\perp$ on Chip CIR (Fig. 8.2(f) CIR) there was an even larger discrepancy with theory (very high experimental temperatures) due to imbalanced optical force during the fluorescence imaging. This was determined via the noticeable centre-of-mass velocity accrued in the direction perpendicular to the grating during time-of-flight. In all the new data

for Figs. 8.1 and 8.2 any imbalanced radiation pressure (mainly for Fig. 8.2) was balanced using a non-zero magnetic field oriented perpendicular to the grating.

Note the significant increase in atom number ($\times 3$) and density ($\times 6$), with lower atomic temperature on chip TRI_{12} compared to chip TRI_{15} – in future we intend to test gratings with even smaller period (larger diffraction angle, and larger overlap volume) to determine if this trend continues.
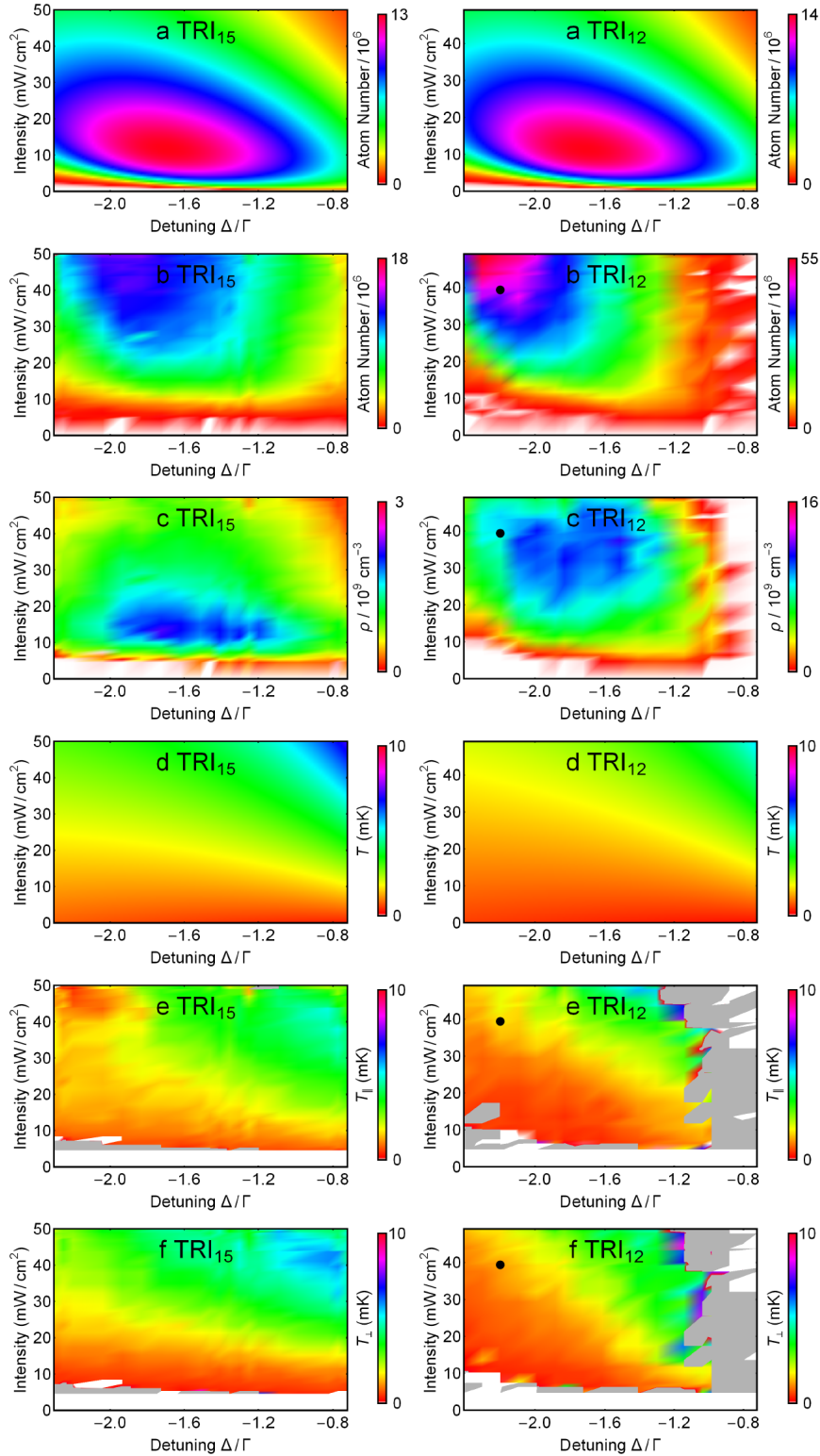
Figure 8.1: The full GMOT characterisation when using chip TRI$_{15}$ and TRI$_{12}$, with beam diffraction angles $\alpha = 32°$ and $41°$. The labels a-f indicate theoretical atom number (a), experimental atom number (b) and spatial density (c), the theoretical temperature (d) and experimental temperatures in directions parallel (e) and perpendicular (f) to the grating. Light grey and white indicates indeterminate and out-of-range data respectively.
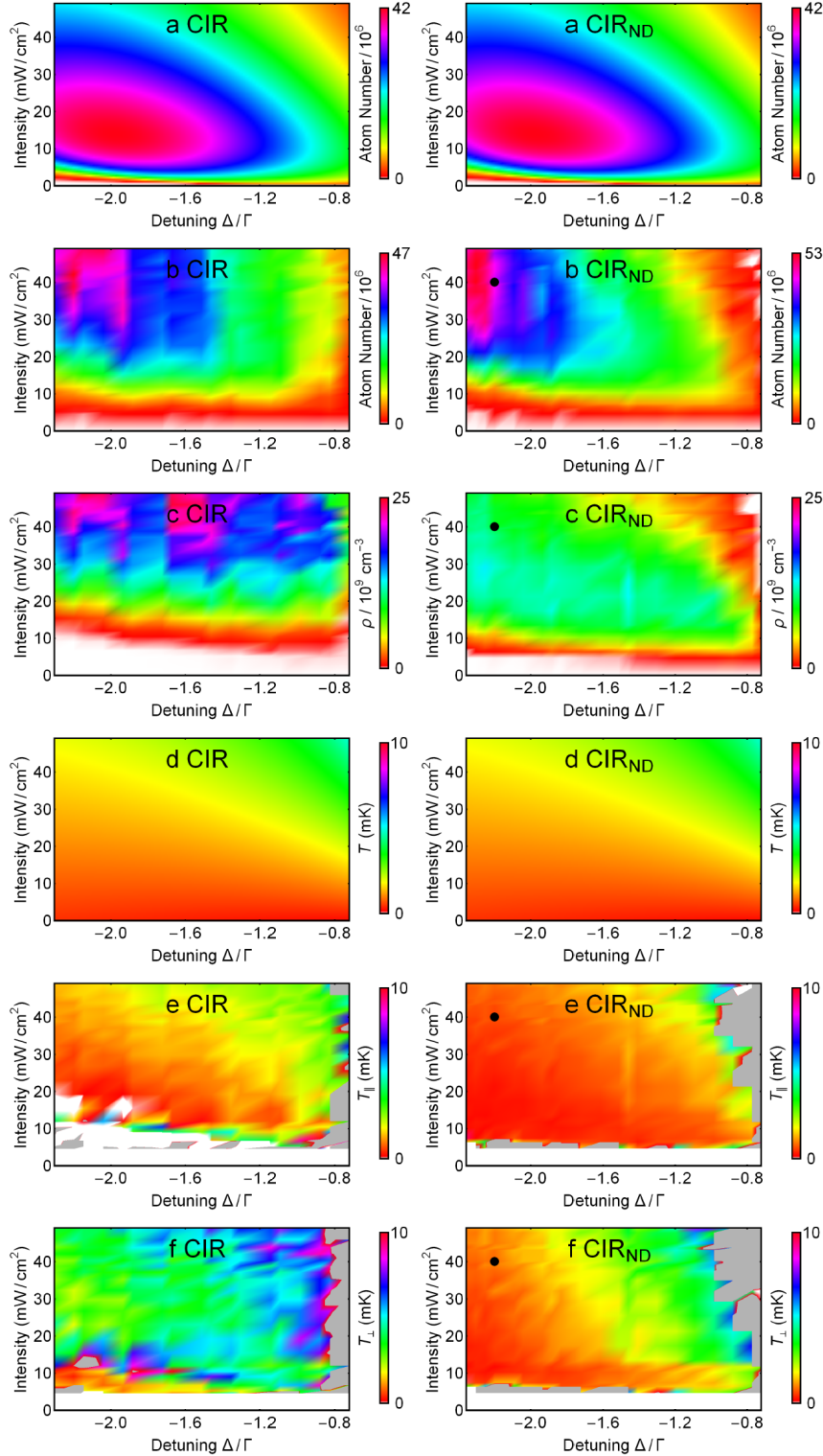
Figure 8.2: The full GMOT characterisation when using chip CIR (standard Gaussian input beam, a-f) and CIR_{ND} (CIR with a T=0.74 ND filter in the central 3 mm diameter of the input beam, a-f), both with beam diffraction angle $\alpha = 41°$. Note the slight increase in atom number, and significant decrease in temperature using chip $CIR_N D$ relative to chip CIR.

8.5.1 Best of both worlds: Large number with low temperature

For many metrological experiments, such as atomic clock measurements, the precision achieved strongly depends upon the temperature and total population of the atomic ensemble. Hence, an understanding of the final number of atoms that can be brought from the MOT stage to ultracold temperatures provides a good indication of the full capability of the GMOT. In Nshii *et al.* [42] we effectively had only binary control of the intensity – this meant we could *either* get a large number of atoms on Chip CIR with high intensity, or good optical molasses on chip TRI_{15} with lower intensity light (and a correspondingly small number of atoms loaded in the MOT).

After analysis of the results presented in Section 8.5, the most suitable gratings for MOT number and temperature are Chip CIR_{ND} and $TRI_{12}$. To study the number of atoms that could be brought to sub-Doppler temperatures, a MOT of intensity $40\,\mathrm{mW/cm^2}$ and detuning of $\Delta/\Gamma = -2.2$ (initial MOT indicated by black dots in experimental Figs. 8.1 TRI_{12} and 8.2 CIR_{ND}) was transferred into optical molasses. The molasses consisted of turning off trapping magnetic fields, whilst using a two-step frequency jump of $\Delta/\Gamma = -5.3$ and $\Delta/\Gamma = -8.3$, each of duration $12\,\mathrm{ms}$. Note that these measurements were taken with the environmental magnetic field as indicated in Fig. 6.10 (a), with no effort to nulling stray gradient fields.

Under these conditions, Chip CIR_{ND} brought 2×10^7 atoms down to a 3D average temperature of $45\,\mu\mathrm{K}$ (Fig. 8.3(a)). Chip TRI_{12} used the same settings with the exception that the molasses intensity was reduced to $23\,\mathrm{mW/cm^2}$ – bringing 2.5×10^7 atoms down to a 3D average temperature of $45\,\mu\mathrm{K}$ (Fig. 8.3(b)). Both temperatures are similar to those achieved by Nshii *et al.* in [42] (with TRI_{15}), but with an order of magnitude more atoms after
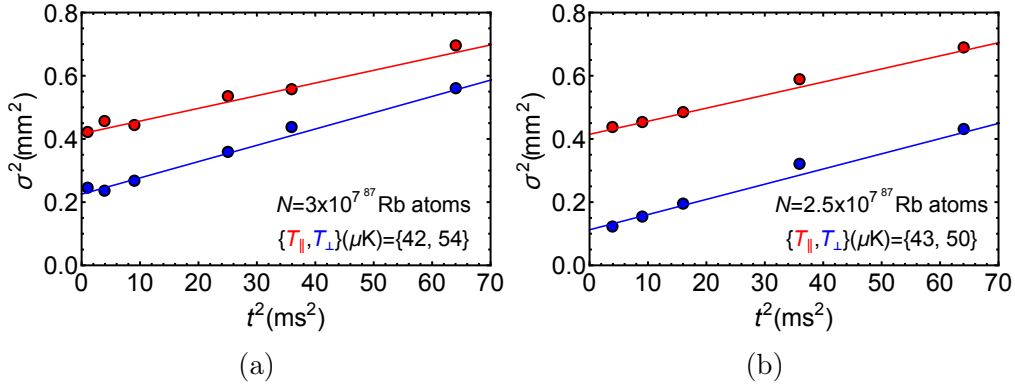
Figure 8.3: Temperature measurements in directions both parallel (red) and perpendicular (blue) to the grating for chip TRI_{12} (a) and $\mathrm{CIR}_{\mathrm{ND}}$ (b). Both chips give a 3D average temperature $T = \frac{2}{3}T_{\parallel} + \frac{1}{3}T_{\perp} = 45\,\mu\mathrm{K}$.

molasses ($N \approx 2 \times 10^6$ in [42], due to the lack of intensity control discussed above). Temperature T is determined by fitting $\sigma^2 = \sigma_0{}^2 + k_B T t^2/m$ to the data, where σ is the standard deviation of the Gaussian fit to the atomic cloud spatial distribution, m is the mass of an ^{87}Rb atom, k_B is Boltzmann's constant and σ_0 is the initial ($t = 0$) standard deviation of the cloud.

8.6 Interpretation and conclusions

Both the experimental MOT atom number and cloud temperature demonstrate surprisingly good agreement with theoretical data trends in Figs. 8.1, 8.2, given the simplicity of the theoretical models employed.

We note that higher densities are achieved on Chip CIR and $\mathrm{CIR}_{\mathrm{ND}}$, largely due to the larger diffraction angle α, with higher associated damping γ and trapping κ coefficients. There is a dramatic density improvement with TRI_{12} over TRI_{15} and this trend may continue with higher values of α toward the tetrahedral configuration $\alpha = \arccos(1/3)$, with the caveat that the capture volume and grating diffraction efficiency will decrease. In Doppler theory the cloud size scales as $\sigma \propto \sqrt{\gamma T/\kappa}$, however we note from the relatively constant experimental MOT density for a variety of detunings and intensities

that we are reaching sufficient atom numbers to likely be entering the MOT 'constant density regime' where reradiation forces become more important than restoring forces [129–131].

In terms of the temperature, significant sub-Doppler effects are not present, however we note that one would only expect sub-Doppler cooling under conditions of low intensity and large negative detunings, where we have insufficient data coverage to draw any further conclusions. The atom number is sufficiently large that effects where the MOT temperature is expected to increase with atom number ($T \propto N^{1/3}$) might also become evident, as has been seen in Refs. [134, 135].

Chapter 9

Publication: Grating chips for quantum technologies

J. P. McGilligan, P. F. Griffin, R. Elvin, S. J. Ingleby, E. Riis, and A. S. Arnold.[1]

We have laser cooled 5×10^6 ^{87}Rb to 3 μK in a micro-fabricated grating magneto-optical trap (GMOT), enabling future mass-deployment in highly accurate compact quantum sensors. In this chapter we build upon our work with the grating magneto-optical trap, GMOT [42, 102, 136, 137], and show it is a viable platform for compact quantum sensing by generating a truly ultra-cold atomic sample with a micro-fabricated chip. This study also focusses on magnetically trapping a cold sample for measurement of the background Rb pressure present in the vacuum chamber. Furthermore, we utilise Larmor spin precession for magnetometry in order to null stray static and gradient fields in the lab environment. Finally, we demonstrate an array of cold atoms generated above a diffractive optic with a single laser, with an outlook to demonstrating a compact, cold atom magnetic gradiometer.

---

[1]The work presented in this chapter is extracted from and expands upon the published results. The published version is provided in Appendix F

9.1 Magnetic sensing for a low temperature molasses

Early magnetic measurements date back to 200 BC, during the Han dynasty of ancient China, where the first compasses were realised to advance navigational capabilities [138]. It was not until 1832 that Carl F. Gauss pioneered the first device sensitive to the strength of a magnetic field by suspending a bar magnet in free space [139]. Advances in magnetic measurements have led to the current atomic magnetometer standard [140, 141]. For the past three decades, the field of magnetometry has been dominated by superconducting quantum interference devices, SQUIDs [142], operating with sensitivities reaching better than 1 fTHz$^{-1/2}$ [141].

As illustrated in Fig. 9.1, a magnetometer working in the femtotesla regime becomes very useful for fields in biomagnetism, with SQUIDs now used in a range of applications from magnetic resonance imaging, MRI, and mapping of the magnetic fields produced from the organs such as the brain for diagnosis of epilepsy and neural responses [143]. As well as medical applications, magnetometers have been demonstrated in a wide variety of applications, such as explosives detection [144], archeology [145], navigation [146], and fundamental physics experiments [147]. In recent years atomic magnetometers have demonstrated sensitivities capable of replacing SQUID devices, without requiring expensive cryogenics.
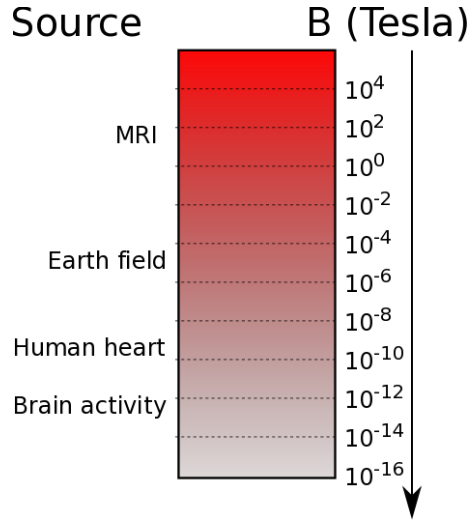
Figure 9.1: Graphical representation of applications requiring specific levels of magnetic field sensitivity.

The shot-noise limited sensitivity achievable for an optically-pumped atomic magnetometer is,

$$\delta B = \frac{1}{\gamma_g \sqrt{n T_2 V t}},$$ (9.1)

where n is the number density of the atoms, T_2 is the spin relaxation time, t is the measurement time, γ_g is the gyromagnetic ratio and V is the measurement volume [147].

For most atomic magnetometers, the spin relaxation time, T_2, is limited by spin-exchange collisions with other atoms in the alkali-metal vapour. This is overcome in the spin-exchange-relaxation-free, SERF, magnetometer through elimination of spin exchange collisions by using high atomic densities in very low magnetic fields, where atomic spin exchange occurs on a timescale much faster than the larmor precession [141].

Optically pumped atomic magnetometers work from the principle of coherent spin precession of a polarised atomic species in the presence of a magnetic field [141, 147]. Larmor spin precession is based on atomic magnetic moments interaction with a local magnetic field, aided by the optical pumping

of atoms with near resonant light into a non-degenerate Zeeman level of the ground state via an excited state transition. Once in the stretched state, the angular momentum vector, **F**, will precess about the axis of an applied magnetic field, $|\mathbf{B}|$, at the Larmor frequency,

$$\omega_L = -\gamma_g |\mathbf{B}|, \tag{9.2}$$

Where ω_L is the Larmor frequency, $\gamma_g = \frac{-eg_F}{2m}$ is the gyromagnetic ratio of the atom, e is the electron charge and m is the atomic mass.

The precession of **F** around **B** changes the optical absorption and dispersion properties of the atomic ensemble by passing in and out of resonance with the incident polarised electric field. Thus, the precession can be observed as a damped oscillation in the optical absorption and dispersion, measured using a polariser and detector, to give a direct measurement of $|\mathbf{B}|$ [148, 149].

Here we measure Larmor precession in the molasses of an un-shielded grating magneto-optical trap to null stray static fields and reduce the level of gradient fields. The set-up uses the same laser source for cooling and probing by splitting the beam into two optical arms. The pump/probe arm is tuned into resonance with the F=2 to F'=3 level using an AOM. The technique chosen was to use an on-resonant pumping beam, such that a constant intensity beam of 0.68 mW/cm^2 and duration of 10 μs would resonantly pump the atoms with circular light into the stretched state. A 10 Γ detuning was then introduced by electronically offsetting the lock-point of the spectroscopy signal for a far off-resonant probe beam. The atomic rotation around an applied magnetic field changes the polarisability of the atomic medium and thus the probing electric field polarisation, allowing a more sensitive detection to be made using a polariser for increased signal-to-noise, seen in Fig. 9.2 (a), as opposed to absorption detection. This experimental procedure was run in
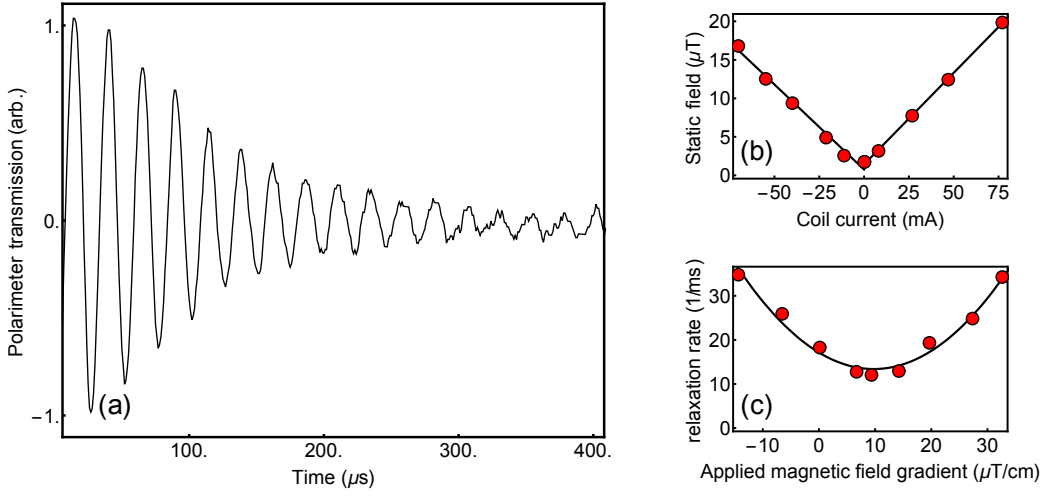
Figure 9.2: (a): Larmor precession measured from the GMOT (b): The static field determined from the Larmor frequency is measured as a function of the Helmholtz coil current with two best fitting lines applied. (c): The relaxation rate is measured as a function of applied magnetic gradient field with a best fitting curve.

conjunction with a Schmitt trigger from the AC mains in order to reduce AC magnetic field noise by making the magnetic measurement at the same point of the 50 Hz cycle each time.

The precession data are fit with $A \exp\left(-t/\tau\right) \sin\left(2\pi\omega_L t + \phi\right)$, where A is the initial signal amplitude, τ is the decay time and ϕ is the phase. Although the precession occurs on a timescale comparable to the pump duration there are no significant effects on the precession during this time. The Larmor frequency, ω_L is directly related to $|\mathbf{B}|$ through Eqn. (9.2), allowing direct correlation of shim current values to the static field in the vicinity of the atomic ensemble. Fig. 9.2 (b) illustrates the measurement of the static magnetic field value as a function of the Helmholtz coil current, used to produce a homogeneous static magnetic field to cancel the stray fields. This was used on both perpendicular axes to bring the measured field down to the level of the lab noise floor, $\sim$800 nT.

Sensitivity to gradient field components is obtained through the transverse

relaxation rate in the ground state coherence, $\gamma = 1/\tau$, which is directly related to the total magnetic field gradient through $\gamma = a|\nabla\mathbf{B}|^2 + \gamma_0$, where a is the coefficient describing the sensitivity to the magnetic field gradient and γ_0 is the relaxation rate in the absence of gradient fields [150]. The measured transverse relaxation rates in the ground state coherence are visible in Fig. 9.2 (c), where the parameter γ is plotted as a function of the difference current between the Helmholtz pair. When applying gradient cancellation on the perpendicular axes to the probe beam by making first order corrections to $d|\mathbf{B}|/dz$ and $d|\mathbf{B}|/dy$ we could improve the transverse decay time from 30 μs to 100 μs. A transverse decay time of 100 μs was the best achievable in our unshielded set-up.

With the magnetic gradient fields nulled as well as possible, the temperature in the molasses was then studied as a function of the applied static magnetic field, to demonstrate the necessity for low stray fields when trying to generate ultra-cold atomic samples. As has been discussed by Lett *et al*, the mechanisms of sub-Doppler cooling indicate a sensitivity of temperature to the magnitude of the static magnetic field due to the Zeeman shifts this will induce, destroying the coherent repopulation of m_F states involved during polarisation gradient cooling [72]. To investigate the level of sensitivity involved in our apparatus we applied static magnetic fields throughout the MOT and molasses stages, measuring the final molasses temperature as a function of the applied static field, as illustrated in Fig. 9.3.

The data presented illustrates a temperature range from 3-120 μK with a 35 μT change in static magnetic field. The data set is plotted with a quadratic fit, as expected from previous literature [72]. We note that our best MOT atom number and molasses temperature combination is (5×10^6, 3(1) μK) - comparable to molasses results in a macro-fabricated grating MOT (1×10^6, 7.6(6) μK) [151] and an optimised pyramidal MOT system
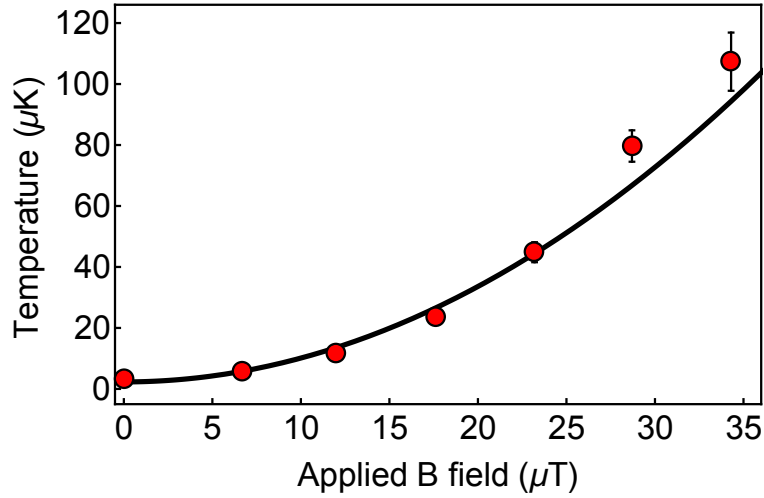
Figure 9.3: Molasses temperature measured as a function of the applied static field with best fitting parabola to guide the eye.

$(4 \times 10^6, 2.5 \ \mu\text{K})$ [152].

9.2 Pressure gauge in a compact apparatus

To achieve a low temperature molasses in a compact apparatus, we designed our vacuum system with scalability and simplicity in mind, such that a single Rb dispensing getter is used in conjunction with a 2 L/s ion pump (Titan ion pump - Gamma Vacuum). To attain a measurement of the vacuum background pressure at the MOT, we use the relation of the magnetic trap lifetime, τ, to the background Rb pressure in the chamber, P, as demonstrated by Monroe [153]. The author estimated a lifetime of 10 s for a background pressure at 7×10^{-10} mbar, with the dominant loss contributor being the van der Waals interaction between the trapped and thermal background atoms. This relation has been utilised in other literature for background pressure measurements at the atoms, each reaching a similar number [76, 154].

The atoms will be magnetically trapped if the magnetic force is larger than that of gravity, where the magnetic force along the gravity direction z can
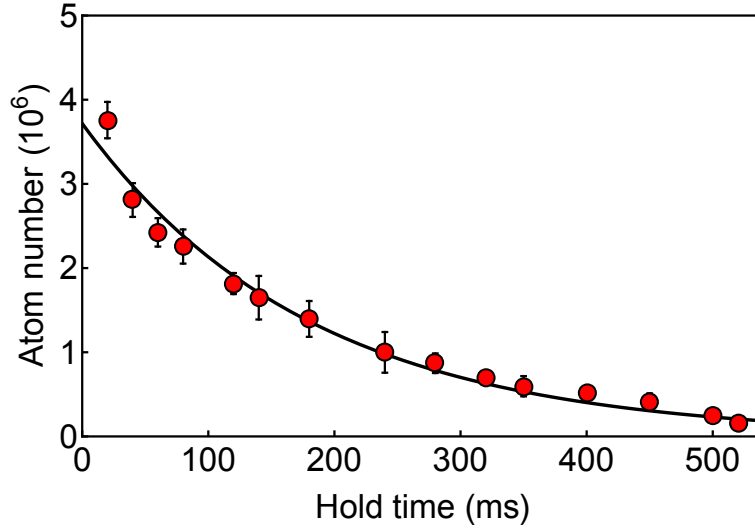
Figure 9.4: Trapped atom number as a function of the hold time in the magnetic trap. The black line indicates an exponential fit to determine a $1/e$ trap lifetime of 180 ± 10 ms

be described mathematically by,

$$F_z = -g_F\mu_B m_F\frac{d\mathbf{B}}{dz}, \tag{9.3}$$

where g_F is the Landé g-factor, μ_B is the Bohr magneton, and m_F is a magnetic level of the total angular momentum state. This force can then be used to trap weak-field-seeking atoms if F_z is greater than gravity.

The experimental procedure to achieve this begins by magneto-optically trapping the atoms in a quadrupole field, with an axial gradient 15 G/cm. At the end of the molasses sequence the trapping light was turned off and a short optical pumping pulse applied to drive the atoms into the weak-field-seeking $F = 2, m_F = 2$ state. The gradient field from the quadrupole coils was afterwards increased to 50 G/cm, whilst florescence images were taken for a varied trap hold time. At this stage we do not have the temperature/density were there are any evident losses from Majorana transitions. This enabled the trapped atom number to be described as a function of time, as seen in Fig. 9.4.

The experimental data points were fit with an exponential decay of the form, $N \exp\left(-t/\tau\right)$, where N is the initial atom number and τ is the 1/e magnetic trap lifetime, determined as 180±10 ms. If we use this τ to determine the background Rb pressure in the vacuum system, using the relation introduced earlier, we estimate a pressure of 4×10^{-8} mbar. This pressure is primarily due to the low pumping rate of the scaled down ion pump in an unbaked chamber. However, a 10^{-8} mbar pressure is achievable in other systems, where the ion pump has been made redundant in place for specialised micro-fabricated vapour cells with low-He-permeation glass [155]. Such apparatus would enable future reduction of the vacuum system volume for an unambiguously compact device.

9.3 A cold-atom array from a single laser

Atomic arrays have been utilised in cold atom experiments ranging from quantum information with physical qubit arrays [156], to metrological measurements in interferometry and gradiometry [157]. Ionic array apparatus have been miniaturised with trapped ion micro-traps to demonstrate 1D and 2D arrays [158], however an array of neutral atoms is favourable due to their weaker interaction with the environment [159]. The typical method for generating a neutral atom array is in an optical lattice, where individual microscopic site addressing and measurement is restricted to the regime of the quantum gas microscopes [85, 160] and optical dipole traps [161].

Large macroscopic arrays of neutral atoms have been achieved in the form of a magnetic lattice loaded from cold atoms, capable of capturing up to 2000 atoms in 500 sites [159]. Macroscopic scaled neutral atom arrays with larger N have also been demonstrated in the form of a 2×2 array of MOTs [162] where the scalability is limited by the optical set-up. Here we introduce the
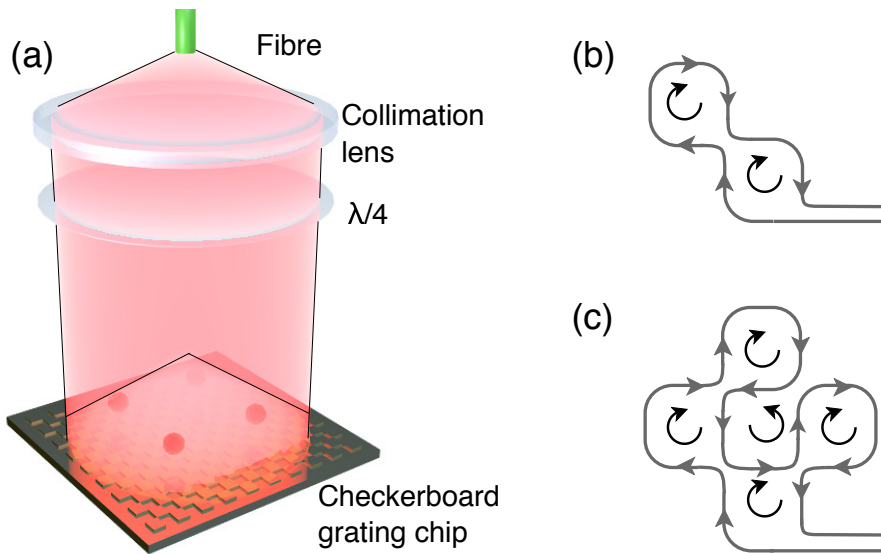
Figure 9.5: (a): Schematic of set-up for generating multiple MOTs above a single checkerboard grating. Linearly polarised light diverges from the optical fibre, is collimated and circularly polarised. (b)/(c) Wire pattern for creation of two/four magnetic minima. Grey lines indicate the wire and black curves emphasize the direction of current flow.

micro-fabricated grating chip as a simple and robust source for generating 1D and 2D arrays of neutral atoms with a single incident laser and patterned coil geometry.

For this study, the holographic checkerboard grating chip geometry, discussed in previous literature [42, 137], was implemented into the set-up. The benefit of the checkerboard grating is the lack of a central symmetry point that exists in the linear gratings. Instead, the overlap volume extends to fill the surface area of the chip [42], making it possible to lay a patterned coil beneath the surface of the grating to form a number of MOTs dependent upon the coil geometry, as can be seen in Figure 9.5 (a).

To create the appropriate inhomogeneous magnetic potential for multiple MOTs, we used the coil design illustrated in Fig. 9.5 with an additional external bias field orientated perpendicular to the plane of the coils. The wire geometries used in Fig. 9.5 (b) and (c) were selected for a 1D and 2D array
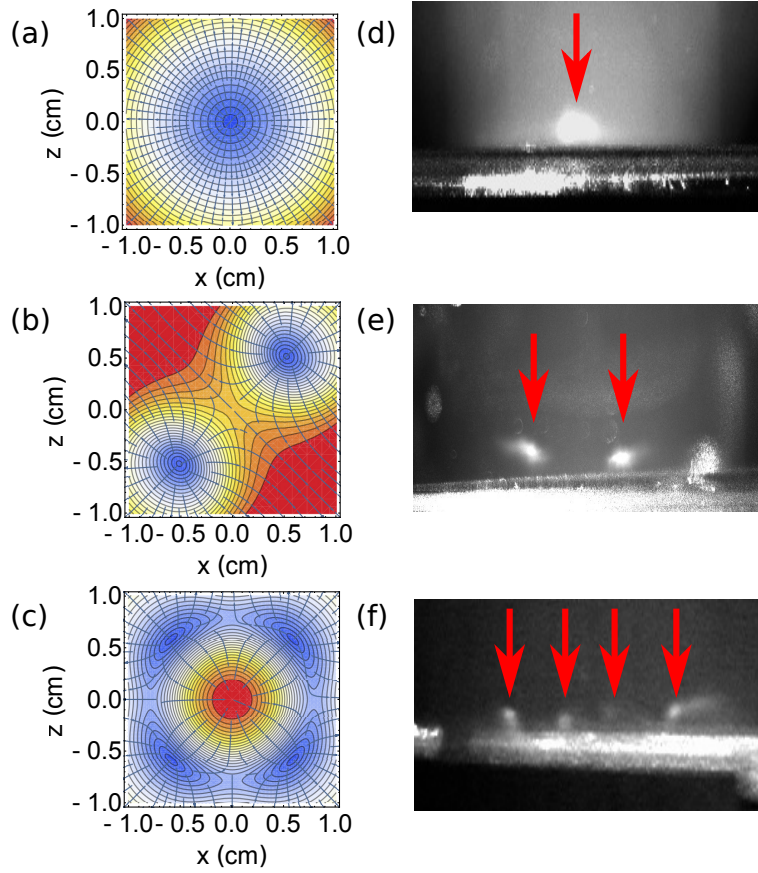
Figure 9.6: (a), (b) and (c): Standard anti-Helmholtz simulation, two magnetic minima simulation for a 1D array and four magnetic minima simulation for a 2D array. (d), (e) and (f): Experimental realisation of one, two and four MOTs.

respectively. Here the grey lines represent the wire formation, with black curves used to emphasize the direction of current flow. For (b), the selected wire formation creates two coils of the same magnitude. In (c), the formation creates five coils, four with the same direction and one in the opposite.

To determine the properties of these wire geometries requires numerical solution of the Biot-Savart law, provided in Sect. 3.2.1. Due to our coils being approximately circular, we assume a perfect circle for our magnetic field calculations. Eqns. (3.18) were used to simulate the magnetic potential for a single MOT, as well for the geometries of Fig. 9.5 (b) and (c), as shown in Fig. 9.6 (a), (b) and (c) respectively. The required wire geometries were

formed in a 3D-printed mount and placed immediately below the grating. The geometry patterned coil would then be run with a small bias coil directly below in conjunction with the upper trap coil to create the appropriate magnetic field required. The experimental observations of this can be seen in Fig. 9.6 (d) for a single MOT, (e) for 2 MOTs in a 1D array and (f) for 4 MOTs in a 2D array. The images seen in (d) and (e) were taken with the grating mounted outside of the vacuum, using ~10 mW/cm^2 to start with 2×10^6 atoms in (d) which was then split into 2 MOTs with 5×10^5 atoms each. For image (f) the grating and patterned coil were mounted inside the vacuum due to the magnetic minima forming close to the grating surface, forming 4 MOTs using ~4 mW/cm^2, with an estimate 10^5 atom number in each trap.

This demonstration proves the potential of the GMOT in future quantum sensing devices requiring an atomic array. Most notably, such a device would prove beneficial to the realisation of a compact magnetic gradiometer, where an array of identical MOTs can be used for cancellation of common mode noise.

Part IV

An atomic clock

Chapter 10

Experiment: Coherent population trapping with a Rb vapour cell

Alkali atoms offer a ground-state with hyperfine levels separated by an energy in the microwave regime that is accessible through the magnetic dipole [163]. However, direct electric dipole transitions between these states are forbidden, and two-photon transitions require sophisticated experimental techniques such as coherent population trapping to optically address the states [164]. Here we discuss the observation of an 85 kHz wide coherent population trapping resonance in a thermal atomic vapour of ^{85}Rb. The contrast and AC-Stark shifts are examined for probing the D_2 state with a homemade ECDL. Finally, an enhanced contrast of the clock resonance is provided from optical pumping on the D_1 line at 795 nm.

10.1   Experimental set-up

The initial coherent population trapping setup used 780 nm light, taken from the cooling apparatus in Fig. 7.1. The 780 nm light was coupled into a Jenoptik (PM785) electro-optical modulator, EOM, to generate two electric fields to couple the ground-states for coherent population trapping, as discussed in
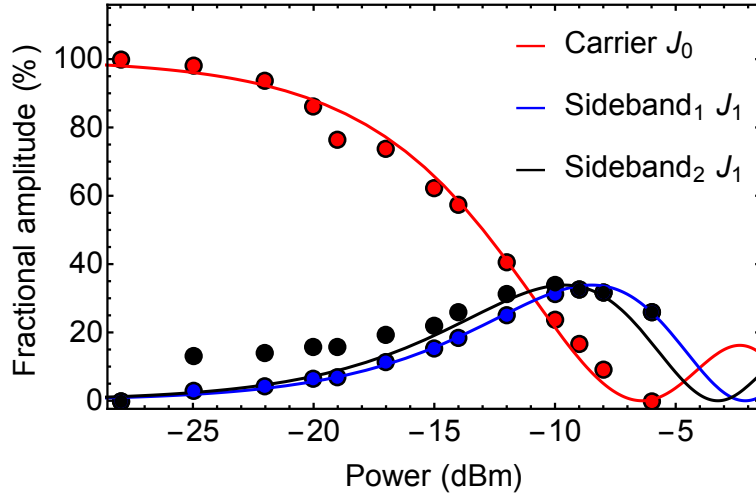
Figure 10.1: The carrier/sideband fractional amplitudes as a function of the RF power applied to the electro-optical modulator. Solid lines are the best fitting Bessel functions for $J_0(dBm)$ in red and $J_1(dBm)$ in blue and black. The blue and black fits have independent variables.

Sect. [2.4] and [11]. The EOM is composed of a $LiNbO_3$ crystal, which is externally modulated to generate sidebands symmetrically separated from the carrier by the drive frequency. Due to the laser electric fields being derived from a single source, the carrier and sidebands are inherently phase stable over space.

The incident carrier frequency was locked on the $F = 3 \rightarrow F' = 3$ transition of the ^{85}Rb atoms, with a sideband modulated at 3.0357324390(60) GHz to couple $F = 2 \rightarrow F' = 3$. Although the non-coupled sideband is non-interacting during CPT, the fractional amplitude may induce AC-Stark shifts on the clock resonance. The sideband fractional amplitude is a function of the depth of the modulation frequency, which is provided from an Agilent (E4433B) signal generator. The fractional amplitudes of the sidebands were analysed with a Fabry-Perot etalon as a function of the applied RF power, depicted in Fig. 10.1. The solid lines depict best fitting Bessel functions of the modulation depth, which varies linearly with the drive voltage. These measurements were used to characterise the capabilities of the EOM, with

attention drawn to the point of equal fractional amplitudes. Equal fractional amplitudes were used for all the CPT experiments described in this thesis, unless otherwise specified.

Vapour cell absorption

The absorption of light in atomic vapour is determined by the Beer-Lambert law,

$$I = I_0 e^{-\alpha L} \tag{10.1}$$

where I is the transmitted intensity, I_0 is the incident intensity, α is the absorption coefficient and L is the path length through the atomic vapour. The experiments reported in this chapter were performed in a 7.5 cm long ThorLabs (GC25075-RB) cell, which is observed to provide 45% absorption at room temperature. To detect the formation of CPT, the sideband frequency was modulated by 6 MHz at a scan frequency of 50 Hz. The 50 Hz scan frequency, combined with the lack of dead time during thermal probing, provided a high averaging rate over a relatively short time.

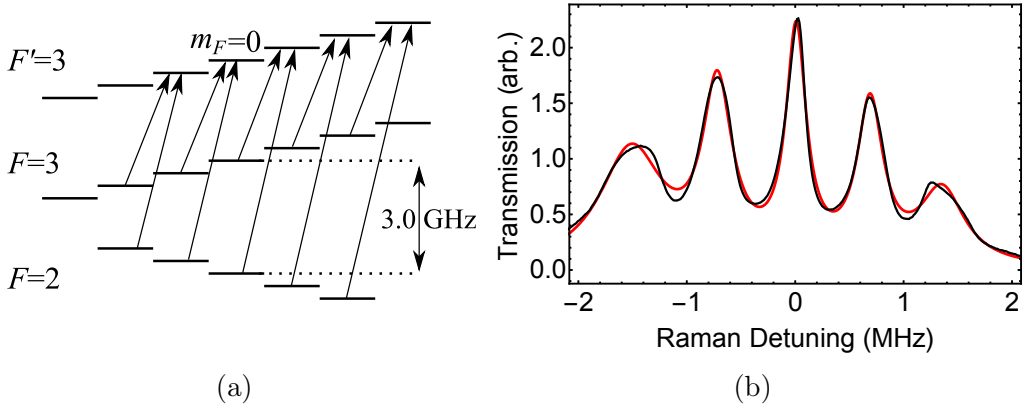(a)   (b)

Figure 10.2: (a): The expected transition cycle for circular σ^+ probing in ^{85}Rb. (b): Experimentally measured coherent population trapping transmission as a function of the Raman detuning. Red fit depicts the best fitting Lorentzian profile composed of five individual peaks of varying amplitude, width and position.

Providing the atomic dipole is quantised along the axis of the probing light, one would expect that circularly polarised light would optically pump the atoms into the stretched state, through the five Raman cycles illustrated in Fig. 10.2 (a). The initial observation of thermal CPT revealed upwards of ten peaks due to the laboratory magnetic environment perturbing the quantisation axis and contributing a π component as well as σ transitions. To attain a clear quantisation of the atomic medium, a three-dimensional Helmholtz coil configuration was implemented for static field cancellation. A small homogeneous magnetic field was applied parallel to the propagation of the laser light to aid optical pumping. The resulting transmission of the laser, when scanning the Raman detuning under these conditions, can be seen in Fig. 10.2 (b). The red line depicts the independent best fitting Lorentzians, used for quantitive analysis of the absorption profiles, described as

$$\sum_i \frac{A_i}{\pi} \frac{\Gamma_i/2}{(x - x_i)^2 + (\Gamma_i/2)^2} + (mx^2 + bx + c), \qquad (10.2)$$

where A_i is the amplitude, Γ_i is the linewidth, x_i is the peak central frequency, and $mx^2 + bx + c$ are variables corresponding to any quadratic function in the background of CPT features.

10.2 Magnetically insensitive state

The application of a homogeneous magnetic field induces non-degeneracy in the atomic states and perturbs the transition frequency of the m_F manifolds proportional to the magnetic field parallel to the electric field, $|\mathbf{B}_\parallel|$. The magnetic sensitivity of these states has previously been exploited in CPT magnetometers [165–167], where the principle of operation is to spectroscopically resolve the Zeeman shifts relative to the magnetically insensitive $m_F = 0$ state.

Here we demonstrate a CPT magnetic measurement to track Zeeman shifts of the $m_F = 0, \pm 1, \pm 2$ states as a function of applied magnetic fields. The induced shifts are calculated from the central frequency of best fitting Lorentzians and plotted as a function of the applied magnetic field, illustrated in Fig. 10.3. The associated error bars were generated from an average of both $m_F = \pm 1, \pm 2$ states with respect to the $m_F = 0$ transition frequency, with the error amplitude of the $m_F = \pm 1$ being comparable to the data point. The error associated with the $m_F = 0$ state was determined from the fitting error. The black, red and blue lines correspond to the theoretical Zeeman shifts calculated from the known Landé-g_F factors [59]. The $m_F = \pm 2$ has noticeably larger error bars, consistent with a wider FWHM of the lower amplitude absorption profile, which degrades the measurement sensitivity of the $m_F = \pm 2$ states central frequency.

10.3   Linewidth and contrast

Our study of CPT in an atomic vapour was focussed on the achievable contrast and linewidth, due to their relative contributions to clock stabil-
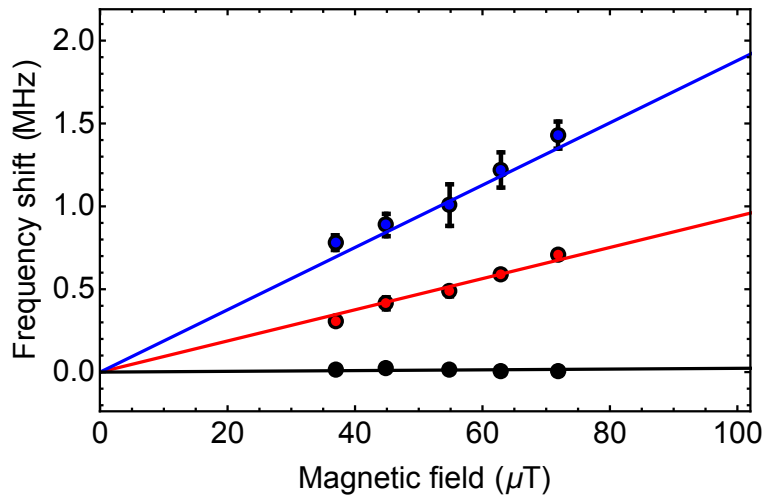
Figure 10.3: Magnetic field sensitivity of $m_F = 0, \pm 1, \pm 2$ states for ^{85}Rb, illustrated in black, red and blue respectively. Solid lines depict the theoretical Zeeman shifts calculated from the Landé-g_F factor.
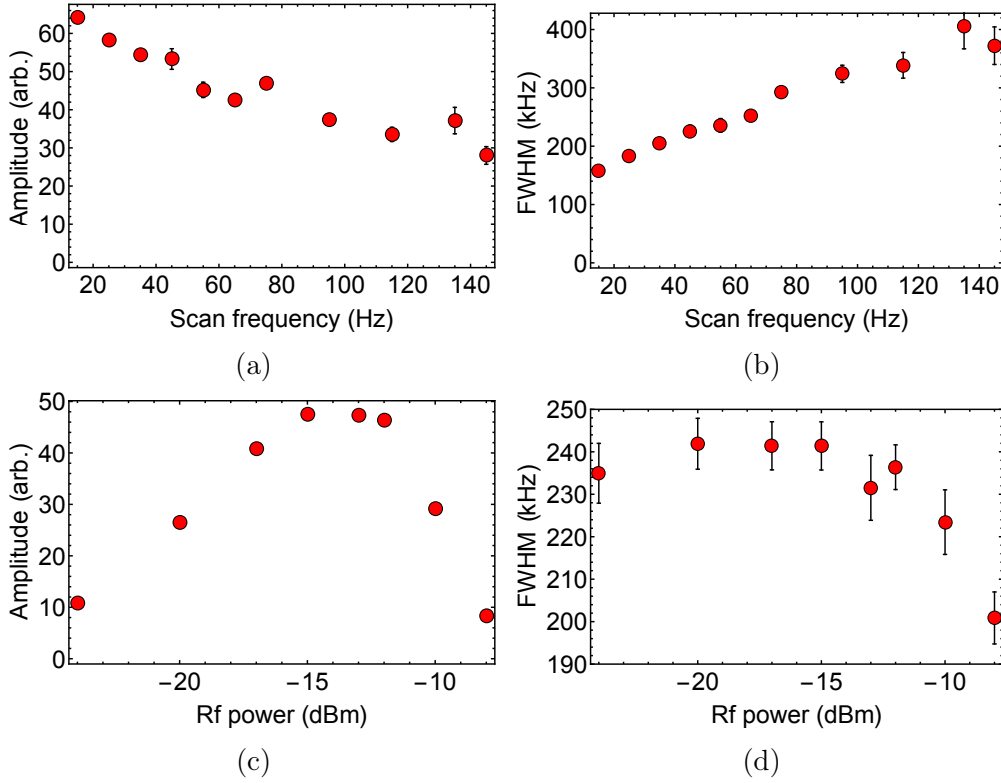
Figure 10.4: Amplitude and full-width-half-maximum measured for CPT absorption on the $m_F = 0$ state of ^{85}Rb as a function of the scan frequency and RF power, (a)(b) and (c)(d) respectively.

ity [39]. A simple estimation of the predicted CPT linewidth for thermal atoms can be obtained from the optical field interaction time. For the case of a room temperature ensemble passing through a 3 mm ($1/e^2$ diameter) beam, $t = \frac{D}{v} = \frac{3 \text{ mm}}{293 \text{ m/s}} = 13.6 \ \mu$s, implying a transit time limited FWHM on the order of 16 kHz. The resonance linewidth is commonly determined by [164],

$$\text{FWHM} = \frac{1}{\pi}(\gamma + \frac{\Omega_R^2}{\Gamma_P}), \tag{10.3}$$

where $\Gamma_p = \Gamma\sqrt{1 + \frac{I}{I_{sat}}}$ is the power broadened natural linewidth of the excited state, γ is the relaxation rate of the ground state coherence typically dominated by collisions, and Ω_R is the Raman Rabi frequency.

The experimental set-up was subject to many potential broadening mech-

anisms that required minimisation to achieve optimum performance. A variety of parameters were experimentally studied, with the dominant broadening contributors being the frequency of the triangular sideband scan frequency and level of RF power supplied to the EOM, illustrated in Fig. 10.4(a), (b) and (c), (d) respectively. Firstly, the sideband scan frequency was shown to reduce the FWHM by over a factor of 2 when measured between 140 Hz and 30 Hz. This was possibly limited by the detection time constant of the simple photodiode used for these measurements. The CPT investigations of Sect. 11 introduce commercial subtraction and normalisation photodiode units. The lower scan rates provided the lowest FWHM and largest achievable amplitude of the CPT feature. Furthermore, the level of RF power supplied to the EOM indicates an optimum CPT amplitude for an applied RF power of $\approx$-13 dBm; corresponding to equal fractional amplitudes of the probing electric fields of Fig. 10.1.

The parameter found to be most critical to the achievable contrast was the probe beam intensity, as seen in Fig. 10.5 (a). The CPT contrast is defined as the signal amplitude divided by the depth of the absorption feature, i.e. $\frac{A_1}{A_2} \times 100$ depicted in Fig. 10.5 (b). From these intensity results we realise a 3 % contrast for a probe intensity of 2 mW/cm^2. Methods of achieving a higher contrast CPT feature are addressed in Sect. [11].

10.3.1 AC-Stark shift

As previously discussed in Sect. [2.3], the AC-Stark shift upon the probed state is proportional to the I/I_s. For ^{85}Rb we can assume I_{sat}=1.67 mW/cm^2, however, that is only applicable for a $|F = 3, m_F = 3\rangle$ to $|F' = 4, m_F = 4\rangle$ transition. Since the two CPT frequencies address different transitions, there is a normalisation factor, β, that must be applied to I_s through the Rabi frequency. The calculation of the Stark shift as described in Ref. [168], including
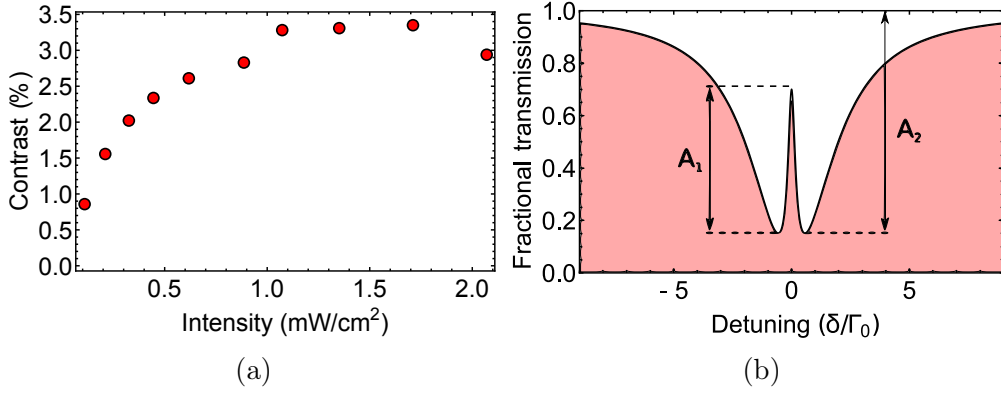
Figure 10.5: Contrast of the CPT clock feature. (a): Experimentally measured contrast as a function of the probing intensity. (b): Graphical representation for defining the CPT contrast as the CPT amplitude/absorption depth represented as A_1 and A_2 respectively.

the correction to I_s is,

$$\Delta E = \pm \frac{|\langle e|\mu_{eg}|g\rangle|^2}{\Delta}|E|^2 = \beta \frac{\hbar\Omega^2}{4\Delta}. \qquad (10.4)$$

For circularly polarised light driving a D_2 transition between the $^2S_{1/2} \rightarrow$ $^2P_{3/2}$ of ^{85}Rb, then I_s is calculated from normalised Clebsch-Gordan coefficient C=3780 provided in Ref. [59], such that a normalisation of the addressed transitions relative to this coefficient will provide the correction factor, β. The Clebsch-Gordan coefficient for a transition between the $|F = 2, m_F = 0\rangle$ to $|F' = 3, m_F = 1\rangle$ and $|F = 3, m_F = 0\rangle$ to $|F' = 3, m_F = 1\rangle$ are given as C=672 and C=1050 respectively [46]. Thus, correction factor $\beta = (\frac{1}{3})(\frac{672}{3780})+$ $(\frac{1}{3})(\frac{1050}{3780}) + (\frac{1}{3})(0) = 0.15185$, where we assume equal intensity amongst the carrier and sidebands, including the sideband that is not coupled to a transition. Accounting for these transition coefficients, Eqn. (10.4) can then be mapped on to the measured shifts of the $m_F = 0$ state as a function of the probe intensity, I, as seen in Fig. 10.6.

The experimental data was collected by scanning the CPT transmission as a
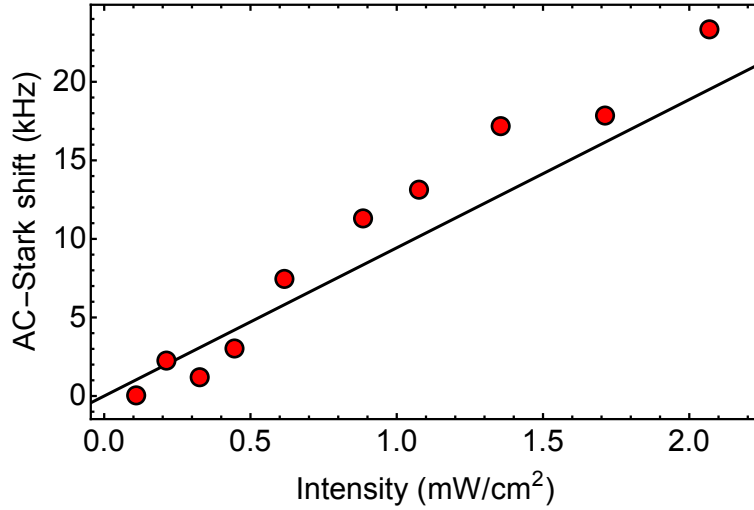
Figure 10.6: Experimentally measurement of the AC-Stark shift upon the central clock transition as a function of incident laser intensity. The black line is the theoretically expected AC-Stark shift as calculated from Eqn. (10.4).

function of the Raman detuning Δ for a known optical detuning and range of incident intensities, whilst measuring the frequency position of the $m_F = 0$ CPT feature relative to the local oscillator defined $\Delta = 0$. Fig. 10.6 depicts a linear AC-Stark shift in the regime of low intensity, with the solid black line indicating a close correlation between prediction and experiment.

10.3.2   D$_1$-D$_2$ comparison

Following the results of Ref. [169], we incorporated a 795 nm ECDL to address the D$_1$ states, with an outlook to achieving a higher contrast. The increased contrast on the D$_1$ line arises from a reduced distribution of atoms amongst the fewer excited states available in the $5^2P_{1/2}$ manifold. To experimentally probe this manifold, the D$_1$ laser was locked to the $F = 3 \rightarrow F' = 3$ transition and coupled through the EOM. The intensity at the vapour cell was controlled using a PBS in conjunction with a $\lambda/2$ wave-plate, for measuring the achievable contrast as a function of the probe intensity.

The results of the investigation are depicted in Fig. 10.7 for D$_1$ and D$_2$

transitions, which depicts a five-fold improvement of the contrast for D_1 probing, revealing a 3% resonance contrast at lowest intensity compared to the 1% resonance for D_2. The narrowest resonance of 85 kHz was observed for a probe intensity of 0.11 mW/cm^2, illustrated in Fig. 10.7 (b). The solid black line depicts the best fitting FWHM, calculated from Eqn. (10.3) with a variable γ and optical pumping pre-factor to the Rabi rate. The optical pumping pre-factor accounts for a saturation intensity defined by the CPT transitions, as opposed to the stretched state. In the case of normalising the Clebsch-Gordan coefficients for σ transitions in the ground states, a theoretical pre-factor to the Rabi frequency of 0.05 is attained. This predicted value is in close relation to the experimentally obtained 0.03, simultaneous with $\gamma = 260$ kHz. Additionally, the measured 85 kHz is significantly larger than the coarsely calculated transit time FWHM of 16 kHz calculated in Sect. [10.3], implying that the linewidth is dominated by other broadening mechanisms.
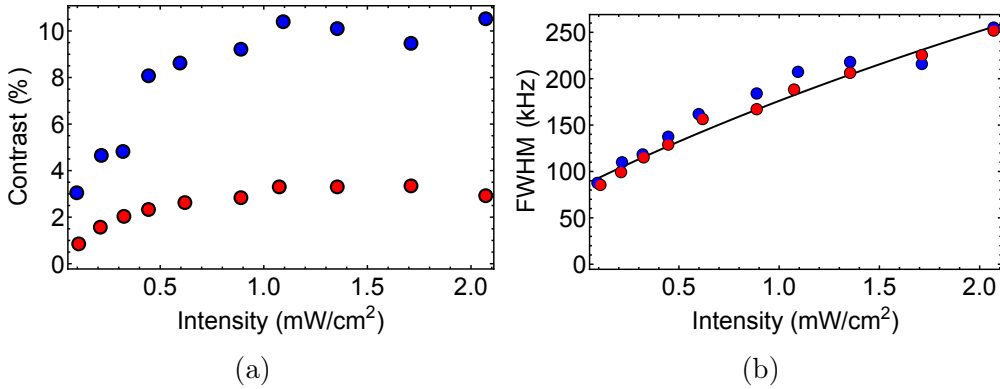
Figure 10.7: D_1 (blue) and D_2 (red) clock transition comparison. (a): Contrast measured as a function of probing intensity. (b): Full-width-half-maximum measured as a function of the probing intensity. Solid black line depicts the best fit to Eqn. (10.3).

10.4   Conclusion

The investigation of coherent population trapping has proven key for characterising equipment that will be implemented for a cold-atom clock resonance. This study facilitated testing of new equipment such as the EOM and D_1 spectroscopy, as well as illustrating the critical parameters for signal optimisation. The most favourable CPT signal in thermal atoms provided a FWHM of 85 kHz at 3% contrast. These results could be significantly improved with the addition of a buffer gas vapour cell to decrease the resonance linewidth, however, the temperature dependent pressure shifts associated with buffer gas led us to use cold atoms.

Chapter 11

Publication: Utilizing diffractive optics towards a compact, cold-atom clock

J. P. McGilligan, R. Elvin, P. F. Griffin, E. Riis, and A. S. Arnold.[1]

Laser cooled atomic samples have resulted in profound advances in precision metrology, however the technology is typically complex and bulky. In recent publications we described a micro-fabricated optical element that greatly facilitates miniaturisation of ultra-cold atom technology [102, 124, 136, 137]. Portable devices should be feasible with an accuracy vastly exceeding that of equivalent room-temperature technology, with a minimal footprint. These laser cooled samples are an ideal platform for quantum technology and metrological measurements. Here we will discuss the implementation of our micro-fabricated diffractive optics towards building a robust, compact cold-atom clock.

---

[1]The work presented in this chapter is extracted from and expands upon the published results. The published version is provided in Appendix G

11.1 Introduction

The continued research into atomic clocks in recent decades has led to considerable advancements in the achievable accuracy and stability. An improved stability is most notable in the atomic fountain and lattice clocks, capable of measuring relative frequencies at the 10^{-16} and 10^{-18} level respectively [15, 19, 29, 87]. Atomic clock research has also led to profound advancements in compact metrological devices, achieving frequency stabilities in the low 10^{-10} in package volumes measuring only a few tens of cubic centimetres [32]. However, the majority of the current compact clocks are based on room temperature ensembles that utilise buffer gas or cell wall coatings in order to increase the relaxation rate and coherence of the atoms, benefiting the system with increased contrast and interrogation times [38, 40, 170]. Ultimately, these coatings and buffer gasses limit the long term performance and accuracy achievable in a clock due to cell degradation and temperature dependent pressure shifts.

To overcome the thermal limitations, a move towards cold atoms is preferable. To date, attempts at miniaturising cold-atom clocks remain confined to thousands of cubic centimetre packages. We begin by proposing the grating magneto-optical trap, GMOT, as a step closer to bridging the gap between high performance cold-atom apparatus and the scale of a thermal package. This project aims at reaching a relative frequency stability better than 10^{-12} in a package on the scale of tens of cubic centimetres.

The CPT investigation presented in Sect. [10] has been carried out in a vapour cell using the conventional spectroscopic interrogation with circularly polarised light, depicted in Fig. 10.2 (a). However, the clock transition is not cyclical and instead favourably populates the stretched states when optically pumped with circular polarisation. Once in the stretched state the atoms
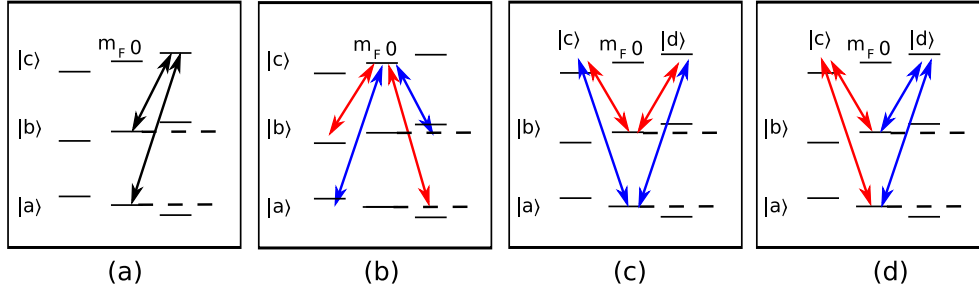
Figure 11.1: Coherent population trapping optical pumping for Λ and double Λ schemes. States $|a\rangle$ and $|b\rangle$ represent the electronic ground states, coupled via excited states $|c\rangle$ and $|d\rangle$. Solid lines with arrows represent addressed transitions with dashed lines highlighting the unperturbed $m_F = 0$ clock transition between ground states. (a): $\sigma\sigma$ - both optical fields are circularly polarised with the same handedness. (b): Lin $\parallel$ Lin - linearly polarised light is decomposed into a circular basis to produce two simultaneous dark states between the $|a, m_F = \pm1\rangle$ and $|b, m_F = \mp1\rangle$ states, coupled by the excited $|c, m_F = 0\rangle$. (c): Lin $\perp$ Lin - two orthogonally linear polarised optical fields are decomposed into a circular basis to generate two simultaneous dark states coupled to the excited $|c\rangle$ and $|d\rangle$ state. (d):Push-pull optical pumping - circular polarisation of the same handedness is pulsed between σ^--σ^+ to realise two Λ configurations coupled via the $|c\rangle$ and $|d\rangle$ states respectively.

are no longer contributing to the contrast of the $m_F = 0$ clock transition, as seen in Fig. 11.1 (a) [35, 171, 172].

To avoid degrading the clock feature contrast, multiple schemes have been demonstrated to generate an optical pumping that favours a maximum contrast in the central $m_F = 0$ transition, such as Lin$\parallel$Lin, Lin$\perp$Lin, and push-pull-optical pumping depicted in Fig. 11.1 (b), (c) and (d) respectively. The need for sophisticated experimental probing techniques to achieve a high contrast from real atoms is due to the unfavourable simultaneous creation of a dark and bright state. As is depicted in Fig. 11.1 (b) and (c), linearly polarised probing light along the axis of quantisation will be decomposed into equal $\sigma_\pm$ components, which generate the double-Λ configurations. Typically we find that one Λ configuration will create a dark state, whilst the other optically pumps atoms into the orthogonal bright state, arising due to the opposite magnitude of the Clebsch-Gordan coefficient in one of the transi-

tions. The orthogonal states simultaneous existence destructively interfere for a poor clock feature, addressed thoroughly in Sect. 11.3 for the chosen experimental approach.

Lin∥Lin was first proposed by A. V. Taichenachev *et al.* [173] to preserve the contrast of the $m_F = 0$ CPT feature for alkali-metal atoms with nuclear spin $I = 3/2$ [174]. The criteria of the Lin∥Lin technique, depicted in Fig. 11.1 (b), requires coupling to an excited $F' = 1$ state to avoid populating the stretched state through optical pumping. In this scenario, dark states are formed between the $|F = 1, m_F = \pm 1\rangle \rightarrow |F = 2, m_F = \mp 1\rangle$, separated by the ground-state splitting. This method has been demonstrated experimentally by F. X. Ensault *et al.* [175] in a cold Rb ensemble, where the double-Λ set-up creates dark states from the opposite magnitude $m_F = \pm 1$ states that remain separated by the ground-state splitting. The dark state coupling for these high contrast CPT schemes are discussed in this chapter, with experimental observations from the GMOT set-up.

An alternative high contrast pumping scheme can be achieved using linearly polarised light rotated by $\pi/2$ relative to each other. The Lin⊥Lin method was first demonstrated in 2005 by T. Zanon *et al.* who showed >50 % CPT contrast in thermal Cs based on a double-Λ scheme [171, 172]. The phase rotation of electric field polarisation aids a constructive interference of the $m_F = 0$ dark state for clock measurements, discussed in detail in Sect. [11.4].

Push-pull optical pumping, PPOP, is more commonly associated with magnetometry, however, recent studies have utilised the pumping configuration for miniature clocks [38, 40]. PPOP was first demonstrated in clocks by Y.-Y. Jau *et al*, [53] who used a pulsed intensity to rapidly switch the two probing CPT electric field polarisations between σ^+ and σ^- such that both Λ configurations would not occur simultaneously. The dark states formed from Λ

are the same as those for Lin⊥Lin, such that this switching technique avoids issues of the bright and dark state interference. Fig. 11.1 (d) illustrates the optical pumping scheme with addressing electric fields transitions for E_1 and E_2 represented in red and blue.

11.2   CPT in the $\sigma\sigma$ configuration

The simplest CPT configuration is the standard $\sigma\sigma$ polarisation, where both optical fields have the same handedness of circular polarisation. The dark state of this configuration is created by two electric fields, $\vec{E}_1(t) = \vec{E}_1 \cos(\omega_1 t)$ and $\vec{E}_2(t) = \vec{E}_2 \cos(\omega_2 t - \eta)$, that couple states $|b\rangle$ and $|a\rangle$ via the excited $|c\rangle$ state, with angular frequency ω and phase difference η, as illustrated in Fig. 11.1 (a). The formation of a dark state requires the atomic ensemble to no longer be interacting with the addressing optical fields, such that the interaction Hamiltonian is zero.

The total atomic wave-function is a superposition of all three atomic states included in the CPT formation,

$$\Psi(t) = c_a(t)e^{-i\omega_a t}|a\rangle + c_b(t)e^{-i\omega_b t}|b\rangle + c_c(t)e^{-i\omega_c t}|c\rangle, \qquad (11.1)$$

where $c_{(a,b,c)}(t)$ are the state amplitudes at a given time [176], following the same derivation as the two-level atom picture in Sect. [2.1].

If we assume that the Hamiltonian describing the system is composed of only the interaction component, $H = H_i = -\vec{d} \cdot \vec{E}_i(t)$, then the coupling of ground states to the excited state can be described as:

$$H_{bc} = \hbar\Omega_1 e^{-i\omega_1 t}|b\rangle\langle c|, \qquad (11.2)$$

$$H_{ac} = \hbar\Omega_2 e^{-i\omega_2 t - i\eta}|a\rangle\langle c|, \qquad (11.3)$$

where $\Omega_i = -\vec{E}_i \frac{\langle c|\vec{d}|i \rangle}{\hbar}$ is the Rabi frequency associated with the indicated transition.

Using Eqns. (11.1)-(11.3) and substituting into Eqn. (2.3) yields:

$$i\dot{c}_c(t) = \Omega_1 e^{i(\omega_{bc} - \omega_1)t} c_b + \Omega_2 e^{i(\omega_{ac} - \omega_2)t - i\eta} c_a, \tag{11.4}$$

$$i\dot{c}_b(t) = \Omega_1 e^{i(\omega_{bc} - \omega_1)t} c_c, \tag{11.5}$$

$$i\dot{c}_a(t) = \Omega_2 e^{i(\omega_{ac} - \omega_2)t - i\eta} c_c. \tag{11.6}$$

If we assume that the ground states are decoupled from the addressing optical fields, the finite lifetime of the excited state will result in $\dot{c}_c(t) = 0$ [177]. Satisfying this condition is possible when arranging Eqn. (11.4) such that:

$$\Omega_1 c_b = -\Omega_2 c_a e^{i(\delta_a t - \delta_b t - \eta)}, \tag{11.7}$$

where $\delta_a = (\omega_{ac} - \omega_2)$ and $\delta_b = (\omega_{bc} - \omega_1)$.

The non interacting state can be calculated at the point of the two-photon resonance, $\delta_a = \delta_b = 0$, by setting $\Omega_1 c_b = -\Omega_2 c_a e^{-i\eta}$ in Eqn. (11.1) to describe a superposition state that is decoupled from the excited state:

$$|Dark\rangle = \frac{1}{\sqrt{\Omega_1^2 + \Omega_2^2}} (\Omega_2 e^{-i\omega_b t} |b\rangle - \Omega_1 e^{-i\omega_a t - i\eta} |a\rangle), \tag{11.8}$$

where $\eta = 2\pi n$, and n is an integer for a fixed relative phase between $\vec{E}_1(t)$ and $\vec{E}_2(t)$.

This dark state formalism allows us to understand the atomic interaction with the coupling optical fields. The atoms are initially equally distributed amongst the ground states $|a\rangle$ and $|b\rangle$, where the optical fields permit excitation to $|c\rangle$. Once in the excited $|c\rangle$ state the atom can spontaneously decay

into either the dark state, or its orthogonal bright state. However, since the bright state is interacting with the optical field, the atoms will continue to be optically pumped until all atoms have spontaneously decayed into the dark state, and steady state is achieved. When the atoms decay to the dark state they are no longer interacting with the addressing fields and the population is 'trapped' for as long as the dark state exists. The dark state will exist during optical pumping as long as the relative phase of the optical fields, η, is maintained, otherwise the optical phase change will empty the dark state to a bright state. The CPT feature measured experimentally is ultimately limited by the inverse of this dark state lifetime.

The $\sigma\sigma$ configuration was employed within the GMOT, using a single D_1 ECDL and EOM, with a circularly polarised output, similar to Sect. [10.1]. Alignment of the optical field to the atomic ensemble was optimised phenomenologically by maximising the single pass absorption, measured via
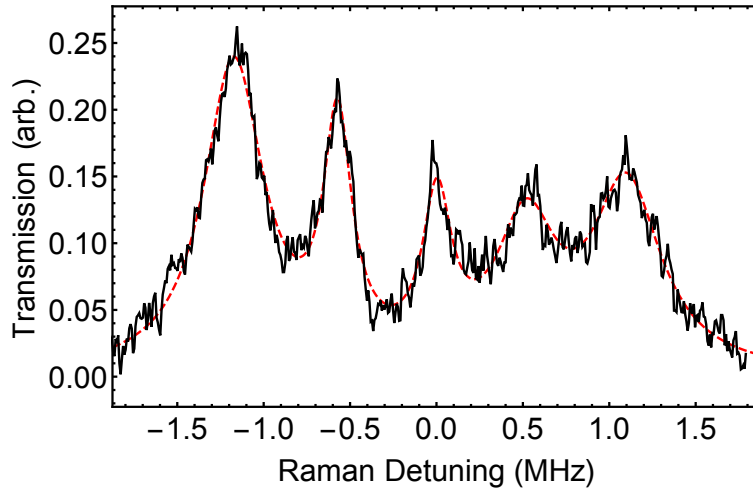
Figure 11.2: Experimentally measured cold-atom CPT transmission through the atomic medium as a function of Raman detuning, revealing five peaks relating to a dark state formation at the relative two-photon detuning of each possible dark state between the ground state manifolds using circularly polarised light. This effect noticeably favours populating the stretched state, indicated by the increased amplitude of population in this state. The dashed red line corresponds to the sum of the five best fitting individual Lorentzian profiles, plus a quadratic background to aid fitting.

transmission to a photodiode, whilst adjusting the incident beam position and angle. Using cooling methods previously discussed, 10^7 ^{85}Rb atoms were cooled to sub-Doppler temperatures for probing. ^{85}Rb was used at this point due to the lack of available RF electronics at the required ground-state splitting of 6.8 GHz for ^{87}Rb. During ballistic expansion, a small magnetic field remained on parallel to the probe beam. The probe beam was triggered to modulate the EOM sideband over a 4 MHz range with a triangle wave at a duty cycle of 500 Hz, revealing the transmission depicted in Fig. 11.2. Following the discussion in Ref. [172], Fig. 11.2 iterates that the circularly polarised light optically pumps atoms to sample each m_F level towards the stretched state, where population and transmission are maximised. The circular light method is therefore a non-ideal candidate for achieving the highest contrast in the desired $m_F = 0$ level.

11.3   Lin ∥ Lin

This scheme, illustrated in Fig. 11.1 (b), couples the $|a, m_F = \pm 1\rangle \rightarrow |b, m_F = \mp 1\rangle$ states via an excited $|c, m_F = 0\rangle$ state. When the electric field is resonant with the excited state transition and the Raman detuning is equal to the hyper-fine splitting of the ground state, the two-photon resonance induces two dark states between the ground state manifolds. The coupling between the ground state m_F levels occurs for both optical fields being on resonance, due to the Zeeman shifts being equal and opposite for the ground state manifolds for small magnetic fields.

The experimental setup constructed for this scheme, Fig. 11.3, uses a single ECDL coupled with an EOM to generate phase stable optical fields of the same polarisation. An AOM was used to switch the light before being fibre coupled and aligned with the MOT.
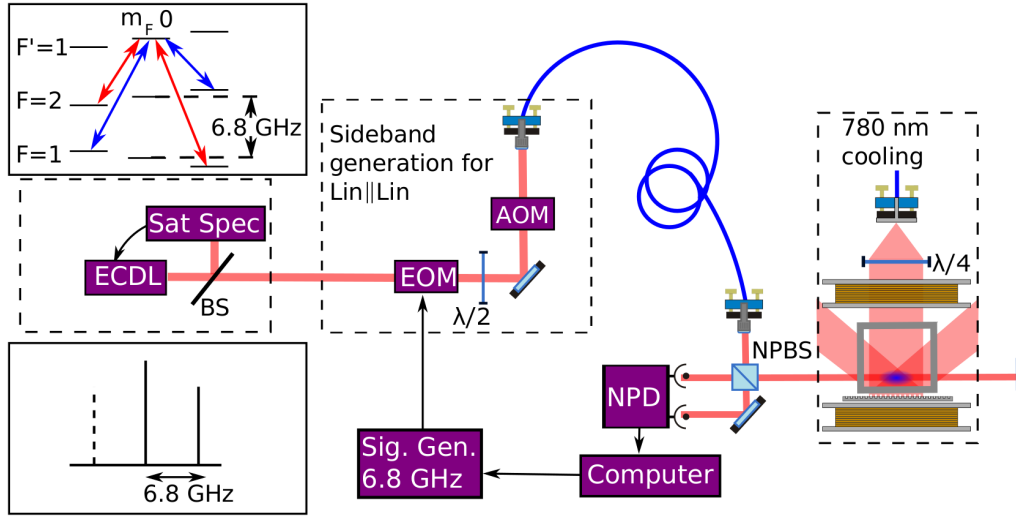
Figure 11.3: Experimental set-up for the Lin∥Lin CPT interrogation of the $F' = 1, 2$ excited states. AOM: Acousto-optical modulator. EOM: Electro-optical modulator. ECDL: External-cavity-diode-laser at 795 nm. NPBS: Non-polarising beam splitter. NPD: Normalising photodiode. Insets illustrate the total angular momentum configuration for ^{87}Rb, probed by two electric fields separated by 6.8 GHz and π out of phase. The 780 nm cooling light is provided from the set-up illustrated in Fig. 7.1

When the carrier is locked to drive the $F = 2$ level to the excited $F' = 1$ state, the conditions are satisfied to induce cyclic transitions for maximum contrast of the clock states. Fig. 11.4 (a) illustrates that when the field is non-zero and lifts the Zeeman degeneracy, the largest amplitude is observed for the $m_F = 0$ transition. The magnetic sensitivity of the $m_F = \pm 1$ states was again exploited for magnetic sensing along the axis of $\mathbf{B}_{\parallel}$ in the cold atoms. The frequency shifts, measured relative to the transition frequency of the ground state $m_F = 0$ CPT feature, are given in Fig. 11.4 (b), with the resolution limited by the linewidth of the sub-level dark states, which are sensitive to power and transit-time broadening mechanisms. The magnetic sensing demonstrates a noise-floor measured between the $m_F = \pm 1$ and the $m_F = 0$ down to the same level as the previous Larmor precession study of $\simeq 800$ nT.
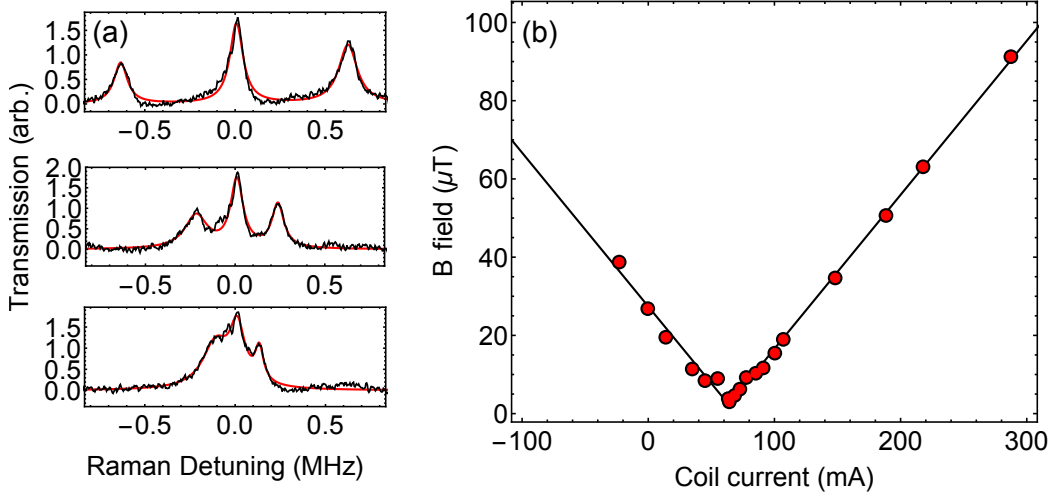
Figure 11.4: Experimentally measured Lin‖Lin CPT as a function of the Raman detuning for different values of the applied magnetic field. (a): The scanned transmission from the probe for three distinct applied magnetic fields is depicted with a black line, with a best fitting red line for parameter characterisation. (b): The measured magnetic field, determined from the resonance frequency of the $m_F = \pm 1$, as a function of applied coil current. The induced frequency shift is then converted to a measured static magnetic field using the Landé-g value.

11.4   Lin ⊥ Lin

For the case of Lin⊥Lin CPT interactions, the probing electric fields are both propagating along the z axis, with a small magnetic field to separate the linear components of the electric fields into a circular basis. The interaction hamiltonians for the system are therefore,

$$H_i = H_1 + H_2 = -\vec{d} \cdot \vec{E}(t) = -\vec{d} \cdot (\vec{E}_1 + \vec{E}_2) = 0, \qquad (11.9)$$

where $\vec{d}$ is the electric dipole, H_1 and H_2 are the interaction Hamiltonians for electric fields [41],

$$
\begin{aligned}
\vec{E}_1(t) &= \frac{\vec{E}_1}{2}(e^{-i\omega_1 t} + e^{i\omega_1 t})e_x \\
&= \frac{\vec{E}_1}{2\sqrt{2}}(e^{-i\omega_1 t} + e^{i\omega_1 t})(e_- - e_+),
\end{aligned}
\tag{11.10}
$$

$$
\begin{aligned}
\vec{E}_2(t) &= \frac{\vec{E}_2}{2}(e^{-i(\omega_2 t - \eta)} + e^{i(\omega_2 t - \eta)})(\cos(\theta)e_x + \sin(\theta)e_y) \\
&= \frac{\vec{E}_2}{2\sqrt{2}}(e^{-i(\omega_2 t - \eta)} + e^{i(\omega_2 t - \eta)})(e^{i\theta}e_- - e^{-i\theta}e_+),
\end{aligned}
\tag{11.11}
$$

where $e_\pm = \mp \frac{(e_x \pm i e_y)}{\sqrt{2}}$, and θ is the rotation of the polarisation axis of $E_2(t)$ with respect to $E_1(t)$.

Hence, substituting Eqns. (11.10), (11.11) into Eqn. (11.9) results in,

$$
H_1 = -\vec{d} \cdot \vec{E}_1(t) = \frac{\vec{E}_1}{2\sqrt{2}}(e^{-i\omega_1 t} + e^{i\omega_1 t})(d_+ - d_-),
\tag{11.12}
$$

$$
H_2 = -\vec{d} \cdot \vec{E}_2(t) = \frac{\vec{E}_2}{2\sqrt{2}}(e^{-i(\omega_2 t - \eta)} + e^{i(\omega_2 t - \eta)})(e^{-i\theta}d_+ - e^{i\theta}d_-),
\tag{11.13}
$$

where $d_\pm = \mp(d_x \pm i d_y)/\sqrt{2}$ accounts for the circular components of the linearly polarised light, described with the Clebsch-Gordan coefficients, $\langle i|d|j \rangle = C_{ij}d$.

The decomposition of the linear light into circular components, allows us to see that the $|a\rangle$ and $|b\rangle$ ground states are coupled via the $|c\rangle$ and $|d\rangle$ manifolds of the excited state to form two separate Λ configurations, as illustrated in Fig. 11.1 (c). If the systems separate evolution is transformed into a rotating frame, as introduced in Sect. [2.1], the interaction hamiltonian has been

shown to be [41],

$$\tilde{H}_1 = \frac{d\vec{E}_1}{2\sqrt{2}}(c_{da}|d\rangle\langle a| - c_{ca}|c\rangle\langle a| + c_{da}|a\rangle\langle d| - c_{ca}|a\rangle\langle c|), \tag{11.14}$$

$$\tilde{H}_2 = \frac{d\vec{E}_2}{2\sqrt{2}}(e^{i(\eta-\theta)}c_{db}|d\rangle\langle b| - e^{i(\eta+\theta)}c_{cb}|c\rangle\langle b| + e^{-i(\eta-\theta)}c_{db}|b\rangle\langle d|$$
$$- e^{-i(\eta+\theta)}c_{cb}|b\rangle\langle c|). \tag{11.15}$$

Achieving a high contrast clock CPT feature requires simultaneous dark state formation from both Λ configurations addressed, where the each dark state is a superposition of both ground states $|Dark\rangle = m|a\rangle + n|b\rangle$, such that,

$$\tilde{H}_i|Dark\rangle = \frac{d}{2\sqrt{2}}\left[\vec{E}_2n\left(e^{i(\eta-\theta)}c_{db}|d\rangle - e^{i(\eta+\theta)}c_{cb}|c\rangle\right) + \vec{E}_1m\left(c_{da}|d\rangle - c_{ca}|c\rangle\right)\right]. \tag{11.16}$$

Separation of Eqn. (11.16) into its constituent parts provides the dark state of each Λ configurations as,

$$|Dark\rangle_c = -\frac{d}{2\sqrt{2}}\left[\vec{E}_2ne^{i(\eta+\theta)}c_{cb} + \vec{E}_1mc_{ca}\right], \tag{11.17}$$

$$|Dark\rangle_d = \frac{d}{2\sqrt{2}}\left[\vec{E}_2ne^{i(\eta-\theta)}c_{db} + \vec{E}_1mc_{da}\right], \tag{11.18}$$

where the notation $|Dark\rangle_c$ and $|Dark\rangle_d$ refer to the dark states occurring for the Λ configurations coupled to the excited $|c\rangle$ and $|d\rangle$ states respectively.

If we rearrange the darks states to solve for values of m and n that satisfy a common dark state, we find,

$$e^{i2\theta} = \frac{c_{db}}{c_{da}}\frac{c_{ca}}{c_{cb}}. \tag{11.19}$$

In the case of probing on the ^{87}Rb D_1 line, the ground state is composed of two total angular momentum manifolds of $|F = 1, 2, m_F = 0\rangle$ connected via an excited $|F' = 1, m_F = \pm1\rangle$. The Clebsch-Gordan coefficients for these

real transitions are $c_{ca} = c_{cb} = c_{da} = -c_{db}$, such that their magnitudes define their relative superposition states as,

$$|Dark\rangle_c = \frac{1}{\sqrt{E_1^2 + E_2^2}}\big(E_2|1\rangle - E_1 e^{-i(\eta+\theta)}|2\rangle\big), \tag{11.20}$$

$$|Dark\rangle_d = \frac{1}{\sqrt{E_1^2 + E_2^2}}\big(E_2|1\rangle + E_1 e^{-i(\eta-\theta)}|2\rangle\big). \tag{11.21}$$

If we assume again that $\eta = 2\pi n$, and $E_1 = E_2$, we realise when $\theta = 0$ a bright state occurs for $|d\rangle$ whilst a simultaneous dark state is generated for $|c\rangle$. A common dark state can only be satisfied with the rotation of relative electric field polarisation by $\theta = \pi/2$. This gives rise to the method being described as Lin⊥Lin coherent population trapping.

Experimentally achieving a polarisation rotation between two phase stable electric fields required a new method of probing, illustrated in Fig. 11.5. The
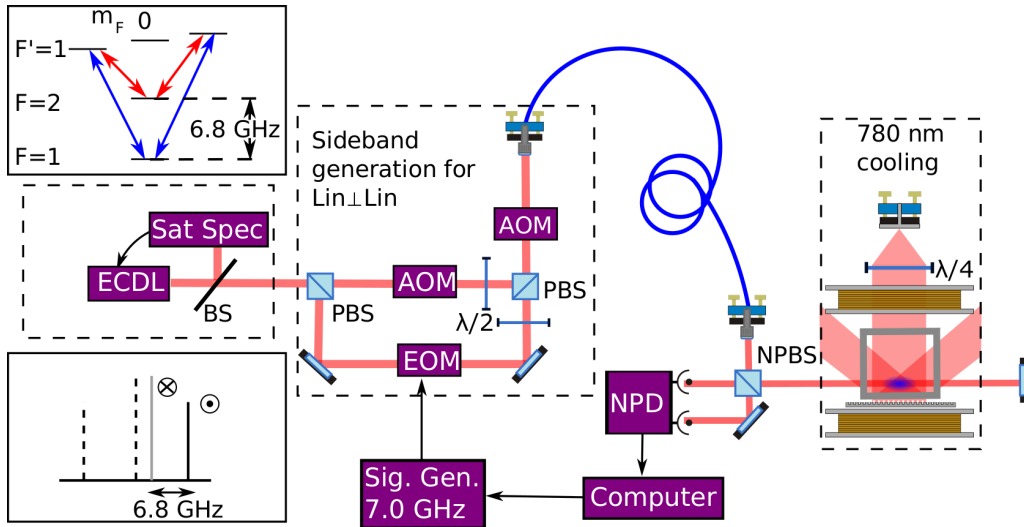
Figure 11.5:   Experimental set-up for achieving Lin⊥Lin CPT. AOM: Acousto-optical modulator.   EOM: Electro-optical modulator.   ECDL: External-cavity-diode-laser at 795 nm. NPBS: Non-polarising beam splitter. NPD: Normalising photodiode. The upper inset depicts the total angular momentum configuration used in this regime. The lower inset illustrates the amplitude of the probing electric fields as a function of their relative frequency difference and polarisations at the atoms, were black lines pass through the EOM and the grey line through the first AOM.

ECDL is spectroscopically locked with a frequency offset of 400 MHz relative to resonance with the $F = 2 \rightarrow F' = 1$ transition. The output beam is split on a PBS, with equal amounts in each arm; referred to from here as the carrier and sideband arms. The sideband arm is coupled to the EOM, adding sidebands at +200 MHz to the off-resonant carrier. The carrier arm uses an AOM to decrease the frequency offset to 200 MHz from resonance, before combining with the orthogonally polarised sideband arm on a PBS. Both beams were aligned through a final switching AOM to bring the carrier arm resonant with the $F = 2 \rightarrow F' = 1$ transition and one sideband to the $F = 1 \rightarrow F' = 1$ transition, as illustrated in Fig. 11.5. The other sideband and off-resonant carrier are still present, but for a cold atom sample with no Doppler broadening, there were no measured shifts to the central clock feature.

The CPT data in Fig. 11.6 were taken using a pulsed Raman detuning sequence for individual MOTs as opposed to the frequency sweep through the single MOT. This means the laser-cooled atoms were interrogated with a single Raman detuning for each clock cycle iteration (capture, cooling, measurement), whilst monitoring the probe transmission through the atomic
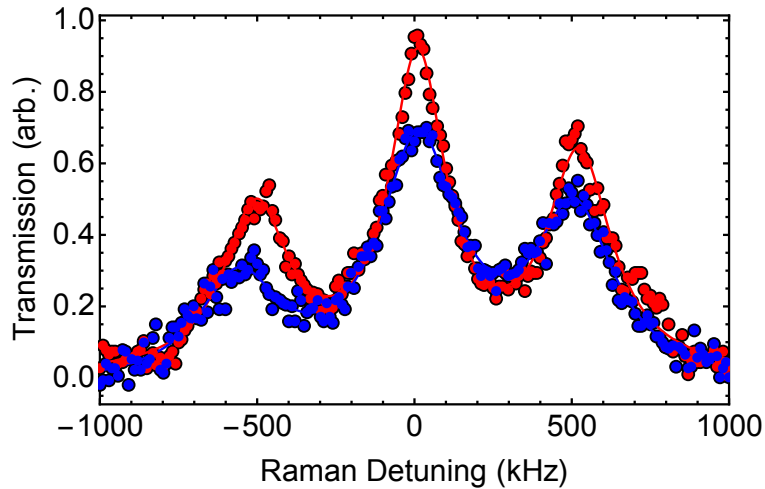
Figure 11.6: Experimentally measured Lin⊥Lin CPT transmission for coupling to excited states $F' = 1, 2$ (red, blue) as a function of Raman detuning.

medium. The total procedure is repeated to build up an averaged amplitude for each Raman detuning, the results of which are plotted for both excited states of the D_1 transitions. The Lin⊥Lin scheme's ability to produce a population cycling around the clock transition is shown by a 70 % contrast for the $F' = 1$ state, compared to a 51 % when driving to $F' = 2$. Both contrasts are defined by the method illustrated in Fig. 10.5 (b). The use of a pulsed CPT readout provides the ability to convert coherent population trapping into a Raman-Ramsey regime with relative ease, as discussed in the next chapter.

Chapter 12

A compact cold-atom clock based on Lin ⊥ Lin Raman-Ramsey interrogation

An increased timing precision is actively sought after in commercial applications of navigation, telecommunication, manufacturing and cyber security [178]. This pursuit has lead to profound advancements in the capabilities and scale of miniaturised atomic clocks, which utilise spectroscopic techniques to derive an atomic ground-state splitting. One such spectroscopic technique is coherent population trapping, with its reduced optical footprint providing a compact alternative to microwave cavities [38, 171, 179]. However, previously discussed thermal clock studies with coherent population trapping have demonstrated a critical compromise between achievable resonance linewidth and signal amplitude, as highlighted in Sect. [10.3.2].

The limitations of CW CPT interrogation can be overcome by implementing the separated oscillating field method, proposed by N. F. Ramsey in 1950 [11]. The Ramsey technique adopts two $\pi/2$ pulses of length τ and separated by a time T to generate a series of narrow frequency fringes with a spacing

determined only by the pulse separation $1/2T$. Due to this revolution in atomic metrology, Ramsey was awarded the Nobel prize in physics in 1989 [12]. The method discussed in this chapter is analogous to the Ramsey style experiment, where the first pulse drives the atoms into a superposition of the ground states using coherent population trapping, opposed to a standard $\pi/2$ pulse. Following the first pulse, the phase of the dark state evolves freely unperturbed for a duration, T. Finally, the second coherent population trapping pulse translates the phase of the dark state, relative to the optical phase, into atomic absorption. The transmission of the optical field is then measured as a function of the Raman detuning, to reveal Ramsey fringes with a linewidth $\Delta f = 1/(2T)$.

12.1   Ramsey's separated oscillating field method

The theory of Ramsey's separated oscillating field method makes use of a simple two-level system, where the general expression of the state can be described as,

$$|\Psi(t)\rangle = c_g(t)|g\rangle + c_e(t)|e\rangle = \begin{pmatrix} c_g(t) \\ c_e(t) \end{pmatrix}. \qquad (12.1)$$

The expansion of this two-level system has been derived in Sect. [2.1], where the Hamiltonian in a rotating frame is described as,

$$H_R = \frac{\hbar}{2} \begin{pmatrix} \delta & \Omega e^{-i\phi} \\ \Omega e^{i\phi} & -\delta \end{pmatrix} \qquad (12.2)$$

where ϕ is the phase of the electric field, and subscript R is to denote the introduction of the rotation operator described in Ref. [180],

$$R = \begin{pmatrix} e^{i\delta t/2} & 0 \\ 0 & e^{-i\delta t/2} \end{pmatrix}. \qquad (12.3)$$

The system described in Eqn. (12.2) uses this frame to derive the eigenvalues of the matrix $\lambda_\pm = \pm\frac{\hbar\Omega_r}{2}$, where $\Omega_r = \sqrt{\Omega^2 + \delta^2}$ is the off-resonant Rabi frequency. For simplicity, I refer to the eigenvectors of this matrix as they are defined by Cohen-Tannoudji *et al.* in Ref. [181],

$$|\lambda_+\rangle = \cos\left(\frac{\theta}{2}\right)|e\rangle_R e^{-i\phi/2} + \sin\left(\frac{\theta}{2}\right)|g\rangle_R e^{i\phi/2}, \tag{12.4}$$

$$|\lambda_-\rangle = -\sin\left(\frac{\theta}{2}\right)|e\rangle_R e^{-i\phi/2} + \cos\left(\frac{\theta}{2}\right)|g\rangle_R e^{i\phi/2}, \tag{12.5}$$

where $\sin\theta = \Omega/\Omega_r$ and $\cos\theta = -\delta/\Omega_r$ with $0 \leq \theta \leq \pi$.

To describe a system with an initial state $|\Psi(t_0)\rangle$ in a time-independent evolution, the initial state must also be transformed to the rotating frame using Eqn. (12.3). The wavefunction in the rotating frame is described,

$$|\Psi(t_0)\rangle_R = c_g(t_0)e^{\delta t_0/2}|g\rangle + c_e(t_0)e^{-\delta t_0/2}|e\rangle = c_g(t_0)|g\rangle_R + c_e(t_0)|e\rangle_R \tag{12.6}$$

The system dynamics during a pulse of oscillating field, τ, evolve according to the Eqn. (12.2), with application of the time-evolution operator $U(t_0, \tau)$:

$$|\Psi(t_0 + \tau)\rangle_R = U(t_0, \tau)|\Psi(t_0)\rangle_R, \tag{12.7}$$

where the projection of the evolution operator onto the two eigenvector basis gives [182]

$$U(t_0, \tau) = e^{-iH_R(\tau-t_0)/\hbar} = e^{-iH_R(\tau-t_0)/\hbar}(|\lambda_+\rangle\langle\lambda_+| + |\lambda_-\rangle\langle\lambda_-|) \tag{12.8}$$

$$= e^{i\lambda_+(\tau-t_0)/\hbar}|\lambda_+\rangle\langle\lambda_+| + e^{i\lambda_-(\tau-t_0)/\hbar}|\lambda_-\rangle\langle\lambda_-|. \tag{12.9}$$

Finally, we can use the rotation operator, $R(t_0 + \tau)$, to convert back to the original basis of $|g\rangle, |e\rangle$ by using the description,

$$|\Psi(t_0 + \tau)\rangle = R(t_0 + \tau)|\Psi(t_0 + \tau)\rangle_R \qquad (12.10)$$

Using Eqn. (12.10), converts back to the original basis, where the excited state amplitude after interaction with the laser field for a time, τ, is [183]

$$c_e(t_0 + \tau) = e^{-i\delta\tau/2}\Big(c_e(t_0)\Big[\cos\Big(\frac{\Omega_r\tau}{2}\Big) - i\cos\theta\sin\Big(\frac{\Omega_r\tau}{2}\Big)\Big]$$
$$+ c_g(t_0)e^{-i(\delta t_0+\phi)}\Big[-i\sin\theta\sin\Big(\frac{\Omega_r\tau}{2}\Big)\Big]\Big), \quad (12.11)$$

$$c_g(t_0 + \tau) = e^{i\delta\tau/2}\Big(c_e(t_0)e^{i(\delta t_0+\phi)}\Big[-i\sin\theta\sin\Big(\frac{\Omega_r\tau}{2}\Big)\Big]$$
$$+ c_g(t_0)\Big[\cos\Big(\frac{\Omega_r\tau}{2}\Big) + i\cos\theta\sin\Big(\frac{\Omega_r\tau}{2}\Big)\Big]\Big). \quad (12.12)$$

If we consider the pulse of length τ, defined as $\Omega_r\tau = \pi/2$, to be interacting with the two-level atom initially populating the ground-state, such that $c_e(0) = 0, c_g(0) = 1$, then Eqns. (12.11), (12.12) result in the probability amplitudes,

$$c_e(\tau) = e^{-i\delta\tau/2}e^{-i\phi}(-i\sin\theta/\sqrt{2}) \qquad (12.13)$$

$$c_g(\tau) = e^{i\delta\tau/2}(1 + i\cos\theta/\sqrt{2}). \qquad (12.14)$$

Using the separated oscillatory fields technique [11], the first pulse is followed by a period of free state evolution, T, before a second identical pulse is applied. After this sequence, the system dynamics have been calculated calculated using Eqns. (12.11), (12.12) to describe the final excited state
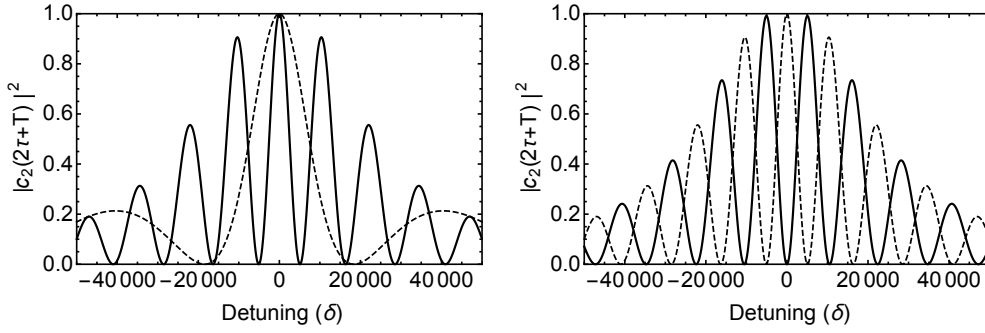
Figure 12.1: Ramsey fringes determined from Eqn. 12.16. (a): Excited state population as a function of detuning for different pulse separation T. τ=100 μs and T=(500, 100) μs with solid and dashed line respectively. (b): Excited state population as a function of detuning for relative phase differences between pulse one and two. τ=100 μs and T=500 μs with $\phi = \pi, 0$ for the solid and dashed line respectively.

population as [183],

$$c_e(2\tau + T) = e^{-i\delta\tau/2}\Big(c_e(\tau)(1 - i\cos\theta) + c_g(\tau)e^{-i(\delta\tau+\delta T+\phi)}(-i\sin\theta) \Big)/\sqrt{2},$$

$$(12.15)$$

such that the probability of the atom being in the excited state after this sequence is,

$$|c_e(2\tau + T)|^2 = \sin^2\theta\left[\cos\left(\frac{\delta T - \phi}{2}\right) + \cos\theta\sin\left(\frac{\delta T - \phi}{2}\right)\right]^2. \qquad (12.16)$$

In the case of probing with near resonant light, $|\delta| \ll \Omega_{eg}$, then $\cos\theta \simeq 0$, $\sin\theta \simeq 1$ and the excited state population is described as [183]

$$|c_e(2\tau + T)|^2 \simeq \frac{1}{2}[1 + \cos(\delta T - \phi)]. \qquad (12.17)$$

This final excited state population depicts an oscillation period directly related to the free evolution time, T, through the relation $f = 1/T$, as illustrated in Fig. 12.1 (a) for $T = (500, 100)$ μs in solid and dashed lines respectively. The critical aspect of the relative phase between the pulses is highlighted in Fig. 12.1 (b), where the final excited state population is tracked for $\phi = (\pi, 0)$ in solid and dashed lines, demonstrating that when the

second pulse is π out of the phase the no atoms are optically pumped to the excited state. Hence, for a maximum state population at $\delta = 0$ both pulse require phase stability over the pulse separation period T.

12.2 Experimental realisation

The first experimental observations of Ramsey fringes within a CPT resonance were noted by J. E. Thomas *et al.*, with a central fringe spacing of 650 Hz being recognised for its potential application to frequency standards [184]. The high contrast superposition states, discussed in Chapter. [11], have since led to numerous atomic clock developments based on a Raman-Ramsey interrogation [38, 171, 175, 185–187]. To exploit this technique for the grating magneto-optical trap, a high contrast coherent population trapping signal is first required for efficient preparation of the dark state. Due to the lack of Mu-metal shielding and the magnetic sensitivity for the Lin$\|$Lin discussed in Ref. [188], the experiment was taken forward using the Lin$\perp$Lin set-up discussed in Sec. [11.4].

Similarly to the pulsed CPT data, the MOT would be loaded with 2×10^7 atoms that were cooled to ≈ 20 μK. Following the cold-atom preparation, the cooling light was extinguished with an AOM and mechanical shutters to ensure that no light leakage could pollute the dark state pumping. After a 1 ms period to ensure complete closure of the shutters, the CPT pump was applied for $\tau_1 = 500$ μs to optically pump into the dark state. Following the pumping time, the phase of the dark state was free to evolve for a time T before applying the second pulse, $\tau_2 = 10\mu$s, to measure the relative phase accumulation between the Raman beams and the dark state.

The transmission of the both Raman-Ramsey pulses were measured through an NPBS via a Newport Nirvana normalisation photodiode unit (2013
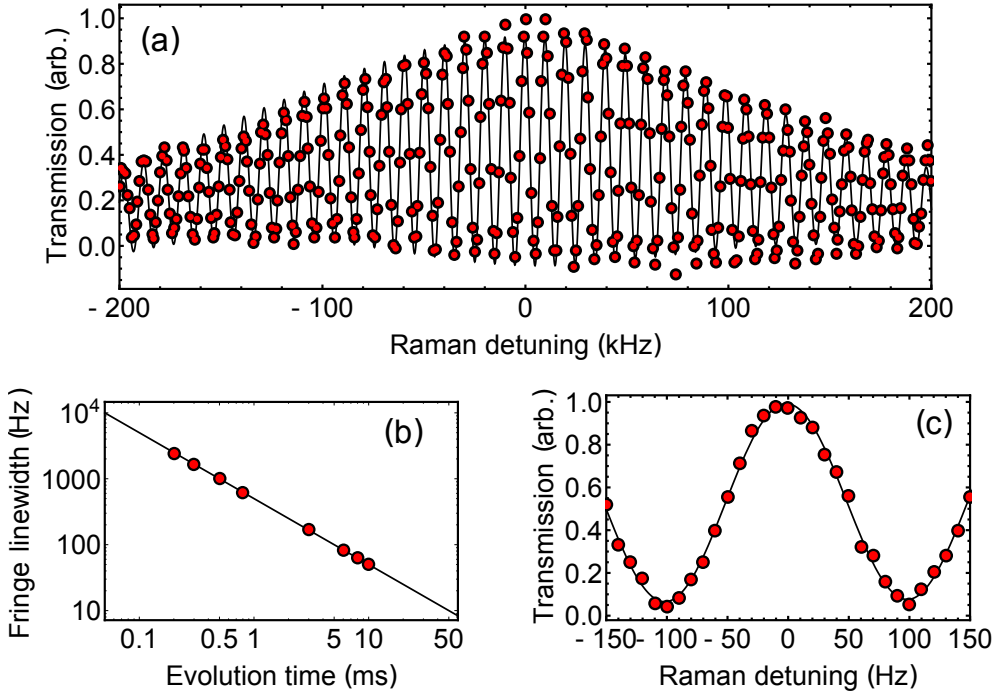
Figure 12.2: (a): Experimentally measured Raman-Ramsey fringes. Transmission for the second pulse through the atomic ensemble was measured as a function of the Raman detuning. (b): Measured Raman-Ramsey line-width as a function of the evolution time of the dark state, T. Black line is the expected $1/2T$ relation. (c): Central Raman-Ramsey fringe measured for T=5 ms

model). The transmitted signal was read through the DAQ card for amalgamation in LabView, to produce the data seen in Fig. 12.2 (a). The measured fringe envelope is comparable to the CPT absorption induced by τ_1. Following the first pulse, the phase of the prepared state was left to evolve for a variable time T, which determined the fringe period through the relation of $f = 1/2T$. Fig. 12.2 (b) demonstrates this relation experimentally with measured data fit to the linewidth predicted from this relation. The measured period was determined from a sine fit to the central fringes, as depicted in Fig. 12.2 (c). The total procedural time for the MOT load, cooling and clock probing of the atomic sample is cycled with a time of $\approx$200 μs between consecutive data points.

12.3 Noise reduction

Defining the performance of an atomic clock requires calculation of the achievable accuracy and precision in the system. In the case of the Raman-Ramsey fringes, the precision is indicative of the measured reproducibility of the central fringe, such that noise reduction is crucial for a high performance clock.

Signal-to-noise

For the collection of larger data sets, a cycle average was implemented within the LabView control to average out the random fluctuations in the measurements. A fringe cycle would consist of one measurement per Raman detuning, such that the averaging process was less sensitive to longer timescale drifts.

To measure the noise reduction of the averaging process, the signal-to-noise of the central fringe was measured as a function of the number of cycle averages, as illustrated in Fig. 12.3. For this measurement the signal-to-noise was defined as the central fringe peak-to-peak amplitude divided by the average error bar amplitude across the central fringe. These error bars were calculated from the standard error of the mean, [189],

$$\sigma_{error} = \frac{\sigma_{N-1}}{\sqrt{N}} \qquad (12.18)$$

where σ_{N-1} is the standard deviation for a data set containing N values.

Eqn. (12.18) defines the error associated with the determined mean, such that a larger number of averages provides a better definition of the mean with a square root dependence on N. It is because of the $\sqrt{N}$ scaling that the S/N in Fig. 12.3 tends to a particular value with the number of averages, as opposed to the constant increase of a standard deviation.
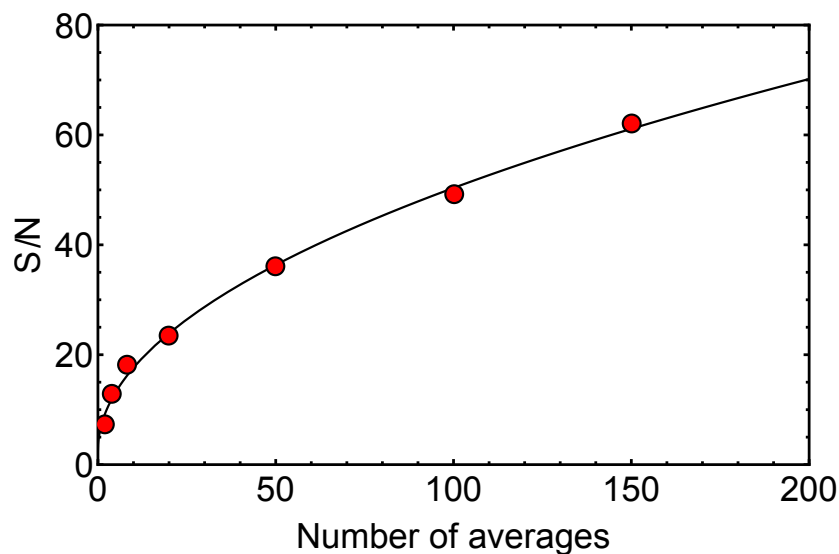
Figure 12.3: Signal-to-noise of the central Raman-Ramsey fringe as a function of the number of cycle averages. The black line is the best fitting with a square-root dependence.

Pulse normalisation

During the course of the Raman-Ramsey study, the detection photodiode was varied in an attempt to find the best bandwidth and gain for a pulsed signal, resulting in the Newport Nirvana being replaced by a ThorLabs (PDB210A) subtraction unit. The reference beam on the subtraction unit was derived from an NPBS before the light interacted with the atoms, and power set by a neutral density filter wheel. Although the subtraction photodiode would allow common mode noise cancellation in optical fluctuations, the main source of noise reduction was a Raman-Ramsey pulse division for dark state normalisation. This technique uses the amplitudes of τ_2/τ_1 for an estimation of the number of atoms that have been driven into the dark state by τ_1 when assuming there is no noise introduced during the separation time T, as has been discussed in Ref. [175, 190].

When aided by proper subtraction of the reference signal, as illustrated in Fig. 11.5, the transmission of the optical pumping pulse would be directly

related to the number of atoms under interrogation, such that if no atoms were present the measured pulse voltage would have zero amplitude. Alternatively, if atoms were present, absorption would occur, such that the two arms of the photodiode will be uneven and voltage amplitude measured. In the following analysis this well subtracted voltage, corresponding to the absorption, will be referred to as amplitude. However, in the case of polarisation fluctuations that are still detected by the NPBS, this subtracted level can fluctuate, resulting in a measured DC value when there are no atoms. In the following analysis, the DC voltage measured is referred to as the total amplitude.

The data provided in Fig. 12.4 (a) and (b) tracks these pulse amplitudes against the intensity of τ_1. Despite both data sets illustrating a linear dependence with the pump intensity, (a) is dominated by the DC level of the intensity, whereas the well nulled pulse in (b) has already subtracted the DC term well enough to reveal a gradient change between the two probing regimes of low and intermediate intensity.

More importantly, for dark state normalisation a clear correlation should be depicted from the amplitude as a function of the number of atoms being probed. For this study, the atom number was measured by time-of-flight imaging for a specific intensity of cooling light, followed by a Ramsey interrogation at the central frequency to determine the atom number's effect on the pulse amplitudes. Due to the DC coupling, the total amplitude has a poor correlation to the initial atom number, opposed by (d) where a linear relation is measured only when measuring the DC subtracted amplitude. Due to the findings of this study, the transmission measured in τ_2 was divided by the amplitude discussed in Fig. 12.4 (d) of τ_1 for efficient normalisation of atom number fluctuations.
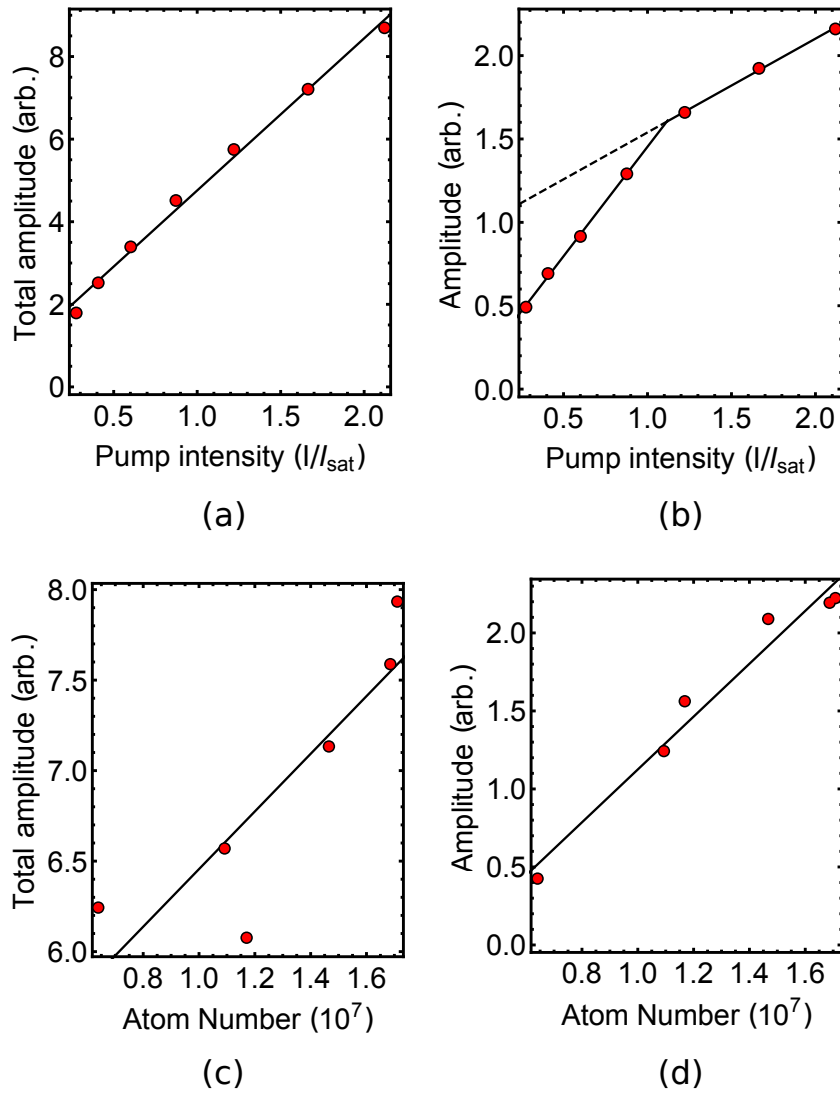
Figure 12.4: τ_1 amplitude analysis. (a)-(b): Amplitudes are given as a function of the pump intensity. (c)-(d): Amplitudes are given as a function of the atom number in the MOT.

12.4   Shift minimisation

The electro-optical modulator used to generate the probing optical fields is frequency referenced to a 10 MHz clock, such that any deviations in the relative optical field frequency are assumed to be induced by external perturbations to the atomic medium. Any perturbations to the measured clock frequency act to degrade the accuracy, hence significant effort is used when nulling the measured shift of the central Raman-Ramsey fringe with respect
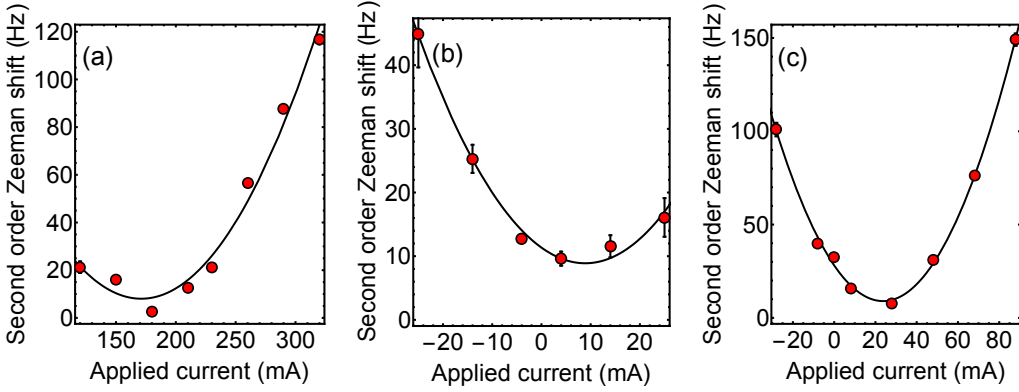
Figure 12.5: Second order Zeeman shift observed for the central peak of the Raman-Ramsey fringe as a function of the applied coil current in all three axes.

to a stabilised quartz oven reference oscillator (Keysight E8257D).

Although the dark state is a superposition of the $m_F = 0$ ground-states with a magnetic insensitivity to first order Zeeman shifts, a quadratic Zeeman shift perturbs the dark state. Derivation from the Breit-Rabi equation in Sec. 2.5.1 has been used to describe the magnetic sensitivity between $m_F = 0$ states as

$$\Delta\omega_{clock} = \frac{(g_J - g_I)^2 \mu_B^2}{2\hbar\Delta E_{hfs}} B^2, \tag{12.19}$$

where g_J, g_I are the Landé-g factors, μ_B is the Bohr magneton, E_{hfs} is the ground state splitting and B is the applied magnetic field [59].

This quadratic shift can be measured experimentally by applying a range of static magnetic field values on each axis, whilst tracking the position of the central Raman-Ramsey fringe in the frequency domain. This was employed for the GMOT using the Helmholtz shimming coils for each axis of confinement, the results of which are provided in Fig. 12.5. The frequency position and associated error were determined from a best fitting sin function to the central fringe of the collected data for the applied coil current. The fit results were plotted to reveal the quadratic shift induced on this transition,

permitting second order field nulling in each axis.

Calibrated shift

Nulling the static magnetic fields in all three axis is not possible due to the necessity of a non-degenerate ground-state to satisfy the double-Λ scheme. As a result of this, a small magnetic field was required to remain on $\mathbf{B}_\parallel$ to aid optical pumping and lift the degeneracy. Initial studies into the affect of the $\mathbf{B}_\parallel$ to the Raman-Ramsey fringe revealed a change in the central fringe amplitude for the two coil currents illustrated in Fig. 12.6 (a). With the clock predicted performance being strongly correlated to the fringe amplitude through the Allan variance, the $\mathbf{B}_\parallel$ value would ideally be optimised for the largest fringe amplitude, with the resulting second-order shift subtracted from the ground-state-splitting to centralise the fringe symmetrically at $\Delta = 0$, where $\Delta = 0$ is the unperturbed hyperfine splitting in the ground-state.

The measured fringe amplitude was determined from the best fitting theory lines depicted in red and black in Fig. 12.6 (a). The fringe amplitude was seen to initially increase as a function of applied current due to the small magnetic shift induced upon the states satisfying the double-Λ scheme. The increased magnetic field separates the $m_F = \pm 1$ states resonance frequency by enough to be individually addressed, whilst having a small enough shift from the laser detuning that they are still addressable by the optical fields and permit an efficient optical pumping of atoms into the dark state, Fig. 12.6 (c). From the lowest applied coil current to the largest signal demonstrated, a best fitting parabolic trend, expected from the quadratic shift Eqn. (12.19), leads to a fringe amplitude increase of $\approx \times 6$. This trend was only true for a small range of current values, after which the amplitude would reduce and plateaux at a non-zero value. Although the fringe amplitude characterised
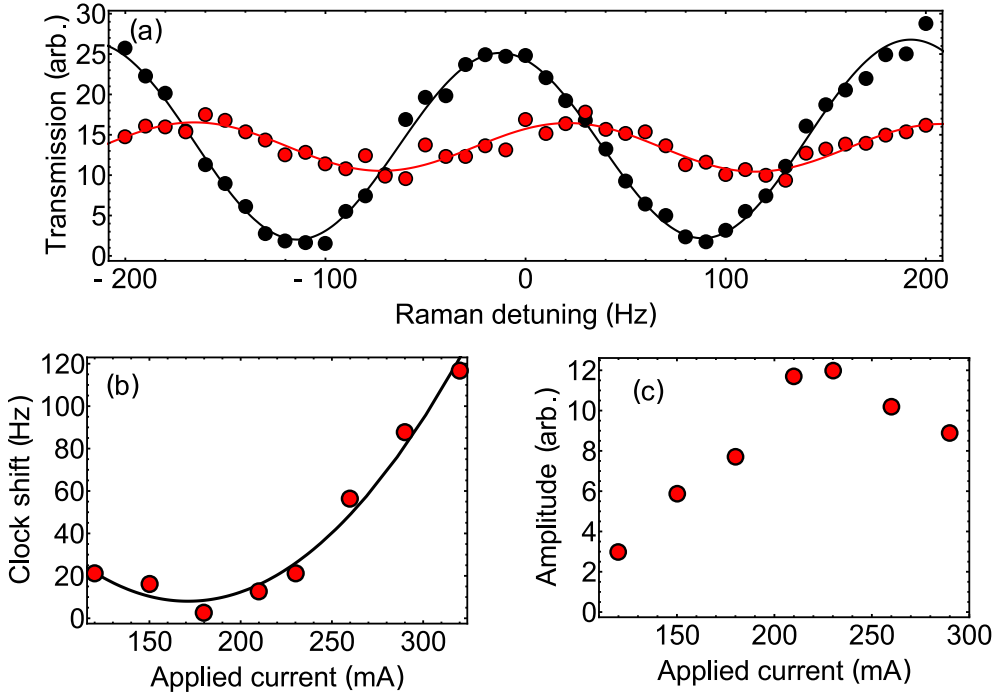
Figure 12.6: (a): The measured Raman-Ramsey transmission as a function of Raman detuning for two applied coil current values in $\mathbf{B}_{\parallel}$ of $(120, 210)$ mA, represented in red and black respectively. (b): The corresponding second order Zeeman shift measured for the $m_F = 0$ state as a function of the applied current in $\mathbf{B}_{\parallel}$. (c): The central fringe amplitude as a function of the same applied current points plotted in (b).

the defined optimum $\mathbf{B}_{\parallel}$ value, the applied field also induced a quadratic shift on the clock state, as discussed in Sec. [12.4]. Measuring the quadratic shift for the chosen $\mathbf{B}_{\parallel}$ in Fig. 12.6 (b), allowed the known shift to be accounted for in the applied ground-state-splitting, such that the central fringe will be again centred around $\Delta = 0$ Hz.

12.5   Allan variance

The Allan variance gained its name sake from its first proposal by D. W. Allan in Ref. [9], which later became the *'IEEE sub-committee on frequency stabilities'* recommended analysis for measurements in the frequency-domain [8]. Allan variance now dominates metrological measurements as the accepted analysis

for frequency stability. Much like a standard variance measurement, the Allan variance is a measure of the fractional frequency fluctuations. However, unlike the standard variance analysis, the Allan variance is convergent for most forms of divergent clock noise.

This analysis takes an array of dimensionless fractional frequencies, defined as

$$y(t) = \frac{f(t) - f_0}{f_{hfs}} = \frac{\Delta f(t)}{f_{hfs}}, \tag{12.20}$$

where $f(t)$ is the measured central fringe frequency at a given time, f_0 is the local oscillator defined $\Delta = 0$, such that Δf is the measured shift of the transition frequency, f_{hfs}.

The fractional frequency array can then be used to calculate the two standard methods of Allan variance, non-overlapping and overlapping, by averaging the fractional frequencies over an interval, τ. The non-overlapping was the originally proposed analysis, looking at the variance between adjacent values of $y(t)$ through the relation

$$\sigma_y^2(\tau)_{non} = \frac{1}{2(M-1)} \sum_{i=1}^{M-1} (y_{i+1} - y_i)^2, \tag{12.21}$$

where y_i and associated t_i are the ith values in a list of measured $y(t)$ that has M fractional frequency values that are averaged over an integration period of τ.

The non-overlapping Allan variance has now been largely superseded by the technique of overlapping samples. This method involves outlining all possible combinations of the data array to improve the confidence of the calculated stability. In the case of the overlapping method, the Allan variance is calcu-

lated as,

$$\sigma_y^2(\tau)_{overlap} = \frac{1}{2m^2(M - 2m + 1)} \sum_{j=1}^{(M-2m+1)} \sum_{i=j}^{(j+m-1)} (y_{i+m} - y_i)^2, \quad (12.22)$$

where m is an integer for the ratio of the sampling time, τ, to the experimental cycle time, τ_0, such that $\tau = m\tau_0$.

Both these methods converge the frequency noise, commonly associated with a harmonic oscillation, when plotted in a σ vs τ diagram [9]. The noise source can then be determined from the slope to reveal the power law decay function, such that:

- τ^{-1} - White phase noise and flicker phase noise

- $\tau^{-1/2}$ - White frequency noise

- τ^0 - Flicker frequency noise

- $\tau^{1/2}$ - Random walk of frequency

- τ^1 - Frequency drift

Performance of the unlocked clock

Typically for short-term instability performance, the clock does not require to be locked, i.e. include a steering or feedback mechanism to control drifts. Instead, in the sampling time where $\tau < 1000$ s, the clock drifts are minimal and there are no significant contributions to performance.

The analysis for the experimental Allan variance was again carried out in a custom built LabView code, which began by calibrating the change in photodiode voltage, Δv, to the frequency drift of the central fringe, f, through

the linear relation at the side of the fringe:

$$f = \frac{\Delta v}{4\pi v_0}\Delta f, \tag{12.23}$$

where v_0 is the central fringe amplitude and $\Delta f = 1/T$ is the width of the fringe. This linear relation can be used to calibrate the photodiode voltage to a frequency drift from data points taken from this region of the fringe.

This calibration required a short Raman-Ramsey cycle to determine the amplitude and width of the central fringe. These central fringe characteristics are used to calculate the calibration in Eqn. (12.23). Once a relationship between the recorded photodiode voltage and corresponding frequency is realised, consecutive shots are taken at $f = 0 \pm \frac{1}{4T}$ relative to the fringe centre, with the difference Δv now capable of tracking frequency and phase drifts whilst remaining insensitive to amplitude fluctuations. Finally, these Δv values are converted frequency shifts via Eqn. (12.23), which is then used to generate an array of fractional frequency fluctuations using Eqn. (12.20).

This array of $y(t)$ values for the measured Allan variance are plotted in Fig. 12.7 (a) as a function of their time in the measurement cycle. When used in conjunction with Eqn. (12.22) this array of $y(t)$ values produces the Allan variance depicted in Fig. 12.7 (b), where the data points for chosen sample times are presented in black, with dashed red lines depicting the clock noise spectrums. The best measured instability for this initial test revealed a relative instability of 2×10^{-11} at 100 s. After 100 s the frequency fluctuations are dominated by long-term instabilities that require feedback mechanisms to 'steer' the clock drifts, a capability that is not provided with an unlocked clock.
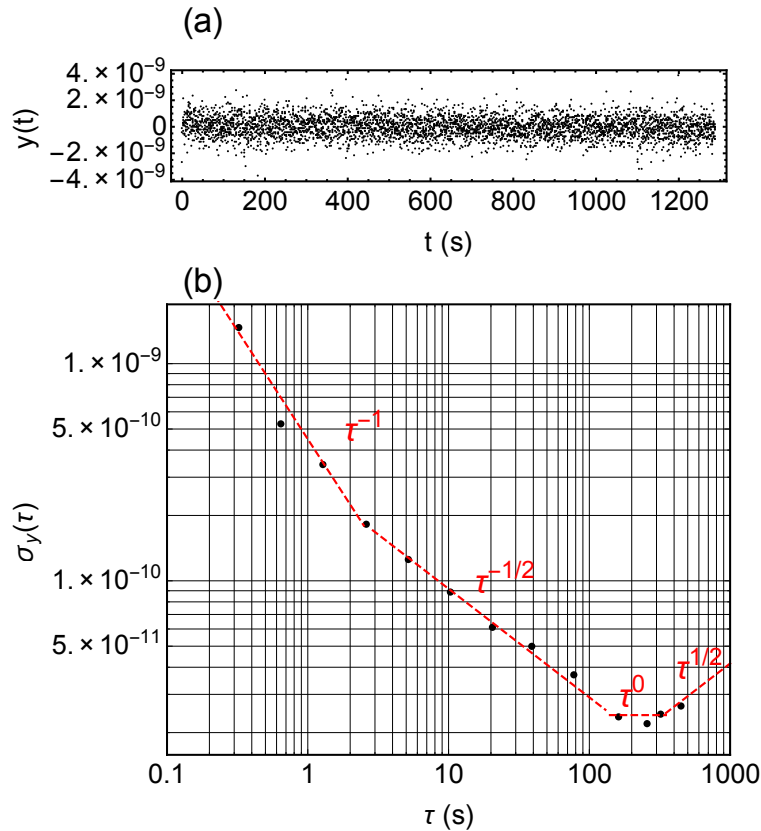
Figure 12.7: Experimentally measured array of y(t) values and their corresponding overlapping Allan deviation. Dashed red line highlights the clock noise domains.

12.6 Outlook

With an outlook to achieving a relative short-term frequency instability on the 10^{-14} level, the system noise and limitations require addressing. The most effective method to map out the relative noise contributors to the clock was to perform Allan variance measurements for the constituent components, such as the optical and electronic input. From early observations of these measurements we concluded that the atomic Allan variance was within one order of magnitude of the electronic noise ground floor, measured with no atomic or optical signal. Furthermore, the optical signal was found to fluctuate due to thermal fluctuations in the laboratory environment, mainly contributed by poor air conditioning. The dominant electronic noise contributions can

be circumvented by a thorough investigation of the detection electronics and digital card noise to determine the cause of the noise. Circumventing the addressed issues would ideally lead to the quantum projection noise limit,

$$\sigma_y(t) = \frac{1}{Q}\sqrt{\frac{T_c}{\tau}}\frac{1}{\sqrt{N}}, \tag{12.24}$$

where $Q = \frac{f_0}{\Delta f_a}$ is the quality factor, T_c is the experimental cycle time between measurements, N is the number of atoms, and τ is the interrogation period.

If we substitute numbers provided in this thesis, f_0=6.8 GHz, f_a=50 Hz, $N = 10^7$, and T_c=100 ms, then a short-term Allan variance of $\sigma_y(100s) = 7.4 \times 10^{-14}$ is realised. Although the current measured value is three orders of magnitude from this goal, the experimentally measured value is a proof-of-principle first measurement, where experimental noise sources require further addressing for continued progress.

Part V

Conclusions and Outlook

Chapter 13

Conclusion

In this thesis, diffractive optics have been utilised for the realisation of a micro-fabricated source of cold-atoms. A simple theory of diffraction efficiency was developed to enable a study of periodicity, wavelength and coatings. This provided valuable information for the characterisation and design of future grating chips that were to be coupled to a laser cooling apparatus. Further studies of the grating chips revealed critical parameters for experimental implementation and opened the door to the possibility of two-colour cooling of more exotic species, such as Sr, in this compact apparatus. Alternatively, two-colour cooling could be applied to Rb to produce visible emission from the MOT at 420 nm, discussed in Appendix A.

Once implemented, the grating chips were rigorously tested for optimum trapping and cooling capabilities. The cold-atom ensemble generated in our set-up produced an atom number and temperature comparable with the standard MOT, whilst significantly reducing the apparatus volume. This compact, cold-atom source was used to demonstrate the nulling of stray magnetic fields using Larmor precession for realisation of an ultra-cold temperature measurement. Furthermore, the checkerboard grating geometry allowed the production of a scalable macroscopic neutral atom array from a single inci-

dent laser.

The final and main study of this thesis was the proof-of-principle Raman-Ramsey based clock. This study spanned across a basic vapour cell coherent population trapping signal, to the implementation of a high contrast dark state in cold atoms. The simple set-up that was used for early coherent population trapping studies was superseded by a narrow Raman-Ramsey feature. The stability of the narrow fringes generated in the experiment was measured using the Allan variance to realise a first generation L/cm^3 scale clock apparatus, capable of measuring time to 1×10^{-11} at 100 s. This early measurement from the set-up is comparable to thermal-atom systems discussed in Sect. [1], whilst only three-orders of magnitude from the quantum projection noise limit

The key areas that remain open for future study are;

- **Clock noise** Following the initial study presented in this thesis, noise sources must be addressed to reduce the electronic noise floor. Additional photodiodes have been added to various sections of the set-up for active monitoring of laser fluctuations throughout the system for post-analysis corrections to the data. Furthermore, the local oscillator has been changed to a GPS satellite received as opposed to the stabilised quartz oven.

- **Electronic and power consumption** Both the laser cooling and clock probing lasers are produced from homebuilt external-cavity-diode-lasers, as opposed to a micro-fabricated solution. One such solution could be the implementation of VCSELs to further reduce the complexity and bulky set-up. As well as further studies into diode replacements, the electronic power consumption must be reduced to aid future miniaturisation.

- **Vacuum system reduction** Current miniaturisation of the clock is ultimately limited by the scalability of the vacuum apparatus. A primary hindrance to the miniaturisation of vacuum technology is the necessity for a reduction of background gasses, with a significant contribution for helium permeation. Standard apparatus requires the use of an ion pump to maintain UHV, however for feasible miniaturisation, a compact solution of maintaining a low pressure environment is required. This issue has been addressed in publications from the Kitching team at NIST [155] and M. Himsworth at the University of Southampton [191], for studies of micro-fabricated cell coatings with properties including low helium permeation.

The consolidation of these issues could be used to couple a micro-fabricated diffractive optic to a MEMS vacuum system, to produce an unambiguously compact, cold-atom platform. Such a device could be implemented across an array of precision measurements and metrological devices for next generation quantum sensors.

Part VI

Appendices

Appendix A

A portable MOT for outreach events and undergraduate experiments

This sections is focussed around the construction and running of a basic laser cooling apparatus used for outreach events and public engagement. The final system consists of a single ECDL coupled to a diffractive optic for generation of a ^{87}Rb cold atom sample. Finally, 776 nm light is used to satisfy blue light generation for emission in the visible spectrum.

A.1   Construction

Laser cooling and trapping of atomic samples has grown into a field of its own, dominating precision measurements and fundamental physics. Cold-atoms also make a useful demonstration tool for the teaching of introductory atomic physics for both undergraduate experiments and public engagement [177, 192]. The miniaturisation and simplification of the laser cooling apparatus, described in recent publications Refs. [42, 102, 103], has been utilised for the construction and demonstration of a portable cold-atom device.
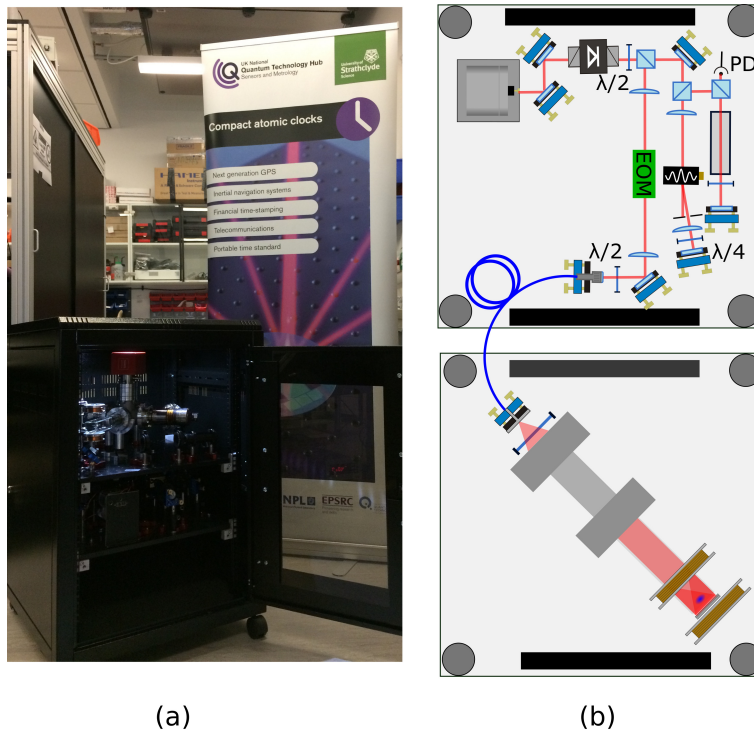
(a) (b)

Figure A.1: Portable set-up for transportation of the clock apparatus.

Due to the aim of an inexpensive experiment, the optical set-up was built around a single laser, as illustrated in Fig. A.1 (b) with the components listed in Table A.1. The homebuilt ECDL was capable of producing 60 mWs output power with a linewidth of $\approx$500 kHz. The laser was locked using standard saturated absorption spectroscopy, with an acousto-optical modulator in line for frequency and intensity control of the cooling light. The locked light was coupled through an electro-optical modulator for sideband generation at 6.8 GHz separation for re-pumping. After fibre coupling, the beam was expanded and collimated with a $1/e^2$ diameter of 2 cm, which was circularly polarised with one inch optics and aligned through the vacuum system. A 1-D triangular grating of period 1180 nm discussed in Ref. [103], was held close to the vacuum glass surface in a 3D printed mount.

The grating chip is carefully aligned with the incident light to ensure the

Table A.1: Portable MOT costs

Equipment	Source	Cost (£)
780 nm laser	Sanyo diode/homebuilt ECDL	200
EOM	New Focus 6.585 GHz Model 4851	2000
Mirrors/mounts	ThorLabs BB1-E03-10 10 pack	497
Optical isolator	ThorLabs IO-5-780-VLP	790
AOM	AA-OptoElectronic MT110-B50A1-IR	700
Vacuum system		5000
Optical fibre	ThorLabs P3-630PM-FC-2	150
Vapour cell	ThorLabs GC25075-RB	356
PBS	ThorLabs PBS102	138
Grating chip	Strathclyde University	1000
Total		10831

reflected order is well retro-reflected to avoid beam imbalance. Furthermore, the beam is apertured to aid the alignment with the centre of the grating chip, which when aligned correctly, all diffracted orders are visible. The vacuum system was baked to achieve pressures on the order of $\approx 10^{-9}$ mbar, using a 20 L/s ion pump and controller.

Following the construction and alignment, a GMOT is achievable with relative ease, requiring only small realignment to achieve upwards of 10^7 atoms. The running system was built onto 20×20 cm optical breadboards to facilitate a portable apparatus. The equipment was mounted into a custom built server rack for the purpose of transportation to outreach events and public engagement across the country.

A.2 Blue MOT

The infra-red emission from the MOT has been seen to reduce the effectiveness of public engagement due to the necessity to use an IR-CCD for physical viewing; in many instances leading to the public questioning the authenticity of the live video stream. To circumvent this issue, an additional ECDL at
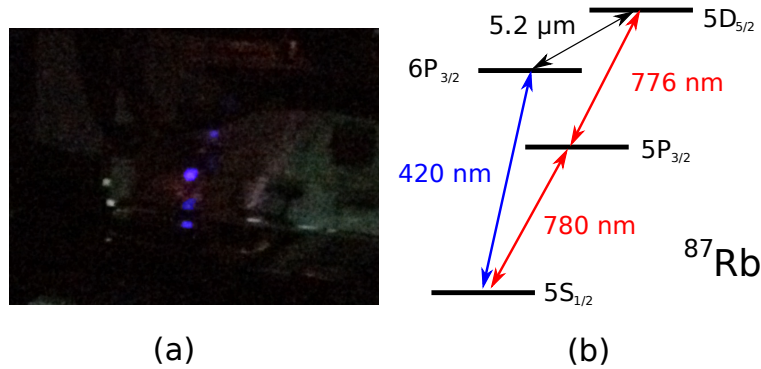
(a)   (b)

Figure A.2: Image of 420 nm emission from ^{87}Rb for visible detection.

776 nm was added to reach the blue emission from the $6P_{3/2} \rightarrow 5S_{1/2}$ state, as depicted in Fig. A.2 (b).

The ECDL was built with a 780 nm diode, which was temperature controlled to pull the emission wavelength down to the 776 nm transition. The temperature was adjusted by controlling the current to a Peltier cooler at the base of the ECDL, implemented for temperature regulation. The 776 nm light was aligned and retro-reflected through the MOT for radiation balance, such that it could be left free-running and only require a small current adjustment every few minutes to maintain a frequency close enough to the 776 nm transition for blue emission from the MOT as in Fig. A.2 (a). The easy control of blue emission makes a useful hands on engagement tool for the public, as well as a useful demonstration of transition frequencies and atomic structure.
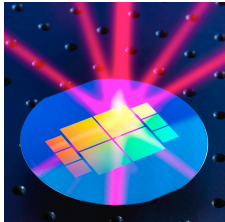
Appendix B

Poster

Building the next-generation atomic clock

J. P. McGilligan, R. Elvin, P. F. Griffin, E. Riis, A. S. Arnold

Experimental Quantum Optics and Photonics Group
University of Strathclyde, Department of Physics

University of **Strathclyde**
Science

Compact atom clocks

With technology becoming ever more dependent on precision measurements it is understandable that there is demand to link commercial systems to the most accurate atomic experiments; atomic clocks.

Currently, the state of the art clock has an accuracy of 1 part in 10^{-18}, i.e. measures better than 1 second in the age of the universe.

This accuracy is strongly sought after in:
- GPS
- Navigation
- Telecommunications
- Financial security
- Quantum information devices…The list goes on.

However, the size of the most accurate atomic clocks limits them from advancing to commercial system. We propose a new technique to facilitate a compact atomic clock that can be made commercially available whilst maintaining a high degree of precision.
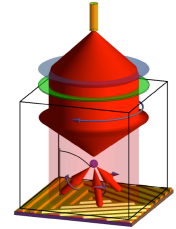
Figure 1

## Idea – Atomic clock

Why use atoms for a clock?

All clocks, from sundial to pendulum, require an oscillator. Atoms offer the ideal oscillator because:

- All identical – universal
- Never age – no calibration
- Well defined frequency – no variation

How does an atomic clock work?

The atomic clock determines time through measurement of the frequency splitting of an electronic transition. This frequency can be directly related to a time.

Clock Transition $|g2\rangle$ $|g1\rangle$
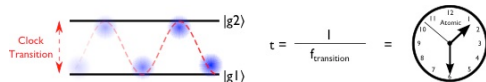
$$t = \frac{1}{f_{transition}}$$

What determines a clocks accuracy?

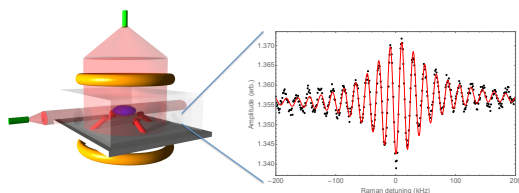The limit to a clocks accuracy is defined by the instability factor:

$$\sigma_y(\tau) = \frac{\Delta f_a}{f_o\sqrt{N\tau}}$$

N: Number of atoms
f_0: Resonance frequency
τ: Measurement time
Δf_a: Linewidth of transition

Thus, trapping atoms will give a large *N*, cold atoms have large long τ and atomic transitions have narrow linewidths, Δf_a.

Design – A compact device

Laser cooling:

Standard laser cooling typically uses 6 counter propagating laser beams to carry momentum away from an atomic ensemble in the form of scattered photons. This reduces the kinetic energy of the system, slowing the atoms and resulting in long measurement times.

However, the apparatus required is complicated and bulky.

Grating Chip $+\eta_1$ η_0 θ $-\eta_1$ λ/4 PBS λ/2

η_1 = diffracted order
η_0 = reflected order
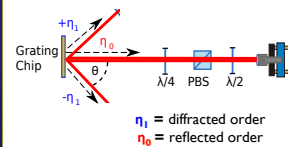
Compact laser cooling:

To simplify laser cooling, we couple 1 laser to a diffraction grating, Figure 1, to generate balanced light forces.

We used the set-up (left) to vary the grating parameters, such as diffraction angle, to find gratings with an <u>intensity balance between incident and diffracted light</u>, which is critical to laser cooling.

Intensity balance(%) θ(deg)

Intensity balance(%) Wavelength (nm) K Rb Cs

During this study we found that the intensity balance has a broadband wavelength dependence, opening doors to many atomic species interesting to atomic physics.

J. P. McGilligan, P. F. Griffin, E. Riis, A. S. Arnold, 'Grating characterization for cold atom experiments', *JOSA B* (2016)

J. P. Cotter, J. P. McGilligan, P. F. Griffin, I. M. Rabey, K. Docherty, E. Riis, A. S. Arnold, E. A. Hinds, *Applied Physics B*, **122** (2016)

Results – Compact cold clock

Once we have a large, cold atom sample we use a probe beam to intersect the atoms and drive the clock transition using a two photon process known as Raman Ramsey interrogation.

Amplitude (arb.) Raman detuning (kHz)

Observation of the probe beam intensity when passing through the atoms and scanning across the clock frequency in a pulsed technique shows atomic absorption, revealing a clock fringe with a **64 Hz linewidth**

Using what we have achieved so far and subbing these values into the instability equation, predicts **we have a compact clock with an accuracy to the $3\times10^{-11}/\tau^{1/2}$**. In the coming year we aim to reduce this value to $3\times10^{-13}/\tau^{1/2}$.
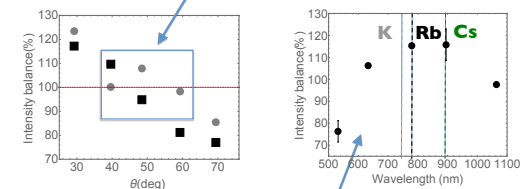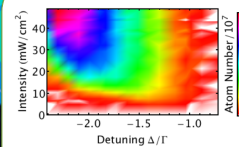
J. P. McGilligan, R. Elvin, P. F. Griffin, E. Riis, A. S. Arnold, *In Preparation* (2016)

Implementation – Cold atoms

Intensity (mW/ cm²) Detuning Δ/Γ Atom Number /10⁷

Intensity (mW/ cm²) Detuning Δ/Γ ρ / 10¹⁰ cm⁻³

Next, the optimum grating was used, as in Figure 1, to produce balance intensity pressure, needed to trap and cool an atomic sample.
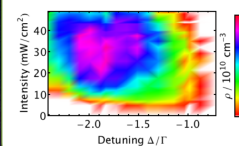
The detuning and intensity of incident laser light was then varied to define peak number, density and temperature:

Atom number:
$N \approx 1\times10^8$

Atom Density:
$\rho \approx 2\times10^{10}$ cm^{-3}

Atom temperature:
$T \approx 5\ \mu K$

J. P. McGilligan, P. F. Griffin, E. Riis, A. S. Arnold, 'Phase space characterization', *Opt. Express* **23**, 8948-8959 (2015)

SUPA dstl University of **Strathclyde** Glasgow esa UK NATIONAL QUANTUM TECHNOLOGIES UK National Quantum Technology Hub in Sensors and Metrology

Appendix C

Publication: Design and fabrication of diffractive atom chips for laser cooling and trapping

Applied Physics B
Lasers and Optics

CrossMark

Design and fabrication of diffractive atom chips for laser cooling and trapping

J. P. Cotter[1,2] · J. P. McGilligan[3] · P. F. Griffin[3] · I. M. Rabey[1] · K. Docherty[4] · E. Riis[3] ·
A. S. Arnold[3] · E. A. Hinds[1]

Abstract It has recently been shown that optical reflection gratings fabricated directly into an atom chip provide a simple and effective way to trap and cool substantial clouds of atoms (Nshii et al. in Nat Nanotechnol 8:321–324, 2013; McGilligan et al. in Opt Express 23(7):8948–8959, 2015). In this article, we describe how the gratings are designed and microfabricated and we characterise their optical properties, which determine their effectiveness as a cold atom source. We use simple scalar diffraction theory to understand how the morphology of the gratings determines the power in the diffracted beams.

1 Introduction

Atom chips [3, 4] are microfabricated devices [5] which control and manipulate ultracold atoms in a small, integrated package. Because they provide a convenient way to trap [6–9], guide [3, 10] and detect atoms [11], atom chips are becoming increasingly important for clocks [12, 13], Bose–Einstein condensates [14–16], matter wave interferometers [17–20] and quantum metrology [20]. In recent years, there has been great progress towards integrating a

✉ J. P. Cotter
 j.cotter@imperial.ac.uk

1 The Centre for Cold Matter, Blackett Laboratory, Imperial College London, London SW7 2AZ, UK

2 Faculty of Physics, VCQ, University of Vienna, Boltzmanngasse 5, 1090 Vienna, Austria

3 Department of Physics, SUPA, University of Strathclyde, Glasgow G4 0NG, UK

4 Kelvin Nanotechnology Ltd, Rankine Building, Oakfield Avenue, Glasgow G12 8LT, UK

wide range of optical, electric and magnetic elements into atom chips, but the magneto-optical trap (MOT) [21, 22]—the element responsible for initial capture and cooling of the atoms—has remained external to the chip.

An early attempt to integrate the MOT used deep pyramidal mirrors etched into a thick silicon substrate [8]. These manipulate a single incident laser beam into the overlapping beams required by a MOT. With beams of size L, the number of atoms captured scales as L^6 [9], a dependence that rolls over to $L^{3.6}$ as the size increases to some centimetres [21]. The large pyramids favoured by this scaling are not compatible with the normal $500\,\mu m$ thickness of a silicon wafer. Although thick wafers are available, days of etching are needed to make pyramids of mm size and additional polishing is required to achieve optical quality surfaces [8, 23, 24]. For these reasons, the integrated pyramid is unsuitable for applications requiring more than $\sim 10^4$ atoms. Figure 1 illustrates a recent extension of this idea where the MOT beams are now formed using microfabricated diffraction gratings, which replace the sloping walls of the pyramid [25, 26]. The gratings are easily fabricated on any standard substrate material and can readily be made on the centimetre scale. This allows the MOT to capture up to 10^8 atoms above the surface of the chip, where they can be conveniently transferred to magnetic traps [3]. Because they only need a small depth of etching, the gratings preserve the 2D nature of the structure and sit comfortably with other elements on the chip. Alternatively, for devices that only require the reliable production of a MOT, the grating chip can be placed outside the wall of a glass cell and used to trap atoms on the inside.

Figure 2 shows two 1D-grating MOT chips, which have already been demonstrated [1]. Chip A has three square grating areas arranged symmetrically to leave a plane area in the centre. Chip B has the same geometry, but the
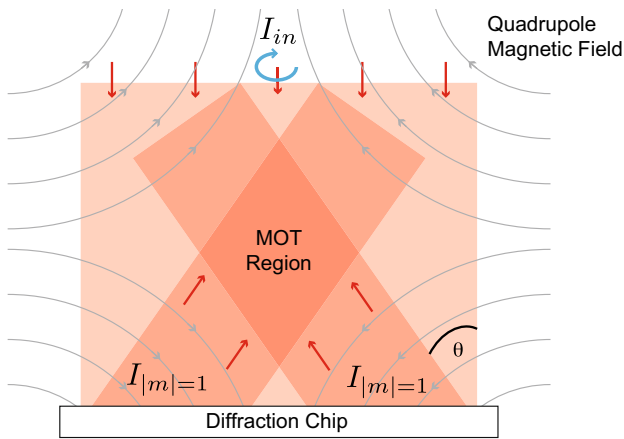
Fig. 1 Principle of the grating chips. A normally incident laser beam of intensity I_{in} is diffracted by metal reflection gratings, written into the surface of a chip. The gratings diffract the incoming light according to the Bragg condition $m\lambda = d\sin\theta$, where λ is the wavelength of light and d the grating period. By design, these structures diffract light only into the first-order beams ($m = \pm 1$) with an intensity $I_{|m|=1}$. Together with the magnetic quadrupole field, oriented as illustrated, the overlapping beams provide the light required for a magneto-optical trap (MOT). The angular momentum of the input beam, indicated by the *blue arrow*, is opposite to the local magnetic field direction, and the helicity of the light is well preserved after diffraction
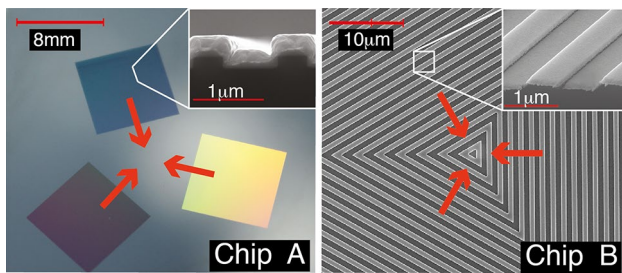

Fig. 2 One-dimensional grating chips of threefold radial symmetry, used to make 4-beam integrated MOTs. *Red arrows* indicate the diffracted beams used for trapping. Chip A is made by optical lithography, while chip B (shown magnified) is patterned by e-beam lithography. *Insets* Scanning electron microscope images of the grating lines

grating pattern covers the whole surface and, in particular, extends all the way to the centre. In this article, we describe the design and fabrication of each chip and compare the expected and measured optical properties of each. The article is organised as follows: in Sect. 2, we outline the simple scalar diffraction model that we used to design the chips. Section 3 describes how the gratings were fabricated. In Sect. 4, we measure the dimensions of the fabricated gratings and the optical properties of the diffracted beams, and we compare the performance achieved with the theoretical expectations. Finally, in Sect. 5 we summarise our findings.
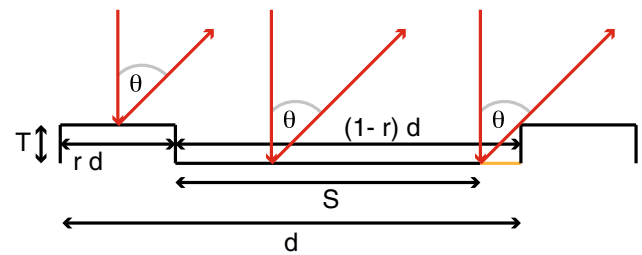

Fig. 3 Idealised diffraction grating profile, with period d, duty factor r, and depth T. S represents the effective length of the bottom facet, which is shortened because some light is shadowed by the step. Normally incident light is diffracted at an angle θ

2 Design of the chips

The atoms trapped by the MOT are held by optical scattering forces in the presence of a magnetic quadrupole field. Ideally, these forces should sum to zero at the centre of the quadrupole, which can be achieved by appropriate choices of intensity and polarisation of the light. The chips described here have symmetry that automatically balances the forces parallel to the surface, but balance in the normal direction has to be designed. Let the incident power P_{in} over an area A of the chip produce power ηP_{in} in each diffracted beam. The corresponding intensity is $I_{diff} = \eta P_{in}/(A\cos\theta)$, where θ is the angle to the normal, as shown in Fig. 1. With N diffracted beams participating in the MOT, the total intensity contributing to the upward force is $N I_{diff}\cos\theta = N\eta P_{in}/A = N\eta I_{in}$. The vertical balance of intensities therefore requires $N\eta = 1$. For chips A and B in Fig. 2, which use three diffracted beams, this condition becomes $\eta = 1/3$ [26]. In practice, the optimum diffracted intensity is somewhat higher because the polarisations of the upward and downward beams are not the same.

To estimate the power diffracted from our gratings, we approximate them by the ideal profile shown in Fig. 3. The elementary period d contains a top face of width rd and a bottom face of width $(1 - r)d$ that is lower by a depth T. Light diffracted at an angle θ from the lower face is shadowed by the step, so that the effective width of the face is $S = (1 - r)d - T\tan\theta$. The phase difference between rays coming from the centre of the top surface and the centre of the effective bottom surface is

$$\phi = k\left[\frac{1}{2}(d - T\tan\theta)\sin\theta - T(1 + \cos\theta)\right], \qquad (1)$$

where $k = 2\pi/\lambda$ and λ is the wavelength of the light. With a normally incident field E_{in}, and assuming power reflectivity ρ, the diffracted field at (large) distance R is approximated by the Fraunhofer integral.
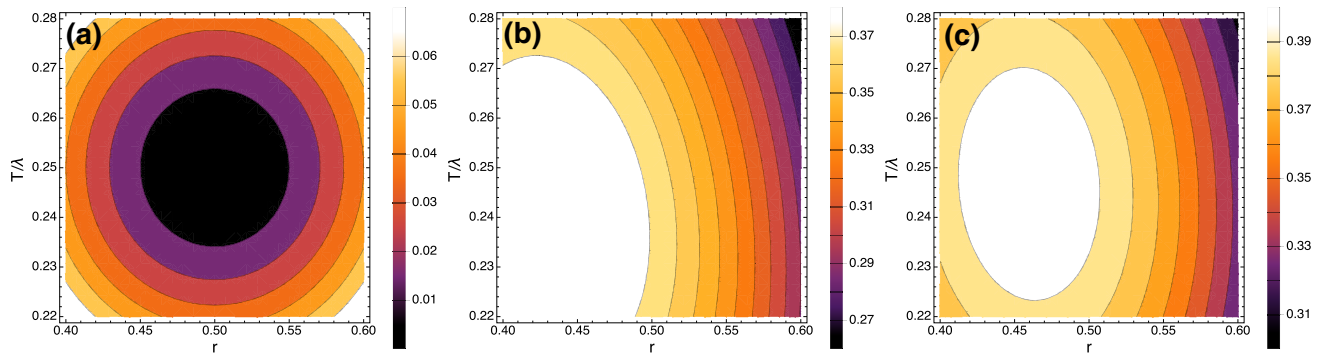
Fig. 4 Power in a single diffraction order, normalised to the incident power and plotted as a function of duty factor r and grating depth T divided by wavelength λ. Reflectivity is taken to be $\rho = 1$. **a** The zero-order case given by Eq. (5). This is the region near minimum power, where $r \simeq 1/2$ and $T \simeq \lambda/4$. The minimum is wide enough to forgive minor fabrication errors. **b** Fraction of power in the $m = +1$ order of chip A, calculated from Eq. (4) with $d = 1.19\,\mu m$ and $\lambda = 780\,nm$. **c** Fraction of power in the $m = +1$ order of chip B, calculated from Eq. (4) with $d = 1.48\,\mu m$ and $\lambda = 780\,nm$

$$\frac{E(\theta)}{E_{in}} = \frac{\sqrt{\rho}}{\sqrt{R}\lambda} \left[\int_{-rd/2}^{rd/2} dx e^{ikx\sin\theta} + e^{i\phi} \int_{-S/2}^{S/2} dx e^{ikx\sin\theta} \right]$$
$$\times \left(\sum_{n=1}^{N} e^{iknd\sin\theta} \right). \tag{2}$$

Here, the first line describes the diffraction from one elementary unit of the grating, as illustrated in Fig. 3, while the last factor sums over the contribution from all N grating periods.

The intensity distribution, obtained by squaring equation (2), has a comb of narrow peaks coming from the grating factor, with maxima at the Bragg angles given by $\sin\theta = m\lambda/d$, where m is an integer. Because many lines of the grating are illuminated, the single-period factor is essentially constant over the small angular spread across one of the Bragg peaks. This makes it straightforward to integrate across the mth Bragg peak to find the total diffracted power P_m in that order. The result is

$$\frac{P_m}{P_{in}} = \frac{\rho}{d^2} \left| \int_{-rd/2}^{rd/2} dx e^{i2\pi mx/d} + e^{i\phi} \int_{-S/2}^{S/2} dx e^{i2\pi mx/d} \right|^2, \tag{3}$$

P_{in} being the power incident on the N illuminated lines of the grating. Evaluating these integrals,

$$\frac{P_m}{P_{in}} = \frac{\rho}{m^2\pi^2} [\sin^2(m\pi r) + \sin^2(m\pi S/d)$$
$$+ 2\cos(\phi)\sin(m\pi r)\sin(m\pi S/d)]. \tag{4}$$

Let us first consider diffraction into the $m = 0$ order—i.e. retro-reflection of the incident beam. This needs to be avoided as a strong upward beam of the wrong polarisation is detrimental to the MOT [1]. For chip A, there is a plane surface in the central region, which can either be cut away to leave an aperture, or coated with an absorbing layer. For chip B, where the grating structure runs all the way into the middle, the retro-reflection can be suppressed instead by a suitable choice of the grating parameters. On using Eq. (1) to eliminate ϕ, Eq. (4) gives

$$\frac{P_0}{P_{in}} = \rho \left[1 + 2r(r-1)\left(1 - \cos\left(\frac{4\pi T}{\lambda}\right)\right) \right]. \tag{5}$$

This goes to zero when $r = \frac{1}{2}\left(1 + \frac{i}{\tan(2\pi T/\lambda)}\right)$. Since r must be real, we require $\tan(2\pi T/\lambda) = \infty$, which leaves $r = \frac{1}{2}$. It is desirable to minimise the depth T so that S remains as large as possible for the first diffraction order. We therefore choose $T = \lambda/4$. Figure 4a shows how P_0/P_{in} varies when r and T deviate from this ideal condition, as they inevitably will in practice. We see that deviations of up to 10 % in either T or r give rise to a P_0/P_{in} of only one or two per cent, making the design robust against minor fabrication errors.

We turn now to the first-order beams, which (together with the incident beam) are responsible for making the MOT. To ensure efficient use of the available power, we choose gratings where $d < \lambda/2$, so that there are no diffracted beams except for those having $m = 0$ and $|m| = 1$.

The plots in Fig. 4b (for chip A) and Fig. 4c (for chip B) show the power P_1 in the $m = +1$ order (normalised to P_{in}) when the grating depth T and duty factor r are varied. We see that this power is close to a maximum when the retro-reflected power is zero, but can be increased a little by reducing r slightly below 0.5. This has the effect of making rd and S more nearly equal, which improves the contrast of the grating. A little is also gained by reducing T/λ, so that the width S of the lower surface is increased. As with the minimum of P_0, this maximum of P_1 is sufficiently forgiving that we are not troubled by minor fabrication errors.
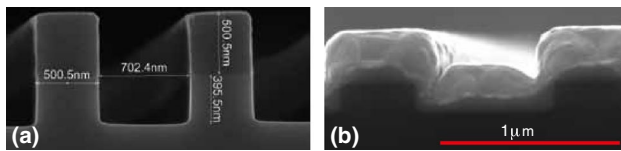
Fig. 5 **a** Scanning electron microscope images of chip A. **a** A deep trench calibrates the etching rate prior to the main fabrication and shows a profile close to that of our model, as illustrated in Fig. 3. **b** The final chip after etching to a depth of $T\sim$195nm and coating with 200nm of gold. This brings the duty factor r close to 1 / 2

Fig. 6 Scanning electron microscope images of chip B. **a** The centre of chip B, etched to a depth of 195nm, before coating. The triangles are equilateral, but distorted by the angle of view. **b** After coating with aluminium

The MOT works because the scattering force in the presence of a magnetic field depends on the polarisation of the light [25]. For that reason, it would be ideal to go beyond this simple scalar model of the diffraction to consider polarisation. However, that theory is quite challenging and is beyond the scope of this article. Instead we have relied on experiment to determine the polarisation of the diffracted beam, as discussed further in Sect. 4.

3 Fabrication

Chips A and B are produced by two different fabrication methods, which we now describe.

3.1 Chip A: photolithography using silicon substrate

Chip A, as shown in Fig. 2a, is a 32mm square of silicon in which three 8-mm-square lamellar gratings are etched by photolithography. This is then covered with gold to achieve the desired high reflectivity at 780nm. We choose a grating period of $1.2\,\mu$m, which is close to the minimum that can be reliably made by this method. Although we aim for a duty factor of $r = \frac{1}{2}$, the bottom face is designed to be 700 nm wide, anticipating that r will move towards 1 / 2 after the gold is added.

To begin, we make a reticle by direct ebeam writing on chromium-coated quartz. This is a $5\times$ magnified version of one square grating. A $\langle 100 \rangle$-oriented 150-mm-diameter silicon wafer is then coated with SPR660 photoresist to a thickness of 0.8μm and exposed to de-magnified images of the reticle, using light of 365nm wavelength. A stepper motor manoeuvres the reticle to each grating position in turn, to produce an image of 12 chips—32 gratings in total—on the wafer. The resist is then developed, and the exposed silicon is removed by reactive ion etching using an inductively coupled SF_6/C_4F_8 plasma. With a typical etch rate of $\sim$5nm/s, this forms a grating of the desired depth—$\lambda/4 = $ 195nm—in under 1minute. The wafer is then stripped of the remaining resist by plasma ashing, before cleaning with a piranha solution to remove any remaining
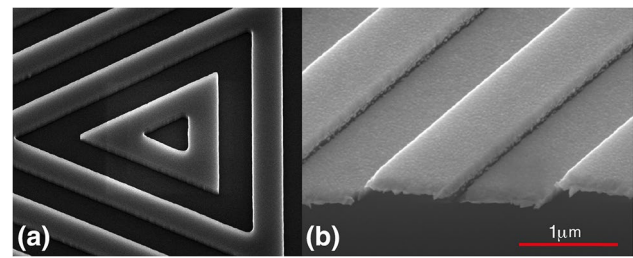
organic contaminants. Figure 5a shows a scanning electron microscope image of a deep grating that was made to calibrate the etch rate. One can see in this image the high quality of the profile and the few-nm accuracy of the widths produced.

In order to give the gratings a high reflectivity, we apply a 5nm-thick adhesion layer of chromium (by dc sputtering) followed by 200nm-thick layer of gold (by rf sputtering). The finished grating is shown in Fig. 5b. From this and similar scans, we measure a final depth of $T = 207(5)$nm, a period of $d = 1.19(1)\,\mu$m and a duty factor of $r = 0.51(5)$, the latter being due in part to some systematic variation across the chip.

3.2 Chip B: electron-beam lithography using silicon substrate

Chip B is a 22mm square of silicon, coated with aluminium, in which a grating is etched by electron-beam lithography. The grating consists of nested triangles, as shown magnified in Fig. 2b, that continue outward to fill a 20mm square. The lamellar surface profile is designed to have a depth of 195nm, a period of $1.5\,\mu$m and a duty factor of 1 / 2 . Unlike the photolithography used for chip A, the e-beam fabrication used here is not at all challenged by the resolution we require. However, the large size of the pattern over all does present a challenge.

A $\langle 100 \rangle$-oriented 100-mm-diameter silicon wafer is coated with ZEP520A e-beam resist to a thickness of 350 nm, which is then patterned using a high-speed e-beam writer (Vistec VB6 with 50MHz scan speed). With 11 chips, covering a total area of 44 cm^2, this takes 25h of continuous writing. Particular care is needed to ensure the electron-beam direction does not drift over this time, thereby introducing phase variations across individual gratings. The wafer is then etched and cleaned in the same way as chip A. The scanning electron microscope image in Fig. 6a shows the centre of the etched grating and illustrates the high quality of the fabrication.

After evaporating 100nm of aluminium, the grating is imaged again, as shown in Fig. 6b. From this and similar scans, we measure the final parameters $T = 190(5)$ nm, $d = 1.48(1)$ μm and $r = 0.46(5)$.

4 Measurement of optical properties

The two different coatings—gold for chip A and aluminium for chip B—are motivated by two ways of operating. With the chip inside a vacuum, the required ∼1/3 power in each diffracted beam (see Sect. 2) is provided by an aluminium coating. The higher reflectivity of gold is needed for a chip outside the window of a glass cell because the diffracted beams suffer reflection loses when they pass through the window. There is no significance to the different thicknesses used—it is sufficient for the metal film to be large compared with the skin depth. The reflectivity of each chip was determined by measuring the power in a 780nm laser beam reflected from a flat, un-etched area and comparing this with the incident power. We found $\rho = 0.972(6)$ for chip A and $\rho = 0.822(6)$ for chip B.

In order to measure the diffracted power ratio P_m/P_{in}, a few-milliwatt laser beam of 780nm wavelength was spatially filtered using a single-mode fibre and then collimated to form a beam of approximately 1mm full-width-half-maximum. This was sent through a polarising beam splitter and then circularly polarised by a quarter-wave plate, as it would be to make a MOT. Roughly 1 m from the wave plate, the light was retro-reflected from a flat area of the chip and sent back through the wave plate and beam splitter. The circular polarisation of the incident light was optimised by adjusting the angle of the quarter-wave plate to extinguish the light returning through the beam splitter. Next, a translation stage moved the chip so that the light was incident on a grating, and a power meter then recorded the incident power P_{in} and the power P_1 diffracted into first order. (The $m = 1$ beams were easily separated from $m = 0$ because of the large diffraction angle – 41° for grating A and 32° for B).

We measured each of the three gratings on chip A, with the results $P_1/P_{in} = 0.326(2), 0.323(2)\ 0.386(2)$. These are to be compared with the power ratio given by Eq. (4) after inserting the measured grating dimensions and reflectivity. That gives $0.340^{+(21)}_{-(36)}$, in good agreement with the measurements. The small variation in both theory and experiment is due predominantly to r. This translates into a variation of the diffracted power because chip A, having $r = 0.51(5)$, operates on the high-r side of the maximum plotted in Fig. 4b, where the derivative with respect to r is not zero.

Measurements on the three gratings of chip B gave $P_1/P_{in} = 0.381(2), 0.381(2)\ 0.380(2)$, showing a good

level of reproducibility. This is due in part to better uniformity of the e-beam lithography, but also, chip B operates with $r = 0.46(5)$, which is very close to the maximum of the plot in Fig. 4c, where P_1 is insensitive to variation of r. The power ratio given by Eq. (4) for chip B is $0.328^{+(2)}_{-(9)}$. While this is qualitatively similar to the measured fraction, it does not agree within the measurement uncertainty, and we cannot find any plausible adjustment of parameters that might bring them into agreement. We are forced to conclude that our diffraction theory is not able to predict the diffracted power with this high level of accuracy and suspect that the limitation is due to our use of the effective width S, defined by ray optics and therefore not strictly justified. In the case of chip B, the zeroth-order beam passes through the MOT, so it is important with this chip to have a low P_0. In order to measure this, we rotated the chip by approximately 5mrad to separate the $m = 0$ diffracted beam from the incident beam. This measurement gave $P_0 = 0.005(1)$, in good agreement with $0.007^{+(20)}_{-(7)}$ from Eq. (4).

The magneto-optical trapping force depends on the polarisation of the light, relative to the direction of the local magnetic field [21]. This is discussed for our particular geometry in [25], which shows that the MOT works well when diffraction of the beam reverses its helicity. We therefore checked the polarisation of the first-order diffracted beams using a second combination of quarter-wave plate and polarising beam splitter, adjusted to project the state of the beam onto the basis of left- and right-handed polarisations. Photodetectors at the two beam splitter outputs measured the powers P_L and P_R in each circular polarisation. The fraction of power with reversed helicity from the three gratings on Chip A was 88, 90 and 98 %, and we note that better helicity reversal coincided in each case with higher power. On chip B, we measured 97, 98 and 99 %. This high degree of polarisation is more than adequate to make a strong MOT with either chip [1]. Indeed, although we do not have any calculation for comparison, it seems surprisingly high given the obvious anisotropy of the surface and of the diffraction geometry. We note that the variation in polarisation is greater across chip A than chip B, and again, we ascribe this to the two different methods of fabrication.

5 Summary and conclusions

Optical reflection gratings fabricated on an atom chip offer a simple way to build a large, robust, integrated magneto-optical trap (MOT) for atoms [1]. In this paper, we have discussed the main design considerations and have described how suitable chips can be fabricated using two methods: optical lithography and e-beam lithography. Using scalar Fraunhofer diffraction theory and an idealised model

of the lamellar profile, we have provided an account of the expected MOT beam intensities. This theory agrees well with experiment down to the level of a few per cent of the incident power, but not with the higher-precision measurements made on the aluminium-coated chip B. We have shown that it is possible to suppress the back-reflection, while at the same time diffracting a large fraction of the power into the two first-order beams. The power in these beams depends on the choice of period d, duty factor r and depth T of the grating. These parameters vary a little over the optically fabricated chip A, and rather less over the e-beam fabricated chip B. In either case, we show how to minimise the effect of inhomogeneity on the diffracted beam intensity by operating at the intensity maximum with respect to r and T. We also find that the circular polarisation of the light is surprisingly well preserved after diffraction into the first-order beams.

The design principles and theoretical model developed here make this new method accessible to anyone who may wish to incorporate such an integrated trap into an atom chip. We anticipate that this approach will facilitate future quantum technologies using cold and ultracold atoms [27].

References

1. C.C. Nshii, M. Vangeleyn, J.P. Cotter, P.F. Griffin, E.A. Hinds, C.N. Ironside, P. See, A.G. Sinclair, E. Riis, A.S. Arnold, A surface-patterned chip as a strong source of ultracold atoms for quantum technologies. Nat. Nanotechnol. **8**, 321–324 (2013)

2. J.P. McGilligan, P.F. Griffin, E. Riis, A.S. Arnold, Phase-space properties of magneto-optical traps utilising micro-fabricated gratings. Opt. Express **23**(7), 8948–8959 (2015)

3. E.A. Hinds, I.G. Hughes, Magnetic atom optics: mirrors, guides, traps, and chips for atoms. J. Phys. D Appl. Phys. **32**(18), R119 (1999)

4. J. Reichel, V. Vuletic (eds.), *Atom Chips*. (Wiley-VCH, Berlin, 2011)

5. R. Folman, Material science for quantum computing with atom chips. Quantum Inf. Proc. **10**(6), 995–1036 (2011)

6. J. Fortágh, C. Zimmermann, Magnetic microtraps for ultracold atoms. Rev. Mod. Phys. **79**, 235–289 (2007)

7. G.N. Lewis, Z. Moktadir, C. Gollasch, M. Kraft, S. Pollock, F. Ramirez-Martinez, J. Ashmore, A. Laliotis, M. Trupke, E.A. Hinds, Fabrication of magnetooptical atom traps on a chip. J. MEMS **18**, 347–353 (2009)

8. S. Pollock, J.P. Cotter, A. Laliotis, E.A. Hinds, Integrated magneto-optical traps on a chip using silicon pyramid structures. Opt. Express **17**, 14109–14114 (2009)

9. S. Pollock, J.P. Cotter, A. Laliotis, F. Ramirez-Martinez, E.A. Hinds, Characteristics of integrated magneto-optical traps for atom chips. New J. Phys. **13**, 043029 (2011)

10. N.H. Dekker, C.S. Lee, V. Lorent, J.H. Thywissen, S.P. Smith, M. Drndić, R.M. Westervelt, M. Prentiss, Guiding neutral atoms on a chip. Phys. Rev. Lett. **84**, 1124 (2000)

11. S. Eriksson, M. Trupke, H.F. Powell, D. Sahagun, C.D.J. Sinclair, E.A. Curtis, B.E. Sauer, E.A. Hinds, Z. Moktadir, C.O. Gollasch, M. Kraft, Integrated optical components on atom chips. Eur. Phys. J. D **35**, 135–139 (2005)

12. P. Treutlein, P. Hommelhoff, T. Steinmetz, T.W. Hänsch, J. Reichel, Coherence in microchip traps. Phys. Rev. Lett. **92**, 203005 (2004)

13. R. Szmuk, V. Dugrain, W. Maineult, J. Reichel, P. Rosenbusch, Stability of a trapped-atom clock on a chip. Phys. Rev. A **92**, 012106 (2015)

14. W. Hänsel, P. Hommelhoff, T.W. Hänsch, J. Reichel, Bose–Einstein condensation on a microelectronic chips. Nature **413**, 498–501 (2001)

15. H. Ott, J. Fortágh, F. Schlotterback, A. Grossmann, C. Zimmermann, Bose–Einstein condensation in a surface microtraps. Phys. Rev. Lett. **23**, 230401 (2001)

16. J. Reichel, Microchip traps and Bose–Einstein condensation. Appl. Phys. B **74**(6), 469–487 (2002)

17. T. Schumm, S. Hofferberth, L.M. Andersson, S. Wildermuth, S. Groth, I. Bar-Joseph, J. Schmiedmayer, P. Krüger, Matter-wave interferometry in a double well on an atom chip. Nat. Phys. **1**, 57–62 (2005)

18. F. Baumgärtner, R.J. Sewell, S. Eriksson, I. Llorente-Garcia, J. Dingjan, J.P. Cotter, E.A. Hinds, Measuring energy differences by BEC interferometry on a chips. Phys. Rev. Lett. **105**, 243003 (2010)

19. Y. Margalit, Z. Zhou, S. Machluf, D. Rohrlich, Y. Japha, R. Folman, A self-interfering clock as a which path witness. Science **349**, 1205–1208, (2015)

20. M.F. Riedel, P. Böhi, Y. Li, T.W. Hänsch, A. Sinatra, P. Treutlein, Atom-chip-based generation of entanglement for quantum metrology. Nature **464**, 1170 (2010)

21. K. Lindquist, M. Stephens, C. Wieman, Experimental and theoretical study of the vapor-cell Zeeman optical trap. Phys. Rev. A **46**(7), 4082–4090 (1992)

22. J. Reichel, W. Hänsel, T.W. Hänsch, Atomic micromanipulation with magnetic surface traps. Phys. Rev. Lett. **83**, 3398–3401 (1999)

23. A. Laliotis, M. Trupke, J.P. Cotter, G. Lewis, M. Kraft, E.A. Hinds, ICP polishing of silicon for high-quality optical resonators on a chip. J. Micromech. Microeng. **22**(12), 125011 (2012)

24. J.P. Cotter, I. Zeimpekis, M. Kraft, E.A. Hinds, Improved surface quality of anisotropically etched silicon {111} planes for mm-scale optics. J. Micromech. Microeng. **23**(11), 117006 (2013)

25. M. Vangeleyn, P.F. Griffin, E. Riis, A.S. Arnold, Single-laser, one beam, tetrahedral magneto-optical trap. Opt. Express **17**(16), 13601–13608 (2009)

26. M. Vangeleyn, P.F. Griffin, E. Riis, A.S. Arnold, Laser cooling with a single laser beam and a planar diffractor. Opt. Lett. **35**(20), 3453–3455 (2010)

27. J.A. Rushton, M. Aldous, M.D. Himsworth, Contributed review: the feasibility of a fully miniaturized magneto-optical trap for portable ultracold quantum technology. Rev. Sci. Instrum. **85**(12), 121501 (2014)

Appendix D

Publication: Diffraction grating characterisation for cold atom experiments

Diffraction-grating characterization for cold-atom experiments

J. P. McGilligan, P. F. Griffin, E. Riis, and A. S. Arnold*

Department of Physics, SUPA, University of Strathclyde, Glasgow G4 0NG, UK
*Corresponding author: aidan.arnold@strath.ac.uk

We have studied the optical properties of gratings microfabricated into semiconductor wafers, which can be used for simplifying cold-atom experiments. The study entailed the characterization of the diffraction efficiency as a function of the coating, periodicity, duty cycle, and geometry using over 100 distinct gratings. The critical parameters of experimental use, such as the diffraction angle and wavelength, are also discussed, with an outlook to achieving optimal ultracold experimental conditions.   © 2016 Optical Society of America

OCIS codes: (140.3320) Laser cooling; (140.7010) Laser trapping; (050.1950) Diffraction gratings; (050.1960) Diffraction theory.

http://dx.doi.org/10.1364/JOSAB.33.001271

1. INTRODUCTION

Cold-atom technologies have dominated precision measurements in recent years [1–4]. The preference for cold atoms arises from the increased interrogation time that is provided in an isolated environment, allowing higher precision to be taken from a measurement [5]. Although many metrological experiments benefit from cold-atom measurements [6,7], the standard apparatus required is typically too large for portable devices. Despite the fact that current miniaturized metrological devices have proven highly successful [8], their precision and accuracy are limited by their use of thermal atoms.

The source of cold atoms in most experiments is a standard magneto-optical trap (MOT) [9,10], which utilizes six independent beams, each with their own alignment and polarization optics. We have previously demonstrated a device that collects cold atoms in an optically compact geometry using a grating MOT (GMOT) [11,12], which is an extension of the equivalent MOT using a tetrahedral reflector [13]. Such MOTs are grating/mirror variants of the original 4-beam MOT by Shimizu *et al.* [14]. The simple design of the GMOT reduces the standard 6-beam MOT experimental setup to one incident beam upon a surface-etched, silicon wafer diffraction grating. The grating uses the incident light and first diffracted orders to produce balanced radiation pressure, allowing us to trap a large number of atoms at sub-Doppler temperatures [12,15]. This greatly reduces the scale and complexity of the optics used in laser cooling apparatus to facilitate applications [16–18].

In this paper, we present a detailed optical characterization of these microfabricated diffraction gratings, with a view to aiding future cold-atom quantum technologies. Comparisons are made with basic theoretical models of the light diffracted from binary periodic diffraction gratings. This study will be aimed

toward an understanding of how metal coatings, periodicity, duty cycles, and geometry affect the diffraction efficiency, a crucial parameter for creating balanced radiation pressure. Finally, we discuss additional parameters that have proven critical during our studies.

2. THEORY: DIFFRACTION GRATINGS

Previous efforts made toward producing a reliable theory of diffraction require a typically complex derivation of Maxwell's equations [19,20]. However, significant insight into the optical performance of our MOT gratings can be obtained from a simplified theory for the determination of the first- and zeroth-order diffraction efficiencies. We would like to draw attention to the optical theory expounded in Ref. [21] and use the same notation throughout this paper for convenience in comparison. However, here we use an even simpler phasor-based version of the theory, which gives a surprisingly good agreement to the experiment. Note also that the zeroth order is calculated via an alternative method.

The diffraction gratings considered in this work are composed of a combination of reflecting elements arranged in a periodic array, separated by a distance comparable to the wavelength of study, and alternate elements etched into the surface, as seen in Fig. 1. This structure is directly analogous to transmissive classical slits [22].

When studying a diffraction grating of period d with incident light of wavelength λ at an angle α to the grating normal, then a diffracted order will be produced at angle θ determined by the grating equation $m\lambda = d(\sin \alpha + \sin \theta)$, where m is an integer representing the diffracted order concerned. For incident light perfectly perpendicular to the grating ($\alpha = 0$), the grating equation simplifies to the Bragg condition,
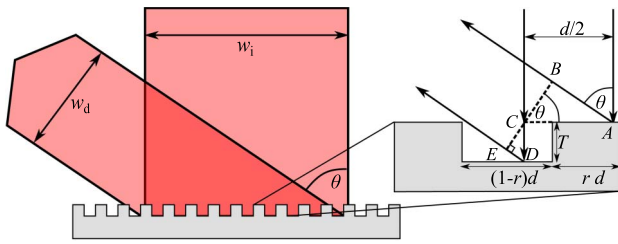
Fig. 1. Surface of a binary diffraction grating of etch depth T, diffraction angle θ, period d, and duty cycle r and 1-r for trough and peak, respectively.

$$m\lambda = d \sin \theta, \qquad (1)$$

where θ is now the angle of diffraction.

Figure 1 shows how the total electric field can be represented as the sum of diffracted orders from the trough and peak of the grating, which are weighted by their relative sizes $(1 - r)d = r_c d$ and rd, respectively, and phase shifted by the path difference between $AB = d/2 \sin \theta (= m\lambda/2)$ from Eq. (1) and $CDE = T(1 + \cos \theta)$, i.e.,

$$E_{\text{tot}}/\rho^{1/2} \propto (r + r_c e^{i\phi}) \qquad (2)$$

where $\quad \phi = \frac{2\pi}{\lambda}(m\lambda/2 - T(1 + \cos \theta))$,

where T is the etch depth, λ the wavelength of incident light, and ρ is the metal reflectivity. This gives a simple "phasor" model of the diffraction efficiency.

Using this electric field, in the case of a 50/50 duty cycle, $r = r_c = 0.5$, and a one-dimensional (1D) grating, the intensity efficiency, η_1, in the first diffracted orders can be calculated via

$$\eta_1 = \rho \frac{|1 + \exp[i\pi(1 - 2T(1 + \cos \theta)/\lambda)]|^2}{8}, \qquad (3)$$

where ρ is the reflectivity of the coating metal used, allowing for losses (see more on this in Section 4).

Equation (3) now provides a simple relation between the intensity of the light diffracted in the first order relative to the period of the grating. A simple model could thus assume that, for lossless diffraction with no grating orders $|m| \geq 1$, the zeroth order can be described by

$$2\eta_1 + \eta_0 = \rho. \qquad (4)$$

If the etch depth, T, is designed such that $T = \lambda_d/4$, where λ_d is the design wavelength and $\cos \theta \approx 1$, then Eq. (3) simplifies further to

$$\eta_1 = R \frac{\left(1 + \exp\left(i\frac{\pi \lambda_d}{2\lambda}\right)\right)^2}{8}. \qquad (5)$$

Note that to apply first-order diffraction efficiencies η_1 to two-dimensional (2D) gratings, we simply multiply by 1/2, to account for twice as many diffracted beams.

To determine how these diffracted efficiencies relate to creating a balanced radiation pressure, we must account for the vertical intensity balance between the incident, I_i, and the diffracted orders, I_d, described as $\frac{I_d}{I_i} = \eta_1 \frac{w_i}{w_d} = \frac{\eta_1}{\cos \theta}$, where w_i

(Fig. 1) is the incident beam waist and w_d is the diffracted beam waist. The radial balance is not considered, as this is automatic if the beam center is positioned on the grating center. The net incident intensity on the grating $I_i(1 - \eta_0)$ is ideally balanced with the component of the diffracted intensity, which is anti-parallel to the incident light, i.e., $NI_d \cos \theta$, where N accounts for the number of diffracted first orders, which simplifies to $NI_i\eta_1$. Thus, for all models, the balance between incident and diffracted light, perpendicular to the grating and taking the zeroth order into account, is described mathematically through the dimensionless quantity

$$\eta_B = N\eta_1/(1 - \eta_0), \qquad (6)$$

which is ideally one.

In summary, we have used a simple model, adapted from Ref. [21], for zeroth- and first-order diffraction efficiency η_0 and η_1 and thereby the radiation balance η_B. The model uses a simple two-phasor addition [Eqs. (3) and (4)], which can be shown to be directly proportional to a more complete phase integral across the grating, but ignoring the effect of shadowing.

3. EXPERIMENT: GRATING CHARACTERIZATION

The diffraction gratings used were manufactured with a dry etch into silicon wafers and patterned using electron beam lithography [23,24] to an ideal etch depth of $h = \lambda_d/4$ ($\lambda_d = 780$ nm) and the chosen periodicity. The wafer on which the Au gratings were etched is composed of silicon topped with 10 nm Ti and 20 nm Pt, whereas no adhesion layer was required for an Al grating. These are then sputter coated with a variable thickness coating layer. The geometry of the etch can vary between 1D and 2D gratings, as illustrated in the scanning electron microscope images in Figs. 2(a) and 2(b), respectively. The 2D grating produces four first-order diffracted terms compared to the two produced in a 1D geometry.

To produce the ideal grating, a thorough investigation of how fabrication parameters affect the diffraction efficiency is

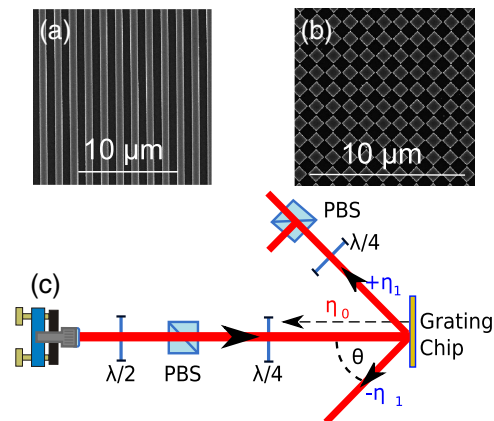**Fig. 2.** (a) and (b) Scanning electron microscope images of 1D and 2D gratings, respectively. (c) Setup used for grating efficiency and polarization purity analysis. Abbreviations are $\lambda/2$ and $\lambda/4$ for the half and quarter wave-plates, respectively, PBS for polarizing beam splitter, η_i represents the relative power in the ith order of diffraction, and θ is the angle of diffraction.

required. To determine the optimum settings for future diffraction gratings, we commissioned the construction of over one hundred 2 mm × 2 mm gratings, produced with a variety of periodicities, duty cycles, geometrical layouts, coating metals, and coating thicknesses. In order to measure the properties of the large quantity of diffraction gratings, we constructed a dedicated testing station with incident-collimated, circularly polarized light of known wavelength and power, as can be seen in Fig. 2.

Once the grating was mounted in the setup, the zeroth order was carefully aligned to ensure that the incident light was perpendicular to the grating. The inherent need for this alignment will be discussed later. The position of the diffracted order was noted, and θ measured. This allowed the periodicity to be inferred through the Bragg condition, Eq. (1). The diffracted order is measured for diffracted power, then passes through a $\lambda/4$ plate and polarizing beam splitter (PBS) to measure any degradation of polarization that may have occurred during diffraction. The results of this investigation can be seen in Figs. 3 and 4, and in greater detail in the associated Figs. 7 and 8 (Appendix A), respectively.

Figure 3 depicts how the relative diffracted power and beam intensity balance vary with diffraction angle θ for 1D and 2D gratings. The circles and squares represent gratings with spatial dimension etched:unetched duty cycles over one grating period of 60%:40% and 50%:50%, respectively. Both data sets provided have a coating of 80 nm Au; however, further investigation was carried out into thicker coatings on Au as well as Al, with both 1D and 2D geometries. The results provided in Fig. 3 are typical of all data sets recorded. Associated Figs. 7 and 8 (Appendix A) provide detailed diffraction efficiency and polarization purity information, respectively, for 1D and 2D gratings with two different thicknesses of gold and aluminum coatings. Moreover, Fig. 7 also shows that for the 1D gratings, gold with a thin 20 nm alumina coating has similar reflectivity to plain gold. The purpose of the alumina coating was to introduce a layer between the Au surface of the grating and the

Rb metal vapor inside the vacuum system, which corrodes the Au.

The first point of interest is the decrease of the diffracted order relative to diffraction angle. As the first order decreases, the light in the zeroth order increases at the same rate, maintaining a close to constant total power. This decay is weaker in the gratings with the 60%:40% duty cycle, making this the preferable choice to the 50%:50% duty cycle. Analysis of experimental data proved that a thicker coating material causes no notable change in the 1D gratings. However, the diffraction efficiency was seen to increase by $\approx$ 10% when twice the coating thickness was applied to 2D gratings. A gold coating produces a stronger diffracted order than that of the aluminum of a similar coating depth due to the higher reflectivity of gold. The results from the duty cycle are conclusive that the 60%:40% duty cycle produces a lower zeroth order and higher diffraction efficiency. The reasoning for this is not completely understood, but may be related to the effective duty cycle of the coating, as opposed to the etched wafer [22].

Figure 3 also illustrates the balance of light forces from Eq. (6) for the respective geometry of the gratings' intended use as a function of the diffraction angle. Axial balance between the incident downward beam and diffracted upward orders is achieved at 100% in Fig. 3. This balancing force is notably higher in the 1D gratings compared to the 2D gratings, as the 1D gratings only diffract into 2 beams rather than 4. However, with the appropriate filtering of the incident beam, this can be overcome to produce the well-balanced radiation forces [15] required for laser cooling [25,26]. Using a 4-beam configuration with a linear grating provides close to ideal balance already without the need for further adaptations to the apparatus. The results are typical of 1D and 2D gratings. Testing was also carried out on Au-coated gratings with a top layer of alumina. Although there was no difference in diffraction efficiency between the gratings with and without the alumina, the additional layer was observed to degrade the polarization purity of the diffracted order (Fig. 4).
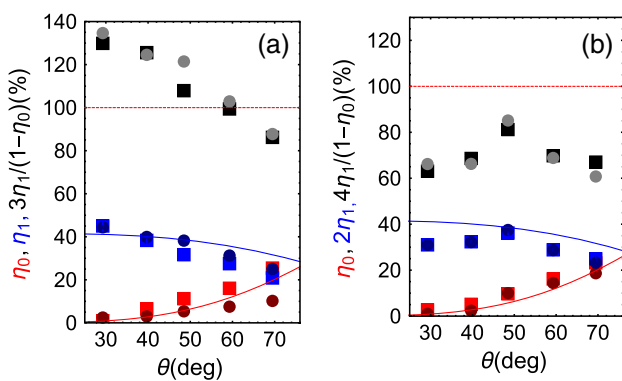
Fig. 3. Diffraction angle versus radiation balance and diffraction efficiency. (a) 1D gratings with 80 nm Au coating. (b) 2D gratings with 80 nm Au coating. Blue and red represent the diffracted (η_1) and reflected (η_0) orders, respectively, with black illustrating the radiation balance for gratings with duty cycles of 40%:60% and 50%:50% (circles and squares). The theory models are based on Eqs. (3) and (4) (solid curves).
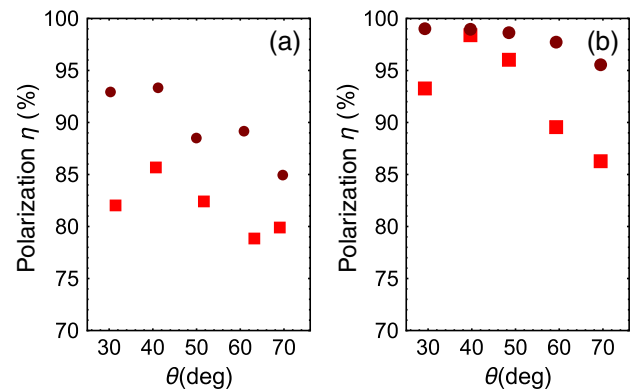
Fig. 4. Diffraction angle versus polarization purity. (a) 1D gratings with 80 nm Au and alumina layer. (b) 1D gratings with 80 nm Au. Associated Fig. 8 (Appendix A) provides detailed polarization efficiency information for 1D and 2D gratings with two different thicknesses of gold and aluminum coatings. Figure 8 also shows the effect of the 20 nm alumina coating for three sets of 1D grating chips. In all images, duty cycles of 60%:40% and 50%:50% are indicated by circles and squares, respectively.

The polarization purity η refers to the ratio of correctly handed circular light (for MOT operation) to total light after the polarization analyzer PBS [Fig. 2(c)] in the first diffracted order. When measured against the periodicity, this purity was typically above 95% for a 60%:40% duty cycle (circles). The lower duty cycle of 50%:50% (squares) consistently produced a weaker purity, which was noted to worsen in the case of an alumina coating. This side effect of using alumina coating could be mildly detrimental to experiments requiring in-vacuo gratings, as the trapping force is proportional to $2\eta - 1$ [11]. An interesting point to note is that a circular polarization purity of 90% can be achieved with an elliptically polarized beam with an intensity ratio of $4:1$ in the two perpendicular polarization components [11].

4. EXPERIMENT: LOST LIGHT

As has been pointed out with the diffraction efficiency data, the total power measured in the diffracted orders fell short of the incident power by $\approx 18\%$. The theoretical reasoning for this can be conceived as the shadowing of the beam [21] or diffraction losses in the pits of the grating. Here, we discuss experimental measurements of the losses. An initial investigation into the elusive light was carried out through the investigation of the absorption profile of a grating by measuring the transfer of light
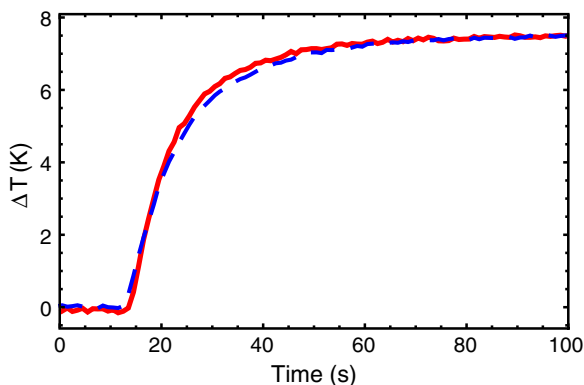

Fig. 5. Absorption rate of 1D Au-coated grating heated with laser light (red) and calibrated with Ohmic heating (dashed blue).

to heat. For this, a small thermistor was well insulated to the back of a 4 mm × 4 mm Au-coated diffraction grating to read out the heating rate of the grating with a known incident laser power. This absorption rate can be seen in Fig. 5.

To calibrate the grating heating to a known power, Ohmic heating was applied through a 1.5 kΩ resistor thermally attached to the back of the grating, separate from the thermistor. This resistor was connected in series to a voltage supply to deposit known amounts of power onto the grating while measuring the heating rate. This Ohmic heating rate was then matched to that of the laser heating to determine the amount of laser power absorbed by the grating during the heating process.

In order to account for thermal gradients in the area of the grating, the measurement procedure was also carried out for a plain Au-coated wafer. Since plain Au has a known 3% absorption at 780 nm [27], we could use this to account for thermal gradients in the measurement area, which could then be applied to the grating data. Applying this correction factor allows us to deduce that $12 \pm 2\%$ of incident light is absorbed by the diffraction grating.

A further study into the possibility of the missing light being scattered was carried out to see if fabrication imperfections were projecting light into unwanted diffraction angles [28]. This was carried out by taking long exposure images around a 90° plane of diffraction and normalizing the range of exposure times to determine the relative power in the minuscule peaks found. The data from this proved that <1% of lost light was being scattered by the grating.

5. EXPERIMENT: CRITICAL PARAMETERS

When implementing the diffraction grating into an experimental setup, it is mounted perpendicular to the incident beam; however, the extent to which this angle of incidence can be varied is an important consideration. We investigated the angle sensitivity using the same setup as in Fig. 2(c), with a variable tilt applied to the grating mount. While in this configuration, a known amount of light was incident upon the grating, held at a variable tilt angle while the diffracted orders where measured. This procedure was carried out for both 1D and 2D gratings, the results of which are seen in Figs. 6(a) and 6(b).
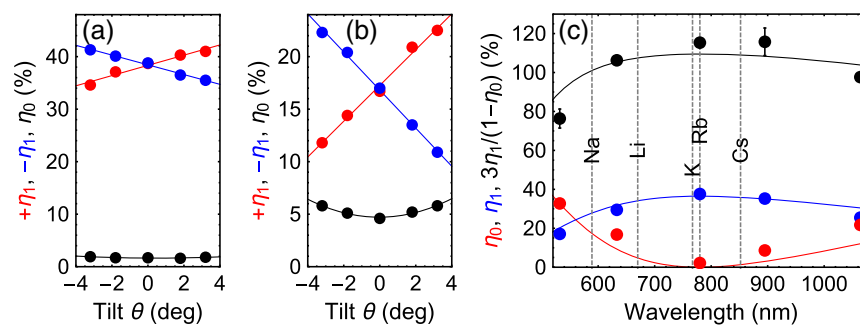
Fig. 6. Left: The grating angle tilt versus the power in the relative diffracted orders with simple linear/parabolic fits for (a) Al 1D grating, $d = 1478$ nm and (b) Au 2D grating, $d = 1056$ nm. (c) Using the same grating as in (a), the wavelength of incident light is varied and recorded against the powers of first and zeroth diffracted orders and fitted against the theory from Eq. (5). Black data points represent the intensity balance from Eq. (6). The same setup as in Fig. 2 was used, except the $\lambda/4$ wave-plates were replaced by Fresnel rhombs due to their achromatic retardance. The alkali D_2 line wavelengths typically used for laser cooling are indicated by dashed vertical lines, showing wide grating versatility.

The blue and red data sets represent the opposite first diffracted orders, with black representing the zeroth, with best fitting lines and parabolas applied. Figures 6(a) and 6(b) demonstrate that a small deviation from 90° will symmetrically imbalance the first diffracted orders and increase the unwanted zeroth order. This asymmetry versus angle is markedly more for 2D gratings (b) in comparison to 1D gratings (a).

It would also be of importance to know how the diffraction gratings' diffracted efficiency varies with the wavelength of incident light, as a wide bandwidth of wavelengths could unlock alkaline earth metals as possible species to be used in the grating

MOT configuration. Additionally, knowing the dependence upon λ would also provide an understanding of the etch depth, where $h = \lambda/4$. For this investigation, the same setup was used as in Fig. 2, with five different lasers covering the range of wavelengths seen in Fig. 6(c). The red and blue data points depict the measurements of first and zeroth diffracted orders, with the fits derived from Eq. (5). The black data points again depict the intensity balance from Eq. (6). As is illustrated, the grating would deliver reasonably balanced cooling within ± 200 nm of the design wavelength of 780 nm and would be useful for cooling a variety of alkali metals.

Fig. 7. Diffraction efficiency for 1D (upper row), 1D alumina coated (middle row), and 2D (lower row) gratings, color scheme as per Fig. 3.

6. CONCLUSIONS AND OUTLOOK

In summary, we have presented our findings on producing next-generation diffraction gratings for cold-atom experiments. This study has illustrated the preferred fabrication parameters for optimizing the grating diffraction efficiency and polarization purity.

We conclude that future gratings should be created with a higher duty cycle, as was seen from our study between 50%:50% and 60%:40% duty cycles. The study of coating thickness has also demonstrated that for the 2D geometry, the thicker coating metal is preferable for higher diffraction efficiency. If an additional coating of alumina is placed on top of the grating for use within a vacuum system, then a degradation of the polarization purity is noted. However, the efficiency of the weaker polarization, with the correct duty cycle, does not hinder the creation of a MOT.

Finally, the critical parameters discussed demonstrate that, when implemented experimentally, the grating should be as

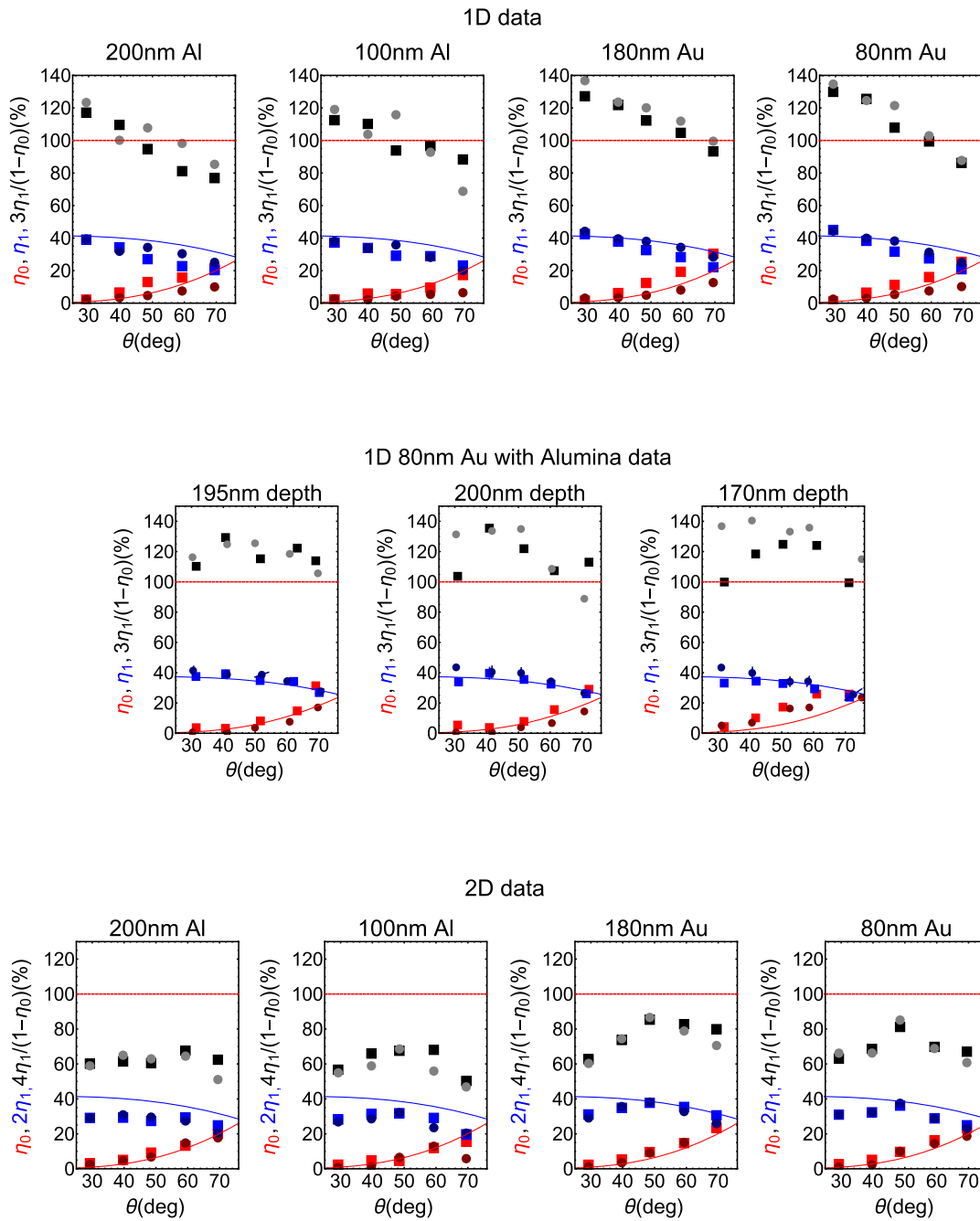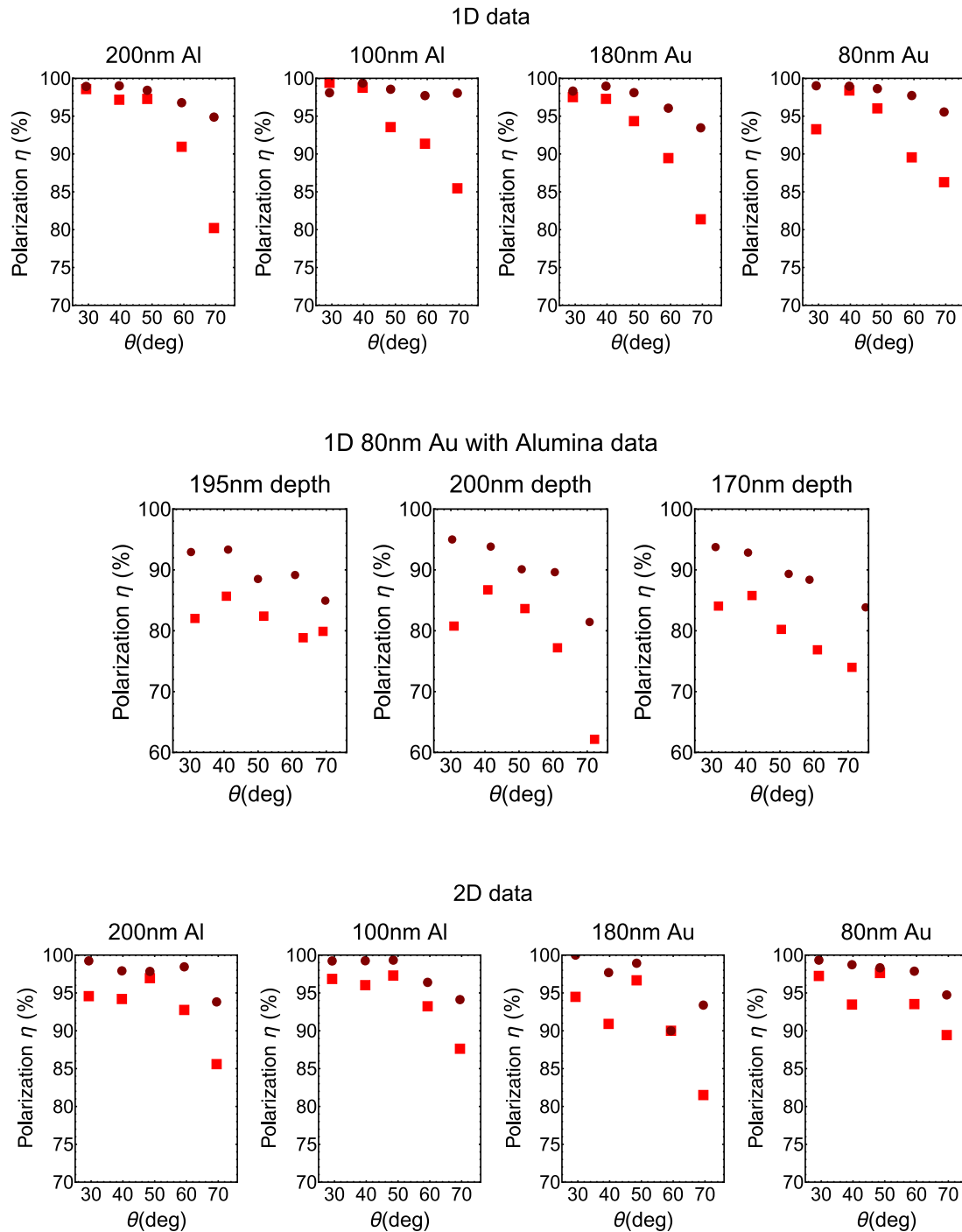**Fig. 8.**   Polarization purity for 1D (upper row), 1D alumina coated (middle row), and 2D (lower row) gratings, color scheme as per Fig. 4.

close to perfectly perpendicular as possible to maintain balance between the diffracted orders, especially for the 2D gratings. The study of the wavelength demonstrates broadband diffractive efficiency, opening the door to the cooling of elements on multiple atomic transitions. The dataset for this paper is available at [29].

APPENDIX A: CHARACTERIZING GRATING DIFFRACTION AND POLARIZATION EFFECTS VERSUS COATING

Please see Figs. 7 and 8.

REFERENCES

1. M. Takamoto, F. L. Hong, R. Higashi, and H. Katori, "An optical lattice clock," Nature **435**, 321–324 (2005).
2. C. Deutsch, F. Ramirez-Martinez, C. Lacroûte, F. Reinhard, T. Schneider, J. N. Fuchs, F. Piéchon, F. Laloë, J. Reichel, and P. Rosenbusch, "Spin self-rephasing and very long coherence times in a trapped atomic ensemble," Phys. Rev. Lett. **105**, 020401 (2010).
3. N. Poli, F. Y. Wang, M. G. Tarallo, A. Alberti, M. Prevedelli, and G. M. Tino, "Precision measurement of gravity with cold atoms in an optical lattice and comparison with a classical gravimeter," Phys. Rev. Lett. **106**, 038501 (2011).
4. C. Gross, T. Zibold, E. Nicklas, J. Estève, and M. K. Oberthaler, "Nonlinear atom interferometer surpasses classical precision limit," Nature **464**, 1165–1169 (2010).
5. S. Bize, P. Laurent, M. Abgrall, H. Marion, I. Maksimovic, L. Cacciapuoti, J. Grunert, C. Vian, F. Pereira dos Santos, P. Rosenbusch, P. Lemonde, G. Santarelli, P. Wolf, A. Clairon, A. Luiten, M. Tobar, and C. Salomon, "Cold atom clocks and applications," J. Phys. B **38**, S449–S468 (2005).
6. B. J. Bloom, T. L. Nicholson, J. R. Williams, S. L. Campbell, M. Bishof, X. Zhang, W. Zhang, S. L. Bromley, and J. Ye, "An optical lattice clock with accuracy and stability at the 10^{-18} level," Nature **506**, 71–75 (2014).
7. M. E. Zawadzki, P. F. Griffin, E. Riis, and A. S. Arnold, "Spatial interference from well-separated split condensates," Phys. Rev. A **81**, 043608 (2010).
8. P. D. D. Schwindt, S. Knappe, V. Shah, L. Hollberg, J. Kitching, L. A. Liew, and J. Moreland, "Chip-scale atomic magnetometer," Appl. Phys. Lett. **85**, 6409–6411 (2004).
9. E. L. Raab, M. Prentiss, A. Cable, S. Chu, and D. E. Pritchard, "Trapping of neutral Sodium atoms with radiation pressure," Phys. Rev. Lett. **59**, 2631–2634 (1987).
10. C. Monroe, W. Swann, H. Robinson, and C. Wieman, "Very cold trapped atoms in a vapor cell," Phys. Rev. Lett. **65**, 1571–1574 (1990).
11. M. Vangeleyn, P. F. Griffin, E. Riis, and A. S. Arnold, "Laser cooling with a single laser beam and a planar diffractor," Opt. Lett. **35**, 3453–3455 (2010).
12. C. C. Nshii, M. Vangeleyn, J. P. Cotter, P. F. Griffin, E. A. Hinds, C. N. Ironside, P. See, A. G. Sinclair, E. Riis, and A. S. Arnold, "A surface-patterned chip as a strong source of ultracold atoms for quantum technologies," Nat. Nanotechnol. **8**, 321–324 (2013).
13. M. Vangeleyn, P. F. Griffin, E. Riis, and A. S. Arnold, "Single-laser, one beam, tetrahedral magneto-optical trap," Opt. Express **17**, 13601–13608 (2009).
14. F. Shimizu, K. Shimizu, and H. Takuma, "Four-beam laser trap of neutral atoms," Opt. Lett. **16**, 339–341 (1991).
15. J. P. McGilligan, P. F. Griffin, E. Riis, and A. S. Arnold, "Phase-space properties of magneto-optical traps utilising micro-fabricated gratings," Opt. Express **23**, 8948–8959 (2015).
16. J. A. Rushton, M. Aldous, and M. D. Himsworth, "The feasibility of a fully miniaturized magneto-optical trap for ultracold quantum technology," Rev. Sci. Instrum. **85**, 121501 (2014).
17. J. Lee, J. A. Grover, L. A. Orozco, and S. L. Rolston, "Sub-Doppler cooling of neutral atoms in a grating magneto-optical trap," J. Opt. Soc. Am. B **30**, 2869–2874 (2013).
18. R. Szmuk, V. Dugrain, W. Maineult, J. Reichel, and P. Rosenbusch, "Stability of a trapped atom clock on a chip," Phys. Rev. A **92**, 012106 (1985).
19. M. A. Golub and A. A. Friesem, "Effective grating theory for resonance domain surface-relief diffraction gratings," J. Opt. Soc. Am. A **22**, 1115–1126 (2005).
20. E. G. Loewen, D. Maystre, R. C. McPhedran, and I. Wilson, "Correlation between efficiency of diffraction gratings and theoretical calculations over a wide range," J. Appl. Phys. **14**, 143–152 (1975).
21. J. P. Cotter, J. P. McGilligan, P. F. Griffin, I. M. Rabey, K. Docherty, E. Riis, A. S. Arnold, and E. A. Hinds, arXiv:1601.05548 (2016).
22. C. A. Palmer and E. G. Loewen, *Diffraction Grating Handbook* (Newport Corporation, 2005).
23. A. A. Tseng, C. Kuan, C. D. Chen, and K. J. Ma, "Electron beam lithography in nanoscale fabrication: recent development," IEEE Trans. Electron. Packag. Manuf. **26**, 141–149 (2003).
24. U. D. Zeitner, M. Oliva, F. Fuchs, D. Michaelis, T. Benkenstein, T. Harzendorf, and E.-B. Kley, "High performance diffraction gratings made by e-beam lithography," Appl. Phys. A **109**, 789–796 (2012).
25. S. Chu, L. Hollberg, J. E. Bjorkholm, A. Cable, and A. Ashkin, "Three-dimensional viscous confinement and cooling of atoms by resonance radiation pressure," Phys. Rev. Lett. **55**, 48–51 (1985).
26. J. Dalibard and C. Cohen-Tannoudji, "Laser cooling below the Doppler limit by polarization gradients: simple theoretical models," J. Opt. Soc. Am. B **6**, 2023–2045 (1989).
27. V. R. Weidner and J. J. Hsia, "NBS measurement services: spectral reflectance," in *Center for Radiation Research* (National Measurement Laboratory, 1987).
28. T. N. Woods, R. T. Wrigley III, G. J. Rottman, and R. E. Haring, "Scattered-light properties of diffraction gratings," Appl. Opt. **33**, 4273–4285 (1994).
29. dx.doi.org/10.15129/9da656b2-32e8-4396-a683-deda1d63d291.

Appendix E

Publication: Phase-space properties of magneto-optical traps utilising micro-fabricated gratings.

Phase-space properties of magneto-optical traps utilising micro-fabricated gratings.

J. P. McGilligan, P. F. Griffin, E. Riis, and A. S. Arnold[*]

Dept. of Physics, SUPA, University of Strathclyde, Glasgow G4 0NG, UK

[*]aidan.arnold@strath.ac.uk

Abstract: We have used diffraction gratings to simplify the fabrication, and dramatically increase the atomic collection efficiency, of magneto-optical traps using micro-fabricated optics. The atom number enhancement was mainly due to the increased beam capture volume, afforded by the large area ($4\,\text{cm}^2$) shallow etch ($\sim 200\,\text{nm}$) binary grating chips. Here we provide a detailed theoretical and experimental investigation of the on-chip magneto-optical trap temperature and density in four different chip geometries using ^{87}Rb, whilst studying effects due to MOT radiation pressure imbalance. With optimal initial MOTs on two of the chips we obtain both large atom number (2×10^7) *and* sub-Doppler temperatures ($50\,\mu\text{K}$) after optical molasses.

© 2015 Optical Society of America

OCIS codes: (020.3320) Laser cooling; (020.7010) Laser trapping.

References and links

1. S. Chu, L. Hollberg, J. E. Bjorkholm, A. Cable, and A. Ashkin, "Three-dimensional viscous confinement and cooling of atoms by resonance radiation pressure," Phys. Rev. Lett. **55**, 48–51 (1985).
2. E. L. Raab, M. Prentiss, A. Cable, S. Chu, and D. E. Pritchard, "Trapping of neutral sodium atoms with radiation pressure," Phys. Rev. Lett. **59**, 2631–2634 (1987).
3. C. Monroe, W. Swann, H. Robinson, and C. Wieman, "Very cold trapped atoms in a vapor cell," Phys. Rev. Lett. **65**, 1571–1574 (1990).
4. Z. Hu and H. J. Kimble, "Observation of a single atom in a magneto-optical trap," Opt. Lett. **19**, 1888–1890 (1994).
5. G. Labeyrie, E. Tesio, P. M. Gomes, G. L. Oppo, W. J. Firth, G. R. M. Robb, A. S. Arnold, R. Kaiser, and T. Ackemann, "Optomechanical self-structuring in a cold atomic gas," Nature Phot. **8**, 321–325 (2014).
6. A. Camara, R. Kaiser, and G. Labeyrie, "Behavior of a very large magneto-optical trap," Phys. Rev. A **90**, 063404 (2014).
7. J. Miao, J. Hostetter, G. Stratis, and M. Saffman, "Magneto-optical trapping of holmium atoms," Phys. Rev. A **89**, 041401 (2014).
8. J. F. Barry, D. J. McCarron, E. B. Norrgard, M. H. Steinecker, and D. DeMille, "Magneto-optical trapping of a diatomic molecule," Nature **512**, 286–289 (2014).
9. C. C. Nshii, M. Vangeleyn, J. P. Cotter, P. F. Griffin, E. A. Hinds, C. N. Ironside, P. See, A. G. Sinclair, E. Riis, and A. S. Arnold, "A surface-patterned chip as a strong source of ultracold atoms for quantum technologies," Nature Nanotech. **8**, 321-324 (2013).
10. S. Pollock, J. P. Cotter, A. Laliotis, and E. A. Hinds, "Integrated magneto-optical traps on a chip using silicon pyramid structures," Opt. Express **17**, 14109–14114 (2009).
11. S. Pollock, J. P. Cotter, A. Laliotis, F. Ramirez-Martinez, and E. A. Hinds, "Characteristics of integrated magneto-optical traps for atom chips," New J. Phys. **13**, 043029 (2011).
12. M. Vangeleyn, P. F. Griffin, E. Riis, and A. S. Arnold, "Single-laser, one beam, tetrahedral magneto-optical trap," Opt. Express **17**, 13601–13608 (2009).
13. M. Vangeleyn, P. F. Griffin, E. Riis, and A. S. Arnold, "Laser cooling with a single laser beam and a planar diffractor," Opt. Lett. **35**, 3453–3455 (2010).

14. F. Shimizu, K. Shimizu, and H. Takuma, "Four-beam laser trap of neutral atoms," Opt. Lett. **16**, 339–341 (1991).
15. K. I. Lee, J. A. Kim, H. R. Noh, and W. Jhe, "Single-beam atom trap in a pyramidal and conical hollow mirror," Opt. Lett. **21**, 1177–1179 (1996).
16. K. Lindquist, M. Stephens, and C. E. Wieman, "Experimental and theoretical study of the vapor-cell Zeeman optical trap," Phys. Rev. A **46**, 4082–4090 (1992).
17. L. Huet, M. Ammar, E. Morvan, N. Sarazin, J. P. Pocholle, J. Reichel, C. Guerlin, and S. Schwartz, "Experimental investigation of transparent silicon carbide for atom chips," Appl. Phys. Lett. **100**, 121114 (2012).
18. J. Reichel, W. Hänsel, and T. W. Hänsch, "Atomic micromanipulation with magnetic surface traps," Phys. Rev. Lett. **83**, 3398–3401 (1999).
19. W. Hänsel, P. Hommelhoff, T. W. Hänsch, and J. Reichel, "Bose-Einstein condensation on a microelectronic chip," Nature **413**, 498–501 (2001).
20. J. P. Cotter, P. F. Griffin, E. A. Hinds, P. See, A. G. Sinclair, E. Riis and A. S. Arnold, in preparation.
21. P. D. Lett, R. N. Watts, C. I. Westbrook, W. D. Phillips, P. L. Gould, and H. J. Metcalf, "Observation of atoms laser cooled below the Doppler limit," Phys. Rev. Lett. **61**, 169–172 (1998).
22. J. Dalibard and C. Cohen-Tannoudji, "Laser cooling below the Doppler limit by polarization gradients: simple theoretical models," J. Opt. Soc. Am. B **6**, 2023–2045 (1989).
23. D. S. Weiss, E. Riis, Y. Shevy, P. J. Ungar, and S. Chu, "Optical molasses and multilevel atoms: experiment," J. Opt. Soc. Am. B **6**, 2072–2083 (1989).
24. P. D. Lett, W. D. Phillips, S. L. Rolston, C. E. Tanner, R. N. Watts, and C. I. Westbrook, "Optical molasses," J. Opt. Soc. Am. B **6**, 2084–2107 (1989).
25. D. W. Sesko, T. G. Walker, and C. E. Wieman, "Behavior of neutral atoms in a spontaneous force trap," J. Opt. Soc. Am. B **8**, 946–958 (1991).
26. W. Ketterle, K. B. Davis, M. A. Joffe, A. Martin, and D. E. Pritchard, "High densities of cold atoms in a dark spontaneous force optical trap," Phys. Rev. Lett. **70**, 2253–2256 (1993).
27. A. S. Arnold and P. J. Manson, "Atomic density and temperature distributions in magneto-optical traps," J. Opt. Soc. Am. B **17**, 497–506 (2000).
28. N. Radwell, G. Walker, and S. Franke-Arnold, "Cold-atom densities of more than $10^{12} \, cm^{-3}$ in a holographically shaped dark spontaneous-force optical trap," Phys. Rev. A **88**, 043409 (2013).
29. C. D. Wallace, T. P. Dinneen, K-Y. N. Tan, T. T. Grove, and P. L. Gould, "Isotopic difference in trap loss collisions of laser cooled rubidium atoms," Phys. Rev. Lett. **69** 897–900 (1992).
30. A. S. Arnold, Fig. 4.12 (DPhil thesis, Sussex, 1999).
31. K. Jooya, N. Musterer, K. W. Madison, and J. L. Booth, "Photon-scattering-rate measurement of atoms in a magneto-optical trap," Phys. Rev. A **88**, 063401 (2013).
32. C. G. Townsend, N. H. Edwards, C. J. Cooper, K. P. Zetie, C. J. Foot, A. M. Steane, P. Szriftgiser, H. Perrin, and J. Dalibard, "Phase-space density in the magneto-optical trap," Phys. Rev. A **52**, 1423–1440 (1995).
33. M. Drewsen, P. H. Laurent, A. Nadir, G. Santarelli, A. Clairon, Y. Castin, D. Grison, and C. Salomon, "Investigation of sub-Doppler cooling effects in cesium magneto-optical trap," Appl. Phys. B **59**, 283–298 (1994).
34. C. J. Cooper, G. Hillenbrand, J. Rink, C. G. Townsend, K. Zetie, and C. J. Foot, "The temperature of atoms in a magneto-optical trap," Europhys. Lett. **28**, 397–402 (1994).
35. N. Poli, M. Schioppo, S. Vogt, St. Falke, U. Sterr, Ch. Lisdat, and G. M. Tino "A transportable strontium optical lattice clock," Appl. Phys. B **117**, 1107–1116 (2014).
36. F.-X. Esnault, E. Blanshan, E. N. Ivanov, R. E. Scholten, J. Kitching, and E. A. Donley, "Cold-atom double-Λ coherent population trapping clock," Phys. Rev. A **88**, 042120 (2013).
37. J. A. Rushton, M. Aldous, and M. D. Himsworth, "The feasibility of a fully miniaturized magneto-optical trap for portable ultracold quantum technology," Rev. Sci. Instrum. **85**, 121501 (2014).
38. J. P. McGilligan, P. F. Griffin, E. Riis, and A. S. Arnold, in preparation (2015).
39. J. Lee, J. A. Grover, L. A. Orozco, and S. L. Rolston, "Sub-Doppler cooling of neutral atoms in a grating magneto-optical trap," J. Opt. Soc. Am. B **30**, 2869–2874 (2013).

---

1. Introduction

Laser cooling [1] revolutionised atomic physics by making it possible to rapidly and robustly chill dilute clouds of atoms to below a millionth of room temperature. At such slow speeds it is possible to observe and interact with atoms a thousand times longer. This makes measurements of atomic transitions correspondingly more accurate, suitable for advanced quantum metrological devices. The starting point for the majority of cold atom experiments is a magneto-optical trap (MOT) [2, 3]. A MOT both cools and traps atoms surrounded in red-detuned laser light via changes in the overall radiation pressure due to the Doppler and Zeeman effects, respectively. MOTs contain from one [4] to $\approx 10^{11}$ [5, 6] atoms at milliKelvin typical temperatures,

and the atomic species cooled usually has a simple energy level structure – which covers all alkali metals, alkaline earth species and metastable noble gases. Other atomic species can also be very effectively cooled (e.g. holmium [7]), and very recently the first molecular MOT was obtained [8].

We have recently highlighted the benefits of using surface-patterned chips to make MOTs with relatively large numbers of ultracold atoms [9], compared to prior micro-fabricated magneto-optical traps (MOTs) [10, 11]. The design requires only the alignment of a single input laser beam, and extends our previous work on tetrahedral mirror [12] and grating [13] geometries, which are four-beam [14] equivalents of pyramidal MOTs [15]. Figure 1 depicts a 'like-for-like' graphical comparison of the optical setup in a standard 6-beam MOT (Fig. 1(a) [2, 16, 17]), a mirror MOT (Fig. 1(b) [18, 19]) and a grating MOT (GMOT, Fig. 1(c) [9]).

Here we study the atom-number characteristics of four different chip systems, and more complete details of different fabrication methods for the chips are discussed by Cotter *et al.* [20]. The two chip geometries we used are shown in Fig. 2. One chip style (Fig. 2(a)) comprises three one-dimensional gratings arranged in a pattern with 3-fold rotational symmetry (we used chips with periods of $d = 1470$ nm and $d = 1200$ nm). The other chip style (Fig. 2(b)) is a two-dimensional grating generated with circular regions centred in square units cells of side length $d = 1080$ nm. Hereafter the chips will be referred to as TRI_{15}, TRI_{12} (Fig. 2(a)) and CIR (Fig. 2(b)). Although we have used chips TRI_{15} and CIR previously (chips B and C in Nshii *et al.* [9]), purely for number characterisation, here we present density and temperature data for these chips. Moreover, we also investigate MOTs with improved capture efficiency for the 1D structure (i.e. the new chip TRI_{12}) and improved radiation balance for the 2D structure (chip CIR_{ND}: identical to CIR but with an input beam intensity spatially sculpted with a neutral density filter – for which the rationale is given in Sec. 4).

We begin by introducing simple theoretical models for the MOT temperature (Sec. 2) and atom number (Sec. 3), then consider the amelioration of any effects caused by imbalanced radiation pressure in grating MOTs (Sec. 4). We then present the experimental data (Sec. 5),

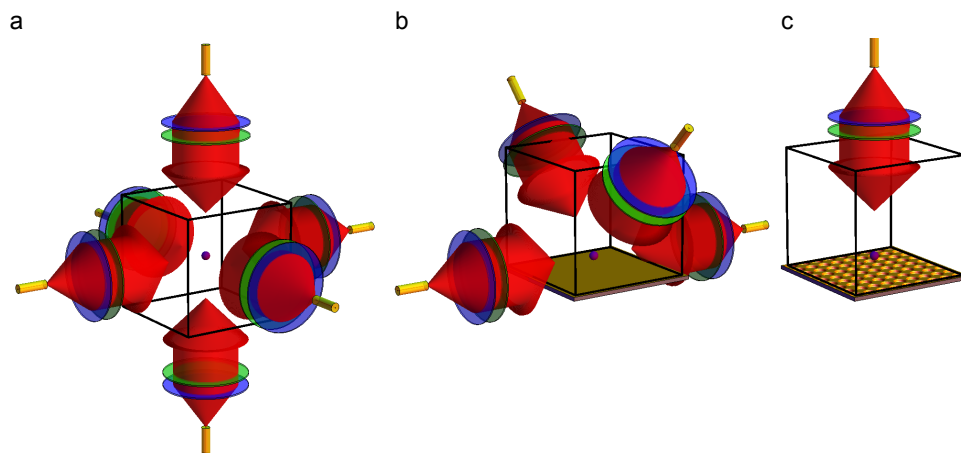

Fig. 1. Magneto-optical trap geometries: six-beam MOT (a), reflection MOT (b) and grating MOT (c). The black cuboid indicates a vacuum cell, yellow fibers deliver cooling and repumping light (red) which is collimated by lenses (blue) and appropriately circularly-polarised with quarter waveplates (green). The vacuum pump, atom source, anti-Helmholtz magnetic coils etc. are omitted for clarity.
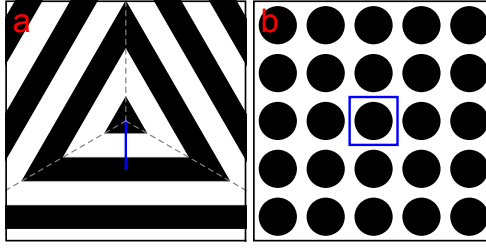
Fig. 2. The 'zoomed in' microstructure on the different $2 \times 2\,\text{cm}^2$ chips used in our studies. The black and white zones are separated by a height difference of $\sim 200\,\text{nm}$, one quarter of the wavelength of the rubidium cooling light (780 nm). Chips TRI$_{15}$ and TRI$_{12}$ have the pattern shown in (a), comprising three one-dimensional gratings with period d (blue line) of 1470 and 1200 nm, respectively. The other chip, CIR, has the pattern shown in (b), with a grating unit cell (blue square) side length $d = 1080\,\text{nm}$. First order Bragg-diffracted beams have angles $32°$ (TRI$_{15}$), $41°$ (TRI$_{12}$), $46°$ (CIR) with respect to the chip surface normal.

comparing and contrasting with the theoretical predictions. Finally we present 'best of both worlds' findings (Sec. 6) – by permitting analog temporal evolution of both MOT intensity and detuning we go beyond Nshii *et al.* [9] to achieve high atom numbers and sub-Doppler temperatures *simultaneously* using both 1D and 2D grating structures.

2. Theory: Doppler temperature

Whilst sub-Doppler cold atom temperatures can be reached in optical molasses (Sec. 6) [21–23], the conditions for atom collection in a MOT are in stark contrast to those required to reach the lowest temperatures: a MOT needs high beam intensities relative to the saturation intensity ($I \gg I_S$), detuning of a few natural linewidths $\Delta \approx -2\Gamma$ and a magnetic gradient $\approx 10\,\text{G/cm}$ for a typical alkali metal vapour cell MOT with 25 mm beam diameter. For this reason the considerably simpler Doppler theory is a good description for our MOT temperature. The standard 3D Doppler result for a sample of atoms uniformly and isotropically illuminated in three dimensions by light of total intensity I_T, with corresponding saturation parameter $\beta_T = I_T/I_S$, and detuning Δ [24] is:

$$T_U = T_D \frac{1 + \beta_T + 4\Delta^2/\Gamma^2}{-4\Delta/\Gamma}, \tag{1}$$

where $T_D = \frac{\hbar\Gamma}{2k_B}$. In our ^{87}Rb experiment we cool using the rubidium D2 transition which has a natural linewidth $\Gamma = 2\pi \times 6.07\,\text{MHz}$. The standard Doppler temperature minimum in the limit of low intensity and detuning $\Delta = -\Gamma/2$ is T_D, i.e. $146\,\mu\text{K}$ for rubidium, with the more general lowest temperature $T_D\sqrt{1 + \beta_T}$ minimised at a detuning $\Delta = -\sqrt{1 + \beta_T}\,\Gamma/2$. Throughout this paper, for consistency, we use the saturation intensity averaged over all polarisations and magnetic sub-levels $I_S = 3.57\,\text{mW/cm}^2$ – however we note that using the stretched state saturation intensity $I_S = 1.67\,\text{mW/cm}^2$ for the theoretical temperature of Eq. (1) leads to much better agreement with our experimentally measured temperatures (Sec. 5).

Although the velocity distribution in a magneto-optical trap is Gaussian, the system is by no means in thermal equilibrium in the usual sense, with the typical light scattering rate from atoms vastly larger than the interatomic elastic collision rate. The final 'temperature' in a given direction is given by the balance between the heating (cf. diffusion coefficient and light scattering rate) and the velocity damping constant γ. In our system the effective temperature parallel to and perpendicular to the grating are therefore expected to be different.

For our gratings if the incident beam has a spatially uniform intensity I_0 and wavevector $\mathbf{k}_0 = k\{0,0,-1\}$, for balanced optical pressure from N diffracted orders each should ideally carry an intensity of $I_i = I_0/(N\cos\alpha)$ with $i \in \{1,...,N\}$. The wavevectors of the diffracted beams are $\mathbf{k}_i = k\{\sin\alpha\sin\frac{2\pi i}{N}, \sin\alpha\cos\frac{2\pi i}{N}, \cos\alpha\}$, where α is the angle the diffracted orders make to the grating normal $\{0,0,1\}$ ($\alpha = 2\theta$ cf. [12, 13]). The total intensity is therefore $I_T = \sum_{i=0}^{N} I_i = (1+\sec\alpha)I_0$, with each beam of intensity I_i contributing a relative intensity-dependent heating proportional to its intensity along the beam direction due to absorption, and an equal associated heating rate due to spontaneous emission. The heating from spontaneous emission is assumed for simplicity to be isotropic, with the heating rate for light with a wavevector $\mathbf{k}_i = \{k_{i_x}, k_{i_y}, k_{i_z}\}$ proportional to $\hbar^2 R_i k^2 \{\frac{1}{3}, \frac{1}{3}, \frac{1}{3}\}$ in the x, y and z dimensions, for a scattering rate

$$R_i(\mathbf{v}) = \frac{\Gamma}{2}\frac{I_i/I_S}{1+\beta_T+4(\Delta-\mathbf{k}_i\cdot\mathbf{v})^2/\Gamma^2}, \text{ with } R_i(\mathbf{0}) = \frac{I_i}{I_S}R = \beta_i R. \tag{2}$$

Assuming dipolar (as opposed to isotropic) spontaneous emission from a circularly polarised atom adds complexity and does not significantly alter the predicted temperatures. The heating due to absorption is apportioned $\hbar^2 R_i\{k_{i_x}{}^2, k_{i_y}{}^2, k_{i_z}{}^2\}$ in the three spatial dimensions. The total heating rate near zero velocity in each dimension is thus:

$$\mathbf{D} = \sum_{i=0}^{N} \hbar^2 \beta_i R \left\{ k_{i_x}{}^2 + \frac{k^2}{3}, k_{i_y}{}^2 + \frac{k^2}{3}, k_{i_z}{}^2 + \frac{k^2}{3} \right\} \tag{3}$$

which simplifies to

$$\mathbf{D} = \hbar^2 k^2 \frac{I_0}{6I_S} R \left(\{2,2,8\} + \sec\alpha \left\{ 3\sin^2\alpha + 2, 3\sin^2\alpha + 2, 6\cos^2\alpha + 2 \right\} \right) \tag{4}$$

In balanced laser cooling the relative damping constants can be determined by the Taylor expansion of the total force equation $\mathbf{F} = \sum_{i=0}^{N} \hbar\mathbf{k}_i R_i(\mathbf{v})$ about $\mathbf{v} = \mathbf{0}$. The damping constants in the xy directions ($\gamma_\parallel$ parallel to the grating) and z direction ($\gamma_\perp$ perpendicular to the grating) are thus given by [12]:

$$\begin{aligned}
\mathbf{F}(\mathbf{v}) &\approx -\gamma\cdot\mathbf{v} = -\{\gamma_\parallel v_x, \gamma_\parallel v_y, \gamma_\perp v_z\} \\
\{\gamma_\parallel, \gamma_\perp\} &= \gamma_6 \left\{ \frac{\sin\alpha\tan\alpha}{4}, \frac{1+\cos\alpha}{2} \right\}, \text{ where } \gamma_6 = \frac{-16\hbar I_0 k^2 R\Delta}{I_S\Gamma^2(1+\beta_T+\frac{4\Delta^2}{\Gamma^2})}
\end{aligned} \tag{5}$$

is the damping force in a standard 6-beam MOT. The temperature in each dimension can then be determined as proportional to the ratio of the diffusion $\mathbf{D}$ (Eq. (4)) to the damping γ (Eq. (5)):

$$\{T_\parallel, T_\perp\} = \frac{T_U}{6}\left\{3+\csc^2(\alpha/2), 3+\sec\alpha\right\}, \tag{6}$$

which reduces to the standard isotropic temperature T_U when $\alpha = \arccos(1/3)$. Note this temperature only depends on the grating diffraction angle and not on the number of diffracted orders N.

The temperatures obtained experimentally (Sec. 5) do not reflect the theoretical temperature disparity in the directions parallel and perpendicular to the grating. The model above only includes forces due to absorption of light *directly* from the laser beams, however for MOTs with larger atom number and light scattering rate (like in our experiment), there will be a significant contribution to the forces in the MOT due to the $1/r^2$ repulsion from closely packed atoms with inter-particle spacing r due to absorption of spontaneously emitted light from neighbouring atoms [25–28]. These forces effectively mix the energies across dimensions, creating a more

uniform temperature distribution. The theoretical temperature we use in both dimensions is therefore $T = \frac{2}{3}T_\parallel + \frac{1}{3}T_\perp$, which agrees surprisingly well with experimental values given the simplicity of the model.

For completeness and to determine theoretical MOT density, one can also derive the spring constant κ of the trap, expanding the total force $\mathbf{F}$, but this time relative to position. The α dependencies of the damping constants are $\{\kappa_\parallel, \kappa_\perp\} \propto \{\frac{1}{4}\sin\alpha\tan\alpha, 1 - \cos\alpha\}$, the same as derived by Vangeleyn $et\ al.$ in [12]. The damping therefore reduces to an isotropic $\frac{2}{3}$ $(\frac{1}{3})$ of the standard 6-beam MOT radial (axial) κ values, if the GMOT has $\alpha = \arccos(1/3)$ and laser beams of the same intensity as the standard MOT. Under these conditions the GMOT should be spatially isotropic – it will have equal rms cloud radii as a standard MOT in both directions parallel to the grating, but twice the standard MOT extent in the direction perpendicular to the grating. An important caution against using this Doppler spring constant to determine density, however, is that the experimental spring constant of a trap is notoriously difficult to determine, and the reradiative forces [25–28] discussed in the previous paragraph make simple models of the effective spring constant considerably more difficult.

3. Theory: Doppler atom number

In order to predict the number of atoms in the MOT, we use the standard method of Lindquist $et\ al.$ [16]: treat the MOT as a spherical target region with radius r and cross-section $4\pi r^2$, then find the flux of atoms incident on the target, with speeds less than the capture velocity v_c of the MOT slowing region. In the ideal case of a rubidium-dominated vapour both loading and loss mechanisms are proportional to atomic density, which is therefore irrelevant for calculating atom number. It is necessary to know the collisional cross section of cold atoms as seen by hot atoms, which for rubidium is $\sigma = 2 \times 10^{-17}\,\mathrm{m}^2$ [29] (similar to caesium [16]). We make the assumption of a 1D optical molasses from two counter-propagating laser beams. The total acceleration is modified by a prefactor η to allow for geometric effects:

$$a = v\frac{dv}{dx} = \eta\frac{hk\Gamma I}{2mI_S}\left(\frac{1}{1 + \frac{I_T}{I_S} + 4\frac{(\Delta - kv)^2}{\Gamma^2}} - \frac{1}{1 + \frac{I_T}{I_S} + 4\frac{(\Delta + kv)^2}{\Gamma^2}}\right). \tag{7}$$

By rearranging one arrives at an equation of the form $f(v)dv = Bdx$, where $f(v)$ is a quartic polynomial in v and B is a constant. This equation can then be integrated to analytically determine $x(v)$. The integration constant is chosen such that $x(0) = 0$. Setting $x(v_c) = 2r$ (atoms are stopped over a distance of twice the MOT radius) and subsequently inverting gives v_c, the capture velocity. The total steady-state number of atoms in the MOT is then [16]:

$$N = \frac{4\pi r^2}{8\sigma}\left(\frac{v_c}{v_T}\right)^4, \tag{8}$$

where $v_T = \sqrt{2k_BT/m}$ is a thermal velocity in the (hot) background vapour.

We note that the saturation intensity features in the theoretical temperature and both theoretical and experimental atom number, and we therefore consistently use the saturation intensity averaged over all polarisations and magnetic sub-levels $I_S = 3.57\,\mathrm{mW/cm}^2$, which is valid for small detunings [30,31]. There are, however, arguments for using a value closer to the stretched state saturation intensity $I_S = 1.67\,\mathrm{mW/cm}^2$ [32]. We used this value in our previous work on atom number [9] as a precaution to prevent over-counting the atom number, although for high levels of saturation the effect of changing I_S on experimental atom number is negligible.

4. Theory: Non-uniform beam intensity

In the theory so far we have assumed a spatially uniform incident laser intensity. However, real propagating laser beams tend to have Gaussian spatial intensity profiles. If such intensity distributions are apertured, or their intensity is spatially modified in other respects, as long as the modifications occur on large (centimetre size) beams, diffraction effects can be neglected. While various refractive beam shapers which transform Gaussian beams into flat-top intensity beams are available on the market, these tend to be expensive (albeit power efficient) and designed for relatively small output beam diameters. Spatially shaping a Gaussian beam with radial profile $I = I_0 \exp(-2r^2/w^2)$ using an apodizing filter of outer radius r_a with a neutral density $ND = \exp(2(r^2 - r_a^2)/w^2)$ leads to a uniform beam intensity, with reduced intensity $I_0 \exp(-2r_a^2/w^2)$ across the beam. The relative power in the beam is then $2(r_a/w)^2 \exp(-2r_a^2/w^2)$ which has a maximum of $1/e \approx 37\%$ when the aperture radius is $r_a = w/\sqrt{2}$ – i.e. even under optimal conditions it is a fairly lossy solution.

To determine the effect of Gaussian intensity profiles, we fully integrate the acceleration from a MOT with a single input beam and 3 diffracted orders at diffraction angle $41°$, just like Chip TRI$_{12}$ (Fig. 3). We assume similar parameters to the MOT experiment – a Gaussian input trap beam with intensity $10\,\mathrm{mW/cm^2}$ and detuning $\Delta/\Gamma = -1.7$ apertured to a 12 mm radius and a magnetic quadrupole with axial gradient 15 G/cm. In situations where the beam intensity is spatially uniform (Fig. 3(a)) the radiation pressure balance is uniform throughout the beam-overlap volume. However, with a Gaussian beam intensity profile (Fig. 3(b)), the diffracted orders at the MOT location originate from lower and lower intensity regions of the Gaussian beam as the MOT position is raised from the grating surface. This means that the MOT is pushed downwards more, relative to the magnetic quadrupole centre, as the MOT is raised above the grating surface. Moreover, there is a marked change in the relative trapping and damping constants: $\{\kappa_\parallel, \kappa_\perp, \gamma_\parallel, \gamma_\perp,\} = \{0.21, 0.37, 0.21, 1.31\}$ in Fig. 3(a) and $\{0.10, 0.49, 0.16, 0.96\}$ in Fig. 3(b) (compared to the isotropic values of $\{1, 1, 1, 1\}$ for $\alpha = \arccos(1/3)$ and uniform intensity).

The case of uniform intensity is preferable, as long as one has optimal diffraction efficiency in the gratings, as then the MOT and molasses properties do not depend on MOT position. How-
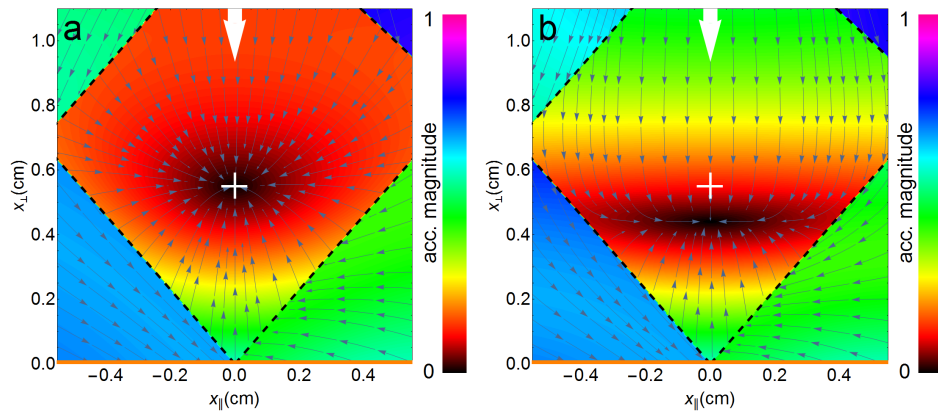
Fig. 3. The full theoretical acceleration above chip TRI$_{12}$, shown both as vector streamlines and magnitude. The white arrow indicates the centre and direction of the beam incident on the grating (gold line at figure base), whereas the white cross indicates the quadrupole magnetic field centre. In figure a, a uniform beam intensity profile is used, whereas in b we use a Gaussian beam with $1/e^2$ radius of $2\,\mathrm{cm}$, like in the experiment. Black dashed lines indicate the boundaries of the beam overlap (capture) volume.

ever, if one uses Gaussian beams and the diffraction efficiency is too high, one can compensate by raising the MOT position to a location where optical forces are balanced and suitable for sub-Doppler cooling. In Sections 5 and 6 with chip CIR_{ND} we show how locally shaping the input beam intensity can dramatically improve both MOT and molasses performance.

5. Experiment

The experimental conditions were very similar to those detailed in the Methods section of Nshii *et al.* [9]. One major difference is that we now have analogue as opposed to binary intensity control, using an acousto-optic modulator (AOM) after our tapered amplifier prior to fiber-coupling. After the MOT reached steady-state atom number, the atoms were ballistically released for 0, 1.5 or 2 ms, and Gaussian fits were used to extrapolate cloud rms radii and thereby MOT temperatures. To build up statistics each drop time was iterated five times. For intensities above and below 10 mW/cm^2 the fluorescent imaging exposure times were 430 μs and 150 μs, respectively.

Figures 4 (Chips TRI_{15} and TRI_{12}) and 5 (Chips CIR and CIR_{ND}) illustrate the intensity- and detuning-dependence of a variety of MOT parameters: theoretical atom number (a), experimental MOT atomic number (b) and spatial density (c) as well as the theoretical Doppler temperature (d) with the temperatures experimentally measured in the directions both parallel (e) and perpendicular (f) to the grating. Note that the theoretical atom number saturates at about three times lower intensity than that observed experimentally – we seem to need three times more laser power experimentally than we would theoretically expect. This discrepancy may be considered relatively minor given the very simple nature of the theoretical model, however we believe further investigation, and full comparison to a standard 6-beam MOT may still be warranted.

In prior measurements of $T_\perp$ on Chip CIR (Fig. 5(f) CIR) there was an even larger discrepancy with theory (very high experimental temperatures) due to imbalanced optical force during the fluorescence imaging. This was determined via the noticeable centre-of-mass velocity accrued in the direction perpendicular to the grating during time-of-flight. In all the new data for Figs. 4 and 5 any imbalanced radiation pressure (mainly for Fig. 5) was balanced using a non-zero magnetic field oriented perpendicular to the grating.

Note the significant increase in atom number ($\times 3$) and density ($\times 6$), with lower atomic temperature on chip TRI_{12} compared to chip TRI_{15} – in future we intend to test gratings with even smaller period (larger diffraction angle) to determine if this trend continues.

6. Experiment: best of both worlds

For many metrological experiments, such as atomic clock measurements, the precision achieved strongly depends upon the temperature and total population of the atomic ensemble. Hence, an understanding of the final number of atoms that can be brought from the MOT stage to ultracold temperatures provides a good indication of the full capability of the GMOT. In Nshii *et al.* [9] we effectively had only binary control of the intensity – this meant we could *either* get a large number of atoms on Chip CIR with high intensity, or good optical molasses on chip TRI_{15} with lower intensity light (and a correspondingly small number of atoms loaded in the MOT).

After analysis of the results presented in Section 5, the most suitable gratings for MOT number and temperature are Chip CIR_{ND} and TRI_{12}. To study the number of atoms that could be brought to sub-Doppler temperatures, a MOT of intensity 40 mW/cm^2 and detuning of $\Delta/\Gamma = -2.2$ (initial MOT indicated by black dots in experimental Figs. 4 TRI_{12} and 5 CIR_{ND}) was transferred into optical molasses. The molasses consisted of turning off trapping magnetic fields, whilst using a two-step frequency jump of $\Delta/\Gamma = -5.3$ and $\Delta/\Gamma = -8.3$, each of duration 12 ms.
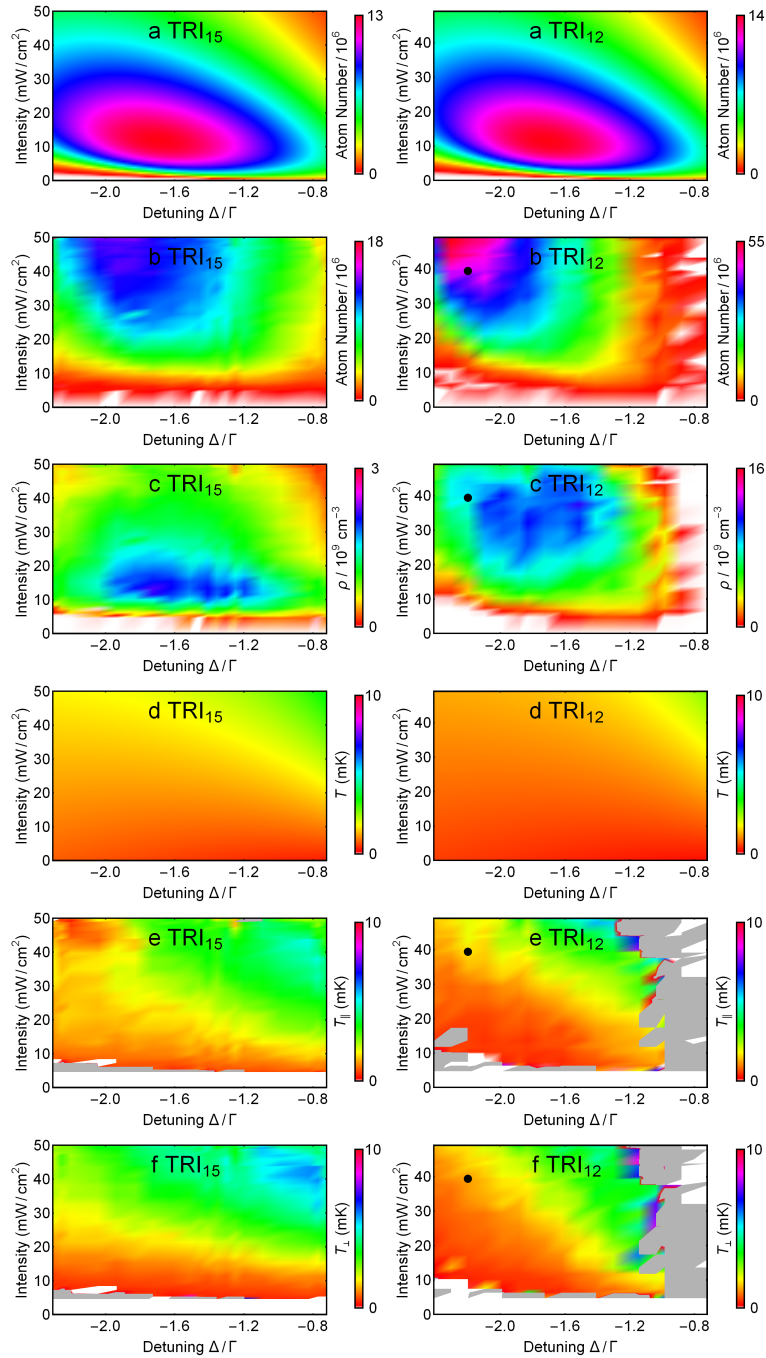
Fig. 4. The full GMOT characterisation when using chips TRI$_{15}$ and TRI$_{12}$ with beam diffraction angles $\alpha = 32°$ and $41°$, respectively. The labels a-f indicate theoretical atom number (a), experimental atom number (b) and spatial density (c), the theoretical temperature (d) and experimental temperatures in directions parallel (e) and perpendicular (f) to the grating. Light gray indicates indeterminate or out-of-range data. Media 1 shows the theoretical temperature (d) for $I_S = 1.67 \, \mathrm{mW/cm^2}$, which has clearer experimental agreement.
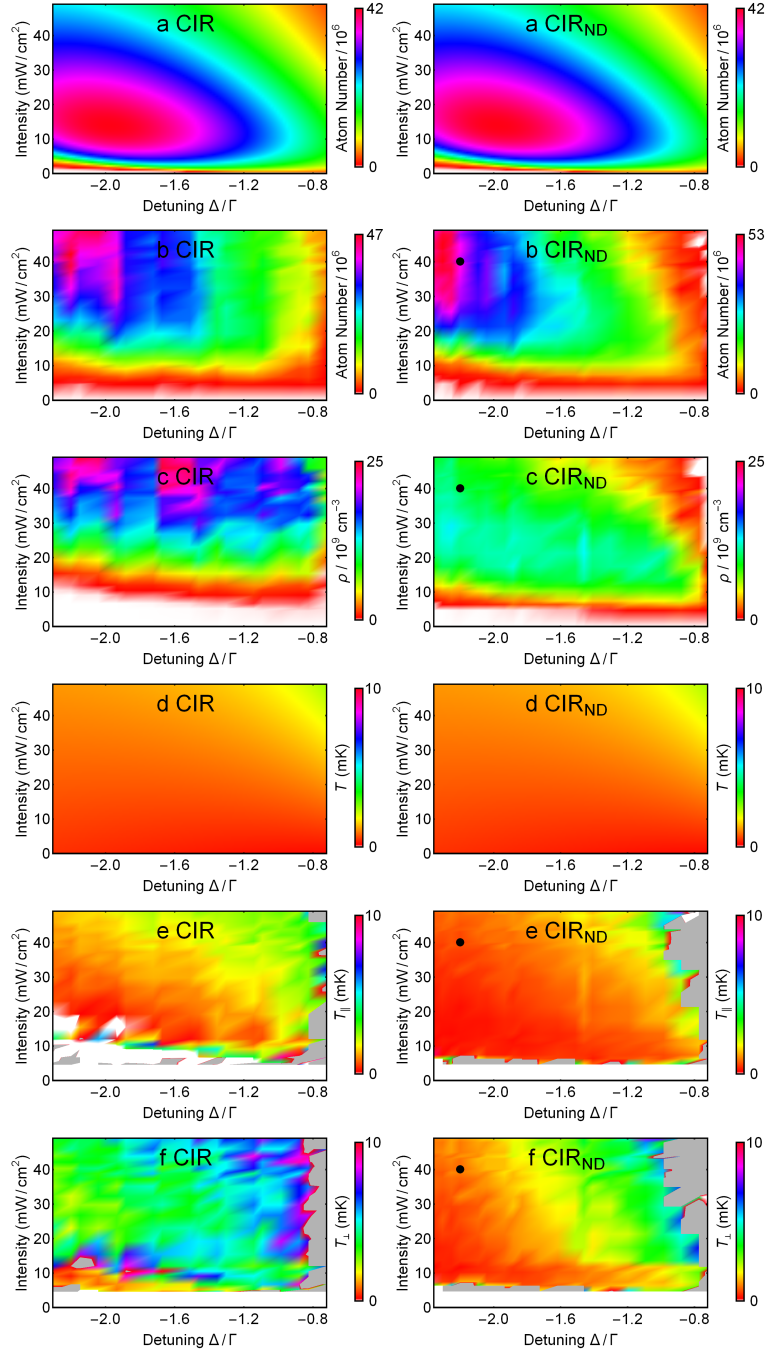
Fig. 5. The full GMOT detuning and intensity characterisation when using chip CIR (standard Gaussian input beam a-f) and CIR_{ND} (CIR with a $T = 0.74$ ND filter in the central $3\,\mathrm{mm}$ diameter of the input beam, a1-f1), both with beam diffraction angle $\alpha = 46°$. Note the slight increase in atom number, and significant decrease in temperature using chip CIR_{ND} relative to chip CIR. Media 2 is the $I_S = 1.67\,\mathrm{mW/cm^2}$ version of the theoretical temperature (images (d)).

Fig. 6. Temperature measurements in directions both parallel (red) and perpendicular (blue) to the grating for chip TRI_{12} (a) and CIR_{ND} (b). Both chips give a 3D average temperature $T = \frac{2}{3}T_{\parallel} + \frac{1}{3}T_{\perp} = 50\,\mu K$.

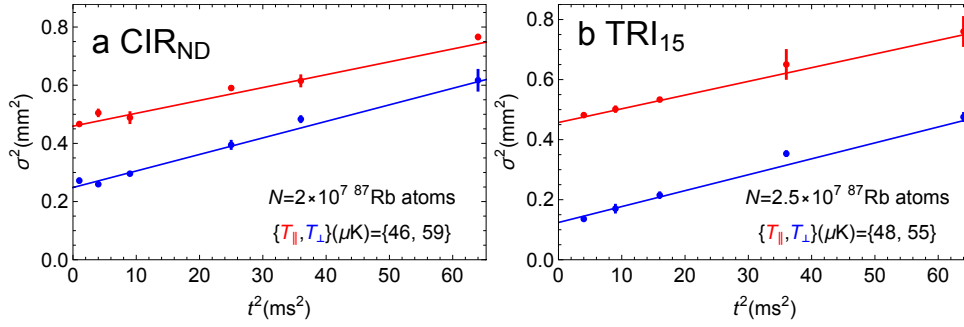Under these conditions, Chip CIR_{ND} brought 2×10^7 atoms down to a 3D average temperature of $50\,\mu K$ (Fig. 6(a)). Chip TRI_{12} used the same settings with the exception that the molasses intensity was reduced to $23\,mW/cm^2$ – bringing 2.5×10^7 atoms down to a 3D average temperature of $50\,\mu K$ (Fig. 6(b)). Both temperatures are similar to those achieved by Nshii *et al.* in [9] (with TRI_{15}), but with an order of magnitude more atoms after molasses ($N \approx 2 \times 10^6$ in [9], due to the lack of intensity control discussed above). Temperature T is determined by fitting $\sigma^2 = \sigma_0^2 + k_B T t^2 / m$ to the data, where σ is the standard deviation of the Gaussian fit to the atomic cloud spatial distribution, m is the mass of an ^{87}Rb atom, k_B is Boltzmann's constant and σ_0 is the initial ($t = 0$) standard deviation of the cloud.

7. Interpretation and conclusions

Both the experimental MOT atom number and cloud temperature demonstrate surprisingly good agreement with theory, given the simplicity of the theoretical models employed.

We note that higher densities are achieved on Chip CIR and CIR_{ND}, largely due to the larger diffraction angle α, with higher associated damping γ and trapping κ coefficients. There is a dramatic density improvement with TRI_{12} over TRI_{15} and this trend may continue with higher values of α toward the tetrahedral configuration $\alpha = \arccos(1/3)$, with the caveat that the capture volume and grating diffraction efficiency will decrease. In Doppler theory the cloud size scales as $\sigma \propto \sqrt{\gamma T / \kappa}$, however we note from the relatively constant experimental MOT density for a variety of detunings and intensities that we are reaching sufficient atom numbers to likely be entering the MOT 'constant density regime' where reradiation forces become more important than restoring forces [25–28].

In terms of the temperature, significant sub-Doppler effects are not present, however we note that one would only expect sub-Doppler cooling under conditions of low intensity and large negative detunings, where we have insufficient data coverage to draw any further conclusions. The atom number is sufficiently large that effects where the MOT temperature is expected to increase with atom number ($T \propto N^{1/3}$) might also become evident [33, 34].

Compact quantum measurement devices are a burgeoning area [35–37], with grating technologies providing a new way to optically simplify transportable ultracold atom experiments. In future we hope to investigate the effect of grating diffraction angle α on both grating optical properties [38] and cooling performance. The current work could also be extended from investigating MOTs into sub-Doppler optical molasses regimes [39], preparing the path for future studies of on-chip Bose-Einstein condensates and extremely stable optical lattices [9].

Acknowledgments

Appendix F

Publication: Grating chips for quantum technologies.

SCIENTIFIC REPORTS

OPEN

Grating chips for quantum technologies

James P. McGilligan, Paul F. Griffin, Rachel Elvin, Stuart J. Ingleby, Erling Riis & Aidan S. Arnold

We have laser cooled 3×10^6 ^{87}Rb atoms to $3\,\mu$K in a micro-fabricated grating magneto-optical trap (GMOT), enabling future mass-deployment in highly accurate compact quantum sensors. We magnetically trap the atoms, and use Larmor spin precession for magnetic sensing in the vicinity of the atomic sample. Finally, we demonstrate an array of magneto-optical traps with a single laser beam, which will be utilised for future cold atom gradiometry.

Laser cooling has led to profound advances in the field of metrology due to the increased interrogation times gained from the low velocity ensembles[1, 2]. The longer interrogation times correspond to narrower transition resonances that have proven critical to the field of quantum sensors. The issue hindering the use of cold atoms as the basis of a portable quantum device is the large spatial scale of the apparatus[3–5]. Significant efforts have been made in recent years to overcome this constraint by developing a compact technology that facilitates ultra-cold atomic ensembles as a portable sensing device[6].

Attempts to achieve a scalable cooling apparatus have been demonstrated in the past in the form of the pyramid magneto-optical trap, PMOT[7–9]. This consists of a structure with four highly reflective walls, angled to overlap the reflected beams with the incident light. The device needs to be maintained in the vacuum, due to the MOT forming within the pyramid volume. Further difficulties arise when imaging these atoms due to optical restrictions caused by the pyramid geometry. An alternative tetrahedral mirror pyramid geometry[10] ameliorates all negative features of the standard PMOT.

In this paper we build upon our work with the grating magneto-optical trap, GMOT[11–14], and show it is a viable platform for compact quantum sensing by generating a truly ultra-cold atomic sample with a micro-fabricated chip. This study also focusses on magnetically trapping a cold sample for measurement of the background Rb pressure present in the vacuum chamber. Furthermore, we utilise Larmor spin precession for magnetometry in order to null stray static and gradient fields in the lab environment. Finally, we demonstrate an array of cold atoms generated above a diffractive optic with a single laser, with an outlook to demonstrating a compact, cold atom gradiometer.

The grating magneto-optical trap

The GMOT cools atoms by a balanced radiation pressure between a single incident laser beam and the diffracted orders generated from the grating surface. Recent investigations of physical geometry have aimed at the optimisation of the diffractive optics for generation of a balanced radiation pressure, with the current conclusion that a 1200 nm period of 60:40 duty cycle in a triangular geometry performs best when used outside the vacuum[12]. In addition to the laser alignment and intensity balance controlled by the diffractive optic[12], the critical parameter to achieve sub-Doppler temperature is the magnetic field.

The GMOT set-up used here is illustrated in Fig. 1. The trapping and probing light is derived from a single external cavity diode laser, ECDL, to address the D_2 transitions of ^{87}Rb. This laser is locked using saturated absorption spectroscopy and then divided into two separate beams for cooling and pump/probing. The cooling arm is fed into a tapered amplifier (ThorLabs TPA780P20) to provide up to $\approx$300 mW of trap light after fiber coupling. This cooling light is then red detuned by 2Γ, i.e. -12 MHz from the $F = 2$ to $F' = 3$ transition via an AOM and combined with re-pumping light on a PBS, before being fibre coupled into the chamber.

The triangular grating is mounted externally from the vacuum system, held horizontally under the glass chamber with the incident light fibre coupled in via a compact tube, which collimates to a $1/e^2$ diameter of 2 cm and circularly polarises with a quarter wave-plate. Two anti-Helmholtz coils of diameter 12 cm are symmetrically aligned above and below the plane of the grating chip to produce 15 G/cm axial magnetic gradient, with a $25 \times 25 \times 12$ cm Helmholtz coil box used to null stray magnetic fields from the lab environment. Cancellation

Department of Physics, SUPA, University of Strathclyde, Glasgow, G4 0NG, UK. Correspondence and requests for materials should be addressed to A.S.A. (email: aidan.arnold@strath.ac.uk)
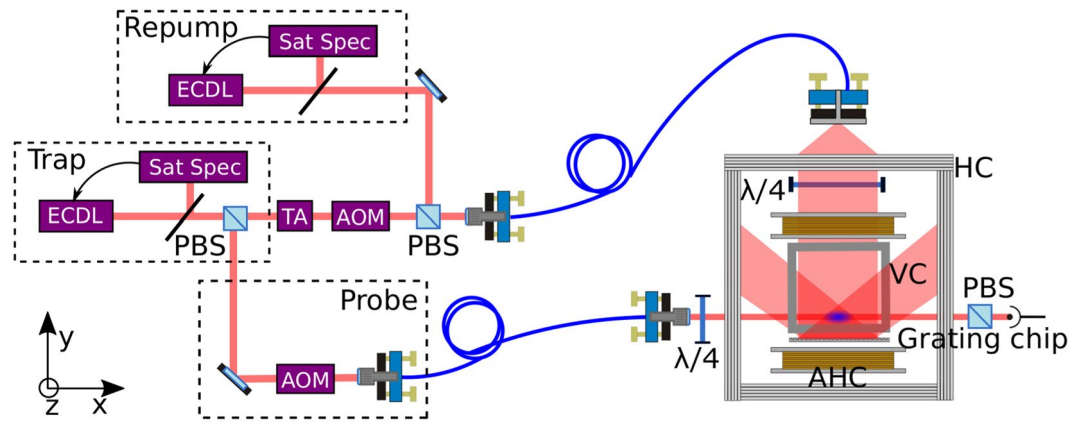
Figure 1. Schematic of the grating MOT experimental set-up. ECDL: External cavity diode laser, Sat Spec: Saturated absorption spectroscopy, TA: Tapered amplifier, AOM: Acousto-optical modulator, PBS: Polarising beam splitter, HC: Helmholtz coils, AHC: Anti-Helmholtz coils, VC: Vacuum chamber.

of these stray magnetic fields has proven critical in achieving a lower temperature optical molasses, resulting in the vacuum system being redesigned with a 2 L/s ion pump to reduce gradient fields in the region of the atomic sample.

The experimental procedure involved a 400 ms MOT load directly from background vapour with incident trap intensity 10 mW/cm², then 10 ms of sub-Doppler cooling in a three-stage molasses. This involved detuning the trap light by 30 MHz and 60 MHz and then halving the intensity in the final stage to achieve temperatures as low as $3.0 \pm 0.7\,\mu$K, as measured from time of flight imaging[15]. This ultra cold ensemble is an ideal starting point for experiments requiring long measurement times and low atomic densities, such as atomic clocks.

Pressure gauge in a compact apparatus.   To achieve a low temperature molasses in a compact apparatus, we designed our vacuum system with scalability and simplicity in mind, such that a single Rb dispensing getter is used in conjunction with a 2 L/s ion pump (Titan ion pump - Gamma Vacuum). To attain a measurement of the vacuum background pressure at the MOT, we use the relation of the magnetic trap lifetime, τ, to the background Rb pressure in the chamber, P, as demonstrated by Monroe[16]. The author estimated a lifetime of 10 s for a background pressure at 7×10^{-10} mbar, with the dominant loss contributor being the van-der Waals interaction between the trapped and thermal background atoms. This relation has been utilised in other literature for background pressure measurements at the atoms, each reaching a similar number[17, 18].

The atoms will be magnetically trapped if the magnetic force is larger than that of gravity, where the magnetic force along the gravity direction z can be described mathematically by,

$$F_z = -g_F\,\mu_B m_F \frac{dB}{dz},$$ (1)

where g_F is the Lande g-factor, μ_B is the Bohr magneton, B the magnetic field magnitude and m_F is the non-degenerate level of the total angular momentum state. This force can then be used to trap weak-field-seeking atoms if F_z is greater than gravity.

The experimental procedure to achieve this begins by trapping the atoms in a quadrupole field, with an axial gradient 15 G/cm. At the end of the molasses sequence the trapping light was turned off and a short optical pumping pulse applied to drive the atoms into the weak-field-seeking $F = 2$, $m_F = 2$ state. The gradient field from the quadrupole coils was afterwards increased to 50 G/cm, whilst florescence images were taken for a varied time of flight. This enabled the trapped atom number to be described as a function of time, as seen in Fig. 2.

The experimental data points were fit with an exponential decay of the form, $N \exp(-t/\tau)$, where N is the initial atom number and τ is the 1/e magnetic trap lifetime, determined as 180 ± 10 ms. If we use this τ to determine the background Rb pressure in the vacuum system, using the relation introduced earlier, we estimate a pressure of 4×10^{-8} mbar. This pressure is primarily due to the low pumping rate of the scaled down ion pump in an unbaked chamber. However, a 10^{-8} mbar pressure is achievable in other systems, where the ion pump has been made redundant in place for specialised micro-fabricated vapour cells with low-He-permeation glass[19]. Such apparatus would enable future reduction of the vacuum system volume for an unambiguously compact device.

Magnetic sensing for a low temperature molasses.   Optically pumped atomic magnetometers work from the principle of coherent spin precession of a polarised atomic species in the presence of a magnetic field. Larmor spin precession is based on atomic magnetic moments interaction with a local magnetic field, aided by the optical pumping of atoms with near resonant light into a non-degenerate Zeeman level of the ground state via an excited state transition. Once in the stretched state, the angular momentum vector, **F**, will precess about the axis of an applied magnetic field, **B**, at the Larmor frequency,

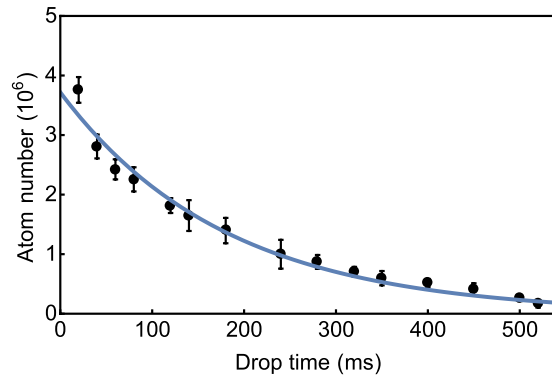$$\omega_L = -\gamma|\mathbf{B}|,$$ (2)

Figure 2. Atom number in the magnetic trap as a function of the ballistic drop time. The blue line indicates an exponential fit to determine a 1/e trap lifetime of 180 ± 10 ms.
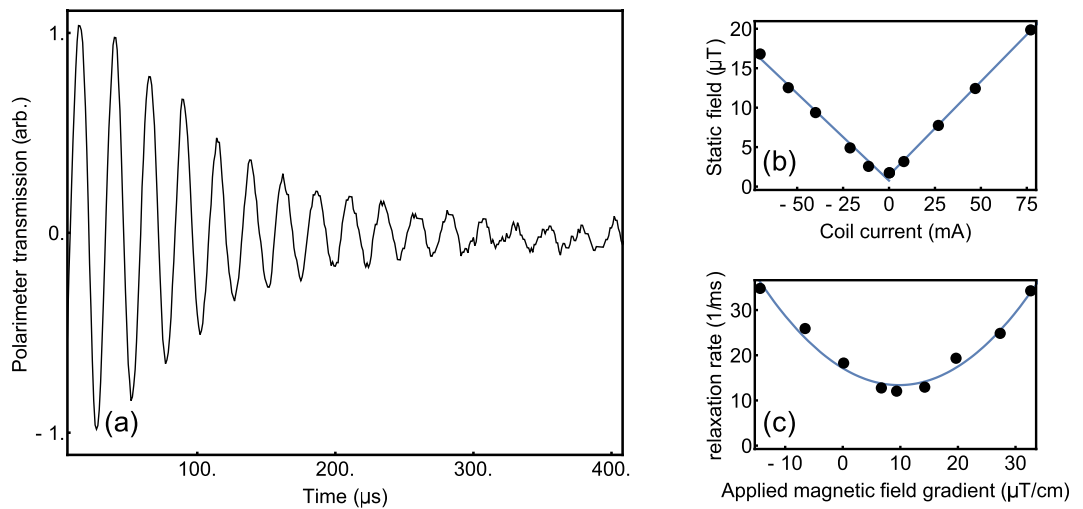

Figure 3. (**a**) Larmor precession measured from the GMOT. (**b**) The static field determined from the Larmor frequency is measured as a function of the Helmholtz coil current with best fitting lines applied. (**c**) The relaxation rate is measured as a function of applied magnetic gradient field with a best fitting curve.

where ω_L is the Larmor frequency, $\gamma = \frac{-eg_F}{2m}$ is the gyromagnetic ratio of the atom, e is the electron charge and m is the electron mass.

The precession of **F** around **B** changes the optical absorption and dispersion properties of the atomic ensemble by passing in and out of resonance with the incident polarised electric field. Thus, the precession can be observed as a damped oscillation in the optical absorption and dispersion, measured using a polariser and detector, to give a direct measurement of $|\mathbf{B}|$[20–23].

Here we measure Larmor precession in an un-shielded grating magneto-optical trap to null stray static fields and reduce the level of gradient fields present during our molasses. The set-up, Fig. 1, uses the same laser source for cooling and probing by splitting the beam into two optical arms. The pump/probe arm is tuned into resonance with the $F = 2$ to $F' = 3$ level using an AOM. The technique chosen was to use an on-resonant pumping beam, such that a constant intensity beam of 0.68 mW/cm² and duration of 10 μs would resonantly pump the atoms with circular light into the stretched state. A 10 Γ detuning was then introduced by electronically offsetting the lock-point of the spectroscopy signal for a far off-resonant probe beam. The atomic rotation around an applied magnetic field changes the probing electric field polarisation, allowing a more sensitive detection to be made using a polariser for increased signal-to-noise, as seen in Fig. 3(a). This experimental procedure was run in conjunction with a Schmitt trigger from the AC mains in order to reduce AC magnetic field noise by making the magnetic measurement at the same point of the 50 Hz cycle each time.

The precession data is fit with $A \exp(-t/\tau) \sin(2\pi\omega_L t + \phi)$, where A is the initial signal amplitude, τ is the decay time and ϕ is the phase. The Larmor frequency, ω_L is directly related to $|\mathbf{B}|$ through Eqn. 2, allowing direct correlation of shim current values to the static field in the vicinity of the atomic ensemble. Figure 3(b) illustrates the measurement of the static magnetic field value as a function of the Helmholtz coil current to null the stray fields. This was used on both perpendicular axes to bring the measured field down to the level of the lab noise floor, ~800 nT.
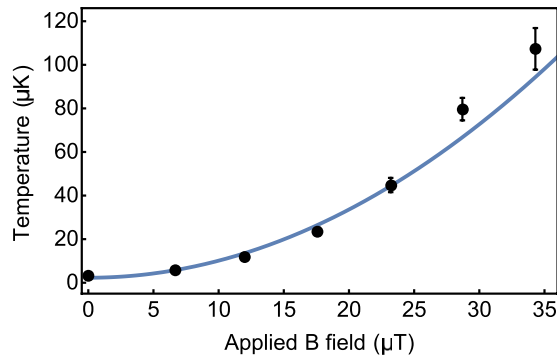
Figure 4. Molasses temperature measured as a function of the applied static field with best fitting curve.
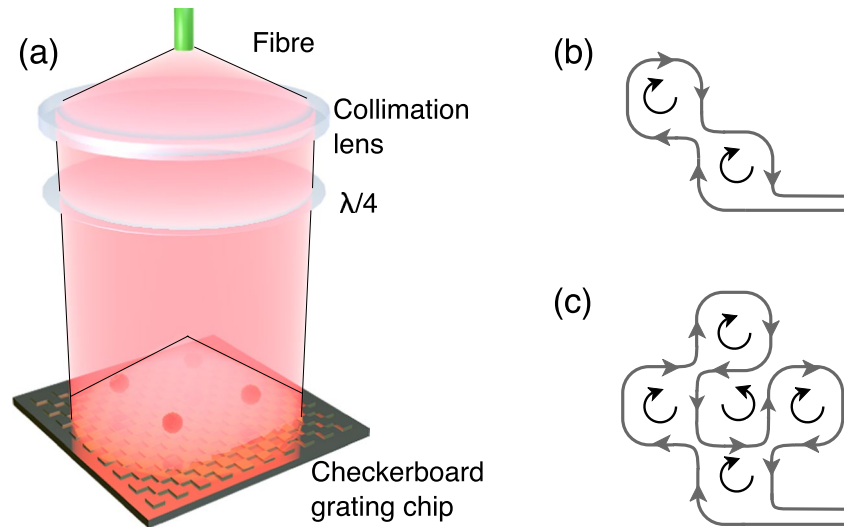

Figure 5. (**a**) Schematic of checkerboard grating. Linearly polarised light diverges from the optical fibre, is collimated and circularly polarised. (**b**)/(**c**) Wire pattern for creation of two/four magnetic minima. Grey lines indicate the wire and black curves emphasize the direction of current flow.

Sensitivity to gradient field components is obtained through the transverse relaxation rate in the ground state coherence, $\gamma = 1/\tau$, which is directly related to the total magnetic field gradient through $\gamma = a|\nabla\mathbf{B}|^2 + \gamma_0$, where a is the coefficient describing the sensitivity to the magnetic field gradient and γ_0 is the relaxation rate in the absence of gradient fields[24]. The measured transverse relaxation rates in the ground state coherence are visible in Fig. 3(c), where the parameter γ is plotted as a function of the difference current between the Helmholtz pair. When applying gradient cancellation on the perpendicular axes by making first order corrections to $d|\mathbf{B}|/dz$ and $d|\mathbf{B}|/dy$ we could improve the transverse decay time from $30\,\mu s$ to $100\,\mu s$. A transverse decay time of $100\,\mu s$ was the best achievable in our unshielded set-up.

With the magnetic gradient fields nulled as well as possible, the temperature in the molasses was then studied as a function of the applied static magnetic field, to demonstrate the necessity for low stray fields when trying to generate ultra-cold atomic samples. As has been discussed by Lett *et al.*, the mechanisms of sub-Doppler cooling indicate a sensitivity of temperature to the magnitude of the static magnetic field due to the Zeeman shifts this will induce, destroying the coherent repopulation of m_F states involved during polarisation gradient cooling[25]. To investigate the level of sensitivity involved in our apparatus we applied static magnetic fields throughout the MOT and molasses stages, measuring the final molasses temperature as a function of the applied static field, as illustrated in Fig. 4.

The data presented illustrates a temperature range from $3–120\,\mu K$ with a $35\,\mu T$ change in static magnetic field. The data set is plotted with a quadratic fit, as expected from previous literature[25]. We note that our best MOT atom number and molasses temperature combination is $(5 \times 10^6, 3.0(7)\,\mu K)$ - comparable to results in a macro-fabricated grating MOT $(1 \times 10^6, 7.6(6)\,\mu K)$[5] and an optimised pyramidal MOT system $(4 \times 10^6, 2.5\,\mu K)$[4].

A cold atom array from a single laser. Atomic arrays have been utilised in cold atom experiments ranging from quantum information with physical qubit arrays[26], to metrological measurements in interferometry and gradiometry[27]. Ionic array apparatus have been miniaturised with trapped ion micro-traps to demonstrate 1D
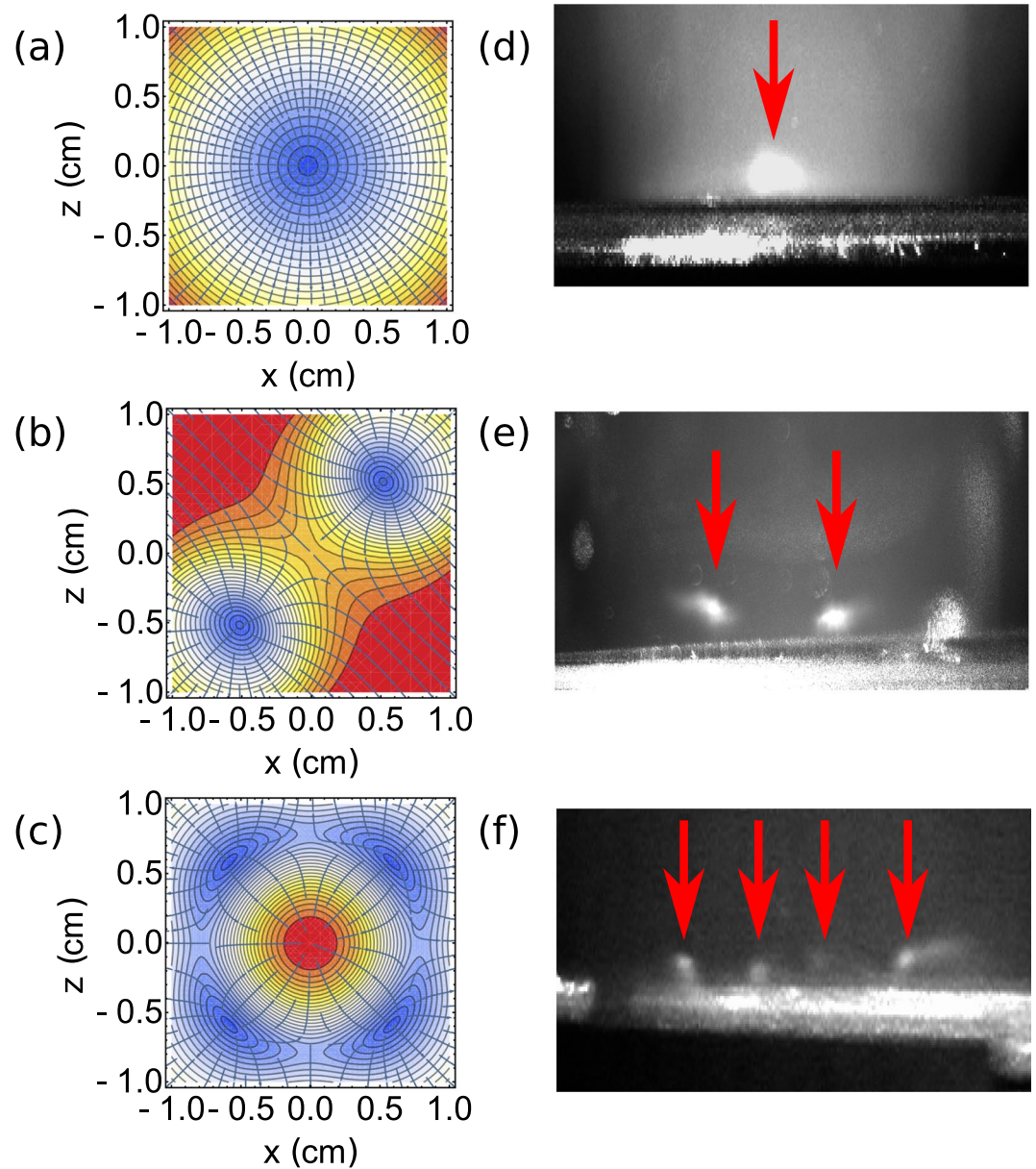
Figure 6. (**a**–**c**) Standard anti-Helmholtz simulation, two magnetic minima simulation for a 1D array and four magnetic minima simulation for a 2D array. (**d**–**f**) Experimental realisation of a one, two and four MOTs.

and 2D arrays[28], however an array of neutral atoms is favourable due to their weaker interaction with the environment[29]. A common method for generating a neutral atom array with a small number/one atom per site is in an optical lattice, where individual microscopic site addressing and measurement is restricted to the regime of the quantum gas microscopes[30, 31] and optical dipole traps[32].

Large macroscopic arrays of neutral atoms have been achieved in the form of a magnetic lattice loaded from cold atoms, capable of capturing up to 2000 atoms in 500 sites[29]. Macroscopic scaled neutral atom arrays with larger N have also been demonstrated in the form of a 2×2 array of MOTs[33] where the scalability is limited by the optical set-up. Here we introduce the micro-fabricated grating chip as a simple and robust source for generating 1D and 2D arrays of neutral atoms with a single incident laser and patterned coil geometry.

For this study, the holographic checkerboard grating chip, discussed in previous literature[11, 13], was implemented into the set-up. The benefit of the checkerboard grating is the lack of a central symmetry point that exists in the linear gratings. Instead, the overlap volume extends to fill the surface area of the chip[11], making it accessible to lay a patterned coil beneath the surface of the grating to form a number of MOTs dependent upon the coil geometry, as can be seen in Fig. 5(a).

To create the appropriate inhomogeneous magnetic potential for multiple MOTs, we used the coil design illustrated in Fig. 5 with an additional external bias field orientated perpendicular to the plane of the coils. The wire geometries used in Fig. 5(b,c) were selected for a 1D and 2D array respectively. Here the grey lines represent the wire formation, with black curves used to emphasize the direction of current flow. For (b), the selected wire

formation creates two coils of the same magnitude. In (c), the formation creates five coils, four with the same direction and one in the opposite.

To determine the properties of these wire geometries requires numerical solution of the Biot-Savart law,

$$\mathbf{B}(\mathbf{r}) = \frac{\mu_0 I}{4\pi} \int \frac{\mathbf{dl} \times (\mathbf{r} - \mathbf{r'})}{|\mathbf{r} - \mathbf{r'}|^3},$$

(3)

where $\mu_0 = 4\pi \times 10^{-7}$ H/m is the permeability of free space, $\mathbf{B}(\mathbf{r})$ is the magnetic field at point $\mathbf{r}$ from a wire element with current I and unit length $\mathbf{dl}$, centred at position $\mathbf{r'}$

Due to our coils being approximately circular, we assume a perfect circle for our magnetic field calculations. It has been shown[34], that when solved in a cylindrical polar co-ordinate basis, the magnetic field from a circular coil, $\mathbf{B}(r, z)$, can be determined for any position (r, z) from the relation of elliptic integrals,

$$
\begin{aligned}
B_r(r, z) &= \frac{\mu_0 I z}{2\pi r} \sqrt{\frac{m}{4\alpha r}} \left[\frac{2 - m}{2 - 2m} E - K \right], \\
B_z(r, z) &= \frac{\mu_0 I}{2\pi r} \sqrt{\frac{m}{4\alpha r}} \left[rK + \frac{\alpha m - r(2 - m)}{2 - 2m} E \right],
\end{aligned}
$$

(4)

where r and z are the radial and axial co-ordinates, α is the coil radius, $m = \frac{4\alpha r}{z^2 + (\alpha + r)^2}$ and the functions E and K refer to the corresponding elliptic integrals $E(m) = \int_0^{\pi/2} (1 - m\sin^2\theta)^{1/2} d\theta$ and $K(m) = \int_0^{\pi/2} \frac{d\theta}{(1 - m\sin^2\theta)^{1/2}}$.

These equations were used to simulate the magnetic potential for a single MOT, as well as for the geometries of Fig. 5(b,c), as shown in Fig. 6 (a–c) respectively. The required wire geometries were formed in a 3D-printed mount and placed immediately below the grating. The geometry patterned coil would then be run with a small bias coil in conjunction with an upper coil to create the appropriate magnetic field required. The experimental observations of this can be seen in Fig. 6(d) for a single MOT, (e) for 2 MOTs in a 1D array and (f) for 4 MOTs in a 2D array. The images seen in (d) and (e) were taken with the grating mounted outside of the vacuum, using $\sim$25 mW/cm^2 to start with 2×10^6 atoms in (d) which was then split into 2 MOTs with 5×10^5 atoms each. For image (f) the grating and patterned coil were mounted inside the vacuum due to the magnetic minima forming close to the grating surface, forming 4 MOTs using $\sim$2 mW/cm^2, with an estimated $<10^5$ atoms in each.

This demonstration proves the potential of the GMOT in future quantum sensing devices requiring an atomic array. Most notably, such a device would prove beneficial to the realisation of a compact gradiometer, where an array of identical MOTs can be used for cancellation of common mode noise.

Conclusions

In summary, we have demonstrated ultra-cold temperatures in a grating magneto-optical trap, as a platform for compact quantum sensing. This demonstration looked at the critical parameters for achieving low temperature systems, such as the magnetic environment.

We conclude that pressure measurements determined by the loss rate from a magnetic trap illustrate that these low temperatures can be achieved in a compact vacuum apparatus, even with pressure on the order of 10^{-7} mbar. The introduction of Larmor precessions in a cold ^{87}Rb atomic sample for the nulling of stray static and gradient magnetic fields provides an accuracy of static field levels below $1 \mu T$ and an order of magnitude improvement of gradients.

Finally, the demonstration of multiple magneto-optical trap locations from a single incident laser beam coupled to a 2-dimensional diffractive optic opens the door to a compact cold-atom gradiometer. This can be taken further to introduce an array of cold atomic ensembles, with the array number and geometry solely determined by the trapping coil design.

The dataset for this paper is available at doi:10.15129/79a69c9c-3f61-428f-b52e-366017fafa89.

References

1. Takamoto, M., Hong, F. L., Higashi, R. & Katori, H. An optical lattice clock. *Nature* **435**, 321–324 (2005).
2. Ludlow, A. D. & Ye, J. Progress on the optical lattice clock. *Comptes Rendus Physique* **16**, 499–505 (2015).
3. Esnault, F. X., Donley, E. A., Kitching, J. & Ivanov, E. N. Status of a compact cold-atom CPT frequency standard. Proc. 2011 Joint Mtg. IEEE Intl. Freq. Cont. Symp. and EFTF conf. 612–614 (2012).
4. Bodart, Q. *et al.* A cold atom pyramidal gravimeter with a single laser beam. *Appl. Phys. Lett.* **96**, 134101 (2010).
5. Lee, J., Grover, J. A., Orozco, L. A. & Rolston, S. L. Sub-Doppler cooling of neutral atoms in a grating magneto-optical trap. *J. Opt. Soc. Am. B* **30**, 2869–2874 (2013).
6. Zhang, H., Li, T. & Yin, Y. Microtrap on a concave grating reflector for atom trapping. *Chinese Phys. B* **25**, 087802 (2016).
7. Pollock, S., Cotter, J. P., Laliotis, A. & Hinds, E. A. Integrated magneto-optical traps on a chip using silicon pyramid structures. *Opt. Express* **17**, 14109–14114 (2009).
8. Camposeo, A. *et al.* A cold cesium atomic beam produced out of a pyramidal funnel. *Opt. Commun.* **200**, 231–239 (2001).
9. Arlt, J. J., Marago, O., Webster, S., Hopkins, S. & Foot, C. J. A pyramidal magneto-optical trap as a source of slow atoms. *Optics Commun.* **157**, 303–309 (1998).
10. Vangeleyn, M., Griffin, P. F., Riis, E. & Arnold, A. S. Single-laser, one beam, tetrahedral magneto-optical trap. *Opt. Express* **17**, 13601–13608 (2009).
11. Nshii, C. C. *et al.* A surface-patterned chip as a strong source of ultracold atoms for quantum technologies. *Nature Nanotech.* **8**, 321–324 (2013).
12. McGilligan, J. P., Griffin, P. F., Riis, E. & Arnold, A. S. Diffraction grating characterisation for cold-atom experiments. *J. Opt. Soc. Am. B* **33**, 1271–1277 (2016).
13. McGilligan, J. P., Griffin, P. F., Riis, E. & Arnold, A. S. Phase-space properties of magneto-optical traps utilising micro-fabricated gratings. *Opt. Express* **23**, 8948–8959 (2015).

14. Cotter, J. P. *et al.* Design and fabrication of diffractive atom chips for laser cooling and trapping. *Appl. Phys. B* **122**, 1–6 (2016).
15. Lett, P. D. *et al.* Observation of atoms laser cooled below the Doppler limit. *Phys. Rev. Lett.* **61**, 169–173 (1988).
16. Monroe, C. *PhD Thesis*, University of Colorado (1992).
17. Weatherill, K. J. *et al.* A versatile and reliably reusable ultrahigh vacuum viewport. *Rev. Sci. Instrum.* **80**, 026105 (2009).
18. Monroe, C., Swann, W., Robinson, H. & Wieman, C. Very cold trapped atoms in a vapor cell. *Phys. Rev. Lett.* **65**, 1571–1574 (1990).
19. Dellis, A. T., Shah, V., Donley, E. A., Knappe, S. & Kitching, J. Low helium permeation cells for atomic microsystems technology. *Opt. Lett.* **41**, 2775–2778 (2016).
20. Behbood, N. *et al.* Real time vector field tracking with a cold-atom magnetometer. *Appl. Phys. Lett.* **102**, 173504 (2013).
21. Sycz, K., Wojciechowski, A. M. & Gawlik, W. Magneto-optical effects and rf magnetic field detection in cold rubidium atoms. *J. Phys.: Conf. Series* **497**, 012006 (2014).
22. Isayama, T. *et al.* Observation of Larmor spin precession of laser-cooled Rb atoms via paramagnetic Faraday rotation. *Phys. Rev. A* **59**, 4836–4839 (1999).
23. Takahashi, Y. *et al.* Observation of spin echoes of laser-cooled Rb atoms. *Phys. Rev. A* **59**, 3761–3765 (1999).
24. Pustelny, S., Kimball, D. F., Rochester, S. M., Yashchuk, V. V. & Budker, D. Influence of magnetic-field inhomogeneity on nonlinear magneto-optical resonances. *Phys. Rev. A* **74**, 063406 (2006).
25. Lett, P. D. *et al.* Optical molasses. *J. Opt. Soc. Am. B* **6**, 2084–2107 (1989).
26. Cirac, J. I. & Zoller, P. A scalable quantum computer with ions in an array of microtraps. *Nature* **404**, 579–581 (2000).
27. Rakholia, A. V., McGuinness, H. J. & Biedermann, G. W. Dual-axis high-data-rate atom interferometer via cold ensemble exchange. *Phys. Rev. Applied* **2**, 054012 (2014).
28. Stick, D. *et al.* Ion trap in a semiconductor chip. *Nature Phys.* **2**, 36–39 (2006).
29. Whitlock, S., Gerritsma, R., Fernholz, T. & Spreeuw, R. J. C. Two-dimensional array of microtraps with atomic shift register on a chip. *New J. Phys.* **11**, 023021 (2009).
30. Haller, E. *et al.* Single-atom imaging of fermions in a quantum-gas microscope. *Nature Phys.* **11**, 738 (2015).
31. Sherson, J. F. *et al.* Single-spin addressing in an atomic Mott insulator. *Nature* **471**, 319–324 (2010).
32. Bergamini, S. *et al.* Holographic generation of microtrap arrays for single atoms by use of a programmable phase modulator. *J. Opt. Soc. Am. B* **21**, 1889–1894 (2004).
33. Grabowski, A. & Pfau, T. A lattice of magneto-optical and magnetic traps for cold atoms. *Eur. Phys. J. D* **22**, 347–354 (2003).
34. Good, R. H. Elliptic integrals, the forgotten functions. *Eur. J. Phys.* **22**, 119–126 (2000).

Acknowledgements

Author Contributions

A.S.A., P.F.G. and E.R. conceived the experiment(s), J.P.M. conducted the experiment(s) and wrote the manuscript. All authors reviewed the results and manuscript.

Additional Information

Competing Interests: The authors declare that they have no competing interests.

Publisher's note: Springer Nature remains neutral with regard to jurisdictional claims in published maps and institutional affiliations.

Appendix G

Publication: Utilising diffractive optics towards a compact cold atom clock.

Utilising diffractive optics towards a compact, cold atom clock

James P. McGilligan, Rachel Elvin, Paul F. Griffin, Erling Riis and Aidan S. Arnold

Experimental Quantum Optics and Photonics Group University of Strathclyde

Glasgow, United Kingdom

Email: james.mcgilligan@strath.ac.uk

Abstract—**Laser cooled atomic samples have resulted in profound advances in precision metrology [1], however the technology is typically complex and bulky. In recent publications we described a micro-fabricated optical element, that greatly facilitates miniaturisation of ultra-cold atom technology [2], [3], [4], [5].**

Portable devices should be feasible with accuracy vastly exceeding that of equivalent room-temperature technology, with a minimal footprint. These laser cooled samples are ideal for atomic clocks. Here we will discuss the implementation of our micro-fabricated diffractive optics towards building a robust, compact cold atom clock.

I. INTRODUCTION

The continued research into atomic clocks in recent decades has lead to a considerable rise in the achievable accuracy and stability. This stability is most notable in the atomic fountain and lattice clocks, measuring frequencies at the $10^{-16}\tau^{-1/2}$ and $10^{-18}\tau^{-1/2}$ level respectively [6], [7], [8], [9]. This research has also lead to profound advancement of compact metrological devices, achieving frequency stabilities in the low $10^{-10}\tau^{-1/2}$ in package volumes measuring only a few tens of cubic centimetres [10], [11].

However, the majority of the current compact clocks are based around room temperature apparatus that use buffer gasses and cell wall coatings in order to minimise collisional spin flips, benefiting the system with increased contrast and interrogation times [12]. Ultimately, these coatings and buffer gasses limit the long term performance achievable in a clock due to cell degradation and temperature dependent pressure shifts.

To overcome this, a move towards cold atoms is favourable, with the benefit of long interrogation times and narrow linewidths. To date, attempts at miniaturising cold atom clocks remain confined to thousands of cubic centimetre packages. We begin by proposing the grating magneto-optical traps, GMOT, as a step closer to bridging the gap between high performance cold atom apparatus and the scale of a thermal package. This project aims at reaching a frequency stability better than $10^{-12}\tau^{-1/2}$ in a package on the scale of tens of cubic centimetres.

II. CPT INTEROGATION

Our study begins with the realisation of an atom chip that integrates the laser cooling apparatus into a compact device. The GMOT achieves equalised radiation pressure from balancing the intensities of a single incident beam by the diffracted orders from the grating surface [2], [3]. Previous optical tools for simplifying laser cooling and trapping have

been demonstrated [13], [14], [15], [16], however, as discussed in previous work, the GMOT out-performs these devices on size, reproducibility, robustness and trapping capabilities [5]. These properties make the GMOT the ideal candidate for a compact atomic clock.

To convert this device to a clock experimentally we propose to derive the ground state frequency splitting of ^{87}Rb by means of coherent population trapping, CPT [17]. The experimental set-up used is illustrated in Figure 1. We lock a home made external cavity diode laser, ECDL, to the cooling transition of ^{87}Rb and use an electro-optical modulator, EOM, to frequency modulate a sideband at the re-pumping frequency. An acousto-optical modulator, AOM, is used for switching on and off the cooling beam, that is fibre coupled and circularly polarised before reaching the diffraction grating. The magnetic field zero point, created by anti-Helmholtz coils, is centred on the light overlap volume for trapping the cold atomic sample. For an incident intensity of ≈ 40 mW/cm^2 in a 20 mm beam we trap 10^8 atoms. When sub-Doppler cooling mechanisms are introduced we bring 3×10^7 atoms down to 15 μK.
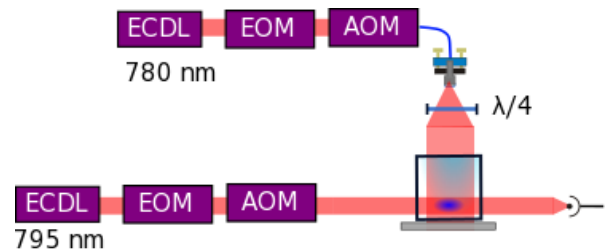

Fig. 1. Simplified grating MOT schematic for the cooling and probing beams. EOM: Electro-optical modulator. AOM: Acousto-optical modulator. ECDL: External cavity diode laser. $\lambda/4$: Quarter wave-plate.

When the cold atoms are free from external perturbation and in ballistic expansion, we apply a Raman probe beam to resolve the ground state clock transition. For this probe beam, a 795 nm laser is used to drive to the D1 states of ^{87}Rb. Once locked, an EOM is used to generate sidebands of equal amplitude to the carrier to couple the two ground states to the $F = 1$ excited state. With a small magnetic field is applied parallel to the clock beam, one can lift the degeneracy of the excited state enough to resolve CPT features of individual sub-levels, as can be seen in Figure 2. A few tens of μW's of laser power is enough to resolve a full width half max, FWHM, of the $m_F = 0$ state to be 5 kHz.

To achieve a narrower clock feature we will convert the CPT procedure to a Raman-Ramsey sequence. The technique has been demonstrated to produce narrow fringes at higher
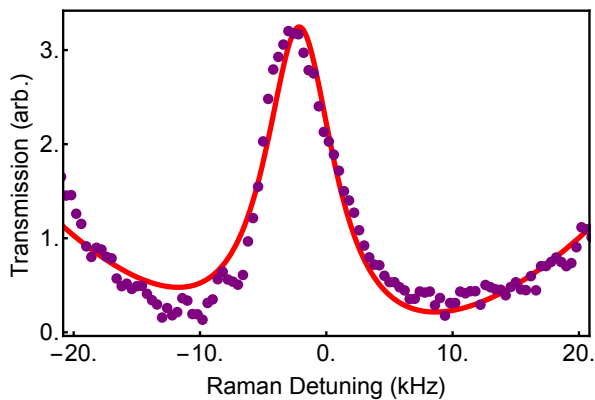
Fig. 2. Coherent population trapping transmission peak for the $m_F = 0$ sub-level of ^{87}Rb. Black line: The experimental data of the peak resolved with a Raman scan through the cold atomic medium. Red line: Lorentzian best fit to the experimental data

contrast than the original CPT feature, benefiting the measured frequency stability [18], [19].

III. Conclusion

The grating magneto-optical trap provides a compact means to cool and trap a large number of atoms, proving beneficial for precision measurements such as atomic clocks. With a coherent population trapping signal optimised to 5 kHz, the apparatus will be used to demonstrate Raman-Ramsey interrogation for a narrow clock reference.

Acknowledgment

References

[1] G. Lamporesi, A. Bertoldi, L. Cacciapuoti, M. Prevedelli and G. M. Tino, "Determination of the Newtonian gravitational constant using atom interferometry" *Phys. Rev. Lett.* **100**, 050801 (2008)

[2] J. P. McGilligan, P. F. Griffin, E. Riis, and A. S. Arnold, "Phase-space properties of magneto-optical traps utilising micro-fabricated gratings.," *Opt. Express* **23**, 8948-8959 (2015)

[3] J. P. McGilligan, P. F. Griffin, E. Riis, and A. S. Arnold, "Diffraction grating characterisation for cold atom experiments" *arXiv:1601.07431(2016)*

[4] J. P. Cotter, J. P. McGilligan, P. F. Griffin, I. M. Rabey, K. Docherty, E. Riis, A. S. Arnold and E. A. Hinds "Design and fabrication of diffractive atom chips for laser cooling and trapping" *arXiv:1601.05548 (2016)*

[5] C. C. Nshii, M. Vangeleyn, J. P. Cotter, P. F. Griffin, E. A. Hinds, C. N. Ironside, P. See, A. G. Sinclair, E. Riis and A. S. Arnold, "A surface-patterned chip as a strong source of ultracold atoms for quantum technologies" *Nat Nanotech.* **8**, 321-324 (2013)

[6] T. P. Heavner, E. A. Donley, F. Levi, G. Costanzo, T. E. Parker, J. H. Shirley, N. Ashby, S. Barlow and S. R. Jefferts, "First accuracy evaluation of NIST-F2", *Metrologia* **51**, 174-182 (2014)

[7] B.J. Bloom, T.L. Nicholson, J.R. Williams, S. Campbell, M. Bishof, X. Zhang, W. Zhang, S.L. Bromley, J. Ye, "An optical lattice clock with accuracy and stability at the 10^{-18} level", *Nature* **506**, 71-75 (2014)

[8] M. Takamoto, F. L. Hong, R. Higashi and H. Katori, "An optical lattice clock" *Nature* **435**, 321-324 (2005)

[9] N. Hinkley, J. A. Sherman, N. B. Phillips, M. Schioppo, N. D. Lemke, K. Beloy, M. Pizzocaro, C. W. Oates, A. D. Ludlow "An Atomic Clock with 10^{-18} Instability", *Science* **341**, 1215-1218 (2013).

[10] P. D. D. Schwindt, S. Knappe, V. Shah, L. Hollberg, J. Kitching, L. A. Liew, and J. Moreland, "Chip-scale atomic magnetometer," *Applied Physics Letters*, **85**, (2004)

[11] R. Lutwak, "The Chip-Scale atomic clock - recent developments", *in Proc. 2009 Joint Meeting IEEE Int. Freqency Control Symp. and EFTF Conf.*, Besancon, France, 2009, pp. 573-577.

[12] X. Liu, J-M. Merolla, S. Guerandel, E. de Clereq and R. Boudot, "Ramsey spectroscopy of high-contrast CPT resonances with push-pull optical pumping in Cs vapor" *Opt. Express* **21**, 12451-12459 (2013)

[13] S. Pollock, J. P. Cotter, A. Laliotis and E. A. Hinds, "Integrated magneto-optical traps on a chip using silicon pyramid structures", *Opt. Express* **17**, 14109-14114 (2009).

[14] S. Pollock, J. P. Cotter, A. Laliotis, F. Ramirez-Martinez and E. A. Hinds, "Characteristics of integrated magneto-optical traps for atom chips", *New J. Phys.* **13**, 043029 (2011).

[15] M. Vangeleyn, P. F. Griffin, E. Riis, and A. S. Arnold, "Single-laser, one beam, tetrahedral magneto-optical trap", *Opt. Express* **17**, 13601-13608 (2009).

[16] M. Vangeleyn, P. F. Griffin, E. Riis, and A. S. Arnold, "Laser cooling with a single laser beam and a planar diffractor", *Opt. Lett* **17**, 3453-3455 (20010).

[17] E. Arimondo, *Prog. Opt.* **35**, 257 (1996).

[18] F. X. Esnault, E. Blanshan, E. N. Ivanov, R. E. Scholten, J. Kitching and E. A. Donley, "Cold-atom double Λ coherent population trapping clock", *Phys. Rev. A.* **88**, 042120 (2013)

[19] X. Chen, G-Q. Yang, J. Wang and M-S. Zhan, "Coherent Population Trapping-Ramsey Interference in Cold Atoms" *Chin. Phys. Lett.* **27**, 113201 (2010)

Bibliography

[1] P. T. H. Fisk, *Trapped-ion and trapped-atom microwave frequency standards*, Reports Prog. Phys. **60**, 761 (1997).

[2] F. Riehle, *Frequency Standards* (Wiley-VCH, 2004).

[3] J. Jespersen, J. Fitz-randolph, and J. Robb, *From Sundials to Atomic Clocks: Understanding Time and Frequency* (Dover Publications, 1999).

[4] D. W. Allan, N. Ashby, and C. C. Hodge, *The Science of Timekeeping*, Hewlett Packard (1997).

[5] M. A. Lombardi, T. P. Heavner, and S. R. Jefferts, *Measure In This Issue : The Realization of the SI Second*, J. Meas. Sci. **2**, 74 (2007).

[6] D. Sobel, *Longitude: The True Story of a Lone Genius Who Solved the Greatest Scientific Problem of His Time* (Bloomsbury Publishing, 2010).

[7] C. J. Foot, *Atomic Physics* (Oxford University Press, 2005).

[8] D. Howe, D. Allan, and J. Barnes, *Properties of signal sources and measurement methods*, Thirty Fifth Annu. Freq. Control Symp. , 669 (1981).

[9] D. W. Allan, *Time and Frequency (Time-Domain) Characterization,*

Estimation, and Prediction of Precision Clocks and Oscillators, IEEE Trans. Ultrason. Ferroelectr. Freq. Control **34**, 647 (1987).

[10] I. Rabi, S. Millmann, P. Kusch, and J. Zacharias, *The Molecular Beam Resonance Methods for Measuring Nuclear Magnetic Moments*, Phys. Rev. **55**, 526 (1939).

[11] N. F. Ramsey, *A Molecular Beam Resonance Method with Separated Oscillating Fields*, Phys. Rev. **78**, 695 (1950).

[12] N. F. Ramsey, *Experiments With Separated Oscillatory Fields and Hydrogen Masers*, Rev. Mod. Phys. **62**, 541 (1989).

[13] L. Essen and J. V. L. Parry, *An Atomic Standard of Frequency and Time Interval: A Caesium Resonator*, Nature **176**, 280 (1955).

[14] M. A. Kasevich, E. Riis, S. Chu, and R. G. DeVoe, *rf spectroscopy in an atomic fountain*, Phys. Rev. Lett. **63**, 612 (1989).

[15] T. P. Heavner *et al.*, *First accuracy evaluation of NIST-F2*, Metrologia **51**, 174 (2014).

[16] C. W. Oates, E. A. Curtis, and L. Hollberg, *Improved short-term stability of optical frequency standards: approaching 1 Hz in 1 s with the Ca standard at 657 nm*, Opt. Lett. **25**, 1603 (2000).

[17] M. Takamoto, F.-L. Hong, R. Higashi, and H. Katori, *An optical lattice clock.*, Nature **435**, 321 (2005).

[18] B. J. Bloom *et al.*, *An optical lattice clock with accuracy and stability at the 10(-18) level.*, Nature **506**, 71 (2014).

[19] N. Hinkley *et al.*, *An Atomic Clock with 10(-18) Instability*, Science. **341**, 1215 (2013).

[20] M. Jardino *et al.*, *Frequency stability of a mercury ion frequency standard*, Appl. Phys. **24**, 107 (1981).

[21] U. Tanaka *et al.*, *The 199 Hg + single ion optical clock: recent progress*, J. Phys. B At. Mol. Opt. Phys. **36**, 545 (2003).

[22] S. A. Diddams *et al.*, *An Optical Clock Based on a Single Trapped 199Hg+ Ion*, Science. **293**, 825 (2001).

[23] D. J. Berkeland, J. D. Miller, J. C. Bergquist, W. M. Itano, and D. J. Wineland, *Laser-Cooled Mercury Ion Frequency Standard*, Phys. Rev. Lett. **80**, 2089 (1998).

[24] T. W. Hänsch, *Nobel Lecture: Passion for precision*, Rev. Mod. Phys. **78**, 1297 (2006).

[25] J. L. Hall, *Nobel Lecture: Defining and measuring optical frequencies*, Rev. Mod. Phys. **78**, 1279 (2006).

[26] T. Rosenband *et al.*, *Frequency Ratio of Al+ and Hg+ Single-Ion Optical Clocks; Metrology at the 17th Decimal Place*, Science. **319**, 1808 (2008).

[27] N. Huntemann, C. Sanner, B. Lipphardt, C. Tamm, and E. Peik, *Single-Ion Atomic Clock with 10(-18) Systematic Uncertainty*, Phys. Rev. Lett. **116**, 63001 (2016).

[28] M. Schioppo *et al.*, *Ultrastable optical clock with two cold-atom ensembles*, Nat Phot. **11**, 48 (2017).

[29] A. D. Ludlow, M. M. Boyd, J. Ye, E. Peik, and P. O. Schmidt, *Optical atomic clocks*, Rev. Mod. Phys. **87**, 637 (2015).

[30] C. W. Chou, D. B. Hume, T. Rosenband, and D. J. Wineland, *Optical Clocks and Relativity*, Science. **329**, 1630 (2010).

[31] S. M. Walport and S. P. L. Knight, *The Quantum Age: technological opportunities*, Www.Gov.Uk/Go-Science , 64 (2016).

[32] S. Knappe *et al.*, *A microfabricated atomic clock*, Appl. Phys. Lett. **85**, 1460 (2004).

[33] P. D. D. Schwindt *et al.*, *Chip-scale atomic magnetometer*, Appl. Phys. Lett. **85**, 6409 (2004).

[34] Microsemi, *CSAC Datasheet*, Data Sheet , 7.

[35] F. X. Esnault *et al.*, *Cold-atom double-Λ coherent population trapping clock*, Phys. Rev. A - At. Mol. Opt. Phys. **88**, 1 (2013).

[36] X. Liu, E. Ivanov, J. Kitching, and E. A. Donley, *Frequency shift mitigation in a cold-atom CPT clock*, p. 2 (2016).

[37] MuQuans, *MuClock: A high performance frequency standard based on cold Rubidium atoms*, Data Sheet **33**, 1.

[38] M. A. Hafiz *et al.*, *A high-performance Raman-Ramsey Cs vapor cell atomic clock*, J. Appl. Phys. **121**, 104903 (2017).

[39] P. Yun *et al.*, *High-Performance Coherent Population Trapping Clock with Polarization Modulation*, Phys. Rev. Appl. **7**, 14018 (2017).

[40] X. Liu, J.-M. Mérolla, S. Guérandel, E. de Clercq, and R. Boudot, *Ramsey spectroscopy of high-contrast CPT resonances with push-pull optical pumping in Cs vapor*, Opt. Express **21**, 12451 (2013).

[41] X. Liu *et al.*, *Coherent-population-trapping resonances in buffer-gas-filled Cs-vapor cells with push-pull optical pumping*, Phys. Rev. A **87**, 13416 (2013).

[42] C. C. Nshii *et al.*, *A surface-patterned chip as a strong source of ultra-cold atoms for quantum technologies*, Nat. Nanotechnol. **8**, 321 (2013).

[43] P. F. Griffin, *Laser Cooling and Loading of Rb into A Large Period, Quasi-Electrostatic, Optical Lattice*, PhD Thesis (2005).

[44] K. Mølmer and Y. Castin, *Monte Carlo wavefunctions in quantum optics*, Quantum Semiclassical Opt. J. Eur. Opt. Soc. Part B **8**, 49 (1996).

[45] J. D. Pritchard, *Cooperative Optical Non-Linearity in a Blockaded Rydberg Ensemble* Springer Theses (Springer Berlin Heidelberg, 2012).

[46] H. J. Metcalf and P. van der Straten, *Laser cooling and trapping of atoms*, J. Opt. Soc. Am. B **20**, 887 (2003).

[47] C. Cohen-Tannoudji, J. Dupont-Roc, and G. Grynberg, *Atom-photon interactions: basic processes and applications* Wiley-Interscience publication (J. Wiley, 1992).

[48] R. Loudon, *The Quantum Theory of Light* (OUP Oxford, 2000).

[49] R. W. Boyd, *Nonlinear Optics*, 3rd editio ed. (Academic Press, USA, 2008).

[50] G. Alzetta, A. Gozzini, L. Moi, and G. Orriols, *An experimental method for the observation of r.f. transitions and laser beat resonances in oriented Na vapour*, Nuovo Cim. B **36**, 5 (1976).

[51] E. Arimondo, *Coherent Population Trapping in Laser Spectroscopy*, volume 35, pp. 257–354, Elsevier, 1996.

[52] R. M. Whitley and C. R. Stroud, *Double optical resonance*, Phys. Rev. A **14**, 1498 (1976).

[53] Y. Y. Jau, E. Miron, A. B. Post, N. N. Kuzma, and W. Happer, *Push-pull optical pumping of pure superposition states*, Phys. Rev. Lett. **93**, 1 (2004).

[54] G. T. Purves, *Absorption And Dispersion In Atomic Vapours: Applications To Interferometery*, PhD Thesis (2006).

[55] M. Fleischhauer, A. Imamoglu, and J. P. Marangos, *Electromagnetically induced transparency: Optics in coherent media*, Rev. Mod. Phys. **77**, 633 (2005).

[56] W. Gerlach and O. Stern, *Der experimentelle Nachweis der Richtungsquantelung im Magnetfeld*, Zeitschrift für Phys. **9**, 349 (1922).

[57] C. S. Adams and E. Riis, *Laser cooling and trapping of neutral atoms*, Prog. Quantum Electron. **21**, 1 (1997).

[58] D. E. Pritchard, *Cooling Neutral Atoms in a Magnetic Trap for Precision Spectroscopy*, Phys. Rev. Lett. **51**, 1336 (1983).

[59] D. Steck, *Rubidium D Line Data* (Unpublished, 2003).

[60] A. L. Schawlow and C. H. Townes, *Infrared and Optical Masers*, Phys. Rev. **112**, 1940 (1958).

[61] T. H. Maiman, *Stimulated Optical Radiation in Ruby*, Nature **187**, 493 (1960).

[62] J. C. Maxwell, *A Treatise on Electricity and Magnetism*, A Treatise on Electricity and Magnetism No. v. 1 (Clarendon Press, 1873).

[63] W. D. Phillips, *Nobel Lecture: Laser cooling and trapping of neutral atoms*, Rev. Mod. Phys. **70**, 721 (1998).

[64] A. Ashkin, *Acceleration and Trapping of Particles by Radiation Pressure*, Phys. Rev. Lett. **24**, 156 (1970).

[65] T. Hänsch and A. Schawlow, *Cooling of gases by laser radiation*, Opt. Commun. **13**, 68 (1975).

[66] D. W. Dehmelt and H., *No Title*, Bull. Am. Phys. Soc. **20**, 637 (1975).

[67] D. J. Wineland, R. E. Drullinger, and F. L. Walls, *Radiation-Pressure Cooling of Bound Resonant Absorbers*, Phys. Rev. Lett. **40**, 1639 (1978).

[68] W. Neuhauser, M. Hohenstatt, P. Toschek, and H. Dehmelt, *Optical-Sideband Cooling of Visible Atom Cloud Confined in Parabolic Well*, Phys. Rev. Lett. **41**, 233 (1978).

[69] W. D. Phillips and H. Metcalf, *Laser Deceleration of an Atomic Beam*, Phys. Rev. Lett. **48**, 596 (1982).

[70] S. Chu, L. Hollberg, J. Bjorkholm, A. Cable, and A. Ashkin, *Three-dimensional viscous confinement and cooling of atoms by resonance radiation pressure.*, Phys. Rev. Lett. **55**, 48 (1985).

[71] A. Arnold, *Preparation and Manipulation of an Rb87 Bose-Einstein Condensate*, PhD Thesis (1999).

[72] P. D. Lett *et al.*, *Optical molasses*, J. Opt. Soc. Am. B **6**, 2084 (1989).

[73] P. D. Lett *et al.*, *Observation of atoms laser cooled below the doppler limit*, Phys. Rev. Lett. **61**, 169 (1988).

[74] Y. Castin, H. Wallis, and J. Dalibard, *Limit of Doppler cooling*, J. Opt. Soc. Am. B **6**, 2046 (1989).

[75] E. L. Raab, M. Prentiss, A. Cable, S. Chu, and D. E. Pritchard, *Trapping of Neutral Sodium Atoms with Radiation Pressure*, Phys. Rev. Lett. **59**, 2631 (1987).

[76] C. Monroe, W. Swann, H. Robinson, and C. Wieman, *Very cold trapped atoms in a vapor cell*, Phys. Rev. Lett. **65**, 1571 (1990).

[77] A. M. Steane, M. Chowdhury, and C. J. Foot, *Radiation force in the magneto-optical trap*, J. Opt. Soc. Am. B **9**, 2142 (1992).

[78] C. D. Wallace, T. P. Dinneen, K.-Y. N. Tan, T. T. Grove, and P. L. Gould, *Isotopic difference in trap loss collisions of laser cooled rubidium atoms*, Phys. Rev. Lett. **69**, 897 (1992).

[79] K. Lindquist, M. Stephens, and C. Wieman, *Experimental and theoretical study of the vapor-cell Zeeman optical trap*, Phys. Rev. A **46**, 4082 (1992).

[80] R. H. Good, *Elliptic integrals, the forgotten functions*, Eur. J. Phys. **22**, 119 (2001).

[81] D. S. Weiss, E. Riis, Y. Shevy, P. J. Ungar, and S. Chu, *Optical molasses and multilevel atoms: experiment*, J. Opt. Soc. Am. B **6**, 2072 (1989).

[82] J. Dalibard and C. Cohen-Tannoudji, *Laser cooling below the Doppler limit by polarization gradients: simple theoretical models*, J. Opt. Soc. Am. B **6**, 2023 (1989).

[83] S. Hopkins and A. Durrant, *Parameters for polarization gradients in three-dimensional electromagnetic standing waves*, Phys. Rev. A **56**, 4012 (1997).

[84] A. Aspect, E. Arimondo, R. Kaiser, N. Vansteenkiste, and C. Cohen-Tannoudji, *Laser cooling below the one-photon recoil energy by velocity-slective coherent population trapping*, Phys. Rev. Lett. **61**, 826 (1988).

[85] E. Haller *et al.*, *Single-atom imaging of fermions in a quantum-gas microscope*, Nat Phys **11**, 738 (2015).

[86] M.-O. Mewes *et al.*, *Bose-Einstein Condensation in a Tightly Confining dc Magnetic Trap*, Phys. Rev. Lett. **77**, 416 (1996).

[87] M. Takamoto, F.-L. Hong, R. Higashi, and H. Katori, *An optical lattice clock.*, Nature **435**, 321 (2005).

[88] F. Sorrentino, G. Ferrari, N. Poli, R. Drullinger, and G. M. Tino, *Laser cooling and trapping of atomic strontium for ultracold atom physics, high-precision spectroscopy and quantum sensors*, Mod. Phys. Lett. B **20** (2006).

[89] C. Gross, T. Zibold, E. Nicklas, J. Estève, and M. K. Oberthaler, *Nonlinear atom interferometer surpasses classical precision limit*, Nature **464**, 1165 (2010).

[90] S. B. Salomon *et al.*, *Cold atom clocks and applications*, J. Phys. B At. Mol. Opt. Phys. **38**, 449 (2005).

[91] M. E. Zawadzki, P. F. Griffin, E. Riis, and A. S. Arnold, *Spatial interference from well-separated split condensates*, Phys. Rev. A **81**, 43608 (2010).

[92] J. Kitching, S. Knappe, and L. Liew, *Chip-scale atomic frequency references*, Gps World , 13 (2007).

[93] S. Pollock, *Integration of Magneto Optical Traps in Atom Chips Integration of Magneto Optical Traps in Atom Chips*, PhD Thesis , 187 (2010).

[94] M. Vangeleyn, P. F. Griffin, E. Riis, and A. S. Arnold, *Single-laser, one beam, tetrahedral magneto-optical trap*, Opt. Express **17**, 13601 (2009).

[95] M. Vangeleyn, P. F. Griffin, E. Riis, and A. S. Arnold, *Laser cooling with a single laser beam and a planar diffractor*, Opt. Lett. **35**, 3453 (2010).

[96] M. A. Golub and A. A. Friesem, *Effective grating theory for resonance domain surface-relief diffraction gratings*, J. Opt. Soc. Am. A **22**, 1115 (2005).

[97] H. Search, C. Journals, A. Contact, M. Iopscience, and I. P. Address, *Correlation between Efficiency of Diffraction Gratings and Theoretical Calculations over a Wide Range*, **143**.

[98] C. Palmer, *Diffraction Grating Handbook*, Newport Corp. , 1 (2005).

[99] M. Okano, H. H. Kikuta, Y. Hirai, K. Yamamoto, and T. Yotsuya, *Optimization of diffraction grating profiles in fabrication by electron-beam lithography*, Appl. Opt. **43**, 5137 (2004).

[100] A. A. Tseng, K. Chen, C. D. Chen, and K. J. Ma, *Electron beam lithography in nanoscale fabrication: recent development*, IEEE Trans. Electron. Packag. Manuf. **26**, 141 (2003).

[101] U. D. Zeitner *et al.*, *High performance diffraction gratings made by e-beam lithography*, Appl. Phys. A **109**, 789 (2012).

[102] J. P. Cotter *et al.*, *Design and fabrication of diffractive atom chips for laser cooling and trapping*, Appl. Phys. B **122**, 1 (2016).

[103] J. P. McGilligan, P. F. Griffin, E. Riis, and A. S. Arnold, *Phase-space properties of magneto-optical traps utilising micro-fabricated gratings*, Opt. Express **23**, 8948 (2015).

[104] T. N. Woods, R. T. Wrigley, G. J. Rottman, and R. E. Haring, *Scattered-light properties of diffraction gratings*, Appl. Opt. **33**, 4273 (1994).

[105] V. R. Weidner, J. J. Hsia, U. States., and N. B. of Standards., *NBS measurement services : spectral reflectance* (U.S. Dept. of Commerce, National Bureau of Standards, Gaithersburg, Md.; Washington, D.C., 1987).

[106] M. H. Anderson, J. R. Ensher, M. R. Matthews, C. E. Wieman, and E. A. Cornell, *Observation of Bose-Einstein Condensation in a Dilute Atomic Vapor*, Science. **269**, 198 (1995).

[107] E. A. Cornell and C. E. Wieman, *Nobel lecture: Bose-Einstein condensation in a dilute gas, the first 70 years and some recent experiments*, Rev. Mod. Phys. **74**, 875 (2002).

[108] H. J. Metcalf and P. van der Straten, *Laser Cooling and Trapping,*Graduate Texts in Contemporary Physics (Springer New York, 2001).

[109] S. D. Saliba and R. E. Scholten, *Linewidths below 100 kHz with external cavity diode lasers*, Appl. Opt. **48**, 6961 (2009).

[110] M. Fleming and A. Mooradian, *Spectral characteristics of external-cavity controlled semiconductor lasers*, IEEE J. Quantum Electron. **17**, 44 (1981).

[111] A. S. Arnold, J. S. Wilson, and M. G. Boshier, *A simple extended-cavity diode laser*, Rev. Sci. Instrum. **69**, 1236 (1998).

[112] K. B. MacAdam, A. Steinbach, and C. Wieman, *A narrowband tunable diode laser system with grating feedback, and a saturated absorption spectrometer for Cs and Rb*, Am. J. Phys. **60**, 1098 (1992).

[113] A. Dinkelaker, *Smooth Inductively Coupled Ring Trap for Cold Atom Optics*, (2013).

[114] M. Vangeleyn, *Atom trapping in non-trivial geometries for micro-fabrication applications*, PhD Thesis , 181 (2011).

[115] C. J. Hawthorn, K. P. Weber, and R. E. Scholten, *Littrow configuration tunable external cavity diode laser with fixed direction output beam*, Rev. Sci. Instrum. **72**, 4477 (2001).

[116] G. W. Hansch, T. W., Schawlow, A. L., Series, *The Spectrum of Atomic Hydrogen*, Sci. Am. **240**, 94 (1979).

[117] K. B. MacAdam, A. Steinbach, and C. Wieman, *A narrow band tunable diode laser system with grating feedback, and a saturatedabsorption spectrometer for Cs and Rb*, Am. J. Phys. **60**, 1098 (1992), 9605103.

[118] D. Jalas *et al.*, *What is and what is not an optical isolator*, Nat Phot. **7**, 579 (2013).

[119] J. N. Walpole, *Semiconductor amplifiers and lasers with tapered gain regions*, Opt. Quantum Electron. **28**, 623 (1996).

[120] G. Santarelli *et al.*, *Quantum Projection Noise in an Atomic Fountain: A High Stability Cesium Frequency Standard*, Phys. Rev. Lett. **82**, 4619 (1999).

[121] E. Donley, T. C. Liebisch, E. Blanshan, and J. Kitching, *Number enhancement for compact laser-cooled atomic samples by use of stimulated radiation forces*, 2010 IEEE Int. Freq. Control Symp. FCS 2010 , 125 (2010).

[122] G. W. Hoth, E. A. Donley, and J. Kitching, *Atom number in magneto-optic traps with millimeter scale laser beams*, Opt. Lett. **38**, 661 (2013).

[123] S. Pollock, J. P. Cotter, A. Laliotis, F. Ramirez-Martinez, and E. A. Hinds, *Characteristics of integrated magneto-optical traps for atom chips*, New J. Phys. **13** (2011).

[124] J. P. McGilligan *et al.*, *Grating chips for quantum technologies*, Sci. Rep. **7**, 384 (2017).

[125] F. Shimizu, K. Shimizu, and H. Takuma, *Four-beam laser trap of neutral atoms*, Opt. Lett. **16**, 339 (1991).

[126] K. I. Lee, J. A. Kim, H. R. Noh, and W. Jhe, *Single-beam atom trap in a pyramidal and conical hollow mirror*, Opt. Lett. **21**, 1177 (1996).

[127] D. S. Weiss, E. Riis, Y. Shevy, P. J. Ungar, and S. Chu, *Optical molasses and multilevel atoms: experiment*, J. Opt. Soc. Am. B **6**, 2072 (1989).

[128] P. D. Lett *et al.*, *Optical molasses*, J. Opt. Soc. Am. B **6**, 2084 (1989).

[129] D. W. Sesko, T. G. Walker, and C. E. Wieman, *Behavior of neutral atoms in a spontaneous force trap*, J. Opt. Soc. Am. B **8**, 946 (1991).

[130] W. Ketterle, K. B. Davis, M. A. Joffe, A. Martin, and D. E. Pritchard, *High densities of cold atoms in a dark spontaneous-force optical trap*, Phys. Rev. Lett. **70**, 2253 (1993).

[131] N. Radwell, G. Walker, and S. Franke-Arnold, *Cold-atom densities of more than 10^{12} cm^{-3} in a holographically shaped dark spontaneous-force optical trap*, Phys. Rev. A **88**, 43409 (2013).

[132] K. Jooya, N. Musterer, K. W. Madison, and J. L. Booth, *Photon-scattering-rate measurement of atoms in a magneto-optical trap*, Phys. Rev. A **88**, 63401 (2013).

[133] C. G. Townsend *et al.*, *Phase-space density in the magneto-optical trap*, Phys. Rev. A **52**, 1423 (1995).

[134] M. Drewsen *et al.*, *Investigation of sub-Doppler cooling effects in a cesium magneto-optical trap*, Appl. Phys. B **59**, 283 (1994).

[135] C. J. C. Foot *et al.*, *The Temperature of Atoms in a Magneto-optical Trap*, Europhysics Lett. **28**, 397 (1994).

[136] J. P. McGilligan, P. F. Griffin, E. Riis, and A. S. Arnold, *Diffraction-grating characterization for cold-atom experiments*, J. Opt. Soc. Am. B **33**, 1271 (2016).

[137] J. P. McGilligan, P. F. Griffin, E. Riis, and A. S. Arnold, *Phase-space properties of magneto-optical traps utilising micro-fabricated gratings*, Opt. Express **23**, 8948 (2015).

[138] M. Guarnieri, *Once Upon a Time?The Compass [Historical]*, IEEE Ind. Electron. Mag. **8**, 60 (2014).

[139] C. F. Gauss, *Intensitas Vis Magneticae Terrestris ad Mensuram Absolutam Revocata* (Springer Berlin Heidelberg, Berlin, Heidelberg, 1877), pp. 79–118.

[140] S. J. Seltzer, *Developments in Alkali-Metal Atomic Magnetometry*, PhD Thesis (2008).

[141] I. K. Kominis, T. W. Kornack, J. C. Allred, and M. V. Romalis, *A subfemtotesla multichannel atomic magnetometer*, Nature **422**, 596 (2003).

[142] D. Robbes, *Highly sensitive magnetometers-a review*, Sensors Actuators, A Phys. **129**, 86 (2006).

[143] E. Boto *et al.*, *On the Potential of a New Generation of Magnetometers for MEG: A Beamformer Simulation Study*, PLoS One **11**, 1 (2016).

[144] A. N. Garroway, M. L. Buess, J. P. Yesinowski, and J. B. Miller, *Narcotics and explosives detection by 14N pure nuclear quadrupole resonance*, 1994.

[145] S. H. Silliman, P. Farnsworth, and K. G. Lightfoot, *Magnetometer prospecting in historical archaeology: Evaluating survey options at a 19th-century rancho site in California*, Hist. Archaeol. **34**, 89 (2000).

[146] L. L. Nettleton, *Gravity and Magnetic Calculations*, Geo. Phys. **7**, 293 (1942).

[147] D. Budker and M. Romalis, *Optical magnetometry*, Nat Phys **3**, 227 (2007).

[148] R. J. Behbood, N., Martin Ciurana, F., Colangelo, G., Napolitano, M., Mitchell, M. W., and Sewell, *Real-time vector field tracking with a cold-atom magnetometer*, Appl. Phys. Lett. **102**, 173504 (2013).

[149] A. Wojciechowski, E. Corsini, J. Zachorowski, and W. Gawlik, *Nonlinear Faraday rotation and detection of superposition states in cold atoms*, Phys. Rev. A - At. Mol. Opt. Phys. **81**, 1 (2010).

[150] S. Pustelny, D. F. Jackson Kimball, S. M. Rochester, V. V. Yashchuk, and D. Budker, *Influence of magnetic-field inhomogeneity on nonlinear magneto-optical resonances*, Phys. Rev. A **74**, 063406 (2006).

[151] J. Lee, J. a. Grover, L. a. Orozco, and S. L. Rolston, *Sub-Doppler cooling of neutral atoms in a grating magneto-optical trap*, J. Opt. Soc. Am. B **30**, 2869 (2013).

[152] Bodart, Q., Merlet, S., Malossi, N., Pereira Dos Santos, F., Bouyer, P., and Landragin, A., *A cold atom pyramidal gravimeter with a single laser beam*, Appl. Phys. Lett. **96**, 134101 (2010).

[153] C. Monroe, *No Title*, PhD thesis, 1992.

[154] E. Weatherill, K. J., Pritchard, J. D., Griffin, P. F., Dammalapati, U., Adams, C. S., and Riis, *A versatile and reliably reusable ultrahigh vacuum viewport*, Rev. Sci. Instrum. **80**, 26105 (2009).

[155] A. T. Dellis, V. Shah, E. A. Donley, S. Knappe, and J. Kitching, *Low helium permeation cells for atomic microsystems technology*, Opt. Lett. **41**, 2775 (2016).

[156] J. I. Cirac and P. Zoller, *A scalable quantum computer with ions in an array of microtraps*, Nature **404**, 579 (2000).

[157] A. V. Rakholia, H. J. McGuinness, and G. W. Biedermann, *Dual-Axis High-Data-Rate Atom Interferometer via Cold Ensemble Exchange*, Phys. Rev. Appl. **2**, 54012 (2014).

[158] D. Stick *et al.*, *Ion trap in a semiconductor chip*, Nat Phys **2**, 36 (2006).

[159] S. Whitlock, R. Gerritsma, T. Fernholz, and R. J. C. Spreeuw, *Two-dimensional array of microtraps with atomic shift register on a chip*, New J. Phys. **11**, 023021 (2009).

[160] C. Weitenberg *et al.*, *Single-spin addressing in an atomic Mott insulator*, Nature **471**, 319 (2011).

[161] S. Bergamini *et al.*, *Holographic generation of microtrap arrays for single atoms by use of a programmable phase modulator*, J. Opt. Soc. Am. B **21**, 1889 (2004).

[162] A. Grabowski and T. Pfau, *A lattice of magneto-optical and magnetic traps for cold atoms*, Eur. Phys. J. D **22**, 347 (2003).

[163] I. I. Rabi, J. R. Zacharias, S. Millman, and P. Kusch, *A New Method of Measuring Nuclear Magnetic Moment*, Phys. Rev. **53**, 318 (1938).

[164] J. Vanier, *Atomic clocks based on coherent population trapping: a review*, Appl. Phys. B **81**, 421 (2005).

[165] J. Schwindt, Peter D D; Knappe, Svenja; Shah, Vishal; Hollberg, Leo; and Kitching, *Chip-scale atomic magnetometer*, Appl. Phys. Lett. **85**, 6409 (2004).

[166] L. G.-B. Si-Hong, D. Run-Chang, L. Chao-Yang, and Gu, *CPT Magnetometer with Atomic Energy Level Modulation*, Chinese Phys. Lett. **25**, 472 (2008).

[167] F. Z. Gu, Y. Tian, Y. Zhang, and Si-Hong, *Coherent population trapping magnetometer by differential detecting magnetoâĂŞoptic rotation effect*, Chinese Phys. B **25**, 94206 (2016).

[168] R. Grimm, M. Weidemüller, and Y. Ovchinnikov, *Optical dipole trap for neutral atoms*, Adv. At. Mol. Opt. Phys. **42**, 95 (2000).

[169] M. Stähler *et al.*, *Coherent population trapping resonances in thermal 85Rb vapor: D1 versus D2 line excitation*, Opt. Lett. **27**, 1472 (2002).

[170] R. Boudot, S. Guerandel, E. de Clercq, N. Dimarcq, and A. Clairon, *Current status of a pulsed CPT Cs cell clock*, IEEE Trans. Instrum. Meas. **58**, 1217 (2009).

[171] T. Zanon *et al.*, *High contrast ramsey fringes with coherent-population-Trapping pulses in a double lambda atomic system*, Phys. Rev. Lett. **94**, 3 (2005).

[172] T. Zanon *et al.*, *Recent results on a pulsed CPT clock*, Proc. IEEE Int. Freq. Control Symp. Expo. **2005**, 774 (2005).

[173] A. V. Taichenachev, V. I. Yudin, V. L. Velichansky, and S. A. Zibrov, *On the unique possibility of significantly increasing the contrast of dark resonances on the D1 line of 87Rb*, J. Exp. Theor. Phys. Lett. **82**, 398 (2005).

[174] S. A. Zibrov *et al.*, *Coherent-population-trapping resonances with linearly polarized light for all-optical miniature atomic clocks*, Phys. Rev. A - At. Mol. Opt. Phys. **81**, 1 (2010).

[175] F. X. Esnault *et al.*, *Cold-atom double-Λ coherent population trapping clock*, Phys. Rev. A - At. Mol. Opt. Phys. **88**, 1 (2013).

[176] R. Wynands and A. Nagel, *Invited paper Precision spectroscopy with coherent dark states*, **25**, 1 (1999).

[177] N. Belcher, E. E. Mikhailov, and I. Novikova, *Atomic clocks and coherent population trapping: Experiments for undergraduate laboratories*, Am. J. Phys. **77**, 988 (2009).

[178] J. Camparo, *The rubidium atomic clock and basic research*, Phys. Today (2007).

[179] F. X. Esnault *et al.*, *Cold-atom double-Λ coherent population trapping clock*, Phys. Rev. A - At. Mol. Opt. Phys. **88**, 1 (2013).

[180] I. I. Rabi, N. F. Ramsey, and J. Schwinger, *Use of rotating coordinaes in magnetic resonance problems*, Rev. Mod. Phys. **26** (1954).

[181] C. Cohen-Tannoudji, B. Diu, and F. Laloë, *Quantum mechanics* (Wiley, 1977).

[182] P. R. Berman, *Atom Interferometry* (Elsevier Science, 1997).

[183] K. Moler, D. S. Weiss, M. Kasevich, and S. Chu, *Theoretical analysis of velocity-selective Raman transitions*, Phys. Rev. A **45**, 342 (1992).

[184] J. E. Thomas *et al.*, *Observation of Ramsey Fringes Using a Stimulated, Resonance Raman Transition in a Sodium Atomic Beam*, Phys. Rev. Lett. **48**, 867 (1982).

[185] G. S. Pati, F. K. Fatemi, and M. S. Shahriar, *Observation of query pulse length dependent Ramsey interference in rubidium vapor using pulsed Raman excitation.*, Opt. Express **19**, 22388 (2011).

[186] K. Kotru, J. M. Brown, D. L. Butts, J. M. Kinast, and R. E. Stoner, *Robust Ramsey sequences with Raman adiabatic rapid passage*, Phys. Rev. A - At. Mol. Opt. Phys. **90** (2014).

[187] Y. Feng, H. Xue, X. Wang, S. Chen, and Z. Zhou, *Observation of Ramsey fringes using stimulated Raman transitions in a laser-cooled continuous rubidium atomic beam*, Appl. Phys. B **118**, 139 (2015).

[188] E. Blanshan, S. M. Rochester, E. A. Donley, and J. Kitching, *Light shifts in a pulsed cold-atom coherent-population-trapping clock*, Phys. Rev. A - At. Mol. Opt. Phys. **91**, 1 (2015).

[189] I. Hughes and T. Hase, *Measurements and their Uncertainties: A practical guide to modern error analysis* (OUP Oxford, 2010).

[190] C. Xi, Y. Guo-Qing, W. Jin, and Z. Ming-Sheng, *Coherent Population Trapping-Ramsey Interference in Cold Atoms*, Chinese Phys. Lett. **27**, 113201 (2010).

[191] J. A. Rushton, M. Aldous, and M. D. Himsworth, *Contributed Review: The feasibility of a fully miniaturized magneto-optical trap for portable ultracold quantum technology*, Rev. Sci. Instrum. **85**, 121501 (2014).

[192] C. Wieman, *Inexpensive laser cooling and trapping experiment for undergraduate laboratories*, Am. J. Phys. **63**, 317 (1995).